UNIVERSITY OF CALIFORNIA,
IRVINE

Expanding Ln(II) Chemistry with Bis(trimethylsilyl)amide Ligands

DISSERTATION

submitted in partial satisfaction of the requirements
for the degree of

DOCTOR OF PHILOSOPHY

in Chemistry

by

Austin Jack Ryan

Dissertation Committee:
Professor William J. Evans, Chair
Associate Professor Jenny Y. Yang
Professor Andy S. Borovik

2020

DEDICATION

To

My Mom and Dad, thank you for your constant support and belief that I can accomplish anything. None of this would have been possible without you.

“If you’re the smartest person in the room, you’re in the wrong room”
-Dad

Table of Contents

List of Figures

List of Tables

ACKNOWLEDGMENTS

Foremost, I would like to express my gratitude to my advisor Bill Evans whose guidance and mentorship have been invaluable in my progression as a scientist. It has been a pleasure being able to work with you for the past few years and your genuine excitement about chemistry is infectious. I have enjoyed every conversion we have had about science and always come away with more to think about. You have been an excellent mentor always seeming to know when to push and when not to. You genuinely care about your students and their well-being beyond what goes on in the lab and you set a prime example for what it means to be a professional that we should all strive to achieve. I look forward to seeing what's next in your long line of breakthroughs in defining the field of low-valent f-element chemistry and hope to continue our conversations about chemistry.

I'd like to thank a mentor and friend in Dr. Joe Ziller. The opportunity to work with you and learn the nuances of X-ray crystallography was one of favorite parts of grad school. The level of care and time you dedicate to your facility cannot be overstated. The proof is in that old Seimens instrument you've kept running for the past 25 or so years despite its best efforts to die on you. Looking forward to a beer at Patsy's sometime soon.

I have had several wonderful collaborators who deserve mention here, Lucy Darago and Colin Gould of UC Berkeley have provided wonderful insight into magnetism of lanthanide complexes and produce only the highest quality of work and thinking which I value and have learned from. Sree Balasubramini has been my theoretical partner in decoding the mysteries these complicated new complexes and I am grateful for our conversations in addition to the work he has put into these projects.

To Professor Jenny Yang, I would like to thank you for allowing me to work with you in the summer before my graduate career started. I am grateful for the time you took to help me start my work at UCI and the mentorship you provided while I worked in your group. It provided me a new way of thinking about chemistry and gave me my first platform to perform research on my own, providing me with invaluable experience going forward.

To Sam Moehring and Dan Huh, I am grateful to have had you two with me for my whole time in the Evans lab. I always had the motivation to do better knowing you two were on the clock cranking out results and rethinking the way our chemistry works.

To all other Evans group members former and present, I am grateful for such a good group of people to help keep our lab running smooth. It is not a one-person job and on top of that you all made it enjoyable more often than not.

I am grateful for all the friends I have made along the way who have made my grad school a pleasure. Two good buds, Drew and Tener, have been my best friends and I look forward to seeing you two well beyond the end of grad school.

Lastly and most importantly I'd like to acknowledge my family for their constant support along the way. Mom, Dad, Jill, Ed, 'Chelle, Brandon, Ana, this one is for you.

Vita
Austin J. Ryan

EDUCATION

University of California-Irvine, Irvine, CA — October 2015 – February 2020
Doctor of Philosophy, Chemistry
GPA: 3.9/4.0

University of Florida, Gainesville, FL — August 2013 – May 2015
Bachelor of Science, Chemistry
GPA: 3.0/4.0

University of Central Florida, Orlando, Fl — August 2011 – August 2013
GPA: 3.6/4.0

RESEARCH EXPERIENCE

Research Assistant, **W. J. Evans Group at University of California, Irvine**
Winter 2016 – Present

Research on synthesizing and investigating the physical properties of low valent f-element complexes especially those relevant to single molecule magnets and molecular qubits
Utilized amide ligand sets in the isolation and characterization of highly reactive divalent rare-earth and uranium species requiring the use of meticulous air-free Schlenk and glove box techniques
Investigated reactivity of non-traditional divalent rare-earth complexes with small molecules such as CO, CO_2, N_2 and NO both in-situ and in high-pressure (80 psi) solid state gas reactions
Isolated ynediolate and enediolate products from the reductive coupling of CO and the first lanthanide end-on bound dinitrogen complexes, Ln-N=N-Ln.
Collaborated with scientists at Cal Tech to design laser ablation experiments with lanthanide metals to form Ln(0) arene complexes
Acquired experience and proficiency in a variety of spectroscopies to characterize and interrogate the physical properties of the above compounds including, Raman, UV-visible, infrared, NMR and EPR spectroscopies as well as X-ray Absorption Near Edge Spectroscopy (XANES), X-Ray Photoelectron Spectroscopy (XPS), SQUID measurements and X-ray crystallography

X-Ray Crystallography Fellow, **University of California, Irvine** — Winter 2018 – Winter 2019
Mounted crystals, set up data acquisition and solved structures for the chemistry department
Solved multi-component twined crystals routinely
Acquired data on powder samples using a Bruker D8 system
Performed system maintenance on Bruker APEX2 systems
Attended American Crystallographic Association (ACA) summer course on single crystal and powder X-ray diffraction

Research Assistant, **J. Y. Yang Group at University of California, Irvine** — Summer 2015
Research on creating catalysts aimed at the reduction of CO_2 through electrocatalysis
Synthesized and characterized heterobimetallic complexes with cobalt and various incorporating a salen-crown ligand aimed at CO_2 capture and functionalization

Performed a series of cyclic voltammetry experiments on salen-crown heterobimetallic complexes under a CO_2 atmosphere to gauge their ability to electrochemically reduce CO_2
Research Assistant, **A. S. Veige Group at University of Florida** Fall 2014 – Summer 2015
Research towards increasing the air stability of a highly active tungsten alkylidyne catalyst used in alkyne polymerization reactions
Helped in characterization of a novel class of cyclic polymers formed by ring expansion through use of trianionic pincer ligands appended to a tungsten alkylidyne
Research Assistant, **W. Tan Group at University of Florida** Winter 2014 – Fall 2015
Worked on DNA aptamer selection using the Cell SELEX method
Utilized PCR to specifically amplify sequences having high binding affinity to a target
Utilized flow cytometry assays to monitor the binding of selected pools with CCRF-CEM cells (target cells) and Ramos cells (negative cells)

HONORS

Phi Eta Sigma Honor Society, University of Central Florida
3rd Place Undergraduate Poster, *Progress Towards an Air Stable Pre-Catalyst for the Ring Expansion Polymerization of Alkyne,* ACS F.A.M.E 2015
University Scholars Travel Grant, to present research at the FAME conference in 2015, University of Florida
Graduate Teaching Fellowship, for the graduate organometallics course in fall 2016, UC-Irvine
Guest Lecturer, for the graduate level organometallics course fall 2017, UC-Irvine
X-ray Crystallography Fellowship, to learn and assist in x-ray diffraction experiments, winter 2018 to winter 2019, UC-Irvine
ACA Summer Course Studentship Grant, to attend a course on X-ray crystallography held by the American Crystallographic Association, summer 2018, Notre Dame University

PUBLICATIONS AND PRESENTATIONS

Publications:
Reath, A. H.; Ziller, J. W.; Tsay, C.; Ryan, A. J.; Yang, J. Y., Redox Potential and Electronic Structure Effects of Proximal Nonredox Active Cations in Cobalt Schiff Base Complexes *Inorg. Chem.* **2017**, *56*, 3713.
Fieser, M. E.; Ferrier, M. G.; Su, J.; Batista, E.; Cary, S. K.; Engle, J. W.; Evans, W. J.; Lezama Pacheco, J. S.; Kozimor, S. A.; Olson, A. C.; Ryan, A. J.; Stein, B. W.; Wagner, G. L.; Woen, D. H.; Vitova, T.; Yang, P., Evaluating the Electronic Structure of Formal Ln^{II} Ions in $Ln^{II}(C_5H_4SiMe_3)_3^{1-}$ using XANES Spectroscopy and DFT Calculations. *Chem. Sci.* **2017,** *8*, 6076.
Ryan, A. J.; Darago, L. E.; Balasubramani, S. G.; Chen, G. P.; Ziller, J. W.; Furche, F.; Long, J. R.; Evans, W. J., Synthesis, Structure, and Magnetism of Tris (amide)$[Ln\{N(SiMe_3)_2\}_3]^{1-}$ Complexes of the Non-traditional+ 2 Lanthanide Ions. *Chem. Eur. J.* **2018,** *24*, 7702.
Ryan, A. J.; Angadol, M. A.; Ziller, J. W.; Evans, W. J., Isolation of U(II) Compounds Using the Strong Donor Ligands, C_5Me_4H and $N(SiMe_3)_2$, Including a Three-Coordinate U(II) Complex. *Chem. Commun.*, **2019**, *55*, 2325.
Ryan A.J., Evans W.J. **2019,** The Periodic Table as a Career Guide: A Journey to Rare Earths. In: . Structure and Bonding. Springer, Berlin, Heidelberg

Ryan, A. J.; Ziller, J. W.; Evans, W. J., The Importance of the Countercation in Isolating Ln(II) Rare-Earth Metal Complexes: Isolation of $[Y^{II}(NR_2)_3]^{1-}$ and CO Reactivity to Form Ynediolate and Enediolate Complexes. *Chem. Sci.* **2020,** *11*, 2006-2014.
Ryan, A. J.; Balasubramini, S.; Ziller, J. W.; Furche, F. F.; Evans, W. J., Formation of the End-on Bound Lanthanide Dinitrogen Complexes, $[(R_2N)_3Ln{-}N{=}N{-}Ln(NR_2)_3]^{2-}$, from Divalent $[(R_2N)_3Ln]^{1-}$ Salts (R = $SiMe_3$). *J. Am. Chem. Soc.* **2020**, *Accepted*

Presentations:

Austin J. Ryan; Christopher D. Roland; Adam S. Veige. *Progress Towards an Air Stable Pre Catalyst for the Ring Expansion Polymerization of Alkynes*. 91st Florida Annual meeting and Exposition, Palm Harbor, FL, May 8th 2015; Florida Local Section of the American Chemical Society. (Poster)
Austin J. Ryan; Joseph W. Ziller, William J. Evans *Synthesis, Structure, and Reactivity of Complexes Containing +2 Ions of Late Lanthanide Metals in Tris(silylamide) Coordination Environments, $\{Ln[N(SiMe_3)_2]_3\}^{1-}$*. 253rd American Chemical Society National Meeting and Exposition, San Francisco, CA, April 6th 2017; The American Chemical Society. (Oral)
Austin J. Ryan; Joseph W. Ziller, William J. Evans *Synthesis and Reactivity of the Isolated Divalent Lanthanide Complexes $\{Ln[N(SiMe_3)_2]_3\}^{1-}$ with Small Molecules: CO and N_2.* 255th American Chemical Society National Meeting and Exposition, New Orleans, LA, March 21st 2018; The American Chemical Society. (Oral)
Austin J. Ryan; Lucy E. Darago; Sree Ganesh Balasubramani; Guo P. Chen; Joseph W. Ziller; Filipp Furche; Jeffrey L. Long; William J. Evans, *Isolation and Dinitrogen Reactivity of the Divalent Lanthanide Complexes$\{Ln[N(SiMe_3)_2]_3\}^{1-}$*. UC-Chemical Symposium 2018, Lake Arrowhead, CA, March 26th 2018; University of California. (Poster)

Abstract of Dissertation

Expanding Ln(II) Chemistry with Bis(trimethylsilyl)amide Ligands

By

Austin J. Ryan

Doctor of Philosophy in Chemistry

University of California, Irvine, 2020

Professor William J. Evans, Chair

This dissertation describes efforts to expand the understanding of Ln(II) chemistry, particularly that of the non-traditional $4f^n5d^1$ ions, through the synthesis and isolation of new Ln(II) species supported by bis(trimethylsilyl)amide ligands and exploration of their reactivity. Described herein is the isolation of a new series of Ln(II) complexes ligated by NR_2 ($R = SiMe_3$) ligands. These ligands were previously not thought to be capable of supporting the non-traditional lanthanide ions in the 2+ oxidation state. Following their isolation, the reaction chemistry of these $[Ln^{II}NR_2)_3]^{1-}$ complexes was investigated to provide insight into the unique reaction chemistry of non-traditional Ln(II) ions. Chapter 1 outlines the synthesis and characterization of a new series of Ln(II) complexes $[M(crypt)][Ln(NR_2)_3]$ (M = K or Rb) and describes their spectroscopic properties as they relate to electron configuration. Chapter 2 discusses the synthesis of the elusive $[Y^{II}(NR_2)_3]^{1-}$ complex in addition to reactions of $[Ln(NR_2)_3]^{1-}$ with CO. Chapter 3 describes new examples of uranium in the +2 oxidation state isolated by reduction of $Cp^{tet}{}_3U$ ($Cp^{tet} = C_5Me_4H$) and $U(NR_2)_3$ ($R = SiMe_3$) in the presence of 2.2.2-cryptand to produce $[K(crypt)][Cp^{tet}{}_3U]$ and $[K(crypt)][U(NR_2)_3]$, respectively. Chapter 4

expands the understanding of lanthanide-based dinitrogen reduction chemistry through discovery of the first end-on $Ln_2(\mu\text{-}\eta^1\text{:}\eta^1\text{-}N_2)$ complexes. The formation of end-on versus the more common side-on $Ln_2(\mu\text{-}\eta^2\text{:}\eta^2\text{-}N_2)$ complexes was possible by using the Ln(II) complexes detailed in Chapters 1 and 2. Chapter 5 details the reaction chemistry of the $[Gd(NR_2)_3]^{1-}$ complexes with toluene and the isolation of a methylcyclohexadienyl dianion. Chapter 6 discusses the reaction chemistry of $[Gd(NR_2)_3]^{1-}$ with $BiPh_3$ and PPh_3 and the formation of a rare example of a complex containing a Ln−Bi bond.

Introduction

The lanthanide series encompasses the fifteen elements from La to Lu. Taken with Sc and Y these seventeen elements compromise a group commonly termed the rare earth elements. The rare earth elements are not rare. In fact, the lighter elements of the series, such as scandium, yttrium, lanthanum and cerium, show an abundance in the earth's crust similar to that of cobalt and copper.[1] Even the least abundant rare earth, thulium, is still more abundant than iodine and an order of magnitude more abundant than the precious and platinum group metals.[1] The term "rare earth" was coined over a century ago when the elements were first identified in minerals which were at the time considered "rare".[2] These elements have however become ubiquitous throughout modern life finding applications in industrial catalysis, wind turbine generators, low-energy lighting, rechargeable batteries and MRI imaging to name a few.[2] They are even considered essential to U.S military application with the majority of missile defense systems containing rare earth components.[3]

In the field of single molecule magnets (SMMs), a rapidly expanding area of research due to potential SMM applications in high-density information storage, the lanthanide ions are the current front runners as a result of their intrinsically large magnetic moments and ability to preserve the orbital angular momentum associated with their valence f orbitals.[4] This preservation of orbital angular momentum arises from the limited radial extension of the f orbitals compared to the valence d-orbitals of the transition metals. The property of radially contracted valence orbitals also dictates much of the chemistry of the lanthanide ions. The lack of radial extension means that there is not sufficient overlap of the 4f metal orbitals with ligand

orbitals which results in mostly ionic interactions.[2] Consequently, the chemistry of the lanthanide ions is largely dictated by electrostatic interactions and steric effects.

Oxidation States of the Lanthanides. Integral parts of any study designed to expand the chemistry of an element involve the redox properties of that element. Early reviews in rare-earth chemistry noted that Eu, Yb and Sm were the only elements capable of accessing the 2+ oxidation state in molecular complexes.[5-7] Nd, Tm and Dy were observed to adopt the 2+ oxidation state in the solid state as LnX_2 (X = Cl, Br, I), but not as molecular species.[7] Similar dihalide complexes were synthesized with Ln = La, Ce, Pr and Gd, however their electronic structure was best described as $Ln(III)(e^-)(X)_2$ where the electron is delocalized throughout the solid in a conduction band rather than localized on the metal.[7]

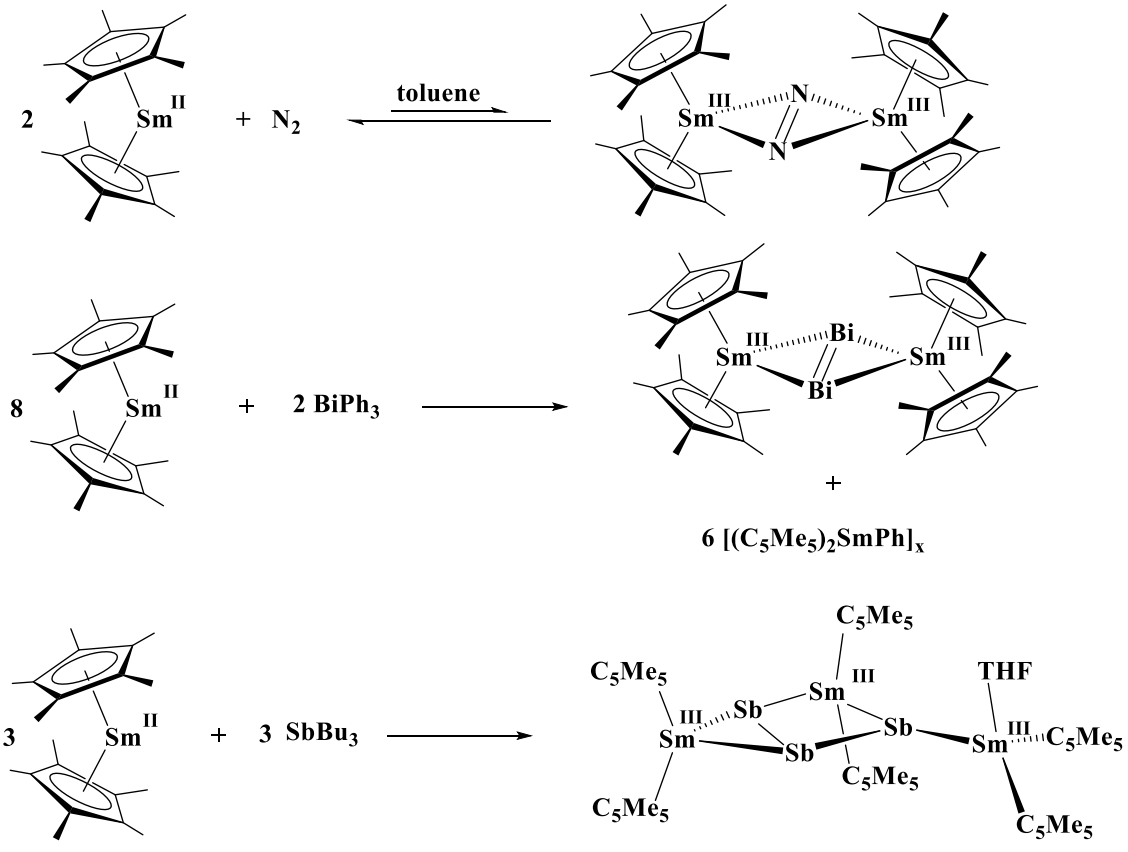

Scheme 0.1. Unique reactivity of $(C_5Me_5)_2Sm$.[8-11]

Following the discovery of Cp^*_2Sm ($Cp^* = C_5Me_5$), a wide range of bond making reductive reactions were observed with this Sm(II) complex not seen in trivalent lanthanide chemistry or in the chemistry of less reducing Eu(II) or Yb(II) ions, including the isolation of the first f element dinitrogen complex. scheme 0.1. It wasn't until the late 1990s that examples of molecular complexes of Nd, Dy and Tm in the 2+ oxidation state were discovered as $LnI_2(solvent)_x$ complexes.[12, 13] The new $LnI_2(solvent)_x$ complexes were good precursors to a number of molecular divalent Tm complexes. However, ligand substitution to form Ln(II)-containing complexes was not observed with NdI_2 and DyI_2 as starting materials.[14] It was not expected that any more oxidation states would be discovered for the lanthanide elements due to very negative estimated reduction potentials for reduction of $4f^n$ Ln(III) ions to $4f^{n+1}$ Ln(II) ions, Table 0.1.

Table 0.1. Calculated reduction potentials for Ln(III)/Ln(II) couple vs SHE based on experimental[a] and thermodynamic[b] data.[5]

Ln	Potential	Ln	Potential
Eu[a]	−0.35	**Ho**[b]	−2.80
Yb[a]	−1.15	**Er**[b]	−2.96
Sm[a]	−1.55	**Pr**[b]	−3.03
Tm[b]	−2.27	**Tb**[b]	−3.47
Dy[b]	−2.42	**La**[b]	−3.74
Nd[b]	−2.62	**Ce**[b]	−3.76
Pm[b]	−2.67	**Gd**[b]	−3.82

This assumption was overturned with the isolation of molecular examples of La and Ce in the 2+ oxidation state supported by silylcyclopentadienyl ligands in the form of $[LnCp''_3]^{1-}$ ($Cp'' = C_5H_3(SiMe_3)_2$).[15] This discovery was astonishing given that the theoretical reduction potentials of

the Ln(III)/Ln(II) couple for La and Ce were – 3.74 and – 3.76 V vs SHE!! As an explanation, the seminal study by Lappert suggested that rather than the reduction of La(III) and Ce(III) occurring in the expected way, with an electron added into an f orbital changing the electron configuration from $4f^n$ to $4f^{n+1}$, the electron introduced was instead added into a 5d orbital creating a mixed quantum number configuration of $4f^n5d^1$.[15]

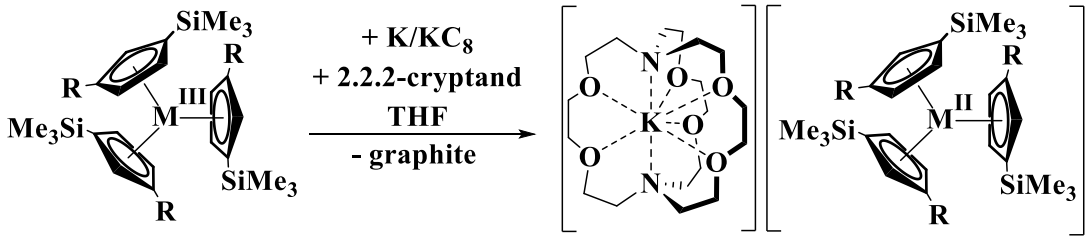

(0.1)

R = $SiMe_3$; M = La, Ce

R = H; M = Y, La, Ce, Pr, Nd, Sm, Gd, Tb, Dy, Ho, Er, Tm, Lu

Upon moving to the slightly smaller silylcyclopentadienyl ligand Cp′, (Cp′ = $C_5H_4SiMe_3$), Evans and coworkers proceeded to synthesize and isolate the entire lanthanide series (except for radioactive Pm), as well as Y, in the 2+ oxidation state in the form of [K(crypt)][$LnCp'_3$], eq 0.1. By maintaining the same $(Cp'_3)^{3-}$ coordination environment across the series, a detailed examination of the physical and electronic properties of these new "non-traditional" divalent ions was possible.[16-19] The findings were illuminating. The "traditional" divalent ions, Eu, Yb, Sm and Tm, all showed the expected $4f^{n+1}$ electron configuration as evidenced by a pronounced change in the Ln−Cp(cnt) distance, 0.1 - 0.2 Å, small extinction coefficients (< 1000 M^{-1} cm^{-1}) in the optical spectra, and magnetic properties consistent with an electron being added to an f-orbital with appropriate angular orbital momentum.[19]

In contrast every other Ln(II) ion in the series showed a $4f^n5d^1$ configuration where, through DFT studies, the electron was proposed to have been added to a d_{z^2} orbital found to be the lowest

energy d orbital in the C_3 symmetric system. Ln−Cp′(cnt) distance changes from 3+ to 2+ for Ln = Y, La, Pr, Nd, Gd, Tb, Dy, Ho, Er, Lu were significantly less, 0.04 - 0.06 Å, than those observed in the traditional systems, 0.1 - 0.2 Å.[19] These new divalent systems also displayed unusually large extinction coefficients in the thousands of M^{-1} cm^{-1} rather than the hundreds, as observed with the traditional ions. The high extinction coefficients were explained with the help of TD-DFT calculations which assigned them as allowed transitions of a 5d electron into a π* ligand orbital.[19]

Further evidence for the mixed $4f^n5d^1$ electron configurations came from magnetic measurements which resulted in magnetic moments best modelled by one electron with no angular momentum contribution (d_{z^2}) coupling to the $4f^n$ electrons.[20] X-ray absorption near edge spectroscopy (XANES) again showed a sharp contrast between the electron configurations of the so called traditional divalent ions and the new non-traditional ions with shifts in the absorption spectrum of 6.6 - 7 eV for the traditional ions compared to a transition metal like shift of 0.02 - 1.9 eV for the non-traditional ions. All of these data supported the assertion that the electron was in fact entering a 5d rather than a 4f orbital.

Rare Earth Amide Complexes. Since its application to chromium in 1972 by Bradley et al.,[21] the bis(trimethylsilyl)amide ligand $(NR_2)^{1-}$ (R = $SiMe_3$), has become ubiquitous throughout inorganic chemistry. When applied to the trivalent rare-earth ions, the steric bulk provided by the $SiMe_3$ groups allowed for isolation of three coordinate complexes across the series.[22, 23] When applied to the divalent ions Sm(II), Eu(II) and Yb(II), neutral[24, 25] or anionic[26, 27] Ln(II) amide complexes could be isolated, Scheme 0.2.

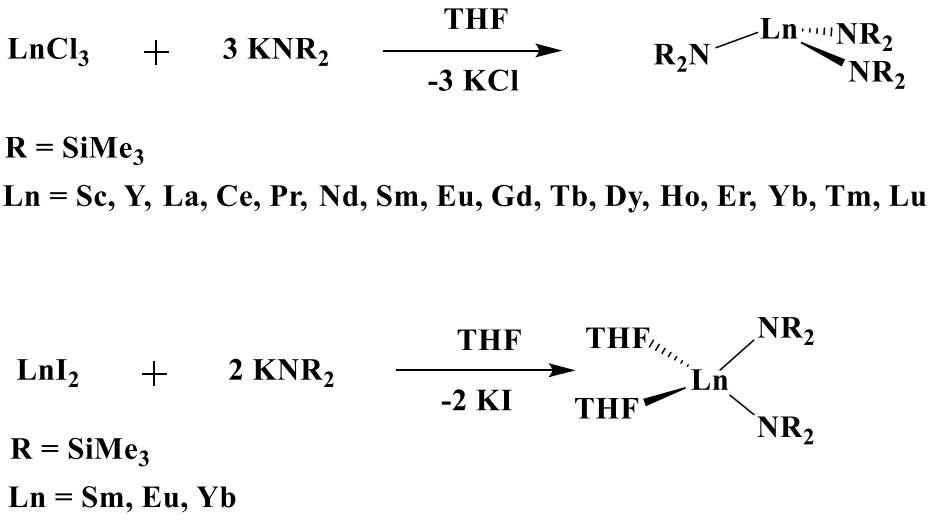

Scheme 0.2. Salt metathesis reactions between rare earth halides and KNR_2.

When reactions of KNR_2 were performed with DyI_2 and NdI_2 under a dinitrogen atmosphere, no Ln(II) complexes were isolated. Rather, a reduced nitrogen complex was isolated featuring a side-on binding mode of the N_2 unit to the Ln(III) ions, $[(R_2N)_2(THF)Ln]_2[\mu\text{-}\eta^2\text{:}\eta^2\text{-}N_2]$.[28] These results prompted further investigations using a LnA_3/M reduction system where M = alkali metal and A = NR_2, eq 0.2, and resulted in isolation of $[(R_2N)_2(THF)Ln]_2[\mu\text{-}\eta^2\text{:}\eta^2\text{-}N_2]$ complexes not only for Ln = Dy, and Nd, which had known examples of molecular species in the 2+ oxidation state, but also for Ln = Nd, Gd, Tb, Dy, Ho, Y, Er, Tm, and Lu, none of which were known to have an accessible 2+ oxidation state.

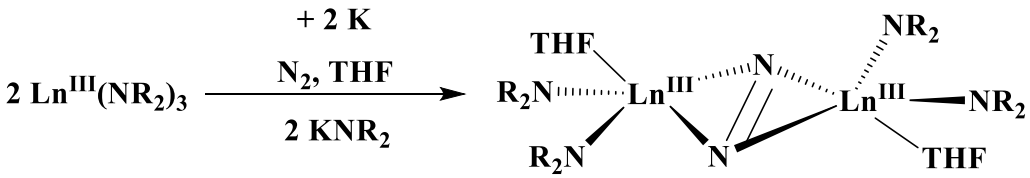

(0.2)

Ln = Nd, Gd, Tb, Dy, Ho, Er, Tm, Lu, Y
R = $SiMe_3$

Reduction of $[(R_2N)_2(THF)Ln]_2[\mu\text{-}\eta^2\text{:}\eta^2\text{-}N_2]$ resulted in the formation of an $(N_2)^{3-}$ complex, $[K(18\text{-crown-}6)]\{[(R_2N)_2(THF)Ln]_2(\mu\text{-}\eta^2\text{:}\eta^2\text{-}N_2)\}$. Upon investigation of the magnetic properties of $[K(18\text{-crown-}6)]\{[(R_2N)_2(THF)Dy]_2(\mu\text{-}\eta^2\text{:}\eta^2\text{-}N_2)\}$, a record-breaking blocking temperature to magnetic relaxation was observed.[29] Measurements of the Tb analog were made shortly after and displayed an even higher blocking temperature,[30] Figure 0.1.

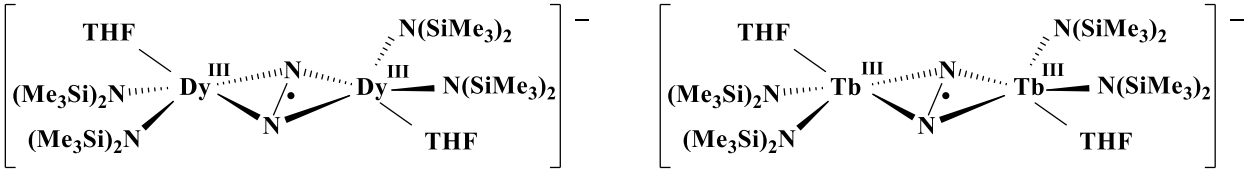

Figure 0.1. $\{[(R_2N)_2(THF)Ln]_2(\mu\text{-}\eta^2\text{:}\eta^2\text{-}N_2)]\}^{1-}$ complexes with magnetic blocking temperatures of 10 and 14K respectively.

Divalent intermediates were postulated for the reactions of eq 0.2, but attempts to isolate them were unsuccessful and only fleeting color changes were observed in reduction reactions.[31] In 2011, an EPR spectrum from the reduction of $Y(NR_2)_3$ with KC_8 in an argon-filled glovebox was acquired showing a doublet centered around a g value of 1.976, consistent with a d^1 system being split by the yttrium ½ nuclear spin. However, no isolated Y(II) product was ever recovered.[32] This led to the generalization that ligands like $(NR_2)^{1-}$ formed $(N{=}N)^{2-}$ complexes in LnA_3/M reactions, eq 0.2, but not isolable Ln(II) complexes, whereas cyclopentadienyl ligands like $(C_5H_4SiMe_3)^{1-}$ and $[C_5H_3(SiMe_3)_2]^{1-}$ gave crystallographically-characterizable Ln(II) complexes, eq 0.1.

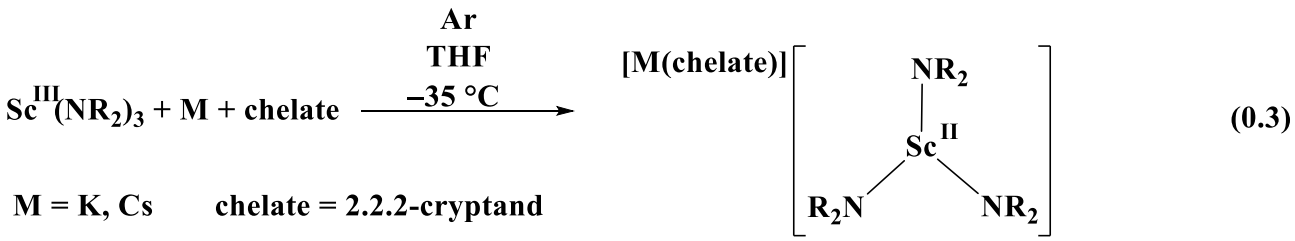

(0.3)

M = K, Cs **chelate = 2.2.2-cryptand**

M = K **chelate = 18-crown-6**

R = $SiMe_3$

Investigations into reduction of $Ln(NR_2)_3$ featuring the smallest rare-earth, Ln = Sc, using K and Cs as reductants in the presence of a chelating ligand, were found to form crystallographically-characterizable Sc(II) complexes, eq 0.3.[33] Although Sc is much smaller than the other rare-earth metals, this discovery was surprising considering the results with congeneric yttrium and the generalization stated above. Since Sc and Y reactions did not appear to be similar, it was of interest to determine if the assumption that Y was similar to the late lanthanides was valid for their reductive chemistry.

Dissertation Outline. The research presented in this dissertation focuses on the use of the $[(NR_2)_3]^{3-}$ (R = $SiMe_3$) ligand set to isolate examples of non-traditional lanthanide ions in the 2+ oxidation state and study the subsequent physical properties and reaction chemistry that they exhibit.

Chapter 1 outlines the synthesis and characterization of a new series of Ln(II) complexes that overturns two previous generalizations in rare-earth metal reduction chemistry: that amide ligands do not form isolable complexes of the highly-reducing non-traditional Ln(II) ions and that yttrium is a good model for the late lanthanides in these reductive reactions. Reduction of $Ln(NR_2)_3$ complexes with K or Rb in the presence of 2.2.2-cryptand (crypt) formed crystallographically-characterizable $[M(crypt)][Ln(NR_2)_3]$ (M = K or Rb) complexes not only for the traditional Tm(II), Nd(II) and Dy(II) ions, but also for the non-traditional Gd(II), Tb(II),

Ho(II), and Er(II) ions where the Ho(II) and Er(II) complexes are only isolable when using Rb as the reductant. Crystallographic data as well as UV-visible, magnetic susceptibility, and density functional theory studies are presented and were consistent with the accessibility of $4f^n5d^1$ configurations for Ln(II) ions in this tris(silylamide) ligand environment.

Chapter 2 discusses the synthesis of the elusive $[Y^{II}(NR_2)_3]^{1-}$ complex made possible through use of the 18-crown-6 (18-c-6) chelator and specific reaction conditions. The faster speed of crystallization with 18-c-6 appears to be important. By changing the potassium chelator from crypt to 18-c-6, the $[Ln(NR_2)_3]^{1-}$ anions can be isolated for Ln = Gd, Tb, Dy, Ho, Er, and Y as salts of a 1:2 potassium:crown sandwich cation, $[K(18\text{-c-}6)_2]^{1+}$, *i.e.* $[K(18\text{-c-}6)_2][Ln(NR_2)_3]$. The $[K(18\text{-c-}6)_2]^{1+}$ counter-cation was superior not only in the synthesis of Ln(II) complexes, but it also allowed the isolation of crystallographically-characterizable products from reactions of CO with the $[Ln(NR_2)_3]^{1-}$ anions, products that were not obtainable from the $[K(crypt)]^{1+}$ analogs. Reaction of CO with $[K(18\text{-c-}6)_2][Ln(NR_2)_3]$, generated in situ, yielded crystals of the ynediolate products, $\{[(R_2N)_3Ln]_2(\mu\text{-}OC{\equiv}CO)\}^{2-}$, which crystallized with counter-cations possessing 2:3 potassium:crown ratios, i.e.$\{[K_2(18\text{-c-}6)_3\}^{2+}$, for Gd, Dy, Ho. In contrast, reaction of CO with a solution of isolated $[K(18\text{-c-}6)_2][Gd(NR_2)_3]$, produced crystals of an *ene*diolate complex isolated with a counter-cation with a 2:2 potassium:crown ratio namely $[K(18\text{-c-}6)]_2^{2+}$ in the complex $[K(18\text{-c-}6)]_2\{[(R_2N)_2Gd_2(\mu\text{-}OCH{=}CHO)_2$

Chapter 3 describes new examples of uranium in the +2 oxidation state isolated by reduction of $Cp^{tet}{}_3U$ ($Cp^{tet} = C_5Me_4H$) and $U(NR_2)_3$ (R = $SiMe_3$) in the presence of 2.2.2-cryptand to produce $[K(crypt)][Cp^{tet}{}_3U]$ and $[K(crypt)][U(NR_2)_3]$, respectively. Both complexes have properties consistent with $5f^36d^1$ electron configurations and demonstrate that the U(II) ion can be isolated with ligands more strongly donating than Cp′ and Cp″.

Chapter 4 expands the understanding of lanthanide-based dinitrogen reduction chemistry through discovery of the first end-on $Ln_2(\mu\text{-}\eta^1\text{:}\eta^1\text{-}N_2)$ complexes. The formation of end-on versus the more common side-on $Ln_2(\mu\text{-}\eta^2\text{:}\eta^2\text{-}N_2)$ complexes was possible by using the Ln(II) complexes detailed in Chapters 1 and 2. $[Tb(NR_2)_3]^{1-}$ reacts with dinitrogen in Et_2O to form the end-on bridging dinitrogen complex $\{[(R_2N)_3Tb]_2[\mu\text{-}\eta^1\text{:}\eta^1\text{-}N_2]\}^{2-}$. The reaction of $[Gd(NR_2)_3]^{1-}$ with dinitrogen forms a complex with the same composition, but with both side-on and end-on bonding of the N_2 unit in the same crystal, $\{[(R_2N)_3Gd]_2[\mu\text{-}\eta^x\text{:}\eta^x\text{-}N_2]\}^{2-}$ (x = 1 *and* 2). All of these reduced dinitrogen complexes, maintain three ancillary amide ligands per metal. In contrast, the side-on bound complexes, $[(THF)(R_2N)_2Ln]_2[\mu\text{-}\eta^2\text{:}\eta^2\text{-}N_2]$, observed previously in $Ln(NR_2)_3/K/N_2$ reactions, have only two amides per metal. A connection between these systems related to their formation was observed in the structure of the bimetallic penta-amide complex, $[K(THF)_6]\{[(THF)(R_2N)_2Gd][\mu\text{-}\eta^2\text{:}\eta^2\text{-}N_2][Gd(NR_2)_3]\}$. Reaction conditions were crucial in this dinitrogen reaction system. If $[Gd(NR_2)_3]^{1-}$ was dissolved in THF instead of Et_2O under N_2, the irreversible formation of an $(N_2)^{3-}$ complex $[K(crypt)][(THF)(R_2N)_2Gd]_2[\mu\text{-}\eta^2\text{:}\eta^2\text{-}N_2]$ was observed.

Chapter 5 details the reaction chemistry of the Gd(II) tris(amide) complexes with toluene. The in situ reactivity of $Gd(NR_2)_3$ with KC_8 and the 18-c-6 chelate in an Et_2O/toluene solution led to formation of $\{[K(18\text{-c-}6)][(C_6H_5Me)Gd(NR_2)_2]\}_x$ exhibiting a methylcyclohexadienyl dianion and a polymeric structure. If the reagents were reacted for shorter time periods a coordination polymer containing a Gd(II) ion, $\{[K(18\text{-c-}6)][Gd(NR_2)_3]\}_x$, was isolated. When the reactions were performed with crypt in place of crown in a THF/toluene solution, the ring-opened THF complex $[K(crypt)][C_4H_9OGd(NR_2)_3]$ was isolated. If the isolated divalent $[K(crypt)][Gd(NR_2)_3]$

was dissolved in toluene, the starting material was recovered but in a different unit cell and displaying a fully planar coordination environment of the amide ligands around the Gd(II) ion.

Chapter 6 discusses the reaction chemistry of $[Gd(NR_2)_3]^{1-}$ with $BiPh_3$ and PPh_3. Reaction of $[K(crypt)][Gd(NR_2)_3]$ with a solution of $BiPh_3$ in Et_2O led to isolation of $[K(crypt)][Ph_2BiGd(NR_2)_3]$, which contained the first Gd−Bi bond and only the third example of a f element Bi bond. If the same conditions were applied with $[K(18\text{-}c\text{-}6)_2][Gd(NR_2)_3]$ as the source of Gd(II), isolation of the phenyl complex $[K(18\text{-}c\text{-}6)_2][PhGd(NR_2)_3]$ was instead observed. This represents only the second observation of a Gd ion bound to a phenyl ligand not a part of a chelate. Reactions of both Gd(II) complexes with PPh_3 led only to the isolation of the cyclometallate $[(NSiMe_2CH_2\text{-}\kappa^2\textit{N},\textit{C})Gd(NR_2)_2]^{1-}$ products despite similar color changes to that of the $BiPh_3$ reactions.

References

1. J. R. Rumble, D. R. Lide and T. J. Bruno, *CRC handbook of chemistry and physics*, **2017**.
2. D. A. Atwood, *The rare earth elements: fundamentals and applications*, John Wiley & Sons, **2013**.
3. V. B. Grasso, *Rare Earth Elements in National Defense: Background, Oversight Issues, and Options for Congress* Congressional Research Service, 2013.
4. D. N. Woodruff, R. E. P. Winpenny and R. A. Layfield, *Chem. Rev.*, **2013**, *113*, 5110-5148.
5. L. R. Morss, *Chem. Rev.*, **1976,** *76*, 827-841.
6. J. Corbett, *Revue de Chimie Minerale*, **1973**, *10*, 239-257.
7. G. Meyer, *Chem. Rev.*, **1988**, *88*, 93-107.
8. W. J. Evans, S. L. Gonzales and J. W. Ziller, *Journal of the American Chemical Society*, **1991**, **113**, 9880-9882.
9. W. J. Evans, S. L. Gonzales and J. W. Ziller, *J. Chem. Soc., Chem. Commun.*, **1992,** DOI: 10.1039/C39920001138, 1138-1139.
10. W. J. Evans, G. W. Rabe, J. W. Ziller and R. J. Doedens, *Inorg. Chem.*, 1994, *33*, 2719-2726.
11. W. J. Evans, T. A. Ulibarri and J. W. Ziller, *J. Am. Chem. Soc.* **1988**, *110*, 6877-6879.
12. W. J. Evans, N. T. Allen and J. W. Ziller, *J. Am. Chem. Soc.* **2000**, 122, 11749-11750.
13. M. N. Bochkarev and A. A. Fagin, *Chem. Eur. J.* **1999**, *5*, 2990-2992.
14. M. N. Bochkarev, *Coord. Chem. Rev.*, 2004, *248*, 835-851.
15. P. B. Hitchcock, M. F. Lappert, L. Maron and A. V. Protchenko, *Angew. Chem. Int. Ed.*, **2008**, **47**, 1488-1491.
16. M. R. MacDonald, J. W. Ziller and W. J. Evans, *J. Am. Chem. Soc.* **2011**, *133*, 15914-15917.
17. M. R. MacDonald, J. E. Bates, M. E. Fieser, J. W. Ziller, F. Furche and W. J. Evans, *Journal of the American Chemical Society*, **2012,** *134*, 8420-8423.
18. M. R. MacDonald, J. E. Bates, J. W. Ziller, F. Furche and W. J. Evans, *J. Am. Chem. Soc.* **2013**, *135*, 9857-9868.
19. M. E. Fieser, M. R. MacDonald, B. T. Krull, J. E. Bates, J. W. Ziller, F. Furche and W. J. Evans, *J. Am. Chem. Soc.* **2015**, *137*, 369-382.
20. K. R. Meihaus, M. E. Fieser, J. F. Corbey, W. J. Evans and J. R. Long, *J. Am. Chem. Soc.* **2015**, *137*, 9855-9860.
21. D. C. Bradley, M. B. Hursthouse, C. W. Newing and A. J. Welch, *J. Chem. Soc., Chem. Commun.*, **1972**, DOI: 10.1039/C39720000567, 567-568.
22. D. C. Bradley, J. S. Ghotra and F. A. Hart, *J. Chem. Soc., Chem. Commun.*, **1972**, DOI: 10.1039/C39720000349, 349-350.
23. J. S. Ghotra, M. B. Hursthouse and A. J. Welch, *J. Chem. Soc., Chem. Commun.*, **1973**, DOI: 10.1039/C39730000669, 669-670.
24. W. J. Evans, D. K. Drummond, H. Zhang and J. L. Atwood, *Inorg. Chem.*, **1988**, *27*, 575-579.

25. A. M. Bienfait, B. M. Wolf, K. W. Törnroos and R. Anwander, *Inorg. Chem.*, **2018**, *57*, 5204-5212.

26. T. D. Tilley, R. A. Andersen and A. Zalkin, *Inorg. Chem.*, **1984**, *23*, 2271-2276.

27. W. J. Evans, M. A. Johnston, R. D. Clark, R. Anwander and J. W. Ziller, *Polyhedron*, **2001**, *20*, 2483-2490.

28. W. J. Evans, G. Zucchi and J. W. Ziller, *J. Am. Chem. Soc.* **2003**, *125*, 10-11.

29. J. D. Rinehart, M. Fang, W. J. Evans and J. R. Long, *Nat. Chem.*, **2011**, **3**, 538-542.

30. J. D. Rinehart, M. Fang, W. J. Evans and J. R. Long, *J. Am. Chem. Soc.* **2011**, *133*, 14236-14239.

31. W. J. Evans, D. S. Lee, D. B. Rego, J. M. Perotti, S. A. Kozimor, E. K. Moore and J. W. Ziller, *J. Am. Chem. Soc.* **2004**, *126*, 14574-14582.

32. M. Fang, D. S. Lee, J. W. Ziller, R. J. Doedens, J. E. Bates, F. Furche and W. J. Evans, *J. Am. Chem. Soc.* **2011**, *133*, 3784-3787.

33. D. H. Woen, G. P. Chen, J. W. Ziller, T. J. Boyle, F. Furche and W. J. Evans, *Angew. Chem. Int. Ed.*, **2017**, *56*, 2050-2053.

Chapter 1

Synthesis, Structure, and Magnetism of Tris(amide) $[Ln\{N(SiMe_3)_2\}_3]^{1-}$ Complexes of the Non-Traditional +2 Lanthanide Ions

Introduction*

This chapter describes the synthesis of a series of Ln^{2+} complexes that overturned two generalizations in rare-earth metal reduction chemistry: that amide ligands would not form isolable complexes of the highly-reducing non-traditional Ln^{2+} ions and that yttrium is a good model for the late lanthanides in these reductive reactions. As outlined in the introductory chapter, studies of reductive rare-earth metal chemistry had shown that in tris(silylcyclopentadienyl) coordination environments the +2 oxidation state is available to all the lanthanides (except Pm which was not studied due to its radioactivity). This overturned previous assumptions about which lanthanide elements were able to access the 2+ oxidation state.[1-7] Previous studies of LnA_3/M reactions (Ln = rare-earth metal; A = anion; M = alkali metal) under conditions similar to those in eq 0.1 but with tris(silylamide) rare-earth metal complexes failed to produce any isolable Ln^{2+} species.[18] These $Ln(NR_2)_3$/M reduction reactions under N_2 did provide excellent routes to reduced dinitrogen complexes of $(N=N)^{2-}$, eq 0.2, and $(N_2)^{3-}$,[18] which suggested intermediate Ln^{2+} species. However, the same reactions under argon typically yielded only $Ln(NR_2)_3$ starting materials after work-up.[18b]

These results were heavily probed with yttrium, since the I = ½ nucleus could provide EPR evidence for Y^{2+}. An EPR spectrum consistent with Y^{2+} was observed in solution from

* Portions of this chapter have been published: Ryan, A. J.; Darago, L. E.; Balasubramani, S. G.; Chen, G. P.; Ziller, J. W.; Furche, F.; Long, J. R.; Evans, W. J. *Chemistry–A European Journal* **2018**, 24, 7702-7709.

$Y(NR_2)_3$/M reactions, but no isolable complexes were obtained.[19] This led to the generalization that ligands like $(NR_2)^{1-}$ form $(N=N)^{2-}$ complexes in LnA_3/M reactions, eq 0.2, but not isolable Ln^{2+} complexes, whereas cyclopentadienyl ligands like $(C_5H_4SiMe_3)^{1-}$ and $[C_5H_3(SiMe_3)_2]^{1-}$ give crystallographically-characterizable Ln^{2+} complexes, eq 0.1.[1-7]

Reductions of the tris(silylamide) scandium complex, $Sc(NR_2)_3$, (R = $SiMe_3$) with K and Cs in the presence of a chelating ligand were found to form crystallographically-characterizable Sc^{2+} complexes, eq 0.3.[20] Although Sc is much smaller than the other rare-earth metals, this result was surprising considering the results with congeneric yttrium and the generalization stated above. Since Sc and Y reactions did not appear to be similar, it was of interest to determine if the assumption that Y was similar to the late lanthanides was valid in reactions of this type. Consequently, re-examination of $Ln(NR_2)_3$/M reductions with the lanthanides and this led to a new series of Ln^{2+} complexes for Nd, Gd, Tb, Dy, Ho, Er, and Tm as reported here.

Results

Gd, Tb, Dy. Addition of pre-chilled (−35 °C) THF solutions containing $Ln(NR_2)_3$, **1-Ln**,[21] for Ln = Gd, Tb, Dy and 2.2.2-cryptand to a pre-chilled vial containing a potassium smear resulted in the formation of intensely-colored solutions, as previously observed for the $(Cp'_3Ln)^{1-}$ and $(Cp''_3Ln)^{1-}$ complexes in eq 0.1.[1-7] The Tb and Dy reactions formed dark blue solutions, while the Gd reaction mixture appeared dark purple. After a reaction time of about 1 h at −35 °C, the solutions were filtered to remove excess potassium metal. Layering hexanes on the THF solution produced crystals of [K(2.2.2-cryptand)][$Ln(NR_2)_3$], **2-Ln** (Ln = Gd, Tb, Dy), within 2 days at −35 °C, eq 1.1. This differed from reductions of **1-Y,** which typically gave **1-Y** as the only isolable product.[19] Each complex was identified by single-crystal X-ray diffraction,

Figure 1.1.

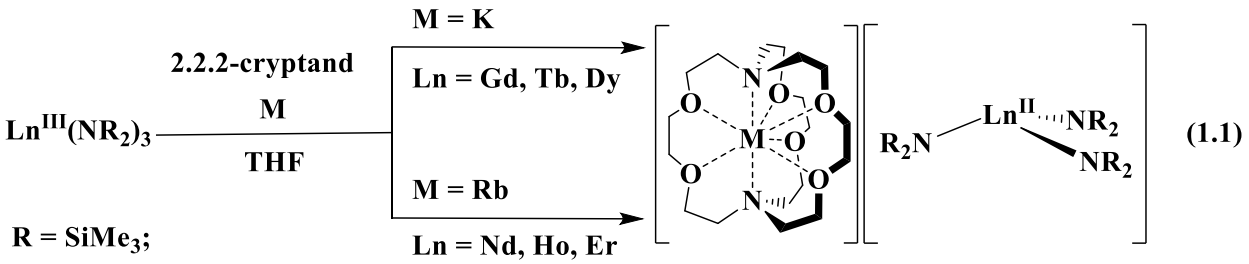

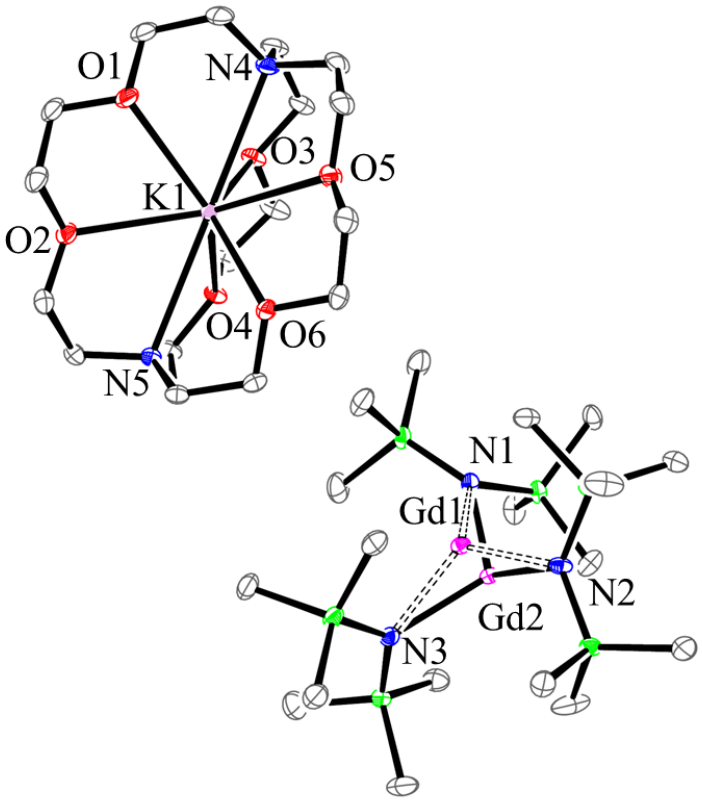

Figure 1.1. ORTEP representation of **2-Gd** with thermal ellipsoids drawn at the 50% probability level. Hydrogen atoms are omitted for clarity. Compounds **2-Tb** and **2-Dy** are isomorphous. In each complex, the Ln ion is disordered over two positions; both are shown here.

Ho and Er. Reductions of **1-Ho** and **1-Er** at −35 °C in reactions analogous to those that produced **2-Gd**, **2-Tb**, and **2-Dy** failed to give crystalline products. However, when rubidium metal was used as the reducing agent, single crystals of [Rb(2.2.2-cryptand)][Ln(NR_2)$_3$], **3-Ln**, were isolated for both metals and crystallographically characterized, Figure 1.2.

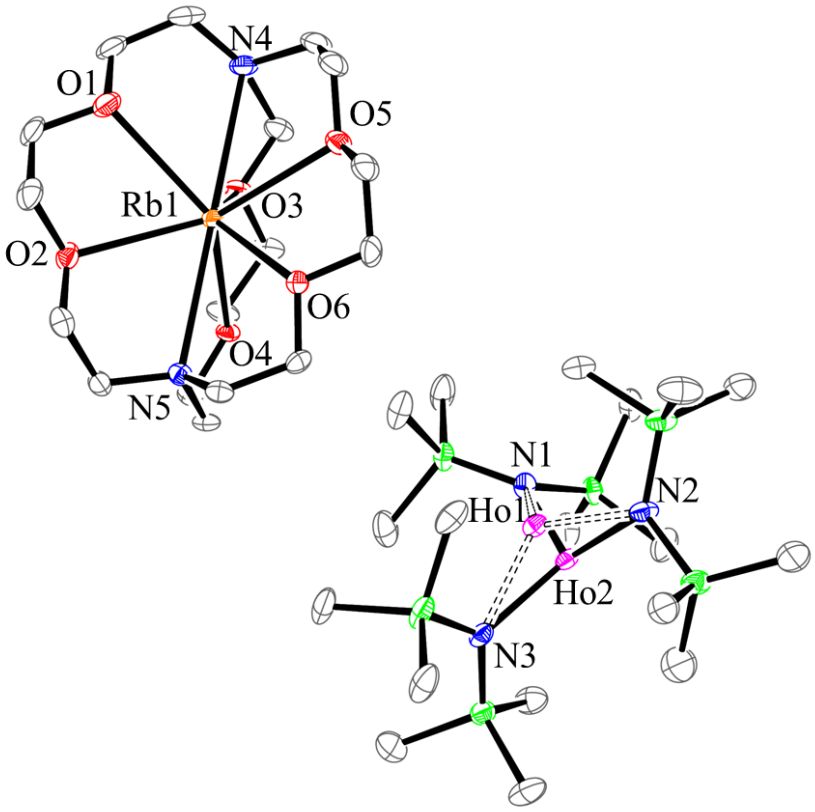

Figure 1.2. ORTEP representation of **3-Ho** with thermal ellipsoids drawn at the 50% probability level. Hydrogen atoms are omitted for clarity. Compounds **3-Nd, 3-Er, and 3-Tm** are isomorphous. In each complex, the Ln ion is disordered over two positions; both are shown here.

Interestingly, the crystals of **3-Ln** were isomorphous with those of **2-Ln**. Both **3-Ho** and **3-Er** decomposed rapidly at room temperature in solution. The origin of the success of the Rb reaction was not clear since K and Rb have such similar reduction potentials, −2.93 and −2.98 V vs SHE, respectively.[22]

Nd. Although the analogous reduction with **1-Nd** gave an intense dark blue color like that found for **2-Tb**, **2-Dy**, **3-Ho**, and **3-Er**, the color faded to brown at −35 °C and no crystalline products were isolated from the reactions. To isolate **3-Nd**, a solution of **1-Nd** in THF was reduced with Rb metal in the cold well of an argon-filled glovebox at −78 °C for 5 min and passed through a pre-chilled pipette filter. By layering with hexanes and storing at −35 °C, single crystals of **3-Nd** were isolated and found to be isomorphous with the other **2-Ln** and **3-Ln** complexes. Although the crystal data confirmed composition, the quality of the data for **3-Nd** and **3-Er** was not sufficient to discuss metrical parameters.

Tm. Reduction of colorless **1-Tm** with Rb metal at −35 °C resulted in a color change similar to those observed for **2-Ln** and **3-Ln**, but the blue-green color was noticeably less intense than that of **2-Ln** and **3-Ln**. Single crystals of **3-Tm** were grown by layering a THF solution with hexanes and storing at −35 °C.

Structural Studies. Each of the isomorphous structures of **2-Ln** (Ln = Gd, Tb, and Dy) and **3-Ho** had a $[M(2.2.2\text{-cryptand})]^{1+}$ cation well separated from the $[Ln(NR_2)_3]^{1-}$ anion. In each complex, the lanthanide metal was disordered by 0.5 – 0.6 Å above and below the plane of the three nitrogen donor atoms. The structures with this disorder were similar to those of the $Ln(NR_2)_3$, **1-Ln**, precursors (Ln = Nd,[23] Eu,[24] Tb,[25] Dy,[26] Er, [26] Yb,[27] Lu[12]) which exhibit similar metal disorder in the range of 0.34 – 0.58 Å.

The Ln–N bond distances in **2-Ln** were 0.04 – 0.06 Å longer than those in the corresponding **1-Ln** compounds, Table 1.1. This difference is similar to the 0.03 Å average difference in Ln-(cyclopentadienyl ring centroid) distances observed between complexes of the $4f^n5d^1$ Ln^{2+} ions in eq 0.1 and their $4f^n$ Ln^{3+} precursors. In contrast, complexes of the traditional $4f^{n+1}$ Ln^{2+} ions have differences ranging from 0.1 – 0.2 Å.[4-7]

Table 1.1. Metrical parameters of the $[Ln(NR_2)_3]^{1-}$ anions.

Metal	Ln–N distance (Avg) (Å)	Change in Ln–N (Å) ($Ln^{3+} \rightarrow Ln^{2+}$)	$Ln–N_{Plane}$ (Avg) (Å)
Gd[a]	2.307	0.06	0.523
Tb	2.282	0.05	0.503
Dy	2.270	0.06	0.523
Ho[a]	2.256	0.04	0.509
Tm[a]	2.320	0.12	0.232

[a] These two Ln^{3+} complexes do not have reported crystal structures, so expected Ln–N distances were interpolated from analogous complexes of metals with similar ionic radii.

X-ray crystallographic studies of single crystals of [Rb(2.2.2-cryptand)][$Tm(NR_2)_3$], **3-Tm**, revealed a trigonal pyramidal arrangement of $(NR_2)^{1-}$ anions around thulium, but with noticeable differences from **2-Ln** and **3-Ln**. The displacement of the disordered Tm atom from the plane of the three N atoms was smaller, 0.232 Å, versus the range of 0.503 – 0.523 Å for **2-Ln** and **3-Ln**, (Table 1.1). The Ln–N bond distances also did not match the trend observed with the other examples in the table. On the basis of the lanthanide contraction, a Tm–N average distance of about 2.26 Å would be expected if the complex were analogous to the others. The 2.320 Å Ln–N average is significantly longer. The difference between $Tm(NR_2)_3$ and **3-Tm** is also estimated to be longer than the other entries in Table 1.1. The structure of $Tm(NR_2)_3$ has not been reported, but, based on interpolation of data on **1-Er**[26] and **1-Yb**,[28] a Tm–N distance in **1-Tm** of 2.20 Å would be expected. The 2.32 Å Tm–N distance observed in **3-Tm** is 0.12 Å longer. This value was consistent with the larger bond distance differences observed between

complexes of $4f^{n+1}$ Ln^{2+} and $4f^{n}$ Ln^{3+} ions of the traditional divalent lanthanides, Sm, Eu, Yb, and Tm.[5-7] As such, **3-Tm** was also assigned to the traditional divalent category.

Electronic Structure Calculations. The anion in **2-Gd** was further investigated by electronic structure calculations in collaboration with Sreeganesh Balasubramini of the Furche group at UCI using the TPSSh meta-generalized gradient hybrid functional[29] and polarized valence triple-ζ basis sets[30] with Stuttgart-Dresden small-core scalar-relativistic pseudopotentials[31]. Upon optimization starting from the X-ray diffraction data, a D_3 symmetric minimum was obtained. The highest occupied spin-unrestricted molecular orbital (HOMO) of the resulting nonet ground state has $5d_z^2$ character, Figure 1.3, supporting the notion of a $4f^7 5d^1$ configuration of Gd^{2+} in $[Gd(NR_2)_3]^{1-}$. The lowest unoccupied molecular orbital (LUMO), on the other hand, is diffuse, and may be characterized as a mixture of a metal 6p orbital and a bound p-type Rydberg state.

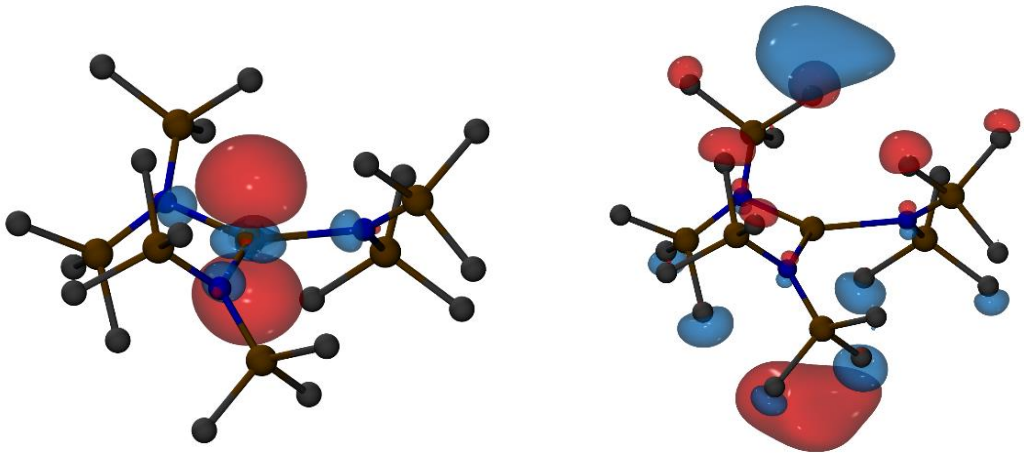

Figure 1.3. Left: $[Gd(NR_2)_3]^{1-}$ HOMO (156α contour value 0.05). **Right:** LUMO+4 (159α contour value 0.017) with the hydrogen atoms excluded for clarity.

Optical Spectroscopy/Time-Dependent-DFT. The UV-Visible spectra of **2-Gd**, **2-Tb**, and **2-Dy**, Figure 1.4, showed broad absorption bands in the visible region with high extinction coefficients, ε, consistent with those of the $4f^n5d^1$ Ln^{2+} complexes in eq 0.1.[1-7] The UV-Vis spectrum of **3-Tm**, Figure 1.4, displayed a significantly lower extinction coefficient, 80 M^{-1} cm^{-1}, in the 550 – 600 nm region compared with those of **2-Ln**. The $(Cp'_3Ln)^{1-}$ complexes of the traditional $4f^n$ Ln^{2+} ions, Eu, Yb, Sm, and Tm, also had lower extinction coefficients.[5]

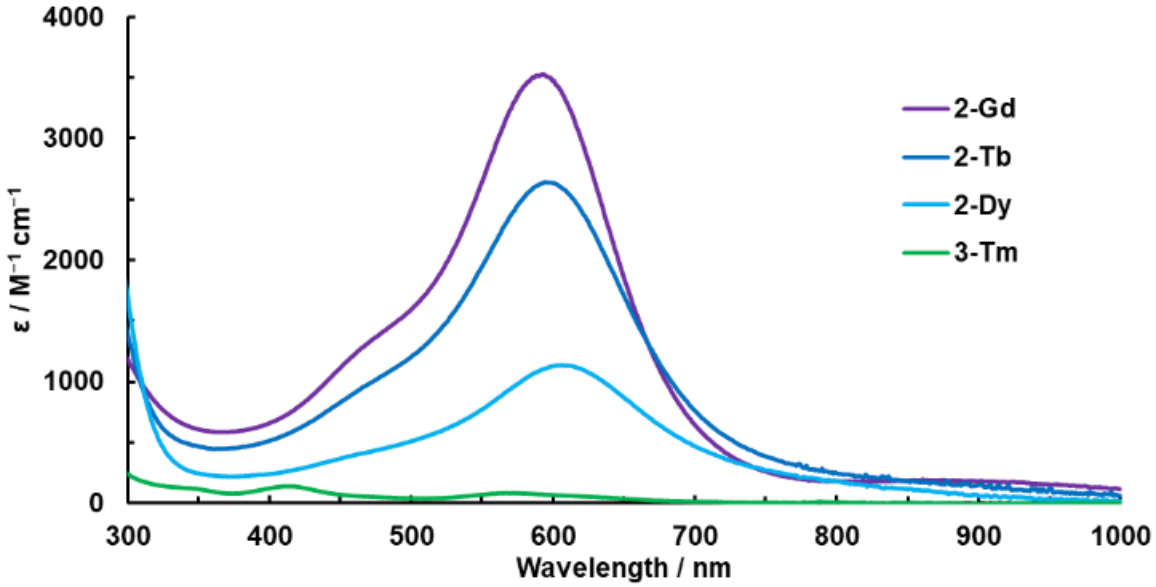

Figure 1.4. Experimental UV-Vis spectra of **2-Gd, 2-Tb, 2-Dy,** and **3-Tm** in THF at 293 K.

Time-dependent DFT (TDDFT) was used to simulate the UV-visible spectrum of $[Gd(NR_2)_3]^{1-}$. To account for the diffuse character of the low-lying unoccupied molecular orbitals, the metal basis sets were augmented by small-exponent primitive p-type Gaussians obtained from downward extrapolation.

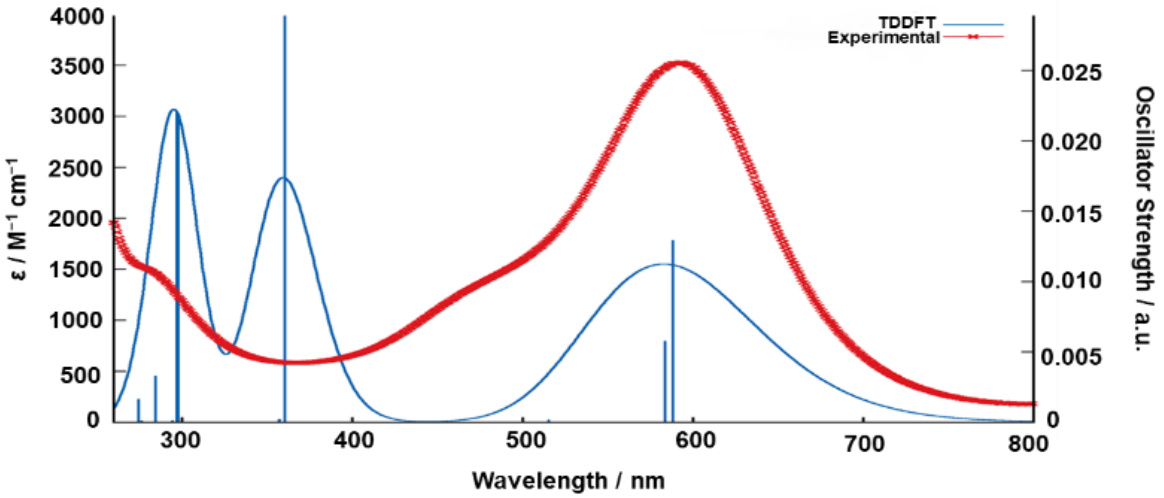

Figure 1.5. UV-Visible spectra of $[Gd(NR_2)_3]^{1-}$ computed using TDDFT(solid line) and the experimental spectra (crosses) in THF solvent for reference.

The simulated TDDFT absorption spectrum of **2-Gd** reproduced the position and intensity of the strong absorption band in the visible experimental spectrum, Figure 1.5. Analysis of the transition density matrices revealed that this band was predominantly a HOMO to LUMO transition. The considerable metal 5d to 6p character of the transition explains the high intensity of the absorption. This may be compared to the visible absorption spectra of the $(Cp'_3Ln)^{1-}$ complexes,[5] which are also dominated by transitions out of metal 5d orbitals, but the final states have ligand π* character. Thus, even in the absence of low-lying π* ligand acceptor orbitals, strong visible absorption was possible with amides as ligands supporting divalent lanthanide ion

Magnetic Measurements. Variable-temperature magnetic susceptibility measurements were performed by Lucy Darago in collaboration with the Long Group at UC Berkeley in order to confirm the electronic configurations of **2-Gd**, **2-Tb**, and **2-Dy** and investigate the nature of the f-d spin interaction in these complexes. Considering a $4f^n5d^1$ configuration, two models have been proposed to describe the magnetic interaction of the 4f and 5d electrons.[33, 34] The first, the

coupled model, assumes that spin-spin coupling is stronger than L-S coupling, producing an overall spin of $S_{TOTAL} = S_{4f} + 1/2$, which then is coupled to the orbital angular momentum, L, of the 4f electrons, yielding a new J value for which a predicted $\chi_M T$ can be calculated. The second, the uncoupled model, assumes that L-S coupling of the 4f electrons is much stronger than coupling of the 5d and 4f electrons, such that the 5d electron precesses with the magnetic field independently of the 4f electrons. This model sums the $\chi_M T$ value expected for the 5d electron (S = 1/2) with that of the J value determined from L-S coupling of the 4f electrons in order to predict a $\chi_M T$ product. Table 1.2 compares the experimental room temperature $\chi_M T$ products with those predicted by the $4f^n5d^1$ and traditional $4f^{n+1}$ models.[34] In the case of the $4f^n5d^1$ models, the 5d electron was assumed to have zero orbital angular momentum. Indeed, it is likely that 5d orbital degeneracy is broken by the ligand field of the amide ligands, similar to the $(Cp'_3Ln)^{1-}$ series, reducing or eliminating the orbital angular momentum of the 5d electron. This assumption is supported by computational study of **2-Gd** described above as well as computations performed on the as-yet-unisolated $[Y(NR_2)_3]^{1-}$ complex[35] and on the reported $[Sc(NR_2)_3]^{1-}$ complex,[20] for which the populated d orbital was predicted to be primarily d_z^2 in character.[20, 35]

Table 1.2. Experimental and predicted (as described in text) $\chi_M T$ products at 298 K for **2-Ln**.

	Exp. μ_{eff}[a]	**Exp. $\chi_M T$ [b]**	**$\chi_M T$ ($4f^n5d^1$) coupled**	**$\chi_M T$ ($4f^{n+1}$)**	**$\chi_M T$ ($4f^n5d^1$) uncoupled**
2-Gd	9.03	10.20	10	11.82	8.26
2-Tb	10.89	14.83	14.42	14.13	12.20
2-Dy	11.67	17.03	17.01	14.07	14.51

[a] Units of μ_B

[b] All $\chi_M T$ data are reported in units of emu·K/mol and were collected under a field of 0.1 T for Tb and Dy and 7 T for Gd

The magnetic moments of the **2-Ln** compounds (Figures 1.6, 1.9, 1.10) were in good agreement with a coupled $4f^n5d^1$ assignment, consistent with the magnetic behavior observed for their analogous $(Cp'_3Ln)^{1-}$ complexes.[34] Magnetization versus field data collected from 2 to 10 K for **2-Gd** could be modeled well using an S = 4 Brillouin function, which confirms a coupled $4f^75d^1$ configuration (Figure 1.9). The room-temperature $\chi_M T$ products of **2-Ln** were in slightly better agreement with the coupled $4f^n5d^1$ model than those of the $(Cp'_3Ln)^{1-}$ (Ln = Gd, Tb, Dy) series, which exhibit lower $\chi_M T$ products than expected for the coupled $4f^n5d^1$ configuration. This observation may suggest that ligand field splitting was stronger in the $(Cp'_3Ln)^{1-}$ (Ln = Gd, Tb, Dy) complexes, which thereby have reduced $\chi_M T$ products compared to the $[Ln(NR_2)_3]^{1-}$ complexes in **2-Ln.** Finally, the 11.67 μ_B magnetic moment of **2-Dy** exceeds the record-high

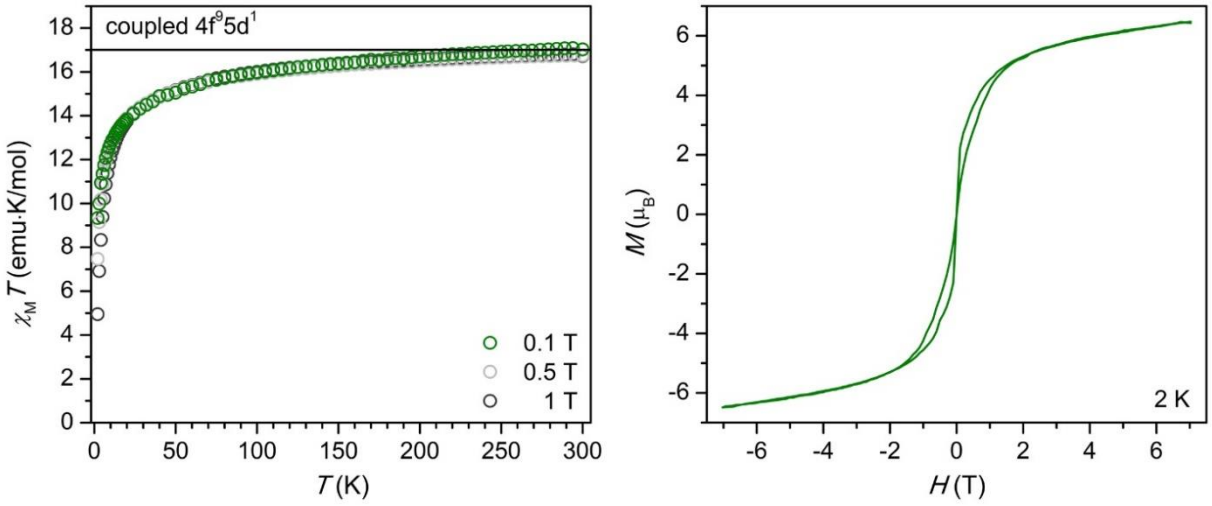

Figure 1.6. Left: Product of magnetic susceptibility times temperature versus temperature data for **2-Dy**, collected under applied fields of 0.1 T, 0.5 T, and 1 T. **Right:** Magnetization versus field data for **2-Dy**, collected at 2 K with a field sweep rate of 2 mT s^{-1}, are represented by a solid line.

single-ion values of 11.20, 11.35, and 11.41 μ_B observed for $[C_6H_3(CMe_3)_3\text{-}1,3,5]_2Dy$,[33] [K(2.2.2-cryptand)][Cp'_3Dy], and [K(2.2.2-cryptand)][Cp'_3Ho],[35] respectively.

Waist-restricted magnetic hysteresis was observed for **2-Dy** at 2 K. However, ac magnetic susceptibility measurements collected at 2 K and 4 K from 1 – 1500 Hz, under applied dc magnetic fields of 0 – 0.4 T, revealed only high-frequency out-of-phase signals without peak maxima, which indicates an absence of single-molecule magnet behavior at 2 K or above. The waist-restricted hysteresis of **2-Dy** may be attributed to intermolecular magnetic interactions that possibly prompt long-range magnetic order at even lower temperatures.

Discussion

Although it appeared for years that Ln^{2+} complexes of $(NR_2)^{1-}$ ligands could only be isolated for Sm,[36] Eu,[37] Yb, [37] and Tm[38], these results indicated that amide ligands are capable of supporting the +2 oxidation state in crystalline molecular complexes for rare-earth ions across the series. The origin of the interesting differences in stability of the [K(2.2.2-cryptand)][$Ln(NR_2)_3$], **2-Ln** and [Rb(2.2.2-cryptand)][$Ln(NR_2)_3$], **3-Ln**, complexes as a function of both the lanthanide and the alkali metal was not clear. Since K and Rb have very similar reduction potentials and since **2-Ln** and **3-Ln** are isomorphous, it was not obvious why Rb gives isolable crystals for Ho and Er and K does not. The order of thermal stability, Nd << Gd > Tb > Dy > Ho, Er is not periodic and suggests there are two competing factors that allow the metals in the middle of the series to be most stable. In the $(Cp'_3Ln)^{1-}$ series, stability decreases regularly from La to Lu as the metals get smaller.[5] The complex of the traditional Tm^{2+} ion, **3-Tm**, appears to be more stable than any of the non-traditional ions.

This series of Ln^{2+} tris(amide) complexes provided a new set of data on the physical properties of non-traditional Ln^{2+} ions and was shown to follow the electron configuration model previously used to analyze the Ln^{2+} complexes in a $(Cp')^{3-}$ ligand environment, eq 0.1.[1-7] The tris(amide) series of complexes has properties consistent with $4f^n5d^1$ electron configurations for the non-traditional divalent ions versus a $4f^{n+1}$ configuration for the traditional Tm^{2+} ion. These assignments are supported by small Ln–N bond length changes consistent with a population of a d orbital,[1-7] as well as intense UV-Vis spectra for the non-traditional divalent ions. TDDFT calculations indicated that the spectra arise from a transition originating from a d_z^2 orbital. However, unlike in the $(Cp'_3Ln)^{1-}$ complexes, the accepting LUMO has metal 6p character with Rydberg admixture. In contrast, a larger change in Ln–N bond length and a less strongly-absorbing UV-Vis spectrum for Tm (Table 1.1) were supportive of a $4f^{n+1}$ configuration. The tris(amide) complexes also provided rare opportunities for magnetic characterization of $4f^n5d^1$ ions, producing a new record-high single-ion magnetic moment of 11.67 μ_B for **2-Dy**.

Conclusions

The previously held assumption that amide ligands could not support non-traditional Ln^{2+} compounds was largely founded on the inability to isolate $[Y(NR_2)_3]^{1-}$.[19] The results suggest that comparison of Y^{2+} with late lanthanide Ln^{2+} ions may not be as valid as previous comparisons of Y^{3+} and late lanthanide Ln^{3+} ions of similar size. The lanthanide amide complexes reported here, along with the recent isolation of $[K(crypt)][Sc(NR_2)_3]$ which instigated this study,[20] surprisingly show similarity between the smallest rare-earth metal, scandium, and the lanthanides, but not the intermediate-sized rare-earth metal, yttrium. The subtleties in these comparisons remain to be explained. Similarly, the origin of the efficacy of Rb versus K to provide crystalline samples of the Ho^{2+} and Er^{2+} complexes, though the crystal structures of **2-Ln** and **3-Ln** are isomorphous,

remains unknown. Clearly, the foregoing results demonstrate that a wider range of strongly-donating ligands should be explored for the isolation of +2 ions of all the lanthanides, and that a variety of reduction methods should be surveyed with each ligand type.

Experimental Details

All manipulations and syntheses described below were conducted with the rigorous exclusion of air and water using standard Schlenk line and glovebox techniques under an argon atmosphere. Solvents were sparged with UHP argon and dried by passage through columns containing Q-5 and molecular sieves prior to use. IR samples were prepared as KBr pellets, and the spectra were obtained on a Jasco FT/IR-4700 - ATR-PRO ONE system. Elemental analyses were performed on a Perkin-Elmer 2400 Series II CHNS elemental analyzer. UV−vis spectra were collected in THF at 298 K using a Varian Cary 50 Scan UV−vis spectrophotometer. Potassium and rubidium metal (Aldrich) were used as received. Anhydrous $LnCl_3$ (Ln = Nd, Gd, Tb, Dy, Ho, Er, Tm)[39], and $Ln(NR_2)_3$ (R = $SiMe_3$)[40] were prepared according to literature procedures. 2.2.2-cryptand (4,7,13,16,21,24-hexaoxa-1,10-diazabicyclo[8.8.8]hexacosane, Aldrich) was placed under vacuum (10^{-4} Torr) for 12 h before use.

[K(2.2.2-cryptand)][Gd(NR$_2$)$_3$], 2-Gd. In an argon-filled glovebox, $Gd(NR_2)_3$ (60 mg, 0.094 mmol) was combined with 2.2.2-cryptand (35 mg 0.094 mmol) in THF (4 mL) and cooled to −35 °C in the glovebox freezer. The cold solution was added to a vial containing a potassium smear (20 mg, 0.51 mmol) that had also been cooled to −35 °C and the mixture was allowed to for 1 h in the glovebox freezer. The solution was removed from the vial containing potassium and layered with cold hexanes before storing in the freezer. After 48 h, dark purple crystals were obtained (83 mg, 84 % yield). IR: 2942s, 2890s, 2819m, 2762w, 2729w, 2697w, 1478m, 1459m, 1446m, 1356s, 1298m, 1260s 1236s, 1135s, 1107s, 1078s, 1060s, 996s, 952s, 934m, 869s, 825s,

769m, 751m, 711m, 690m, 662s, 599m cm^{-1}. Anal. Calcd for $C_{36}H_{90}N_5O_6Si_6KGd$: C, 41.02; H, 8.61; N, 6.64. Found: C, 41.35; H, 8.91; N, 6.51. UV−vis (THF) λ_{max}, nm (ε, M^{-1} cm^{-1}): 285 (1460 shoulder), 470 (1320 shoulder), 597 (3500)

[K(2.2.2-cryptand)][Tb(NR$_2$)$_3$], 2-Tb. As described for **2-Gd**, Tb(NR$_2$)$_3$ (77 mg, 0.12 mmol) and 2.2.2-cryptand (45 mg, 0.12 mmol) in THF (1 mL) were reduced with K (20 mg, 0.51 mmol) to afford **2-Tb** as a dark blue crystalline solid. Single crystals suitable for X-ray diffraction were grown by layering a concentrated THF solution with hexanes (60 mg 61% yield). IR: 2942s, 2889s, 2817m, 2762w, 2730w, 2698w, 1478m, 1458m, 1446m, 1356s, 1299m, 1260s 1237s, 1135s, 1107s, 1078s, 1059s, 992s, 952s, 933m, 869s, 827s, 770m, 752m, 713m, 691m, 663s, 600m cm^{-1}. Anal. Calcd for $C_{36}H_{90}N_5O_6Si_6KTb$: C, 40.96; H, 8.59; N, 6.63. Found: C, 40.81; H, 8.53; N, 6.23. UV−vis (THF) λ_{max}, nm (ε, M^{-1} cm^{-1}): 285 (2000 shoulder), 480 (1000 shoulder), 600 (2630)

[K(2.2.2-cryptand)][Dy(NR$_2$)$_3$], 2-Dy. As described for **2-Gd**, Dy(NR$_2$)$_3$ (60 mg, 0.093 mmol) and 2.2.2-cryptand (35 mg, 0.093 mmol) in THF (1 mL) were treated with K (20 mg, 0.51 mmol) to afford **2-Dy** as a dark blue crystalline solid. Single crystals suitable for X-ray diffraction were grown by layering a concentrated THF solution with hexanes (90 mg, 91% yield). IR: 2945s, 2889s, 2817m, 2761w, 2730w, 2702w, 1958w, 1478m, 1458m, 1446m, 1390w 1355s, 1298m, 1260s 1238s, 1135s, 1107s, 1079s, 1041s, 987s, 951s, 933m, 870s, 827s, 770m, 751m, 712m, 693m, 663s, 600m cm^{-1}. Anal. Calcd for $C_{36}H_{90}N_5O_6Si_6KDy$: C, 40.82; H, 8.56; N, 6.61. Found: C, 40.40; H, 8.37; N, 6.30. UV−vis (THF) λ_{max}, nm (ε, M^{-1} cm^{-1}): 275 (3380 shoulder), 607 (1130)

[Rb(2.2.2-cryptand)][Ho(NR$_2$)$_3$], 3-Ho. As described for **2-Gd**, of Ho(NR$_2$)$_3$ (60 mg, 0.093 mmol) and 2.2.2-cryptand (35 mg, 0.093 mmol) in THF (1 mL) were reduced with Rb (30 mg

0.35 mmol) to afford **3-Ho** as a dark blue crystalline solid. Single crystals suitable for X-ray diffraction were grown by layering a concentrated THF solution with hexanes (80 mg, 78 % yield). IR: 2942s, 2887s, 2817m, 2758w, 2728w, 2700w, 1954w, 1477m, 1458m, 1445m, 1385w 1353s, 1298m, 1258s, 1237s, 1132s, 1106s, 1073s, 994s, 949s, 926m, 870s, 830s, 772m, 751m, 713m, 697m, 664s, 605m cm^{-1}. Anal. Calcd for $C_{36}H_{90}N_5O_6Si_6RbHo$: C, 39.02; H, 8.19; N, 6.32. Found: C, 39.46; H, 8.47; N, 6.05.

[Rb(2.2.2-cryptand)][Er(NR$_2$)$_3$], 3-Er. As described for **2-Gd**, Er(NR$_2$)$_3$ (60 mg, 0.093 mmol) and 2.2.2-cryptand (35 mg, 0.093 mmol) in THF (1 mL) reduced with Rb (30 mg 0.35 mmol) affording **3-Er** as a dark blue crystalline solid. Single crystals suitable for X-ray diffraction were grown by layering a concentrated THF solution with hexanes (98 mg, 95 % yield). IR: 2943s, 2886s, 2816m, 2758w, 2727w, 2700w, 1954w, 1477m, 1459m, 1445m, 1384w 1354s, 1298m, 1258s, 1238s, 1132s, 1106s, 1074s, 996s, 948s, 926m, 870s, 830s, 772m, 751m, 714m, 697m, 663s, 605m cm^{-1}. Anal. Calcd for $C_{36}H_{90}N_5O_6Si_6RbEr$ C, 38.94; H, 8.17; N, 6.31. Found: C, 39.33; H, 8.02; N, 6.00.

[Rb(2.2.2-cryptand)][Tm(NR$_2$)$_3$], 3-Tm. As described for **2-Gd** Tm(NR$_2$)$_3$ (60 mg, 0.093 mmol) and 2.2.2-cryptand (35 mg, 0.093 mmol) in THF (1 mL) were reduced with Rb (30 mg 0.35 mmol) to afford **3-Tm** as a blue crystalline solid. Single crystals suitable for X-ray diffraction were grown by layering a concentrated THF solution with hexanes. IR: 2943s, 2885s, 2817m, 2757w, 2726w, 2700w, 1477m, 1459m, 1445m, 1354s, 1299m, 1258s, 1239s, 1132s, 1106s, 1073s, 977s, 948s, 926m, 870s, 830s, 773m, 750m, 715m, 100m, 663s, 606m cm^{-1}. Anal. Calcd for $C_{36}H_{90}N_5O_6Si_6RbTm$: C, 38.88; H, 8.16; N, 6.30. Found: C, 38.45; H, 7.99; N, 5.92. UV−vis (THF) λ_{max}, nm (ε, M^{-1} cm^{-1}): 245 (130 shoulder), 415 (140), 572 (80)

[Rb(2.2.2-cryptand)][Nd(NR$_2$)$_3$], 3-Nd. As described for **2-Gd** Nd(NR$_2$)$_3$ (60 mg, 0.093 mmol) and 2.2.2-cryptand (35 mg, 0.093 mmol) in THF (1 mL) were reduced with Rb (25 mg 0.14 mmol) at −78 °C to afford **3-Nd** as a blue crystalline solid. Single crystals suitable for X-ray diffraction were grown by layering a concentrated THF solution with hexanes.

Computational details.

Density functional theory (DFT) calculations were performed in collaboration with Sreeganesh Balasubramini of Filipp Furche's group at UC Irvine using the hybrid meta-generalized gradient approximation (hybrid meta-GGA) functional TPSSh[41] with Grimme's D3 dispersion correction[42,43] and the polarized triple-ζvalence (def2-TZVP[44]) basis sets for Gd and polarized split valence (def2-SVP[45]) basis sets for H, C, N and Si. For the TDDFT calculations an additional diffuse p function (with Gaussian exponent of $0.10241120895 \times 10^{-1}$) was added to the Gd basis set by downward extrapolation. Numerical integration grids of size m4[46] were used for evaluating exchange correlation contributions. To account for the THF solvent, the COSMO[47] continuum solvation model was employed with a dielectric constant of 7.52[48]. A convergence threshold of 10^{-8} H was used for self consistent field calculations. Structures were converged to a maximum gradient norm of $\leq 10^{-4}$ a.u.

The initial structure was taken from X-ray diffraction data with C_1 molecular symmetry. Upon optimization a D_3 symmetric structure was obtained. To confirm that the optimized structure corresponds to the minimum in the potential energy surface, numerical vibrational normal mode analysis was carried out.

Time-dependent DFT (TDDFT) using a nonorthonormal Krylov subspace algorithm[32] were used to simulate the UV-visible spectrum of $[Gd\{N(SiMe_3)_2\}_3]^{1-}$. The gauge invariant

implementation of the TPSSh functional[49] was employed. The resulting line spectrum was blue shifted by 0.01 eV and broadened by superimposing Gaussian functions with an RMS line width of 0.17 eV.

The strong absorption at 588 nm mainly corresponds to a transition from the 156α HOMO, which is predominantly a Gd 5d orbital, to 159α, a metal p-type orbital with Rydberg admixture, see Table S8 and Fig. S10. This transition is strongly dipole allowed. The metal p character of the 157-159α orbitals was ascertained by population analysis.

All calculations were performed using TURBOMOLE 7.2[17].

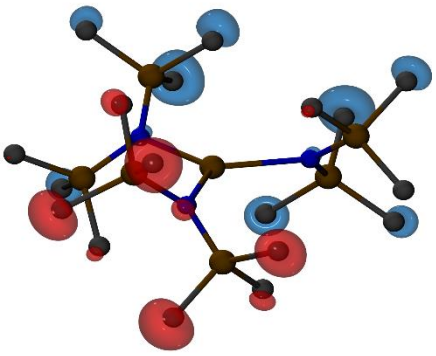

Figure 1.7: LUMO (157α,contour value 0.017) with the hydrogen atoms excluded for clarity

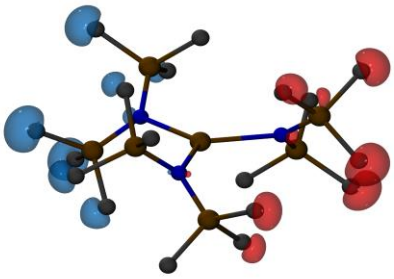

Figure 1.8: Lumo+1 (158α,contour value 0.017)

Table 1.3: Lowest electronic excitations of $[Gd\{N(SiMe_3)_2\}_3]^{1-}$ computed using TPSSh functional. Oscillator strengths are in length representation.

Wavelength (nm)	**Oscillator strength (10^{-2} a.u.)**	**Dominant contributions**			**Assignment**
		Occupied	**Unoccupied**	**%contribution**	
588.14	1.28	HOMO	LUMO+4	99.6	5d to 6p
583.52	0.57	HOMO	LUMO	99.8	5d to 6p
583.48	0.57	HOMO	LUMO+1	99.7	5d to 6p

Magnetic Susceptibility.

Magnetic Measurements. Samples were prepared in collaboration with Lucy Darago of Jeff Long's laboratory at UC Berkeley by adding crystalline powder of **2-Gd**, **2-Tb**, and **2-Dy** (15.2 mg, 8.5 mg, and 8.6 mg) to a 5-mm inner diameter quartz tube containing a raised quartz platform. Solid eicosane was added to cover the sample to prevent crystallite torqueing and provide good thermal contact between the sample and the cryostat. The tubes were fitted with Teflon sealable adapters, evacuated on a Schlenk line, and flame-sealed under static vacuum. Following flame sealing, the solid eicosane was melted in a water bath held at 40 °C. Magnetic susceptibility measurements were performed using a Quantum Design MPMS-XL SQUID magnetometer. Dc magnetic susceptibility measurements were collected in the temperature range 2 – 300 K. Diamagnetic corrections were applied to the data using Pascal's constants to give χ_D = –0.00064615 emu/mol (**2-Gd**), χ_D = –0.00064515 emu/mol (**2-Tb**), χ_D = –0.00064515 emu/mol (**2-Dy**), and χ_D = –0.00024036 emu/mol (eicosane).

Magnetism of 2-Gd. 2-Gd shows a room temperature $\chi_M T$ product of 11.29 emu K·mol^{-1} under an applied dc magnetic field of 0.1 T, which then decreases to a value of 10.20 emu K·mol^{-1} under an applied dc magnetic field of 7 T. The slightly higher than expected $\chi_M T$ product at lower fields may indicate thermal population of excited states in which the 5d electron has some orbital angular momentum. The experimental room temperature $\chi_M T$ products are in good agreement with the expected value of 10 emu K·mol^{-1} for a Gd^{2+} ion with a coupled $4f^7 5d^1$ electronic configuration. The low temperature saturation magnetization at 2 K and 7 T is 8.0 μ_B, in excellent agreement with the expected magnetization of 8 μ_B for a $4f^7 5d^1$ configuration. Magnetization versus field data collected from 2 – 10 K could be modeled with an S = 4 Brillouin function, for which it was assumed that g = 2.00, again supporting a coupled $4f^7 5d^1$electronic configuration.

Ac magnetic susceptibility measurements collected at 2 K from 1 – 1500 Hz and under applied dc magnetic fields of 0 – 0.25 T did not reveal any out out-of-phase peaks, indicating an absence of slow magnetic relaxation behaviors.

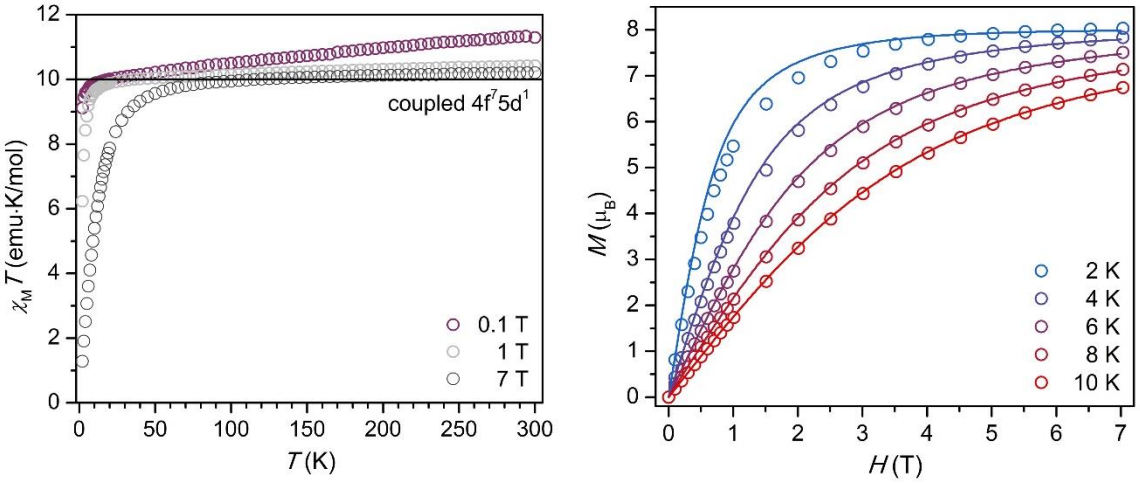

Figure 1.9 (left): Product of magnetic susceptibility times temperature versus temperature data for **2-Gd**, collected under applied fields of 0.1 T, 1 T, and 7 T. (right): Magnetization versus field data for **2-Gd** are represented by colored circles. Solid lines represent the Brilloin function for an $S = 4$ system with g = 2.00.

Magnetism of 2-Tb. 2-Tb shows a room temperature $\chi_M T$ product of 14.83 emu K·mol^{-1} under an applied dc magnetic field of 0.1 T, which then decreases to a value of 14.38 emu K·mol^{-1} under an applied dc magnetic field of 1 T. The experimental room temperature $\chi_M T$ products are in excellent agreement with the expected value of 14.42 emu K·mol^{-1} for a Tb^{2+} ion with a coupled $4f^8 5d^1$ electronic configuration. The slightly higher than expected $\chi_M T$ product at fields below 1 T may indicate thermal population of excited states in which the 5d electron has some orbital angular momentum. Finally, while the observed magnetic moment strongly agrees with a coupled $4f^8 5d^1$ configuration, the room temperature $\chi_M T$ product is also reasonably close to that expected for a $4f^9$ electronic configuration, 14.13 emu K·mol^{-1}. However, UV-Vis spectroscopy of **2-Tb** (as described in the main text) supports population of a d orbital in this complex, allowing a definitive assignment of **2-Tb** to a coupled $4f^8 5d^1$ configuration.

The low temperature saturation magnetization at 2 K and 7 T was 5.9 μ_B. Open magnetic hysteresis was not observed. Ac magnetic susceptibility measurements collected at 2 K from 1 – 1500 Hz and under applied dc magnetic fields of 0 – 0.4 T did not reveal any out out-of-phase peaks, indicating an absence of slow magnetic relaxation behaviors.

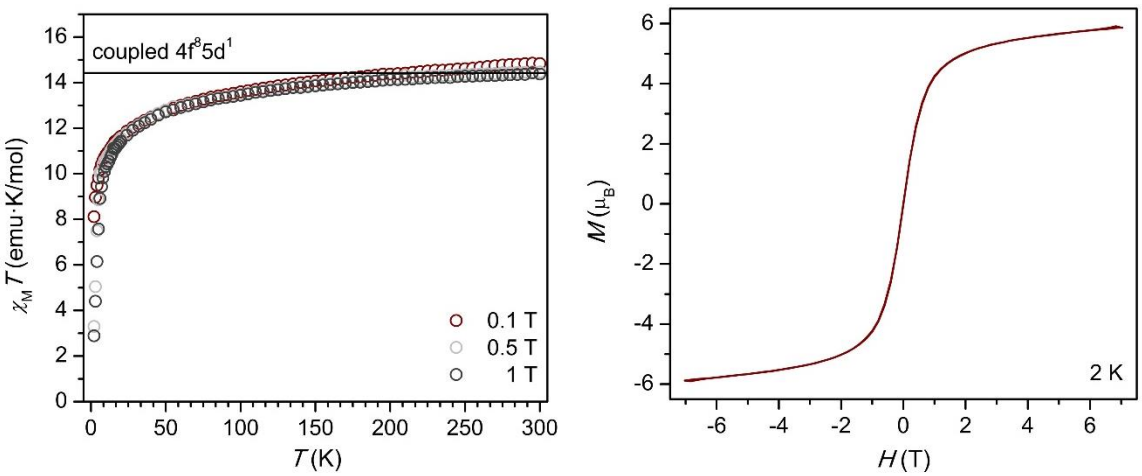

Figure 1.10 (left): Product of magnetic susceptibility times temperature versus temperature data for **2-Tb**, collected under applied fields of 0.1 T, 0.5 T, and 1 T. (right): Magnetization versus field data for **2-Tb**, collected at 2 K with a field sweep rate of 5 mT s^{-1}, are represented by a solid line.

Magnetism of 2-Dy. 2-Dy shows a room temperature $\chi_M T$ product of 17.03 emu K·mol^{-1} under an applied dc magnetic field of 0.1 T, which then decreases to a value of 16.73 emu K·mol^{-1} under an applied dc magnetic field of 1 T. The experimental room temperature $\chi_M T$ products are in excellent agreement with the expected value of 17.01 emu K·mol^{-1} for a Dy^{2+} ion with a coupled $4f^9 5d^1$ electronic configuration. The low temperature saturation magnetization at 2 K and 7 T was 6.4 μ_B. Waist-restricted magnetic hysteresis was observed at 2 K. However, ac magnetic susceptibility measurements collected at 2 K and 4 K from 1 – 1500 Hz, under applied dc magnetic fields of 0 – 0.4 T, revealed only high-frequency out-of-phase signals, without peak maxima, indicating an absence of single-molecule magnet behavior at 2 K or above. The waist-restricted hysteresis of **2-Dy** may be attributed to intermolecular magnetic interactions that possibly prompt long-range magnetic order at even lower temperatures. See Figure 1.6.

X-ray Data Collection, Structure, Solution, Refinement

For 2-Gd a purple crystal of approximate dimensions 0.521 x 0.586 x 0.633 mm was mounted on a glass fiber and transferred to a Bruker SMART APEX II diffractometer. The APEX2[50] program package was used to determine the unit-cell parameters and for data collection (10 sec/frame scan time for a sphere of diffraction data). The raw frame data was processed using SAINT[51] and SADABS[52] to yield the reflection data file. Subsequent calculations were carried out using the SHELXTL[53] program. There were no systematic absences nor any diffraction symmetry other than the Friedel condition. The centrosymmetric triclinic space group $P\bar{1}$ was assigned and later determined to be correct. The structure was solved by direct methods and refined on F^2 by full-matrix least-squares techniques. The analytical scattering factors[54] for neutral atoms were used throughout the analysis. Hydrogen atoms were included using a riding model. The gadolinium atom was disordered over two positions (approximately 75:25). C(10) and C(11) were disordered (50:50) and included using multiple components with partial site-occupancy-factors. At convergence, wR2 = 0.0816 and Goof = 1.069 for 543 variables refined against 13751 data (0.74Å), R1 = 0.0339 for those 12612 data with $I > 2.0\sigma(I)$. There were several high residuals present in the final difference-Fourier map. It was not possible to determine the nature of the residuals although it was probable that hexanes and/or tetrahydrofuran solvents were present. The SQUEEZE[55a] routine in the PLATON[55b] program package was used to account for the electrons in the solvent accessible voids.

For **2-Tb** a purple crystal of approximate dimensions 0.108 x 0.111 x 0.184 mm was mounted in a cryoloop and transferred to a Bruker SMART APEX II diffractometer. The

APEX2[50] program package was used to determine the unit-cell parameters and for data collection (90 sec/frame scan time for a sphere of diffraction data). The raw frame data was processed using SAINT[51] and SADABS[52] to yield the reflection data file. Subsequent calculations were carried out using the SHELXTL[53] program. There were no systematic absences nor any diffraction symmetry other than the Friedel condition. The centrosymmetric triclinic space group $P\bar{1}$ was assigned and later determined to be correct. The structure was solved by direct methods and refined on F^2 by full-matrix least-squares techniques. The analytical scattering factors[54] for neutral atoms were used throughout the analysis. Hydrogen atoms were included using a riding model. The terbium atom was disordered over two positions (approximately 70:30). C(10) and C(11) were disordered and included using multiple components with partial site-occupancy-factors. Least-squares analysis yielded wR2 = 0.1777 and Goof = 1.017 for 523 variables refined against 11917 data (0.80Å), R1 = 0.0737 for those 6847 data with $I > 2.0\sigma(I)$. There were several high residuals present in the final difference-Fourier map. It was not possible to determine the nature of the residuals although it was probable that hexanes and/or tetrahydrofuran solvents were present. The SQUEEZE[55a] routine in the PLATON[55b] program package was used to account for the electrons in the solvent accessible voids.

For **2-Dy** a blue crystal of approximate dimensions 0.285 x 0.319 x 0.347 mm was mounted on a glass fiber and transferred to a Bruker SMART APEX II diffractometer. The APEX2[50] program package was used to determine the unit-cell parameters and for data collection (5 sec/frame scan time for a sphere of diffraction data). The raw frame data was processed using SAINT[51] and SADABS[52] to yield the reflection data file. Subsequent calculations were carried out using the SHELXTL[53] program. There were no systematic absences

nor any diffraction symmetry other than the Friedel condition. The centrosymmetric triclinic space group $P\bar{1}$ was assigned and later determined to be correct. The structure was solved by direct methods and refined on F^2 by full-matrix least-squares techniques. The analytical scattering factors[54] for neutral atoms were used throughout the analysis. Hydrogen atoms were included using a riding model. The dysprosium atom was disordered over two positions (approximately 72:28). C(10) and C(11) were disordered and included using multiple components with partial site-occupancy-factors. At convergence, wR2 = 0.0979 and Goof = 1.045 for 543 variables refined against 13698 data (0.74Å), R1 = 0.0399 for those 11542 data with $I > 2.0\sigma(I)$. There were several high residuals present in the final difference-Fourier map. It was not possible to determine the nature of the residuals although it was probable that hexanes and/or tetrahydrofuran solvents were present. The SQUEEZE[55a] routine in the PLATON[55b] program package was used to account for the electrons in the solvent accessible voids.

For **2-Ho** a purple crystal of approximate dimensions 0.124 x 0.194 x 0.220 mm was mounted in a cryoloop and transferred to a Bruker SMART APEX II diffractometer. The APEX2[50] program package was used to determine the unit-cell parameters and for data collection (90 sec/frame scan time for a sphere of diffraction data). The raw frame data was processed using SAINT[51] and SADABS[52] to yield the reflection data file. Subsequent calculations were carried out using the SHELXTL[53] program. There were no systematic absences nor any diffraction symmetry other than the Friedel condition. The centrosymmetric triclinic space group $P\bar{1}$ was assigned and later determined to be correct. The structure was solved by direct methods and refined on F^2 by full-matrix least-squares techniques. The analytical scattering factors[54] for neutral atoms were used throughout the analysis. Hydrogen atoms were

included using a riding model. The holmium atom was disordered over two positions (approximately 74:26). C(10) and C(11) were disordered and included using multiple components with partial site-occupancy-factors. Least-squares analysis yielded wR2 = 0.1417 and Goof = 1.024 for 523 variables refined against 11796 data (0.80Å), R1 = 0.0568 for those 8232 data with $I > 2.0\sigma(I)$. There were several high residuals present in the final difference-Fourier map. It was not possible to determine the nature of the residuals although it was probable that hexanes and/or tetrahydrofuran solvents were present. The SQUEEZE[55a] routine in the PLATON[55b] program package was used to account for the electrons in the solvent accessible voids.

For **Er-2** A purple crystal of approximate dimensions 0.232 x 0.307 x 0.327 mm was mounted in a cryoloop and transferred to a Bruker SMART APEX II diffractometer. The APEX2[50] program package was used to determine the unit-cell parameters and for data collection (60 sec/frame scan time for a sphere of diffraction data). The raw frame data was processed using SAINT[51] and SADABS[52] to yield the reflection data file. Subsequent calculations were carried out using the SHELXTL[53] program. There were no systematic absences nor any diffraction symmetry other than the Friedel condition. The centrosymmetric triclinic space group $P\bar{1}$ was assigned and later determined to be correct. The structure was solved by dual space methods and refined on F^2 by full-matrix least-squares techniques. The analytical scattering factors[54] for neutral atoms were used throughout the analysis. Hydrogen atoms were included using a riding model. The erbium atom was disordered. Due to the poor data quality it was not possible to refine all atoms anisotropically. Least-squares analysis yielded wR2 = 0.2016 and Goof = 1.164 for 434 variables refined against 10653 data (0.83Å), R1 = 0.0974 for those

7844 data with I > 2.0σ(I). There were several high residuals present in the final difference-Fourier map. It was not possible to determine the nature of the residuals although it was probable that tetrahydrofuran and/or hexane solvents were present. The SQUEEZE[55a] routine in the PLATON[55b] program package was used to account for the electrons in the solvent accessible voids.

For **2-Tm** a green crystal of approximate dimensions 0.190 x 0.231 x 0.332 mm was mounted on a glass fiber and transferred to a Bruker SMART APEX II diffractometer. The APEX2[50] program package was used to determine the unit-cell parameters and for data collection (30 sec/frame scan time for a sphere of diffraction data). The raw frame data was processed using SAINT[51] and SADABS[52] to yield the reflection data file. Subsequent calculations were carried out using the SHELXTL[53] program. There were no systematic absences nor any diffraction symmetry other than the Friedel condition. The centrosymmetric triclinic space group $P\bar{1}$ was assigned and later determined to be correct. The structure was solved by direct methods and refined on F^2 by full-matrix least-squares techniques. The analytical scattering factors[54] for neutral atoms were used throughout the analysis. Hydrogen atoms were included using a riding model. The thulium atom was disordered over two positions (approximately 35% Tm(1), 65% Tm(2)). C(12) was disordered (56:44) and included using multiple components with partial site-occupancy-factors. There was one-half molecule of cyclohexane solvent present. The solvent was located about an inversion center.At convergence, wR2 = 0.1058 and Goof = 1.017 for 545 variables refined against 11934 data (0.80Å), R1 = 0.0429 for those 8484 data with I > 2.0σ(I).

Table 1.4. Crystal data and structure refinement for **2-Gd**.

Identification code	ajr10 (Austin Ryan)	
Empirical formula	C_{36} H_{90} Gd K N_5 O_6 Si_6	
Formula weight	1054.01	
Temperature	133(2) K	
Wavelength	0.71073 Å	
Crystal system	Triclinic	
Space group	$P\bar{1}$	
Unit cell dimensions	a = 11.5089(8) Å	α = 83.9480(8)°.
	b = 15.6793(11) Å	β = 76.5924(8)°.
	c = 16.7864(12) Å	γ = 89.6086(8)°.
Volume	2929.7(4) $Å^3$	
Z	2	
Density (calculated)	1.195 Mg/m^3	
Absorption coefficient	1.364 mm^{-1}	
F(000)	1112	
Crystal color	purple	
Crystal size	0.633 x 0.586 x 0.521 mm^3	
Theta range for data collection	1.254 to 28.705°	
Index ranges	$-15 \le h \le 15$, $-20 \le k \le 20$, $-22 \le l \le 22$	
Reflections collected	33829	
Independent reflections	13751 [R(int) = 0.0154]	
Completeness to theta = 25.500°	99.8 %	
Absorption correction	Semi-empirical from equivalents	
Max. and min. transmission	0.7458 and 0.6483	
Refinement method	Full-matrix least-squares on F^2	
Data / restraints / parameters	13751 / 0 / 543	
Goodness-of-fit on F^2	1.069	
Final R indices [I>2sigma(I) = 12612 data]	R1 = 0.0339, wR2 = 0.0794	
R indices (all data, 0.74 Å)	R1 = 0.0383, wR2 = 0.0816	
Largest diff. peak and hole	1.945 and -1.146 $e.Å^{-3}$	

Table 1.5. Crystal data and structure refinement for **2-Tb**.

Identification code	ajr5 (Austin Ryan)	
Empirical formula	C_{36} H_{90} K N_5 O_6 Si_6 Tb	
Formula weight	1055.68	
Temperature	133(2) K	
Wavelength	0.71073 Å	
Crystal system	Triclinic	
Space group	$P\bar{1}$	
Unit cell dimensions	a = 11.482(2) Å	α = 83.7837(19)°.
	b = 15.704(3) Å	β = 77.0788(19)°.
	c = 16.713(3) Å	γ = 89.4985(19)°.
Volume	2919.8(9) $Å^3$	
Z	2	
Density (calculated)	1.201 Mg/m^3	
Absorption coefficient	1.443 mm^{-1}	
F(000)	1114	
Crystal color	purple	
Crystal size	0.184 x 0.111 x 0.108 mm^3	
Theta range for data collection	1.258 to 26.451°	
Index ranges	$-14 \leq h \leq 14$, $-19 \leq k \leq 19$, $-20 \leq l \leq 20$	
Reflections collected	26446	
Independent reflections	11917 [R(int) = 0.0940]	
Completeness to theta = 25.500°	99.4 %	
Absorption correction	Semi-empirical from equivalents	
Max. and min. transmission	0.7454 and 0.6334	
Refinement method	Full-matrix least-squares on F^2	
Data / restraints / parameters	11917 / 0 / 523	
Goodness-of-fit on F^2	1.017	
Final R indices [I>2sigma(I) = 6847 data]	R1 = 0.0737, wR2 = 0.1501	
R indices (all data, 0.80 Å)	R1 = 0.1454, wR2 = 0.1777	
Largest diff. peak and hole	1.528 and -1.287 $e.Å^{-3}$	

Table 1.6. Crystal data and structure refinement for **2-Dy**.

Identification code	ajr2 (Austin Ryan)	
Empirical formula	C_{36} H_{90} Dy K N_5 O_6 Si_6	
Formula weight	1059.26	
Temperature	133(2) K	
Wavelength	0.71073 Å	
Crystal system	Triclinic	
Space group	$P\bar{1}$	
Unit cell dimensions	a = 11.4843(7) Å	α = 83.9604(8)°.
	b = 15.6509(10) Å	β= 76.7399(8)°.
	c = 16.7396(10) Å	γ = 89.5540(8)°.
Volume	2911.9(3) $Å^3$	
Z	2	
Density (calculated)	1.208 Mg/m^3	
Absorption coefficient	1.516 mm^{-1}	
F(000)	1116	
Crystal color	blue	
Crystal size	0.347 x 0.319 x 0.285 mm^3	
Theta range for data collection	1.257 to 28.772°	
Index ranges	$-15 \leq h \leq 15$, $-20 \leq k \leq 21$, $-22 \leq l \leq 22$	
Reflections collected	34876	
Independent reflections	13698 [R(int) = 0.0283]	
Completeness to theta = 25.500°	99.8 %	
Absorption correction	Semi-empirical from equivalents	
Max. and min. transmission	0.7458 and 0.6634	
Refinement method	Full-matrix least-squares on F^2	
Data / restraints / parameters	13698 / 0 / 543	
Goodness-of-fit on F^2	1.045	
Final R indices [I>2sigma(I) = 11542 data]	R1 = 0.0399, wR2 = 0.0922	
R indices (all data, 0.74 Å)	R1 = 0.0505, wR2 = 0.0979	
Largest diff. peak and hole	1.890 and -1.331 e.$Å^{-3}$	

Table 1.7. Crystal data and structure refinement for **2-Ho**.

Identification code	ajr6 (Austin Ryan)	
Empirical formula	C_{36} H_{90} Ho N_5 O_6 Rb Si_6	
Formula weight	1108.06	
Temperature	133(2) K	
Wavelength	0.71073 Å	
Crystal system	Triclinic	
Space group	$P\bar{1}$	
Unit cell dimensions	a = 11.432(4) Å	α = 83.815(3)°.
	b = 15.711(5) Å	β = 77.564(4)°.
	c = 16.722(5) Å	γ = 89.406(4)°.
Volume	2915.6(16) $Å^3$	
Z	2	
Density (calculated)	1.262 Mg/m^3	
Absorption coefficient	2.348 mm^{-1}	
F(000)	1154	
Crystal color	purple	
Crystal size	0.220 x 0.194 x 0.124 mm^3	
Theta range for data collection	1.254 to 26.429°	
Index ranges	$-14 \le h \le 14$, $-19 \le k \le 19$, $-20 \le l \le 20$	
Reflections collected	23017	
Independent reflections	11796 [R(int) = 0.0452]	
Completeness to theta = 25.500°	98.8 %	
Absorption correction	Semi-empirical from equivalents	
Max. and min. transmission	0.7454 and 0.5526	
Refinement method	Full-matrix least-squares on F^2	
Data / restraints / parameters	11796 / 0 / 523	
Goodness-of-fit on F^2	1.024	
Final R indices [I>2sigma(I) = 8232 data]	R1 = 0.0568, wR2 = 0.1260	
R indices (all data, 0.80 Å)	R1 = 0.0939, wR2 = 0.1417	
Largest diff. peak and hole	1.677 and -1.282 $e.Å^{-3}$	

Table 1.8. Crystal data and structure refinement for **2-Er**.

Identification code	ajr14 (Austin Ryan)	
Empirical formula	C_{36} H_{90} Er N_5 O_6 Rb Si_6	
Formula weight	1110.39	
Temperature	133(2) K	
Wavelength	0.71073 Å	
Crystal system	Triclinic	
Space group	$P\bar{1}$	
Unit cell dimensions	a = 11.371(3) Å	α = 95.918(3)°.
	b = 15.924(4) Å	β = 101.105(3)°.
	c = 16.622(4) Å	γ = 90.810(3)°.
Volume	2935.9(13) $Å^3$	
Z	2	
Density (calculated)	1.256 Mg/m^3	
Absorption coefficient	2.413 mm^{-1}	
F(000)	1156	
Crystal color	purple	
Crystal size	0.327 x 0.307 x 0.232 mm^3	
Theta range for data collection	1.286 to 25.458°	
Index ranges	$-13 \leq h \leq 13$, $-19 \leq k \leq 19$, $-19 \leq l \leq 19$	
Reflections collected	22048	
Independent reflections	10653 [R(int) = 0.0425]	
Completeness to theta = 25.458°	97.9 %	
Absorption correction	Numerical or multi-scan	
Max. and min. transmission	0.7452 and 0.5981	
Refinement method	Full-matrix least-squares on F^2	
Data / restraints / parameters	10653 / 0 / 434	
Goodness-of-fit on F^2	1.164	
Final R indices [I>2sigma(I) = 7844 data]	R1 = 0.0974, wR2 = 0.1906	
R indices (all data, 0.83 Å)	R1 = 0.1284, wR2 = 0.2016	
Largest diff. peak and hole	1.242 and -1.440 $e.Å^{-3}$	

Table 1.9. Crystal data and structure refinement for **2-Tm**.

Identification code	ajr9 (Austin Ryan)	
Empirical formula	C_{36} H_{90} N_5 O_6 Rb Si_6 Tm • ½ (C_6H_{12})	
Formula weight	1154.14	
Temperature	88(2) K	
Wavelength	0.71073 Å	
Crystal system	Triclinic	
Space group	$P\bar{1}$	
Unit cell dimensions	a = 11.5334(12) Å	α = 82.2086(12)°.
	b = 15.9884(17) Å	β = 78.4416(13)°.
	c = 16.4645(17) Å	γ = 90.7332(12)°.
Volume	2944.5(5) $Å^3$	
Z	2	
Density (calculated)	1.302 Mg/m^3	
Absorption coefficient	2.490 mm^{-1}	
F(000)	1206	
Crystal color	green	
Crystal size	0.332 x 0.231 x 0.190 mm^3	
Theta range for data collection	1.679 to 26.381°	
Index ranges	$-14 \leq h \leq 14$, $-19 \leq k \leq 19$, $-20 \leq l \leq 20$	
Reflections collected	24277	
Independent reflections	11934 [R(int) = 0.0360]	
Completeness to theta = 25.500°	99.3 %	
Absorption correction	Semi-empirical from equivalents	
Max. and min. transmission	0.6939 and 0.5554	
Refinement method	Full-matrix least-squares on F^2	
Data / restraints / parameters	11934 / 0 / 545	
Goodness-of-fit on F^2	1.017	
Final R indices [I>2sigma(I) = 8484 data]	R1 = 0.0429, wR2 = 0.0943	
R indices (all data, 0.80 Å)	R1 = 0.0747, wR2 = 0.1058	
Extinction coefficient	n/a	
Largest diff. peak and hole	1.441 and -0.784 $e.Å^{-3}$	

Table 1.10. Crystal data and structure refinement for **2-Nd**.

Identification code	ajr7 (Austin Ryan)	
Empirical formula	C_{36} H_{90} N_5 Nd O_6 Rb Si_6	
Formula weight	1087.37	
Temperature	133(2) K	
Wavelength	0.71073 Å	
Crystal system	Triclinic	
Space group	$P\bar{1}$	
Unit cell dimensions	a = 11.481(3) Å	α = 83.513(3)°.
	b = 15.869(3) Å	β = 78.216(3)°.
	c = 16.607(4) Å	γ = 90.232(3)°.
Volume	2941.9(11) $Å^3$	
Z	2	
Density (calculated)	1.228 Mg/m^3	
Absorption coefficient	1.864 mm^{-1}	
F(000)	1140	
Crystal color	blue	
Crystal size	0.286 x 0.158 x 0.115 mm^3	
Theta range for data collection	1.261 to 26.444°	
Index ranges	$-12 \le h \le 14$, $-19 \le k \le 19$, $-20 \le l \le 20$	
Reflections collected	20711	
Independent reflections	11960 [R(int) = 0.0521]	
Completeness to theta = 25.500°	99.3 %	
Absorption correction	Semi-empirical from equivalents	
Max. and min. transmission	0.7454 and 0.5911	
Refinement method	Full-matrix least-squares on F^2	
Data / restraints / parameters	11960 / 0 / 438	
Goodness-of-fit on F^2	1.034	
Final R indices [I>2sigma(I) = 6097 data]	R1 = 0.0784, wR2 = 0.1772	
R indices (all data, 0.80 Å)	R1 = 0.1646, wR2 = 0.2146	
Largest diff. peak and hole	1.526 and -0.931 $e.Å^{-3}$	

Definitions:

wR2 = [Σ[w(Fo 2 -Fc 2) 2] / Σ[w(Fo 2) 2]] 1/2

R1 = Σ||Fo|-|Fc|| / Σ|Fo|

Goof = S = [Σ[w(Fo 2 -Fc 2) 2] / (n-p)]1/2 where n is the number of reflections and p is the total number of parameters refined

Selected Bond lengths

For **2-Gd** (Å)

Gd(1)-Gd(2)	1.0468(4)
Gd(1)-N(1)	2.289(2)
Gd(1)-N(2)	2.2919(19)
Gd(1)-N(3)	2.3424(18)
Gd(2)-N(3)	2.2921(18)
Gd(2)-N(2)	2.3047(19)
Gd(2)-N(1)	2.326(2)
Si(1)-N(1)	1.726(2)
Si(2)-N(1)	1.698(2)
Si(3)-N(2)	1.7045(19)
Si(4)-N(2)	1.7060(19)
Si(5)-N(3)	1.7011(19)
Si(6)-N(3)	1.708(2)
K(1)-O(2)	2.8083(16)
K(1)-O(3)	2.8107(17)
K(1)-O(1)	2.8203(17)
K(1)-O(6)	2.8248(15)
K(1)-O(4)	2.8397(17)
K(1)-O(5)	2.8748(18)
K(1)-N(5)	3.0189(18)
K(1)-N(4)	3.038(2)
N(1)-Gd(1)-N(2)	116.26(7)
N(1)-Gd(1)-N(3)	111.20(7)
N(2)-Gd(1)-N(3)	117.52(7)

For **2-Tb** (Å)

Tb(1)-Tb(2)	1.0036(12)
Tb(1)-N(2)	2.251(6)
Tb(1)-N(1)	2.286(6)
Tb(1)-N(3)	2.319(5)
Tb(2)-N(1)	2.274(6)
Tb(2)-N(3)	2.279(5)
Tb(2)-N(2)	2.284(6)
Si(1)-N(1)	1.722(6)
Si(2)-N(1)	1.690(6)
Si(3)-N(2)	1.708(6)
Si(3)-C(9)	1.865(8)
Si(4)-N(2)	1.705(6)
Si(5)-N(3)	1.705(6)
Si(6)-N(3)	1.699(6)
K(1)-O(2)	2.803(4)
K(1)-O(3)	2.811(5)
K(1)-O(1)	2.817(5)
K(1)-O(6)	2.827(4)
K(1)-O(4)	2.837(5)
K(1)-O(5)	2.868(5)
K(1)-N(5)	3.026(5)
K(1)-N(4)	3.031(6)
N(2)-Tb(1)-N(1)	116.4(2)
N(2)-Tb(1)-N(3)	118.0(2)
N(1)-Tb(1)-N(3)	110.95(19)

For **2-Dy** (Å)

Dy(1)-Dy(2)	1.0460(5)
Dy(1)-N(2)	2.255(2)
Dy(1)-N(1)	2.256(2)
Dy(1)-N(3)	2.303(2)
Dy(2)-N(3)	2.245(2)
Dy(2)-N(2)	2.268(2)
Dy(2)-N(1)	2.296(2)
Si(1)-N(1)	1.726(2)
Si(2)-N(1)	1.699(2)
Si(3)-N(2)	1.705(2)
Si(4)-N(2)	1.706(2)
Si(5)-N(3)	1.704(2)
Si(6)-N(3)	1.711(2)
K(1)-O(2)	2.8045(19)
K(1)-O(3)	2.8078(19)
K(1)-O(1)	2.816(2)
K(1)-O(6)	2.8229(18)
K(1)-O(4)	2.837(2)
K(1)-O(5)	2.874(2)
K(1)-N(5)	3.016(2)
K(1)-N(4)	3.036(2)
N(2)-Dy(1)-N(1)	116.10(8)
N(2)-Dy(1)-N(3)	117.41(8)
N(1)-Dy(1)-N(3)	110.84(8)

For **3-Ho** (Å)

Ho(1)-Ho(2)	1.0193(11)

Ho(1)-N(2)	2.241(5)
Ho(1)-N(1)	2.253(5)
Ho(1)-N(3)	2.282(4)
Ho(2)-N(1)	2.242(5)
Ho(2)-N(3)	2.256(5)
Ho(2)-N(2)	2.266(5)
Si(1)-N(1)	1.721(5)
Si(2)-N(1)	1.699(5)
Si(3)-N(2)	1.696(5)
Si(4)-N(2)	1.713(5)
Si(5)-N(3)	1.710(5)
Si(6)-N(3)	1.706(5)
Rb(1)-O(2)	2.857(4)
Rb(1)-O(3)	2.870(4)
Rb(1)-O(1)	2.871(4)
Rb(1)-O(6)	2.878(3)
Rb(1)-O(4)	2.889(4)
Rb(1)-O(5)	2.914(4)
Rb(1)-N(5)	3.025(4)
Rb(1)-N(4)	3.030(5)
N(2)-Ho(1)-N(1)	116.46(16)
N(2)-Ho(1)-N(3)	117.64(17)
N(1)-Ho(1)-N(3)	110.63(17)

For **2-Tm** (Å)

Tm(1)-Tm(2)	0.464(3)
Tm(1)-N(2)	2.290(5)

Tm(1)-N(3)	2.331(4)
Tm(1)-N(1)	2.356(5)
Tm(2)-N(1)	2.288(4)
Tm(2)-N(3)	2.325(4)
Tm(2)-N(2)	2.334(4)
Si(1)-N(1)	1.694(4)
Si(2)-N(1)	1.686(4)
Si(3)-N(2)	1.692(4)
Si(4)-N(2)	1.687(3)
Si(5)-N(3)	1.693(3)
Si(6)-N(3)	1.686(4)
Rb(1)-O(1)	2.868(3)
Rb(1)-O(6)	2.872(3)
Rb(1)-O(3)	2.874(3)
Rb(1)-O(2)	2.876(3)
Rb(1)-O(4)	2.886(3)
Rb(1)-O(5)	2.920(3)
Rb(1)-N(4)	3.012(3)
Rb(1)-N(5)	3.023(3)
N(2)-Tm(1)-N(3)	122.98(19)
N(2)-Tm(1)-N(1)	120.38(18)
N(3)-Tm(1)-N(1)	112.57(17)

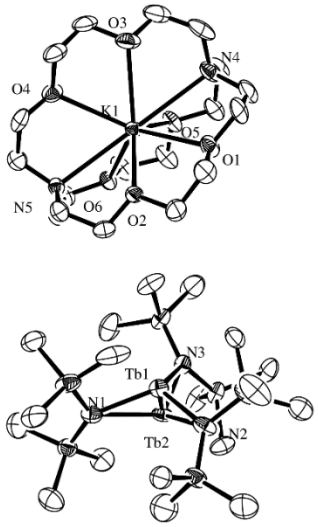

Figure 1.11. Thermal ellipsoid plot of **2-Tb** drawn at 50% probability level. Hydrogen atoms and disordered atoms are omitted for clarity.

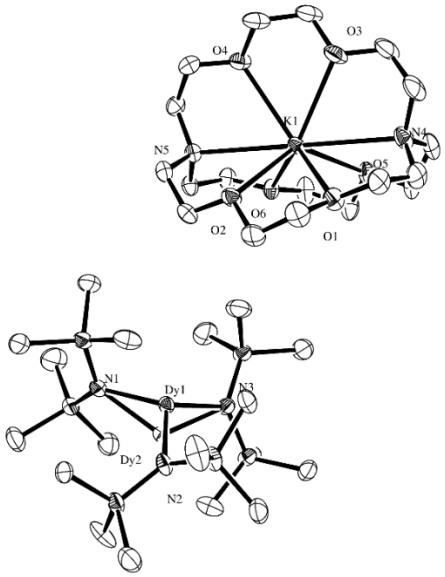

Figure 1.12. Thermal ellipsoid plot of **2-Dy** drawn at 50% probability level. Hydrogen atoms and disordered atoms are omitted for clarity.

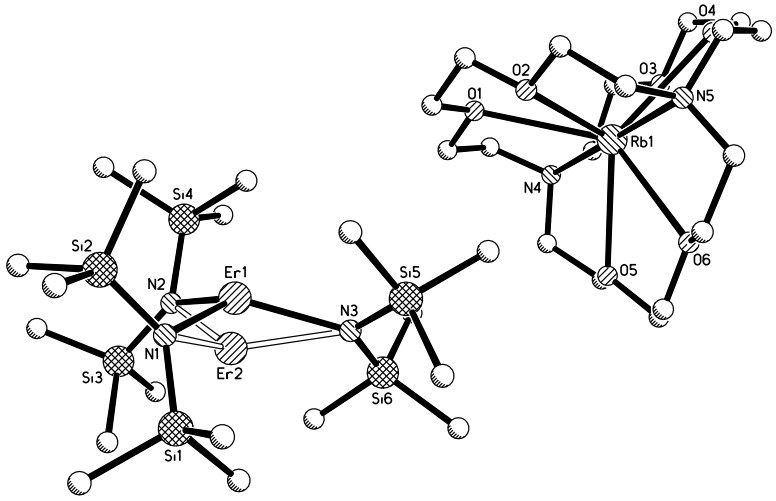

Figure 1.13. Ball-and-stick figure of **3-Er**

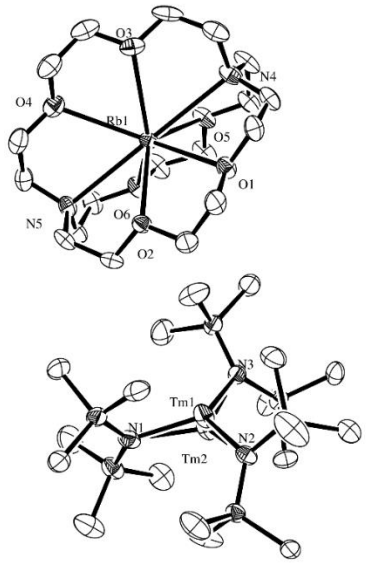

Figure 1.14. Thermal ellipsoid plot of **2-Tb** drawn at 50% probability level. Hydrogen atoms and disordered atoms are omitted for clarity.

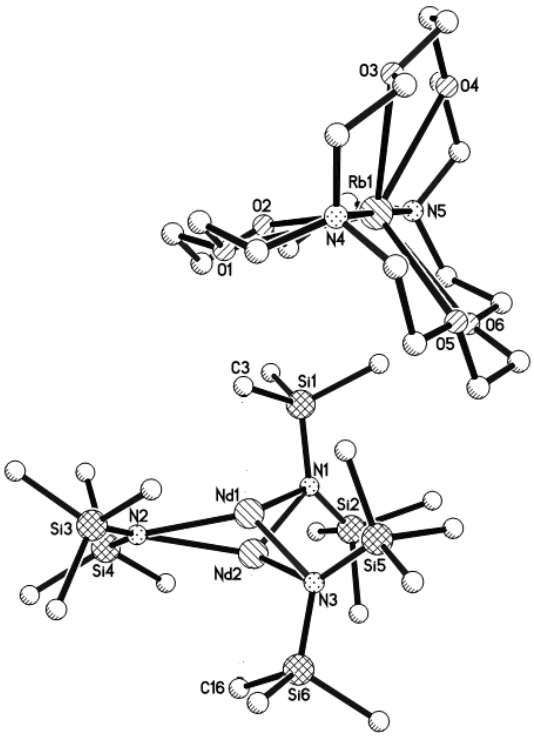

Figure 1.15. Ball-and-stick figure of **3-Nd**

References

1 a) P. B. Hitchcock, M. F. Lappert, L. Maron, A. V. Protchenko, *Angew. Chem. Int. Ed.* **2008**, *47*, 1488-1491;

2 M. R. MacDonald, J. W. Ziller, W. J. Evans, *J. Am. Chem. Soc.* **2011**, *133*, 15914-15917;

3 M. R. MacDonald, J. E. Bates, M. E. Fieser, J. W. Ziller, F. Furche, W. J. Evans, *J. Am. Chem. Soc.* **2012**, *134*, 8420-8423;

4 M. R. MacDonald, J. E. Bates, J. W. Ziller, F. Furche, W. J. Evans, *J. Am. Chem. Soc.* **2013**, *135*, 9857-9868;

5 M. E. Fieser, M. R. MacDonald, B. T. Krull, J. E. Bates, J. W. Ziller, F. Furche, W. J. Evans, *J. Am. Chem. Soc.* **2015**, *137*, 369-382;

6 W. J. Evans, *Organomet.* **2016**, *35*, 3088-3100;

7 D. H. Woen, W. J. Evans, *Handbook on the Physics and Chemistry of Rare Earths* **2016**, *50*, 337-394.

8 a) L. R. Morss, *Chem. Rev.* **1976**, *76*, 827-841; b) N. B. Mikheev, A. N. Kamenskaya, *Coord. Chem. Rev.* **1991**, *109*, 1-59.

9 a) C. Matignon, E. Cazes, *Ann. Chim. Phys.* **1906**, *8*, 417-426; b) G. Jantsch, H. Grubitsch, F. Hoffmann, H. Alber, *Z. Anorg. Allg. Chem.* **1929**, *185*, 49-64; c) W. Klemm, H. Bommer, *Z. Anorg. Allg. Chem.* **1937**, *231*, 138-171; d) J. Corbett, *Revue de Chimie Minerale* **1972**, *10*;

10 G. Meyer, *Chem. Rev.* **1988**, *88*, 93-107;

11 G. Meyer, *Z. Anorg. Allg. Chem.* **2007**, *633*, 2537-2552;

12 D. A. Atwood, *The rare earth elements: fundamentals and applications*, John Wiley & Sons, **2013**.

13 J. Corbett, *Revue de Chimie Minerale* **1973**, *10*, 239-257;

14 a) G. Meyer, H. J. Meyer, *Chem. Mater.* **1992**, *4*, 1157-1168; c) M. N. Bochkarev, A. A. Fagin, *Chem. Eur. J.* **1999**, *5*, 2990-2992; d) G. Meyer, M. S. Wickleder, *Simple and complex halides, Vol. 28*, Elsevier Science BV: Amsterdam, The Netherlands, **2000**; e) M. N. Bochkarev, *Coord. Chem. Rev.* **2004**, *248*, 835-851.

15 F. Jaroschik, F. Nief, X.-F. Le Goff, L. Ricard, *Organomet.* **2007**, *26*, 1123-1125.

16 F. Jaroschik, A. Momin, F. Nief, X. F. Le Goff, G. B. Deacon, P. C. Junk, *Angew. Chem.* **2009**, *121*, 1137-1141.

17 M. E. Fieser, C. T. Palumbo, H. S. La Pierre, D. P. Halter, V. K. Voora, J. W. Ziller, F. Furche, K. Meyer, W. J. Evans, *Chemical science* **2017**, *8*, 7424-7433.

18 a) W. J. Evans, G. Zucchi, J. W. Ziller, *J. Am. Chem. Soc.* **2003**, *125*, 10-11; b) W. J. Evans, D. S. Lee, D. B. Rego, J. M. Perotti, S. A. Kozimor, E. K. Moore, J. W. Ziller, *J. Am. Chem. Soc.* **2004**, *126*, 14574-14582; c) W. J. Evans, D. S. Lee, J. W. Ziller, *J. Am.*

Chem. Soc. **2004**, *126*, 454-455; d) J. D. Rinehart, M. Fang, W. J. Evans, J. R. Long, *Nat. Chem.* **2011**, *3*, 538-542; e) J. D. Rinehart, M. Fang, W. J. Evans, J. R. Long, *J. Am. Chem. Soc.* **2011**, *133*, 14236-14239.

19 M. Fang, D. S. Lee, J. W. Ziller, R. J. Doedens, J. E. Bates, F. Furche, W. J. Evans, *J. Am. Chem. Soc.* **2011**, *133*, 3784-3787.

20 D. H. Woen, G. P. Chen, J. W. Ziller, T. J. Boyle, F. Furche, W. J. Evans, *Angew. Chem. Int. Ed.* **2017**, *56*, 2050-2053.

21 D. C. Bradley, J. S. Ghotra, F. A. Hart, *J. Chem. Soc., Chem. Commun.* **1972**, 349-350.

22 W. M. Haynes, *CRC Handbook of Chemistry and Physics*, CRC press, **2016**.

23 R. A. Andersen, D. H. Templeton, A. Zalkin, *Inorg. Chem.* **1978**, *17*, 2317-2319.

24 J. S. Ghotra, M. B. Hursthouse, A. J. Welch, *J. Chem. Soc., Chem. Commun.* **1973**, 669-670.

25 P. B. Hitchcock, A. G. Hulkes, M. F. Lappert, Z. Li, *Dalt. Trans.* **2004**, 129-136.

26 A. Herrmann Wolfgang, R. Anwander, C. Munck Florian, W. Scherer, V. Dufaud, W. Huber Norbert, R. J. Artus Georg, in *Zeitschrift für Naturforschung B, Vol. 49*, **1994**, p. 1789.

27 P. G. Eller, D. C. Bradley, M. B. Hursthouse, D. W. Meek, *Coord. Chem. Rev.* **1977**, *24*, 1-95.

28 M. Niemeyer, *Z. Anorg. Allg. Chem.* **2002**, *628*, 647-657.

29 Staroverov, V. N.; Scuseria, G. E.; Tao, J.; Perdew, J. P., *J. Chem. Phys.* **2003**, 119, 12129.

30 R. Gulde, P. Pollak, F. Weigend, *J. Chem. Theory Comput.*, **2012**, *8* (11), 4062.

31 M. Dolg, H. Stoll, H. Preuss; *J. Chem. Phys.*, **1989**, 90, 1730.

32 F. Furche, B. T. Krull, B. D. Nguyen, J. J. Kwon, *J. Chem. Phys.* **2016**, 144, 174105.

33 D. M. Anderson, F. G. N. Cloke, P. A. Cox, N. Edelstein, J. C. Green, T. Pang, A. A. Sameh, G. Shalimoff, *J. Chem. Soc., Chem. Commun.* **1989**, 53-55;

34 K. R. Meihaus, M. E. Fieser, J. F. Corbey, W. J. Evans, J. R. Long, *J. Am. Chem. Soc.* **2015**, *137*, 9855-9860.

35 M. E. Fieser, PhD Dissertation, University of California - Irvine **2015**.

36 a) W. J. Evans, D. K. Drummond, H. Zhang, J. L. Atwood, *Inorg. Chem.* **1988**, *27*, 575-579; b) W. J. Evans, M. A. Johnston, R. D. Clark, R. Anwander, J. W. Ziller, *Polyhedron* **2001**, *20*, 2483-2490.

37 T. D. Tilley, R. A. Andersen, A. Zalkin, *Inorg. Chem.* **1984**, *23*, 2271-2276.

38 C. A. P. Goodwin, N. F. Chilton, G. F. Vettese, E. Moreno Pineda, I. F. Crowe, J. W. Ziller, R. E. P. Winpenny, W. J. Evans, D. P. Mills, *Inorg. Chem.* **2016**, *55*, 10057-10067.

39 M. D. Taylor, *Chem. Rev.* **1962**, *62*, 503-511.

40 D. C. Bradley, J. S. Ghotra, F. A. Hart, *J. Chem. Soc., Chem. Commun.* **1972**, 349-350.

41 V. Staroverov, G. Scuseria, J. Tao, J. Perdew, *J. Chem. Phys.*, **2009**, 119, 12129.

42 S. Grimme, *J. Comput. Chem.*, **2006**, 27, 1787-1799.

43 S. Grimme, J. Antony, S. Ehrlich, H. Krieg, *J. Chem. Phys.*, **2010**, 132, 154104.

44 F. Weigend, R. Ahlrichs, *Phys. Chem. Chem. Phys*. **2005**, 7, 3297-3305.

45 A. Schäfer, H. Horn, R. Ahlrichs, *J. Chem. Phys.* **1992,** 97, 2571.

46 O. Treutler, R. Ahlrichs, *J. Chem. Phys.* **1995**, 102, 346.

47 A. Klamt, G. Schüürmann, *J. Chem. Soc., Perkin Trans.* **1993**, 2, 799-805.

48 In *CRC Handbook of Chemistry and Physics*; Lide, D. R., Ed.; CRC Press: Boca Raton,FL, **2008**; Vol. 88, p 136-136.

49 J. E. Bates, F. Furche, *J. Chem. Phys.* **2012,** 137, 164105.

50 APEX2 Version 2014.11-0, Bruker AXS, Inc., Madison, WI, 2014.

51 SAINT Version 8.34a, Bruker AXS, Inc., Madison, WI, 2013.

52 G. M. Sheldrick, SADABS, Version 2014/5, Bruker AXS, Inc., Madison, WI, 2014.

53 G. M. Sheldrick, SHELXTL, Version 2014/7, Bruker AXS, Inc., Madison, WI, 2014.

54 International Tables for Crystallography, Vol. C, Kluwer Academic Publishers, Dordrecht, 1992.

55 (a) Spek, A.L. SQUEEZE, Acta Cryst. 2015, C71, 9-19., (b) Spek, A. L. PLATON, Acta. Cryst. 2009, D65, 148-155

Chapter 2

The Importance of the Counter-cation in Reductive Rare-Earth Metal Chemistry: 18-Crown-6 Instead of 2,2,2-Cryptand Allows Isolation of $[Y^{II}(NR_2)_3]^{1-}$ and Ynediolate and Enediolate Complexes from CO Reactions

Introduction*

As described in the Introduction and Chapter 1, investigations of LnA_3/M reactions (Ln = rare-earth metal; A = anion; M = alkali metal) related to the reduction of dinitrogen which provided $(N_2)^{2-}$ and $(N_2)^{3-}$ complexes,[9-14] showed evidence for an Y(II) ion in solution based on an EPR spectrum of the product obtained from treatment of $Y(NR_2)_3$ (R = $SiMe_3$) with K in THF at −35°C under argon.[15] Although the two-line spectrum arising from the ^{89}Y I = ½ nucleus indicated the presence of Y(II), structural confirmation of an Y(II) amide complex was elusive. By switching from bis(silyl)amide ancillary ligands to the silylcyclopentadienyl ligand, $C_5H_4SiMe_3$ (Cp′), a crystallographically characterizable Y(II) complex was isolated by reduction of Cp'_3Y with KC_8 in the presence of 18-crown-6 (18-c-6), namely [K(18-c-6)][YCp'_3], eq 2.1. [6]

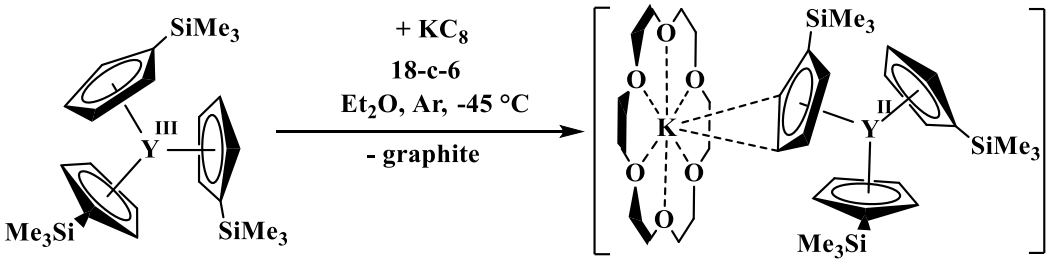

(2.1)

An explanation for the efficacy of the silylcyclopentadienyl ligands was possible from the

*Portions of this chapter have been published: Ryan, A. J.; Ziller, J. W.; Evans, W. J. *Chemical Science* **2020,** Advance Artcle.

hyperfine coupling constants of the EPR spectra of the yttrium complexes. The hyperfine coupling constant of the $Y(NR_2)_3/K$ reduction product, 110 Gauss,[15] was considerably larger than the 36.6 Gauss coupling constant of (Cp'_3Y)[1-6] and suggested that more of the unpaired electron density was located on the metal in the amide complex. It was reasoned that this was the cause of its limited stability and made it too reactive to isolate. Since trivalent complexes of yttrium and lanthanides of similar size, particularly Ho and Er, have always displayed similar chemistry, it was assumed the $[Ln(NR_2)_3]^{1-}$ complexes could not be isolated either.

It was therefore surprising that alkali metal reduction of $Sc(NR_2)_3$ in the presence of both 18-c-6 and crypt generated crystallographically-characterizable Sc(II) complexes, $[Sc(NR_2)_3]^{1-}$, eq 2.2.[18] This indicated that scandium displayed different chemistry from the yttrium congener directly below it in the periodic table.

$$\mathbf{Ln^{III}(NR_2)_3 \;+\; M \xrightarrow[Ar]{\text{chelate}} [M(chelate)][Ln^{II}(NR_2)_3]} \qquad \mathbf{(2.2)}$$

R = $SiMe_3$
Ln = Sc **M(chelate) = K(crypt), K(18-c-6), Cs(Crypt)**
Ln = Gd, Tb, Dy; **M(chelate) = K(crypt)**
Ln = Nd, Ho, Er; **M(chelate) = Rb(crypt)**

This suggested that the yttrium / late lanthanide comparison should be re-evaluated. As described in Chapter 1, it was found that reduction of the $Ln(NR_2)_3$ complexes of Gd, Tb, and Dy with K in the presence of crypt generated crystallographically-characterizable Ln(II) complexes, $[K(crypt)][Ln(NR_2)_3]$, **1-Ln**, like Sc.[19] Hence, these rare-earth metals also differed from yttrium. For Ln = Nd, Ho and Er, however, it was necessary to use Rb as the reductant in the presence of crypt to obtain crystals of the $[Ln(NR_2)_3]^{1-}$ anions as $[Rb(crypt)][Ln(NR_2)_3]$. Attempts to isolate either salt of the yttrium anion, $[Y(NR_2)_3]^{1-}$, were unsuccessful.

Although an Y(II) complex was not yet isolated with amide ligands, the reactivity of the $Y(NR_2)_3$/K system was explored with CO and led to complexes of $(CO)^{1-}$ and $(OC{\equiv}CO)^{2-}$-, eq 2.3.[20]

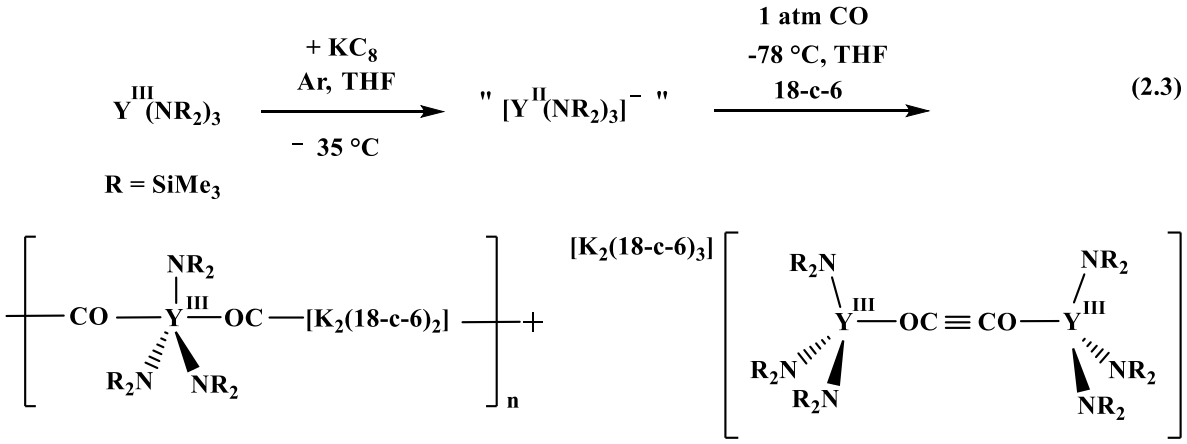

(2.3)

This chapter describes the results of switching from crypt as the potassium chelator to two equivalents of 18-c-6 in the reduction protocol for rare earth $Ln(NR_2)_3$ complexes. By switching from crypt to 18-c-6 not only could Ln(II) complexes of Ho and Er be isolated with K as the reductant, but the $[Y(NR_2)_3]^{1-}$ anion, elusive since 2011, could be isolated and crystallographically characterized. These results were unexpected since the $(YCp'_3)^{1-}$ anion was more stable with crypt as a potassium chelate compared to 18-c-6 and in this study none of the cations were near the anions in the solid state. Stability studies on the 18-c-6 complexes suggested that the speed of crystallization was a critical factor. In addition, it is described how these $[K(18\text{-c-}6)_2]^{1+}$ salts enhanced the reaction chemistry of the Ln(II) complexes by allowing isolation of CO reduction products not obtainable from the $[K(crypt)]^{1+}$ analogs. New ynediolate complexes and an unusual enediolate complex derived from CO reduction and homologation are presented as further examples of the importance of the potassium chelating agent in these rare-earth metal reduction systems.

RESULTS

Synthesis. Gd, Tb, Dy. Initially, potassium graphite reduction of $Tb(NR_2)_3$ (R = $SiMe_3$) was performed with a 1:1 ratio of $Tb(NR_2)_3$ to 18-crown-6 (18-c-6) to evaluate the necessity of the 2.2.2-cryptand (crypt) chelate in isolating the Ln(II) species. Upon reduction, a deep blue solution was produced similar to that of [K(crypt)][$Tb(NR_2)_3$], **1-Tb**. Layering with hexanes yielded dark blue crystals. X-ray diffraction indicated that the $[Tb(NR_2)_3]^{1-}$ anion had formed, but, surprisingly, there were two 18-c-6 units per potassium in the counter-cation: [$K(18\text{-c-}6)_2$][$Tb(NR_2)_3$], **2-Tb,** Figure 2.1. Subsequent reductions were then performed with a 1:2 ratio of $Ln(NR_2)_3$ to 18-c-6 which led to an increased yield, 75%. The same reaction conditions were applied to $Gd(NR_2)_3$ and $Dy(NR_2)_3$ and the analogous complexes, **2-Gd** and **2-Dy**, were isolated in similar yields, eq 2.4.

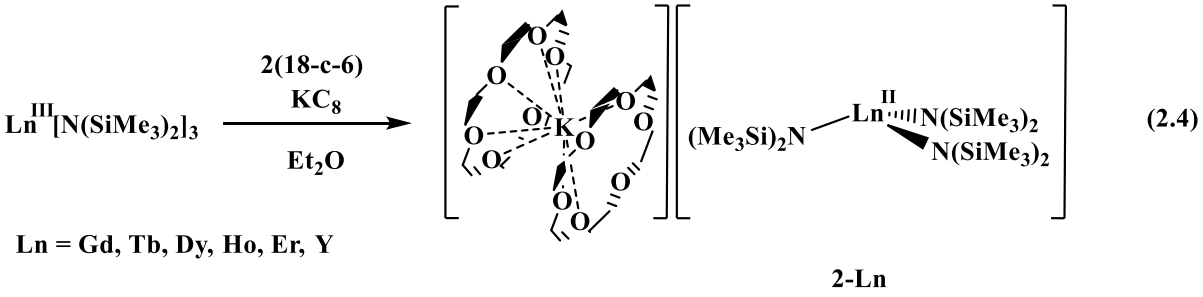

(2.4)

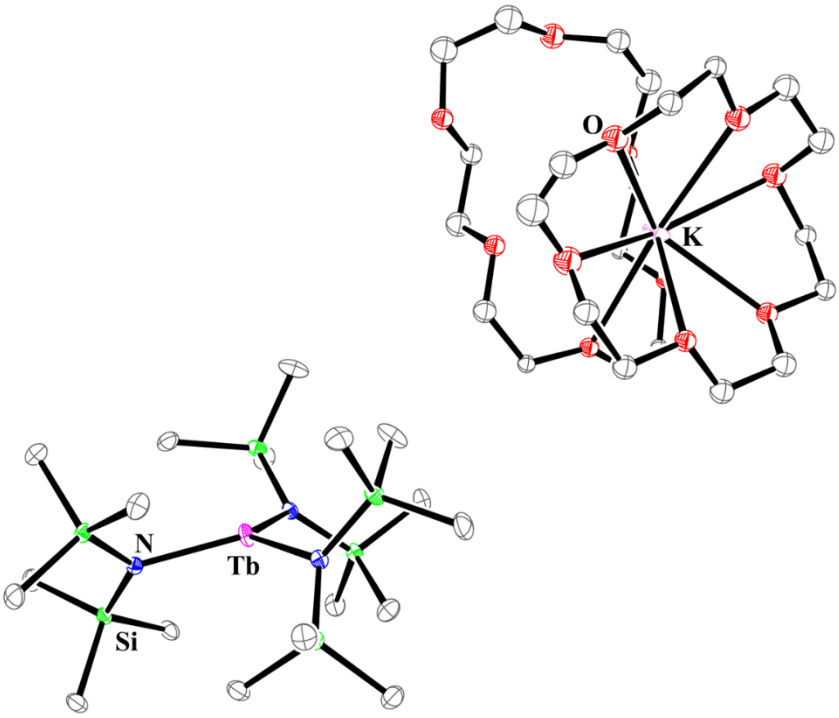

Figure 2.1. Thermal ellipsoid plot of **2-Tb** drawn at the 50% probability level. Hydrogen atoms and disordered 18-c-6 atoms are excluded for clarity. The other **2-Ln** complexes (Ln = Gd, Tb, Dy, Ho, Y, Er) are all isomorphous.

Ho, Er, Tm. Given the success of the reaction above, the protocol was extended to Er and Ho which had previously produced crystals of the $[Ln(NR_2)_3]^{1-}$ anions only with the $[Rb(crypt)]^{1+}$ cation. Crystallographically-characterizable complexes of Ho and Er were also obtainable with K as the reductant using 18-c-6 according to eq 2.4. This synthesis was also examined with Tm, a metal that forms Ln(II) complexes with traditional $4f^{n+1}$ electron configurations in contrast to the metals above that form $4f^n5d^1$ ions.[3, 4, 7, 8, 16] This reaction was also successful and provided $[K(18\text{-}c\text{-}6)_2][Tm(NR_2)_3]$, **2-Tm**.

Yttrium. Given the success of the 18-c-6 protocol observed with the lanthanides, attempts were again made using this chelate in the reduction of $Y(NR_2)_3$. Initial reductions were performed

as shown in eq 2.4 leading to the crystallization of the complex $[K(18\text{-c-}6)_2][Y(NR_2)_3]$, **2-Y**, as determined by X-ray diffraction. Subsequent attempts to synthesize **2-Y** revealed that a temperature of −78 °C helped to avoid significant decomposition of **2-Y** during the synthesis. The EPR spectrum of **2-Y** is indistinguishable from that of the $Y(NR_2)_3$/K reduction product reported in 2011.[15]

Structure. The **2-Ln** complexes of Ln = Gd, Tb, Dy, Ho, Er, and Y, Figure 2.1, are isomorphous and crystallize in the $P2_1/n$ space group. The crypt analogs also formed an isomorphous series, **1-Ln**, for Ln = Gd, Tb, and Dy, and these were also isomorphous with the analogs containing Rb cations, $[Rb(crypt)][Ln(NR_2)_3]$, **1-Ln(Rb)** for Ln = Ho, Er. These all crystallized in the space group P-1. The **2-Tm** complex is not isomorphous with the other **2-Ln** structures and crystallizes with two formula units per unit cell in the space group $P2_12_12_1$.

$Ln(NR_2)_3$ and $[Ln(NR_2)_3]^{1-}$ complexes often show disorder in the position of the metal with respect to the plane of the three nitrogen donor atoms. The $Ln(NR_2)_3$ complexes of Nd,[21] Eu,[22] Tb,[23] Dy,[24] Er,[24] Yb,[25] and Lu[26] exhibit disorder of the metal about an inversion center such that the metal is located above and below the N_3 plane in the range of 0.34 - 0.58 Å. In **1-Gd**, **1-Tb**, **1-Dy**, and **1-Ho(Rb),** the metals are disordered 0.5 - 0.6 Å above and below the plane with disorder in the 65 - 75% range.[19] It should be noted that this disorder depends on reaction and crystallization conditions. For example, **1-Gd**, synthesized in THF and crystallized from THF/hexane formed crystals in the P-1 space group and showed the disorder mentioned above.[17] However, a sample synthesized for this study in Et_2O/toluene and crystallized by layering with hexanes formed crystals in the trigonal space group R32 with no disorder. The structure had an asymmetric unit consisting of one amide ligand on Gd and a potassium cation with one third of

crypt chelate. The disorder in the structures of both $Sc(NR_2)_3$ and $[Sc(NR_2)_3]^{1-}$ was found to be highly dependent on the crystallization conditions.[18]

In comparison, the crystallographic data on **2-Gd**, **2-Tb**, and **2-Tm** were successfully modeled without a disordered metal center. These complexes had trigonal pyramidal structures with the metal out of the plane by 0.055 - 0.201 Å (see below). The data on **2-Dy**, **2-Ho, 2-Er**, and **2-Y** were best modeled with only minor disorder of the metal where 97% of the metal lies above and close to the N_3 plane (within 0.283 Å) and 3% lies below the plane by 0.554 Å.

Metrical data on **1-Ln** and **2-Ln** are presented in Table 2.1. As shown, the structures of the $[Ln(NR_2)_3]^{1-}$ anions in **2-Ln** are identical within experimental error to the anions in **1-Ln** and **1-Ln(Rb)**. The parallels also apply to **1-Tm** and **2-Tm** which are assigned traditional $4f^{n+1}$ electron configurations. As has been found in other series of Ln(II) complexes,[3, 4, 16, 19] different structural parameters are observed for complexes of $4f^{n+1}$ and $4f^n5d^1$ Ln(II) ions. Specifically, the metrical parameters of $[Tm(NR_2)_3]^{1-}$ in **1-Tm** and **2-Tm** have Tm–N distances longer than those in the $Tm(NR_2)_3$ starting material by 0.2 Å. For Gd, Tb, Dy, and Ho, the Ln–N distances are only 0.05 Å longer than in the $Ln(NR_2)_3$ starting materials suggesting that **2-Ln** for Ln = Gd, Tb, Dy and Ho, like those of **1-Ln**, are $4f^n5d^1$. Comparisons cannot be made for **1-Er(Rb)** since the reported structure was of low quality and provided connectivity only. Hence the structure of **2-Er** provided the first opportunity to evaluate this parameter with the $[Er(NR_2)_3]^{1-}$ anion. The data show a change in bond distance of 0.05 Å from Er(III)[24] to Er(II) consistent with a $4f^{11}5d^1$ electron configuration.

Table 2.1. Comparison of metal ligand distances (Å) of [K(crypt)][Ln(NR_2)$_3$], **1-Ln**, [Rb(crypt)][Ln(NR_2)$_3$], **1-Ln(Rb)**, [K(18-c-6)$_2$][Ln(NR_2)$_3$], **2-Ln**, and Ln(NR_2)$_3$.

Metal	**1-Ln** Ln–N avg	**2-Ln** Ln–N avg	Ln(NR_2)$_3$ Ln–N avg	**1-Ln** Ln–N_{plane} avg	**2-Ln** Ln–N_{plane} avg
Gd	2.307	2.309	2.247*	0.523	0.158
Tb	2.282	2.293	2.233	0.503	0.201
Dy	2.270	2.280	2.213	0.523	0.436
Ho	2.256	2.267	2.211*	0.509	0.395
Er	-	2.249	2.210	NA	0.426
Tm	2.320	2.348	2.200*	0.023	0.055
Y	-	2.268	2.224	NA	0.418

* These three Ln(III) complexes do not have reported crystal structures, so expected Ln–N distances were interpolated from analogous complexes of metals with similar ionic radii

Spectroscopy. The UV-visible spectra of **2-Gd** and **2-Dy** are indistinguishable from those of **1-Gd** and **1-Dy** with strong, broad absorbances at 598 nm (ε = 3500 cm^{-1} M^{-1}) and 608 nm (ε = 1200 cm^{-1} M^{-1}). Spectra were also obtained for **2-Ho** and **2-Er** since [Ln(NR_2)$_3$]$^{1-}$ anions of these metals with crypt-based counter-cations were too unstable to provide optical data. These spectra also show strong absorbances around 600 nm (ε = 3000, 1800) similar to those reported for **1-Gd**, **1-Dy**, and **1-Tb**.[19] Interestingly, the spectrum for **2-Y** shows a strong absorbance at a longer wavelength, 650 nm (ε = 3800), than those of **1-Ln** and **2-Ln**. All of the spectra of the [Ln(NR_2)$_3$]$^{1-}$ complexes are shown in Figure 2.2 (individual spectra are shown in the SI). The UV-visible spectra of **1-Tm** and **2-Tm** are not as intense, which is typical of $4f^{n+1}$ Ln(II) ions vs $4f^n5d^1$ Ln(II) ions as seen previously with (Cp′$_3$Ln)$^{1-}$ complexes.[3, 4]

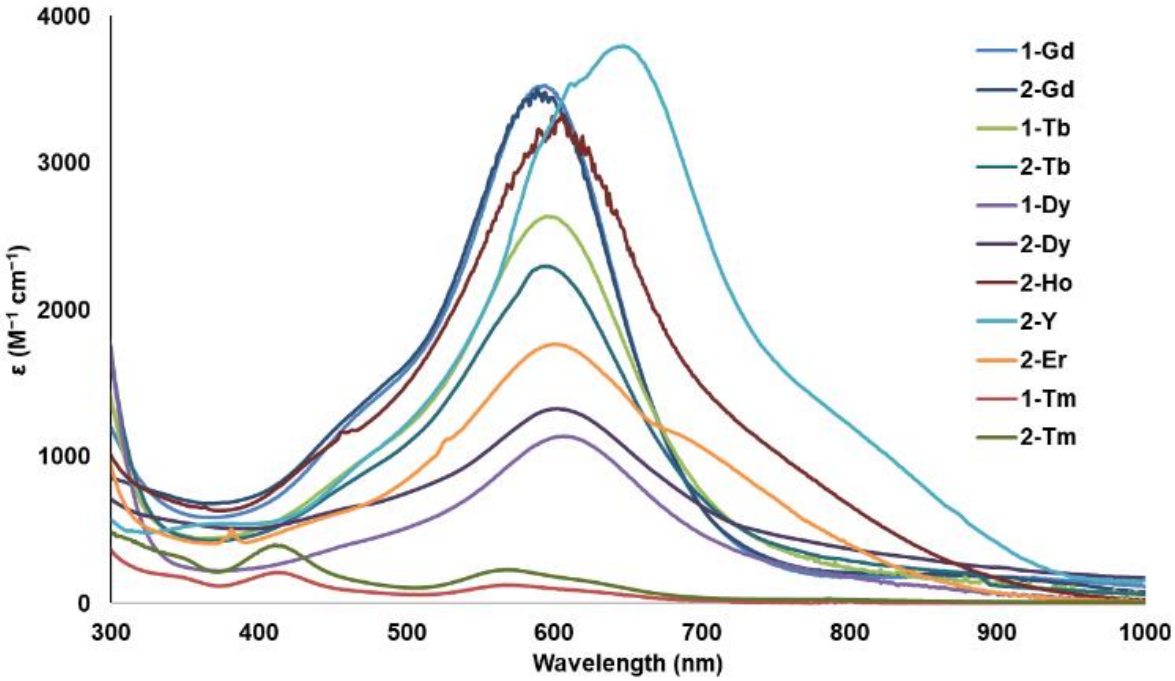

Figure 2.2. UV-visible spectra of **1-Ln**[19] and **2-Ln** in THF and Et_2O respectively

Stability. The $[K(crypt)]^{1+}$ complexes, $[K(crypt)][Ln(NR_2)_3]$, **1-Ln**, showed a trend in solution stability of Tm ~ Gd >> Tb > Dy >> Ho, Er >> Nd.[19] The **2-Ln** complexes have similar stability to those of **1-Ln** and display a similar trend. For **2-Tm**, a half-life of one week was observed, whereas **2-Gd** had a half-life of about 2 days. For **2-Dy**, a compound with moderate stability in the series, the half-life is approximately 5 minutes in a solution of diethyl ether, whereas **1-Dy,** which is not very soluble in Et_2O, shows a 5-minute half-life in THF (SI). The **2-Y** complex is even less stable than the other **2-Ln** compounds showing complete decomposition within 10 seconds at room temperature, which is consistent with the difficulty in isolating it previously. Decomposition products were not isolated, but C-H bond activation of the methyl ligands of $[N(SiMe_3)_2]^{1-}$ ligands to form cyclometalates involving $[N(SiMe_3)(SiMe_2CH_2)]^{2-}$ ligands is a frequent degradation route for rare earth amide complexes.

The stability data indicate that although the 18-c-6 chelate is better than crypt for crystallizing the $[Ln(NR_2)_3]^{1-}$ anions, it does not provide measurably more stable complexes in solution. The advantage of the $[K(18\text{-c-}6)_2]^{1+}$ complexes over the $[K(crypt)]^{1+}$ analogs is in the *rate* of crystallization. The **1-Ln** complexes typically require over 24 hours to crystallize, whereas the **2-Ln** compounds crystallize over the span of 2-3 hours. The more rapid crystallization is the likely reason that these **2-Ln** species of Ho, Er, and Y can be isolated. They are so reactive in solution that prolonged crystallization times lead to decomposition.

Reactivity with CO. Ynediolate Formation. Previously, the $Y(NR_2)_3$/K reaction conducted in situ without an isolated Y(II) complex under CO led to the CO reduction chemistry shown in eq 2.3.[20] Attempts to explore this CO reduction chemistry with isolated complexes of the crypt chelate $[K(crypt)][Ln(NR_2)_3]$, **1-Ln**, for Ln = Gd and Dy did not lead to any crystallizable products. However, reactions of CO with the 18-c-6 chelate, $[K(18\text{-c-}6)_2][Ln(NR_2)_3]$, **2-Ln**, for Ln = Gd, Dy, and Ho did provide crystalline materials as described in the following paragraphs.

In situ Reactions. Due to the limited stability of **2-Ln** in solution, the starting complexes were generated in situ and used without isolation. Reductions of $Ln(NR_2)_3$ (Ln = Gd, Dy, Ho) were performed in Et_2O with KC_8 in an H-shaped tube equipped with greaseless high vacuum stopcocks at −78 °C in the presence of 18-c-6. Introduction of CO gas at 1 atm to the system caused the dark blue solution to turn pale yellow immediately upon thawing. After the solution was allowed to warm to room temperature, pale yellow crystals of the CO-coupled ynediolate complex, $\{K_2(18\text{-c-}6)_3\}\{[(R_2N)_3Ln]_2(\mu\text{-}OC{\equiv}CO)\}$, **3-Ln** (Ln = Gd, Dy, Ho), had formed and could be isolated without further work-up, Figure 2.3, eq 2.5.

These **3-Ln** complexes were isomorphous with those previously reported for Y and Lu, eq 2.3.[20] Hence, the ynediolate products generated in eq 2.3 before any Y(II) and Lu(II) complexes had been identified, can also be formed from solutions containing established Ln(II) ions.

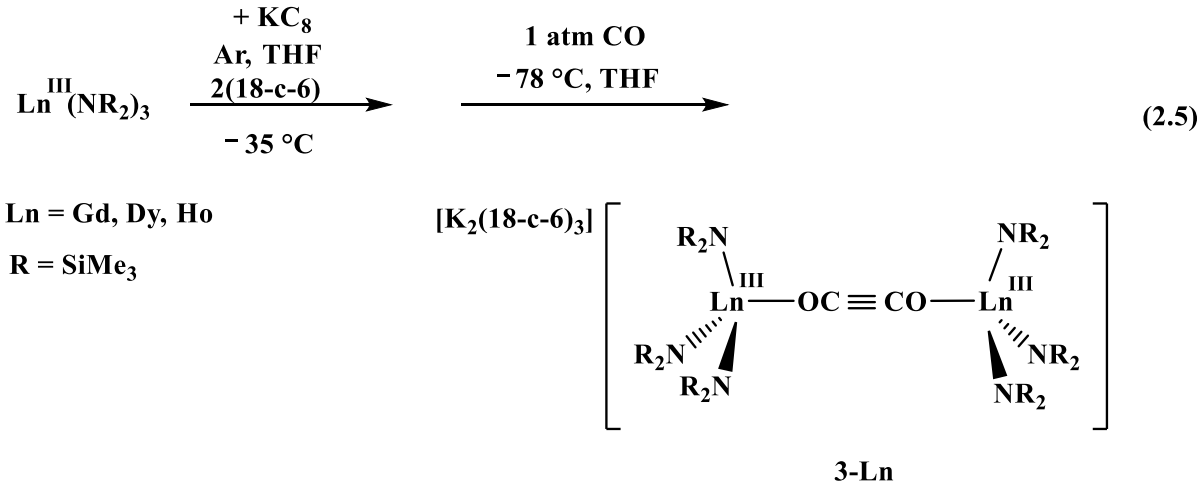

(2.5)

Only the metrical parameters for **3-Dy** and **3-Ho** can be compared with other complexes, since the crystal data on **3-Gd** were not of high enough quality for detailed analysis. As expected for isomorphous complexes, the 1.183(6) - 1.186(4) Å C≡C and 1.301(2) - 1.311(4) Å C−O distances in **3-Dy** and **3-Ho** are very similar to those in **3-Y** and **3-Lu**. These distances also match other ynediolate complexes in the literature such as $[(A)_3U]_2(\mu\text{-OC}\equiv\text{CO})$ (A = $N(SiMe_3)_2$,[27] $OC_6H_2Bu^t_3$-2,4,6[28]), $[U(Tren^{DMSB})]_2(\mu\text{-OC}\equiv\text{CO})$ [$Tren^{DMSB}$ = $N(CH_2CH_2NSiMe_2Bu^t)_3$],[29] and $[(U(C_8H_6{}^{30}{}_2)(C_5Me_5)]_2(\mu\text{-OC}\equiv\text{CO})$.[30] The Ln-O distances vary as expected based on ionic radii:[31] 2.070(2) Å, Dy; 2.0598(14) Å, Ho; 2.057 Å, Y[20]; 2.021 Å, Lu[20].

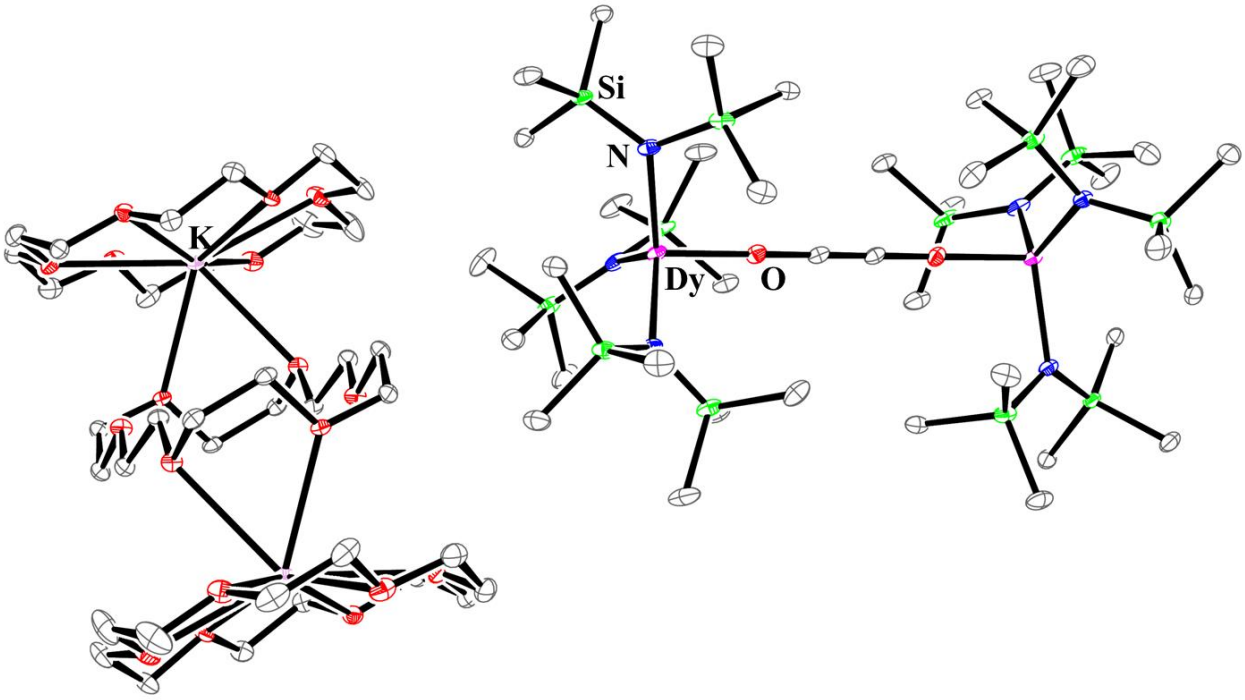

Figure 2.3. Thermal ellipsoid plot of **3-Dy** (**3-Ln** are isomorphous) drawn at the 50% probability level. H atoms and lattice solvent molecules are excluded for clarity.

Reactions with Isolated Complexes. A Thulium Ynediolate. Interestingly, the Tm(II) complex, **2-Tm**, can also form an isomorphous ynediolate product. In this case, since the $4f^{13}$ **2-Tm** is more stable than the $4f^n5d^1$ **2-Ln** complexes, the reaction was carried out with isolated **2-Tm**. When isolated $[K(18\text{-c-}6)_2][Tm(NR_2)_3]$ is dissolved in Et_2O at −78 °C, a dark solution forms. Upon addition of CO, the solution quickly turns pale yellow. Upon warming to room temperature overnight, the ynediolate complex, $\{K_2(18\text{-c-}6)_3\}\{[(R_2N)_3Tm]_2(\mu\text{-}OC{\equiv}CO)\}$, **3-Tm**, crystallizes and was found to have a structure isomorphous with those of **3-Gd**, **3-Dy**, and **3-Ho**, eq 2.6.

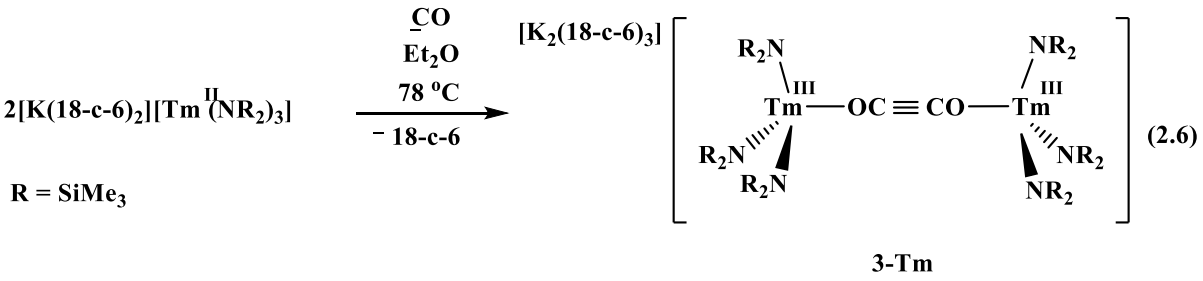

A Gadolinium Enediolate. Since $[K(18\text{-c-}6)_2][Ln(NR_2)_3]$, **2-Gd**, was the most stable $4f^n5d^1$ complex in the **2-Ln** series, a CO reaction with this complex in its isolated form was also examined. Solid **2-Gd** was added to one side of an H-tube with Et_2O stored at −78 °C on the other side. CO was then introduced to the system and the Et_2O was condensed onto **2-Gd** using a liquid nitrogen bath. The solution was then allowed to warm to −78 °C causing the solution to turn from dark blue to colorless. Concentration of the colorless solution produced a small amount of colorless crystals which were identified by X-ray diffraction as the *ene*diolate complex $[K(18\text{-c-}6)]_2\{[(R_2N)_2Gd_2(\mu\text{-OCH=CHO})_2\}$, **4-Gd**, eq 2.7, Figure 2.4. Hence, the CO reduction product that crystallized from this reaction is not the ynediolate of eq 2.3, 2.5, and 2.6, but a derivative in which two hydrogen atoms per two metal centers have been added to what was presumed to be an ynediolate intermediate. In addition, one amide ligand has been lost per Gd metal center compared to the **2-Ln** precursor. The charge of the dianionic bimetallic complex is balanced by two $[K(18\text{-c-}6)]^{1+}$ units each of which is coordinated to an oxygen atom of an enediolate ligand. Although the origin of the additional hydrogen atoms in the enediolate in eq 2.7 versus the **2-Ln** ynediolates is unknown and the yield is not synthetically useful, the reaction demonstrates the subtle differences that occur based on the reduction protocols.

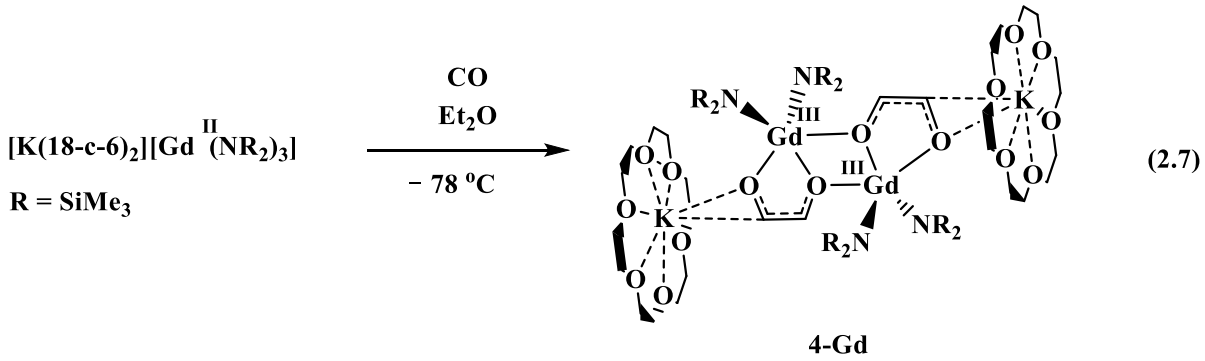

(2.7)

Enediolate complexes of f-elements have previously been obtained from reactions of lanthanide hydride[32, 33] or tris(pentamethylcyclopentadienyl) lanthanide[34, 35] complexes with CO. Additionally, enediolate formation incorporating actinides has been observed by the reductive insertion of CO into actinide alkyl bonds as well as by insertion of a bridging ynediolate into the C−H bond of a silylmethyl group in the complex $[(R_2N)_3U]_2(\mu\text{-}OC{\equiv}CO)\}$ (R = $SiMe_3$).[27]

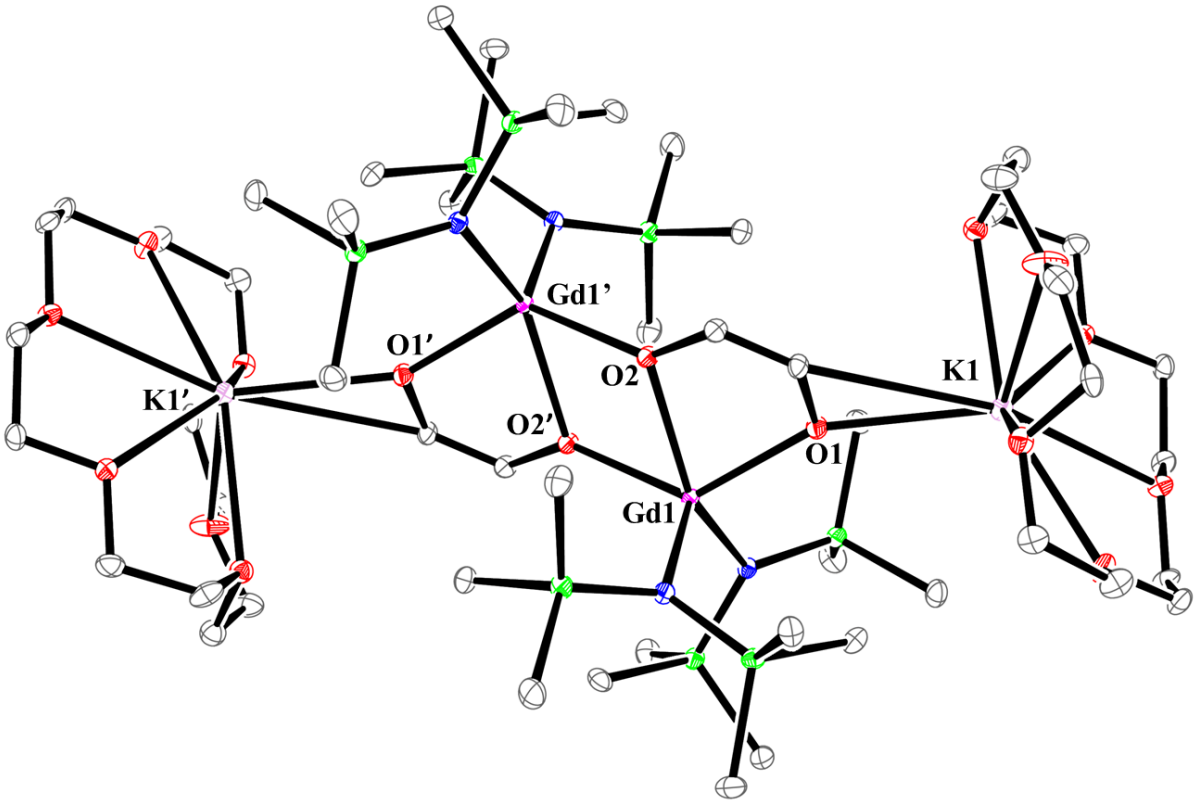

Figure 2.4. Thermal ellipsoid plot of **4-Gd** drawn at the 50% probability level. H atoms and second molecule of **4-Gd** are omitted for clarity.

There are two independent anions in the unit cell of **4-Gd**, but their metrical parameters are similar. For example, the C=C distances in **4-Gd** of 1.334(4) and 1.331(4) Å are consistent with the presence of a double bond.[36] Average bond distances and angles of **4-Gd** are summarized in Figure 2.5 (full data are in the Experimental Details). The 1.372(5) Å average C–O distance involving the oxygen of the enediolate that bridges the two Gd centers (O2) is similar to the 1.352(1) Å C–O distance for the oxygen of the enediolate that bridges Gd and K centers (O1).

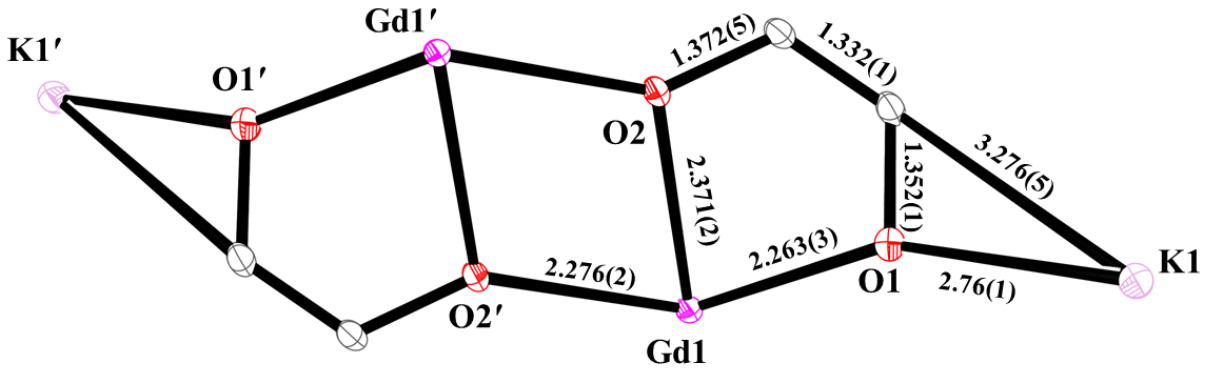

Figure 2.5. Average bond distances (Å) of the two independent molecules in the unit cell for the core atoms of **4-Gd.**

The 2.322(1) to 2.356(5) Å range of Gd–N distances is only slightly larger than the 2.289(5) Å Dy−N average distance in **3-Dy** although five coordinate Gd(III) is estimated to be 0.09 Å larger than 4-coordinate Dy(III) based on extrapolations of Shannon radii.[31] The interior Gd_2O_2 unit is rhombohedral rather than square with 2.371(2) Å Gd-O2 and 2.276(2) Å Gd-O2’ average Gd-O distances. The average 2.263(3) Gd−O1 distance is similar to the Gd-O2’ distance.

The 2.778(2) and 2.745(2) Å K−O(enediolate) distances are longer than the 2.669 Å K−O distances in $[Ta(OOO)(THF)]_2[Ta(OOO)H]_2[OC=C(O)C(O)=C(O)-C(O)=CO]$ $[K(DME)]_2$ where H_3(OOO) is 2,6-bis(3-^{t}Bu-5-Me-2-hydroxybenzyl)-4-^{t}Bu-phenol,[37] but the latter complex has four coordinate potassium, whereas the potassium is formally eight coordinate in **4-Gd**. The 3.271(3) and 3.282(3) Å distances between the potassium cations and carbon atoms on the enediolate are within the 3.046 to 3.305 Å range of K…C distances found for $[K(18\text{-}c\text{-}6)]^{1+}$ to unsaturated carbon atoms found in molecules such as $[K(18\text{-}c\text{-}6)][Al(NON^{Ar})(C_8H_8)]$ (NON^{Ar}=$[O(SiMe_2NAr)_2]^{2-}$, Ar=2,6-^{i}Pr$_2$C$_6$H$_3$),[38] $[K(18\text{-}c\text{-}6)(\eta^5\text{-Pdl*})]$ (Pdl* = dimethylnopadienyl),[39] and $[K(18\text{-}c\text{-}6)][Ln^{40}{}_2(C_6H_6)]$.[40]

Discussion

Reductions of the trivalent $Ln(NR_2)_3$ complexes with KC_8 in the presence of two equivalents of 18-c-6 allowed for the crystallization of the divalent products, $[K(18\text{-}c\text{-}6)_2][Ln(NR_2)_3]$, **2-Ln**, in a matter of 2-4 hours, eq 2.4. In contrast, reductions of $Ln(NR_2)_3$ with K in the presence of crypt required over 24 h to crystallize to $[K(crypt)][Ln(NR_2)_3]$, **1-Ln**. It appears that the faster crystallization times of **2-Ln** allowed for +2 ions of Ho, Er, and Y to be isolated as $[K(18\text{-}c\text{-}6)_2]^{1+}$ salts. The analogous reactions with crypt did not give isolable products presumably due to decomposition during the long crystallization process. While the **2-Ln** complexes did not appear to be any more stable in solution at room temperature than the **1-Ln** series, the increased crystallization speed of **2-Ln** compared to **1-Ln** was the determining factor in the isolation of the more reactive **2-Y**. Hence, this was an important way in which the counter-cation can affect the chemistry.

The data to date on stability of the $[Ln(NR_2)_3]^{1-}$ anions suggests that stability decreases with decreasing size of the metal starting with Gd as the most stable non-traditional ion for both

the **1-Ln** and **2-Ln** series. This may be one reason why the Y(II) derivative was so elusive for so long. The trend of decreasing stability as the metal becomes smaller has also been observed for the $[(C_5H_4SiMe_3)_3Ln]^{1-}$[16] and $[(C_5Me_4H)_3Ln]^{1-}$[41] series of anions, but in those cases the largest lanthanides, La-Pr, form the most stable complexes. For the $[Ln(NR_2)_3]^{1-}$ anions, Gd is the most stable and examples with larger metals are less stable.

The presence of 18-c-6 chelated potassium counter-cations also proved crucial to isolating CO reduction products in reactions of **2-Ln** generated in situ according to eq 2.5 and 2.6. Ynediolate products $\{K_2(18\text{-c-}6)_3\}\{[(R_2N)_3Ln]_2(\mu\text{-}OC{\equiv}CO)\}$ **3-Ln**, were isolable starting from **2-Ln** that could not be isolated from reactions with the crypt-containing complexes $[K(crypt)][Ln(NR_2)_3]$, **1-Ln**. This is not to say that CO does not form ynediolate products with **1-Ln**. Ynediolate formation could have occurred in **1-Ln** reactions, but no products could be isolated to confirm that result. Again, the identity of the counter-cation is important in obtaining isolable crystals before other decomposition reactions occur.

The fact that $4f^{13}$ **2-Tm** made an ynediolate product like the $4f^n5d^1$ **2-Gd**, **2-Dy**, and **2-Ho** complexes indicates that this CO reductive homologation does not necessarily require a $4f^n5d^1$ electron configuration. As described above, ynediolates have previously been made from $5f^3$ U(III) precursors, so d electron character is not a requirement for this reaction.

The isolation of the enediolate complex, $[K(crown)]_2\{[(R_2N)_2Gd_2(\mu\text{-}OCH{=}CHO)_2\}$, **4-Gd**, eq 2.7, from the reaction of CO with isolated **2-Gd** highlights the importance of reaction conditions in generating crystalline products that can be identified by X-ray crystallography. This is essential for these highly paramagnetic complexes. The reaction of CO with **2-Gd** generated in situ resulted in the isolation of ynediolate, **3-Gd**, but the reaction starting with isolated **2-Gd** provided a different crystalline product. Presumably the high reactivity of isolated **2-Gd** allowed C−H bond

activation reactions to occur during the CO reaction which led to the enediolate complexes although the common by-product $HN(SiMe_3)_2$ was not observed. C−H bond activation in Ln(II) complexes has been previously observed.[17, 42-45] Clearly, the details of these rare earth reduction reactions are critical to the isolation of crystalline products.

Conclusion

The importance of the counter-cation in isolating Ln(II) complexes was shown by the fact that the elusive $[Y(NR_2)_3]^{1-}$ anion could be isolated by potassium reduction of $Y(NR_2)_3$ in the presence of 18-c-6, but not crypt. The $[K(18\text{-c-}6)_2][Ln(NR_2)_3]$, **2-Ln**, complexes of Ho and Er were also more readily isolable than their crypt analogs, $[K(crypt)][Ln(NR_2)_3]$, **1-Ln**, which could only be isolated using Rb as a reductant as $[Rb(crypt)][Ln(NR_2)_3]$, **1-Ln(Rb)**. Although the **2-Ln** species were not more stable in solution than **1-Ln** complexes, the fact that they crystallized faster allowed the isolation of the more reactive species in the series. Controlling the speed of crystallization of highly reactive complexes is a major challenge in chemistry that is currently not well understood. It is well known that this is important factor in studies of highly radioactive actinide complexes,[46-48] but it clearly is important for these highly reducing $[Ln(NR_2)_3]^{1-}$ anions as well.

The identity of the counter-cation also affects the ease of isolation of reaction products of the reactive Ln(II) complexes as demonstrated by the CO reactions. Reactions of CO with $[Ln(NR_2)_3]^{1-}$ anions with $[K(18\text{-c-}6)_2]^{1+}$ cations gave isolable products not obtainable with $[K(crypt)]^{1+}$ salts. The 18-c-6 system has the additional advantage over crypt in that it can form potassium chelates with a variety of sizes, charges, and potassium to 18-c-6 ratios, i.e. $[K(18\text{-c-}6)(solvent)_x]^{1+}$ (x = 0, 1, 2), $[K(18\text{-c-}6)_2]^{1+}$, and $[K_2(18\text{-c-}6)_3]^{2+}$.

The difference in reactivity with isolated solids (eq 2.7) versus in situ generated Ln(II) (eq 2.5) reflects the importance of minor details in channeling the Ln(II) reactivity to crystalline products allowing for crystallographic characterization, which is a primary method of characterization for complexes of these highly paramagnetic lanthanide ions. Since the identity of the counter-cation can determine if a complex is isolable or not, the choice of can be critical in several ways for the reaction chemistry. It is clear that the counter-cations must be carefully considered in future rare-earth reductive chemistry.

Experimental Details

All manipulations and syntheses described below were conducted with the rigorous exclusion of air and water using standard Schlenk line and glovebox techniques under an argon or dinitrogen atmosphere. Solvents were sparged with UHP argon and dried by passage through columns containing Q-5 and molecular sieves prior to use. Elemental analyses were conducted on a Perkin-Elmer 2400 Series II CHNS elemental analyzer. Infrared spectra were collected as thin films on either a Thermo Scientific Nicolet iS5 spectrophotometer with an iD5 ATR attachment or an Agilent Cary 630 equipped with a diamond ATR attachment. UV-visible spectra were collected on either a Varian Cary 50 or Agilent Cary 60 UV-visible spectrometer. Evan Method measurements were carried out on Bruker GN500 spectrometer.[49] Anhydrous $LnCl_3$ (Ln = Y, Gd, Tb, Dy, Ho, Er, Tm),[50] $Ln(NR_2)_3$ ($R=SiMe_3$),[51] and KC_8[52] were prepared according to literature procedures. 18-Crown-6 (Alfa Aesar) was sublimed before use. CO (99.99%) was purchased from Airgas and used without further purification.

$[K(18\text{-}c\text{-}6)_2][Y(NR_2)_3]$, 2-Y. In an argon-filled glovebox, $Y(NR_2)_3$ (40 mg, 0.07 mmol) was combined with 18-c-6 (37 mg, 0.14 mmol) in Et_2O (2 mL) and cooled to −78 °C in the glovebox

cold well. The cold solution was added to a vial containing KC_8 (14 mg, 0.11 mmol) that had also been cooled to −78 °C and the mixture was allowed to sit for about 1 min in the glovebox cold well. The solution was filtered through a pipette fit with a glass wool filter and layered with −78 °C hexanes before storing in the cold well. After 4 h, dark blue crystals **2-Y** (42 mg, 52%) were obtained. UV−vis (Et_2O) λ_{max}, nm (ε, M^{-1} cm^{-1}): 600 (3300 shoulder), 650 (3800). Elemental analysis was precluded by the instability of the complex at room temperature IR: 2940m 2888m, 1474w, 1453w, 1351m, 1236s, 1105s, 987s, 961s, 868m, 821s, 775m, 751m, 710w, 689w, 660m, cm^{-1} . Anal. Calcd for $C_{42}H_{102}N_3O_{12}Si_6KY$: C, 44.34; H, 9.04; N, 3.69;. Found: C, 43.80; H, 8.61; N, 3.25.

[K(18-c-6)$_2$][Gd(NR$_2$)$_3$], 2-Gd. In an argon-filled glovebox, $Gd(NR_2)_3$ (40 mg, 0.062 mmol) was combined with 2 equivalents of 18-c-6 (33 mg 0.1825 mmol) in Et_2O (2 mL) and cooled to −35 ºC in the glovebox freezer. The cold solution was added to a vial containing potassium graphite (12 mg, 0.094 mmol) that had also been cooled to −35 °C and the mixture was allowed to react about one minute in the glovebox freezer. The solution was filtered through a pipette fit with a glass wool filter and layered with −35 °C hexanes before being replaced in the glovebox freezer affording crystals suitable for X-ray diffraction after about 2 h (57 mg, 75%). UV−vis (Et_2O) λ_{max}, nm (ε, M^{-1} cm^{-1}): 275 (3380 shoulder), 607 (1130). IR: 2945s, 2889s, 2817m, 2761w, 2730w, 2702w, 1958w, 1478m, 1458m, 1446m, 1390w 1355s, 1298m, 1260s 1238s, 1135s, 1107s, 1079s, 1041s, 987s, 951s, 933m, 870s, 827s, 770m, 751m, 712m, 693m, 663s, 600m cm^{-1}. Anal. Calcd for $C_{42}H_{102}N_3O_{12}Si_6KGd$: C, 41.82; H, 8.52; N, 3.48;. Found: C, 41.40; H, 8.37; N, 3.30.

[K(18-c-6)$_2$][Tb(NR$_2$)$_3$], 2-Tb. As described for **2-Gd**, $Tb(NR_2)_3$ (60 mg, 0.094 mmol) and 18-c-6 (50 mg, 0.188 mmol) in Et_2O (2 mL) were reacted with KC_8 (18 mg, 0.146 mmol) to

afford **2-Tb** as a dark blue crystalline solid. Single crystals suitable for X-ray diffraction were grown by layering a concentrated Et_2O solution with hexanes (71 mg, 63%). UV−vis (Et_2O) λ_{max}, nm (ε, M^{-1} cm^{-1}): 595 (2300). IR: 2942s, 2889s, 2817m, 2762w, 2730w, 2698w, 1478m, 1458m, 1446m, 1356s, 1299m, 1260s 1237s, 1135s, 1107s, 1078s, 1059s, 992s, 952s, 933m, 869s, 827s, 770m, 752m, 713m, 691m, 663s, 600m cm^{-1}. Anal. Calcd for $C_{42}H_{102}N_3O_{12}Si_6KTb$: C, 41.77; H, 8.51; N, 3.48. Found: C, 41.81; H, 8.53; N, 3.23.

[K(18-c-6)$_2$][Dy(NR$_2$)$_3$], 2-Dy. As described for **2-Gd**, $Dy(NR_2)_3$ (60 mg, 0.094 mmol) and 18-c-6 (50 mg, 0.188 mmol) in Et_2O (2 mL) were treated with KC_8 (18 mg, 0.146 mmol) to afford **2-Dy** as a dark blue crystalline solid. Single crystals suitable for X-ray diffraction were grown by layering a concentrated Et_2O solution with hexanes (62 mg, 53%). UV−vis (Et_2O) λ_{max}, nm (ε, M^{-1} cm^{-1}): 607 (1130). IR: 2945m, 2887m, 1475w, 1455w, 1358m, 1241s, 1109s, 992s, 958m, 867s, 827s, 7767m, 753m, 712w, 687w, 670s, 607m cm^{-1}. Anal. Calcd for $C_{42}H_{102}N_3O_{12}Si_6KDy$: C, 41.64; H, 8.49; N, 3.47. Found: C, 41.11; H, 8.98; N, 3.32.

[K(18-c-6)$_2$][Ho(NR$_2$)$_3$], 2-Ho. As described for **2-Gd**, $Ho(NR_2)_3$ (60 mg, 0.093 mmol) and 18-c-6 (46 mg, 0.186) in Et_2O (2 mL) were treated with KC_8 (18 mg, 0.146 mmol) to afford **2-Ho** as a dark blue crystalline solid. Single crystals suitable for X-ray diffraction were grown by layering a concentrated Et_2O solution with hexanes (64 mg, 57%). UV−vis (Et_2O) λ_{max}, nm (ε, M^{-1} cm^{-1}): 600 (1745), 691 (1115 shoulder). IR: 2940m, 2876m, 1475w, 1452w, 1352m, 1297w, 1234m, 1103s, 980s, 864m, 825s, 778m, 752m, 690w, 660m cm^{-1}. Anal. Calcd for $C_{42}H_{102}N_3O_{12}Si_6KHo$: C, 41.56; H, 8.47; N, 3.46. Found: C, 41.33; H, 8.82; N, 3.53.

[K(18-c-6)$_2$][Er(NR$_2$)$_3$], 2-Er. As described for **2-Gd**, $Er(NR_2)_3$ (60 mg, 0.092 mmol) and 18-c-6 (49 mg, 0.185 mmol) in Et_2O (2 mL) were reacted with KC_8 to afford **2-Er** as a dark blue crystalline solid. Single crystals suitable for X-ray diffraction were grown by layering a

concentrated Et_2O solution with hexanes (60 mg, 53%). UV−vis (Et_2O) λ_{max}, nm (ε, M^{-1} cm^{-1}): 600 (1745), 691 (1115 shoulder). IR: 2938m 2893m, 1472w, 1450w, 1347m, 1238w, 1105s, 980s, 871m, 825s, 775m, 750m, 715w, 695w, 660m, 600m cm^{-1}. Anal. Calcd for $C_{42}H_{102}N_3O_{12}Si_6KEr$: C, 41.48; H, 8.45; N, 3.46. Found: C, 41.04; H, 8.39; N, 3.51.

[K(18-c-6)$_2$][Tm(NR$_2$)$_3$], 2-Tm. As described for **2-Gd**, $Tm(NR_2)_3$ and 18-c-6 in Et_2O (2 mL) were reacted with KC_8 to afford **2-Tm** as a blue-green crystalline solid. Single crystals suitable for X-ray diffraction were grown by layering a concentrated Et_2O solution with hexanes. UV−vis (Et_2O) λ_{max}, nm (ε, M^{-1} cm^{-1}): 415 (385), 565 (230). IR: 2937m, 2886m, 1472w, 1471w, 1452w, 1417w, 1351m, 1231m, 1106s, 1053s, 961m, 871m, 815s, 747m, 715w, 657m cm^{-1}. Anal. Calcd for $C_{42}H_{102}N_3O_{12}Si_6KTm$: C, 41.48; H, 8.45; N, 3.46. Found: C, 41.04; H, 8.39; N, 3.51

[K$_2$(18-c-6)$_3$][(R$_2$N)$_3$Ho]$_2$(μ-OC≡CO), 3-Ho. 3-Ho. In an argon filled glove box, an H-shaped tube fitted with a filter frit in the middle (see SI) was loaded with $Ho(NR_2)_3$ (100 mg, 0.147 mmol), 18-c-6(59 mg, 0.221 mmol), and Et_2O on one side and KC_8 (30 mg, 0.221 mmol) on the other. The apparatus was brought outside of the glovebox and attached to a vacuum line. Both sides of the H-tube were cooled to −78 °C and the Et_2O solution was poured onto the KC_8 generating a dark blue color. The mixture was allowed to react for about 10 min before the solution was filtered away from any excess KC_8. The solution was then frozen in liquid nitrogen and CO gas was introduced. The solution was allowed to warm to −78 °C resulting in a color change to pale yellow. The solution was then allowed to warm to room temp overnight producing crystals of **3-Ho**. (49 mg, 27%)**.** IR: 2949m, 2894m, 1445w, 1398w, 1349w, 1239s, 1125m, 1065m, 971s, 860m, 823s, 770m, 751w, 673w, 656m cm^{-1}. Anal. Calcd for $C_{74}H_{180}Ho_2K_2N_6O_{20}Si_{12}$: C, 40.05; H, 8.17; N, 3.79. Found: C, 40.49; H, 7.95; N, 3.67.

[K$_2$(18-c-6)$_3$][(R$_2$N)$_3$Dy]$_2$(μ-OC≡CO), 3-Dy. **3-Dy** was synthesized in a manner analogous to that of **3-Ho** (53 mg 28%)**.** IR: 2949m, 2894m, 1445w, 1398w, 1349w, 1239s, 1125m, 1065m, 971s, 860m, 823s, 770m, 751w, 673w, 656m cm^{-1}.

[K$_2$(18-c-6)$_3$][(R$_2$N)$_3$Gd]$_2$(μ-OC≡CO), 3-Gd. **3-Gd** was synthesized in a manner analogous to that of **3-Ho** (50 mg, 27%). IR: 2947m, 2893m, 1493w, 1464w, 1444w, 1354w, 1332w, 1295w, 1238s, 1105s, 978s, 942m, 858m, 825s, 767m, 656m cm^{-1}. Anal. Calcd for $C_{74}H_{180}Gd_2K_2N_6O_{20}Si_{12}$: C, 40.33; H, 8.23; N, 3.81. Found: C, 40.37; H, 8.20; N, 3.53. μ_{eff} = 14.5 μB (Evans method)

[K$_2$(18-c-6)$_3$][(R$_2$N)$_3$Tm]$_2$(μ-OC≡CO), 3-Tm. In an argon filled glovebox, **2-Tm** (100 mg, 0.082 mmol) was loaded into one side of an H-shaped tube fitted with a glass frit in between the two arms. Et_2O was loaded into the other side and the apparatus was removed from the glovebox and attached to a high vacuum line. Both sides were frozen in liquid nitrogen and CO (1 atm) was introduced to the system. The Et_2O was condensed onto the solid **2-Tm.** The solution was allowed to warm to −78 °C whereupon the solution turned yellow. The solution was allowed to warm to room temperature overnight and crystals of **3-Tm** suitable for X-ray diffraction grew on the side (50 mg, 27%). IR: 2937m, 2872m, 1470w, 1452w, 1393w, 1351m, 1238m, 1104s, 975s, 866m, 821s, 772m, 751w, 698w, 660m cm^{-1}.

[K(18-c-6)]$_2$[(R$_2$N)Gd]$_2$(OHC=CHO)$_2$, 4-Gd. In an argon filled glovebox, an H-shaped tube was loaded with solid [K(18-c-6)$_2$][Gd(NR$_2$)$_3$] on one side and Et_2O on the other. The H-tube was removed from the glovebox and attached to a vacuum line. The Et_2O was frozen with liquid nitrogen and the H-tube was filled with CO gas. Et_2O was then condensed onto the solid [K(18-c-6)$_2$][Gd(NR$_2$)$_3$] and allowed to warm to −78 °C causing the solution to turn from dark blue to

colorless. The solution was then allowed to warm to room temperature overnight and a small amount of colorless crystals of **4-Gd** were recovered.

X-ray Data Collection, Structure, Solution, Refinement

1-Gd in R32.

X-ray Data Collection, Structure Solution and Refinement for ajr46.

A blue crystal of approximate dimensions 0.283 x 0.106 x 0.103 mm was mounted in a cryoloop and transferred to a Bruker SMART APEX II diffractometer. The APEX2[53] program package was used to determine the unit-cell parameters and for data collection (240 sec/frame scan time for a sphere of diffraction data). The raw frame data was processed using SAINT[54] and SADABS[55] to yield the reflection data file. Subsequent calculations were carried out using the SHELXTL[56] program. The systematic absences were consistent with the trigonal space group *R32*. The non-centrosymmetric space group *R*32 was assigned and later determined to be correct.

The structure was solved by direct methods and refined on F^2 by full-matrix least-squares techniques. The analytical scattering factors[57] for neutral atoms were used throughout the analysis. Hydrogen atoms were included using a riding model.

Least-squares analysis yielded wR2 = 0.0426 and Goof = 1.005 for 88 variables refined against 2478 data (0.80 Å), R1 = 0.0235 for those 2264 data with $I > 2.0\sigma(I)$.

There were several high residuals present in the final difference-Fourier map. It was not possible to determine the nature of the residuals although it was probable that toluene solvent was present. The SQUEEZE[58a] routine in the PLATON[58b] program package was used to account for the electrons in the solvent accessible voids.

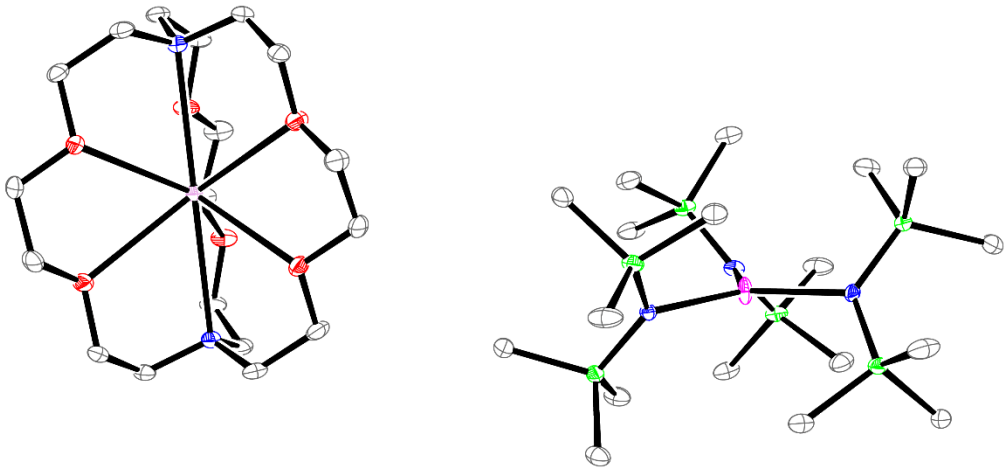

Figure 2.6. Ortep representation of **1-Gd** in R32 space group. Thermal ellipsoids drawn at the 50% probability level. H atoms excluded for clarity.

2-Dy. X-ray Data Collection, Structure Solution and Refinement for ajr19.

A dark blue crystal of approximate dimensions 0.140 x 0.145 x 0.192 mm was mounted in a cryoloop and transferred to a Bruker SMART APEX II diffractometer. The APEX2[53] program

package was used to determine the unit-cell parameters and for data collection (60 sec/frame scan time for a sphere of diffraction data). The raw frame data was processed using SAINT[54] and SADABS[55] to yield the reflection data file. Subsequent calculations were carried out using the SHELXTL[56] program. The diffraction symmetry was 2/*m* and the systematic absences were consistent with the monoclinic space group $P2_1/n$ that was later determined to be correct.

The structure was solved by dual space methods and refined on F^2 by full-matrix least-squares techniques. The analytical scattering factors[57] for neutral atoms were used throughout the analysis. Hydrogen atoms were included using a riding model. Several atoms were disordered and included using multiple components, partial site-occupancy factors and isotropic thermal parameters. The Dy metal center was disordered over two positions and modeled with 95 and 5% occupancy.At convergence, wR2 = 0.1025 and Goof = 1.023 for 553 variables refined against 16185 data (0.73Å), R1 = 0.0426 for those 12098 data with $I > 2.0\sigma(I)$.

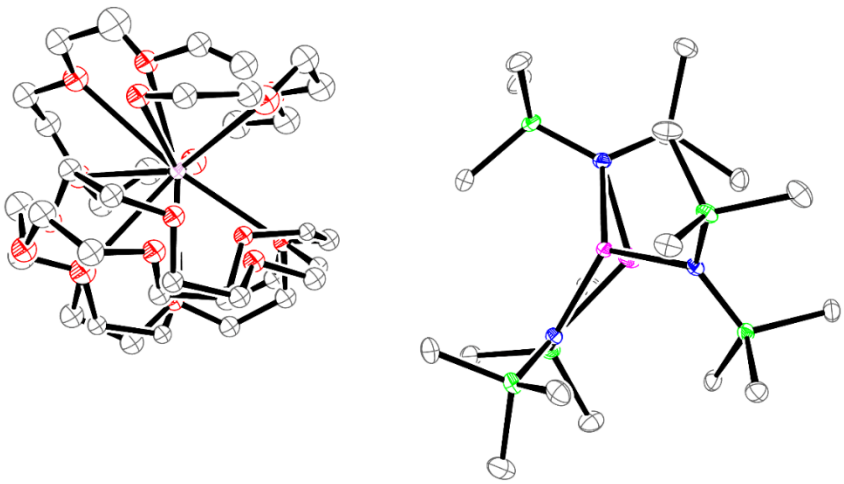

Figure 2.7. Ortep representation of **2-Dy** with thermal ellipsoids drawn at the 50% probability level. Hydrogen atoms excluded for clarity.

2-Er X-ray Data Collection, Structure Solution and Refinement for ajr20.

A dark blue crystal of approximate dimensions 0.252 x 0.229 x 0.205 mm was mounted in a cryoloop and transferred to a Bruker SMART APEX II diffractometer. The APEX2[53] program package was used to determine the unit-cell parameters and for data collection (60 sec/frame scan time for a sphere of diffraction data). The raw frame data was processed using SAINT[54] and SADABS[55] to yield the reflection data file. Subsequent calculations were carried out using the SHELXTL[56] program. The diffraction symmetry was 2/*m* and the systematic absences were consistent with the monoclinic space group $P2_1/n$ that was later determined to be correct.

The structure was solved by dual space methods and refined on F^2 by full-matrix least-squares techniques. The analytical scattering factors[57] for neutral atoms were used throughout the analysis. Hydrogen atoms were included using a riding model. Several atoms were disordered and included using multiple components, partial site-occupancy factors and isotropic thermal parameters. The Er metal center was disordered over two positions and modeled with 97 and 3% occupancy. Least-squares analysis yielded wR2 = 0.1081 and Goof = 1.091 for 553 variables refined against 15353 data (0.74, R1 = 0.0496 for those 12133 data with $I > 2.0\sigma(I)$.

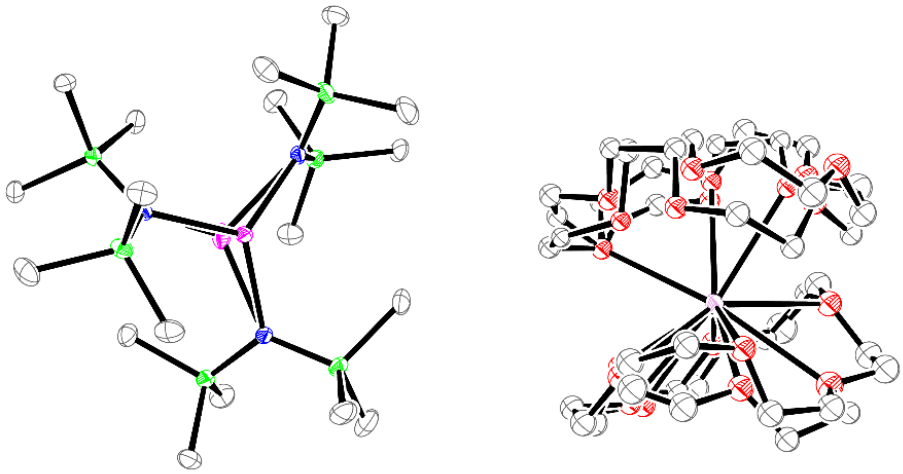

Figure 2.8. Ortep representation of **2-Er** with thermal ellipsoids drawn at the 50% probability level. Hydrogen atoms excluded for clarity

2-Tb, X-ray Data Collection, Structure Solution and Refinement for ajr23.

A dark blue crystal of approximate dimensions 0.348 x 0.228 x 0.227 mm was in a cryoloop and transferred to a Bruker SMART APEX II diffractometer. The APEX2[53] program package was used to determine the unit-cell parameters and for data collection (30 sec/frame scan time for a sphere of diffraction data). The raw frame data was processed using SAINT[54] and SADABS[55] to yield the reflection data file. Subsequent calculations were carried out using the SHELXTL[56] program. The diffraction symmetry was 2/*m* and the systematic absences were consistent with the monoclinic space group $P2_1/n$ that was later determined to be correct.

The structure was solved by dual space methods and refined on F^2 by full-matrix least-squares techniques. The analytical scattering factors[57] for neutral atoms were used throughout the analysis. Hydrogen atoms were included using a riding model. Several atoms were disordered and included using multiple components, partial site-occupancy factors and isotropic thermal parameters.

Least-squares analysis yielded wR2 = 0.0855 and Goof = 1.024 for 544 variables refined against 16174 data (0.73Å), R1 = 0.0356 for those 13695 data with I > 2.0σ(I).

2-Y. X-ray Data Collection, Structure Solution and Refinement for ajr28.

A dark blue crystal of approximate dimensions 0.348 x 0.228 x 0.227 mm was mounted on a in a cryoloop and transferred to a Bruker SMART APEX II diffractometer. The APEX253 program package was used to determine the unit-cell parameters and for data collection (90 sec/frame scan time for a sphere of diffraction data). The raw frame data was processed using SAINT54 and SADABS55 to yield the reflection data file. Subsequent calculations were carried out using the SHELXTL56 program. The diffraction symmetry was 2/*m* and the systematic absences were consistent with the monoclinic space group $P2_1/n$ that was later determined to be correct.

The structure was solved by dual space methods and refined on F^2 by full-matrix least-squares techniques. The analytical scattering factors57 for neutral atoms were used throughout the analysis. Hydrogen atoms were included using a riding model. Disorder in the 18-crown-6 units was modeled isotropically with multiple components. Disorder in the Y metal center was modeled in two parts with 97% and 3% occupancies.

Least-squares analysis yielded wR2 = 0.1383 and Goof = 1.025 for 553 variables refined against 15678 data (0.73 Å), R1 = 0.0516 for those 12476 data with I > 2.0σ(I).

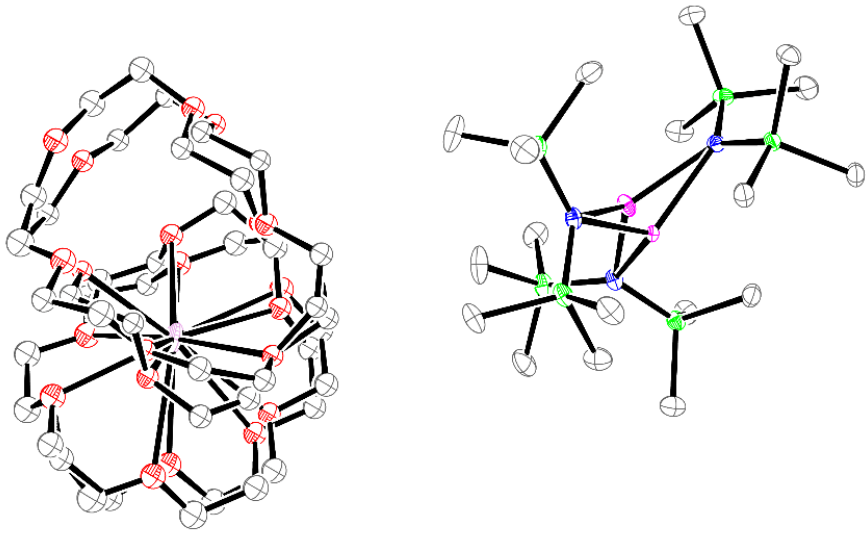

Figure 2.9. Ortep representation of **2-Y** with thermal ellipsoids drawn at the 50% probability level. Hydrogen atoms excluded for clarity

2-Tm. X-ray Data Collection, Structure Solution and Refinement for ajr29.

A purple crystal of approximate dimensions 0.262 x 0.217 x 0.163 mm was mounted in a cryoloop and transferred to a Bruker SMART APEX II diffractometer. The APEX2[53] program package was used to determine the unit-cell parameters and for data collection (90 sec/frame scan time for a sphere of diffraction data). The raw frame data was processed using SAINT[54] and SADABS[55] to yield the reflection data file. Subsequent calculations were carried out using the SHELXTL[56] program. The diffraction symmetry was *mmm* and the systematic absences were consistent with the orthorhombic space group $P2_12_12_1$ that was later determined to be correct.

The structure was solved by dual space methods and refined on F^2 by full-matrix least-squares techniques. The analytical scattering factors[57] for neutral atoms were used throughout the analysis. Hydrogen atoms were included using a riding model.

Least-squares analysis yielded wR2 = 0.1048 and Goof = 1.009 for 1042 variables refined against 26235 data (0.73Å), R1 = 0.0522 for those 18684 with I > 2.0σ(I).

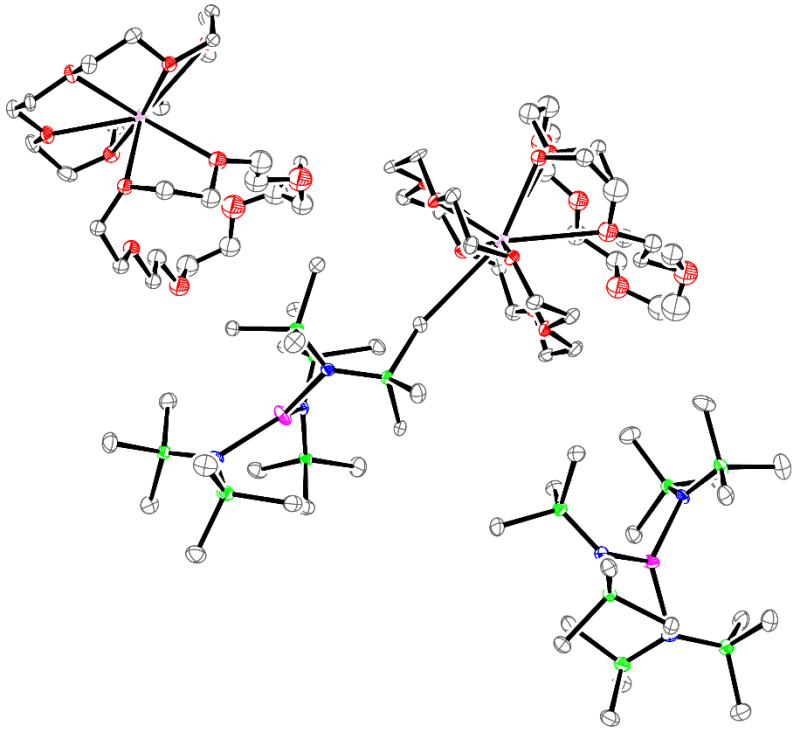

Figure 2.10. Ortep representation of **2-Tm** with thermal ellipsoids drawn at the 50% probability level. Hydrogen atoms excluded for clarity.

2-Gd. X-ray Data Collection, Structure Solution and Refinement for ajr40.

A dark blue crystal of approximate dimensions 0.253 x 0.239 x 0.192 mm was mounted in a cryoloop and transferred to a Bruker SMART APEX II diffractometer. The APEX2[53] program package was used to determine the unit-cell parameters and for data collection (90 sec/frame scan

time for a sphere of diffraction data). The raw frame data was processed using SAINT[54] and SADABS[55] to yield the reflection data file. Subsequent calculations were carried out using the SHELXTL[56] program. The diffraction symmetry was 2/*m* and the systematic absences were consistent with the monoclinic space group $P2_1/n$ that was later determined to be correct.

The structure was solved by dual space methods and refined on F^2 by full-matrix least-squares techniques. The analytical scattering factors[57] for neutral atoms were used throughout the analysis. Hydrogen atoms were included using a riding model

Least-squares analysis yielded wR2 = 0.0953 and Goof = 1.100 for 544 variables refined against 16163 data (0.73Å), R1 = 0.0466 for those 13374 data with $I > 2.0\sigma(I)$.

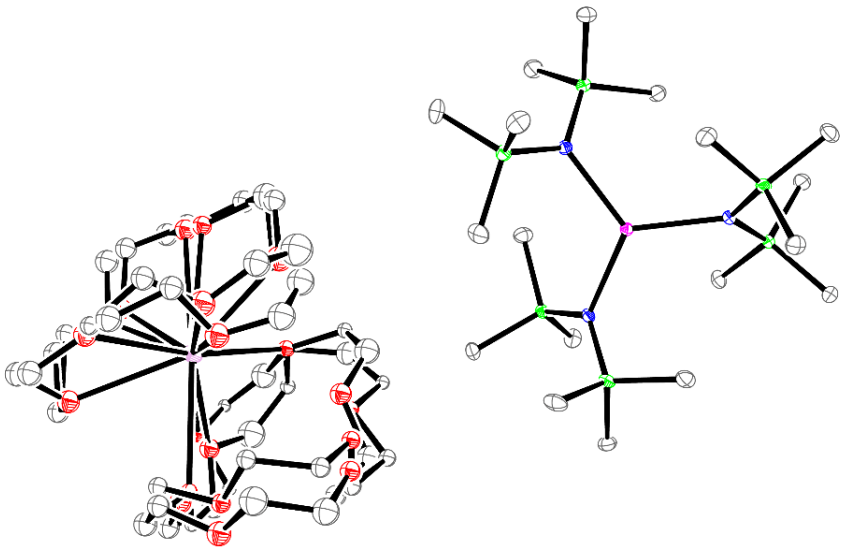

Figure 2.11. Ortep representation of **2-Gd** with thermal ellipsoids drawn at the 50% probability level. Hydrogen atoms excluded for clarity.

2-Ho. X-ray Data Collection, Structure Solution and Refinement for ajr43.

A blue crystal of approximate dimensions 0.378 x 0.375 x 0.367 mm was mounted in a cryoloop and transferred to a Bruker SMART APEX II diffractometer. The APEX2[53] program

package was used to determine the unit-cell parameters and for data collection (20 sec/frame scan time for a sphere of diffraction data). The raw frame data was processed using SAINT[54] and SADABS[55] to yield the reflection data file. Subsequent calculations were carried out using the SHELXTL[56] program. The diffraction symmetry was 2/*m* and the systematic absences were consistent with the monoclinic space group $P2_1/n$ that was later determined to be correct.

The structure was solved by direct methods and refined on F^2 by full-matrix least-squares techniques. The analytical scattering factors[57] for neutral atoms were used throughout the analysis. Hydrogen atoms were included using a riding model.

Least-squares analysis yielded wR2 = 0.0914 and Goof = 1.028 for 553 variables refined against 156608 data (0.74Å), R1 = 0.0368 for those 14019 data with $I > 2.0\sigma(I)$.

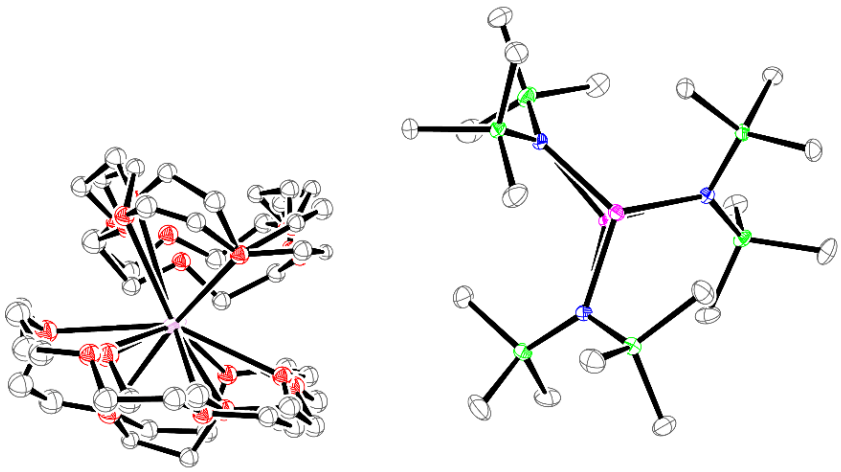

Figure 2.12. Ortep representation of **2-Ho** with thermal ellipsoids drawn at the 50% probability level. Hydrogen atoms excluded for clarity.

3-Dy. X-ray Data Collection, Structure Solution and Refinement for ajr15.

A colorless crystal of approximate dimensions 0.048 x 0.141 x 0.264 mm was mounted in a cryoloop and transferred to a Bruker SMART APEX II diffractometer. The APEX2[53] program package was used to determine the unit-cell parameters and for data collection (30 sec/frame scan time for a sphere of diffraction data). The raw frame data was processed using SAINT[54] and SADABS[55] to yield the reflection data file. Subsequent calculations were carried out using the SHELXTL[56] program. The diffraction symmetry was 2/*m* and the systematic absences were consistent with the monoclinic space groups *Cc* and *C*2/*c*. It was later determined that space group *C*2/*c* was correct.

The structure was solved by dual space methods and refined on F^2 by full-matrix least-squares techniques. The analytical scattering factors[57] for neutral atoms were used throughout the analysis. Hydrogen atoms were included using a riding model. The molecule was dimeric. There was a half-molecule located about an inversion center. Disorder in an Et2O solvent molecule was modeled isotropically

Least-squares analysis yielded wR2 = 0.0846 and Goof = 1.113 for 567 variables refined against 15305 data (0.73 Å), R1 = 0.0373 for those 10683 data with $I > 2.0\sigma(I)$.

3-Ho. X-ray Data Collection, Structure Solution and Refinement for ajr26.

A yellow crystal of approximate dimensions 0.347 x 0.202 x 0.132 mm was mounted in a cryoloop and transferred to a Bruker SMART APEX II diffractometer. The APEX2[53] program package was used to determine the unit-cell parameters and for data collection (30 sec/frame scan time for a sphere of diffraction data). The raw frame data was processed using SAINT[54] and

SADABS[55] to yield the reflection data file. Subsequent calculations were carried out using the SHELXTL[56] program. The diffraction symmetry was 2/*m* and the systematic absences were consistent with the monoclinic space groups *Cc* and *C*2/*c*. It was later determined that space group *C*2/*c* was correct.

The structure was solved by dual space methods and refined on F^2 by full-matrix least-squares techniques. The analytical scattering factors[57] for neutral atoms were used throughout the analysis. Hydrogen atoms were included using a riding model. The molecule was dimeric. There was a half-molecule located about an inversion center. Disorder in an Et2O solvent molecule was modeled isotropically in multiple parts.

Least-squares analysis yielded wR2 = 0.0590 and Goof = 1.026 for 559 variables refined against 14710 data (0.70 Å), R1 = 0.0251 for those 12462 data with $I > 2.0\sigma(I)$.

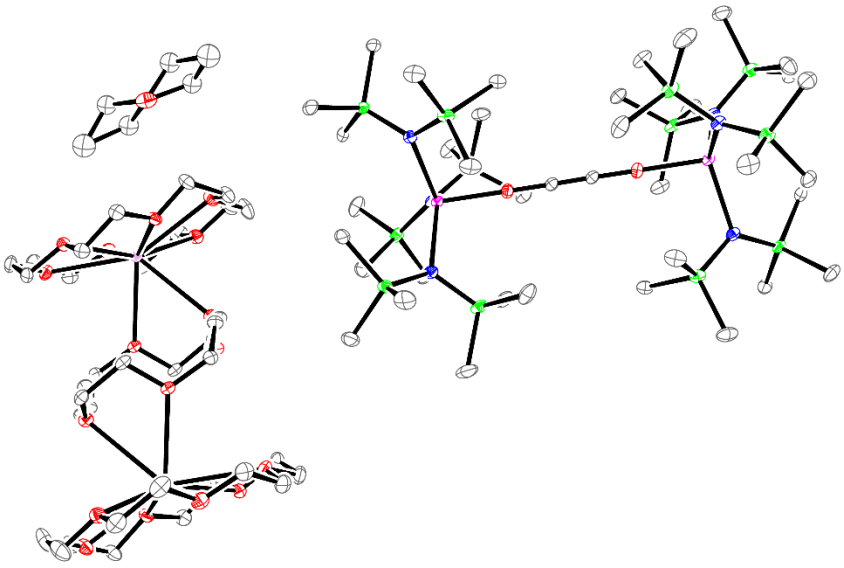

Figure 2.13. Ortep representation of **3-Ho** with thermal ellipsoids drawn at the 50% probability level. Hydrogen atoms excluded for clarity.

3-Tm. X-ray Data Collection, Structure Solution and Refinement for ajr41

A colorless crystal of approximate dimensions 0.214 x 0.200 x 0.196 mm was mounted in a cryoloop and transferred to a Bruker SMART APEX II diffractometer. The APEX2[53] program package was used to determine the unit-cell parameters and for data collection (60 sec/frame scan time for a sphere of diffraction data). The raw frame data was processed using SAINT[54] and SADABS[55] to yield the reflection data file. Subsequent calculations were carried out using the SHELXTL[56] program. The diffraction symmetry was 2/*m* and the systematic absences were consistent with the monoclinic space groups *Cc* and *C*2/*c*. It was later determined that space group *C*2/*c* was correct.

The structure was solved by dual space methods and refined on F^2 by full-matrix least-squares techniques. The analytical scattering factors[57] for neutral atoms were used throughout the analysis. The molecule was dimeric. There was a half-molecules located about an inversion center. Disorder in an Et2O solvent molecule was modeled isotropically. Hydrogen atoms were included using a riding model.

Least-squares analysis yielded wR2 = 0.0554 and Goof = 1.011 for 559 variables refined against 15214 data (0.73Å), R1 = 0.0244 for those 12794 data with $I > 2.0\sigma(I)$.

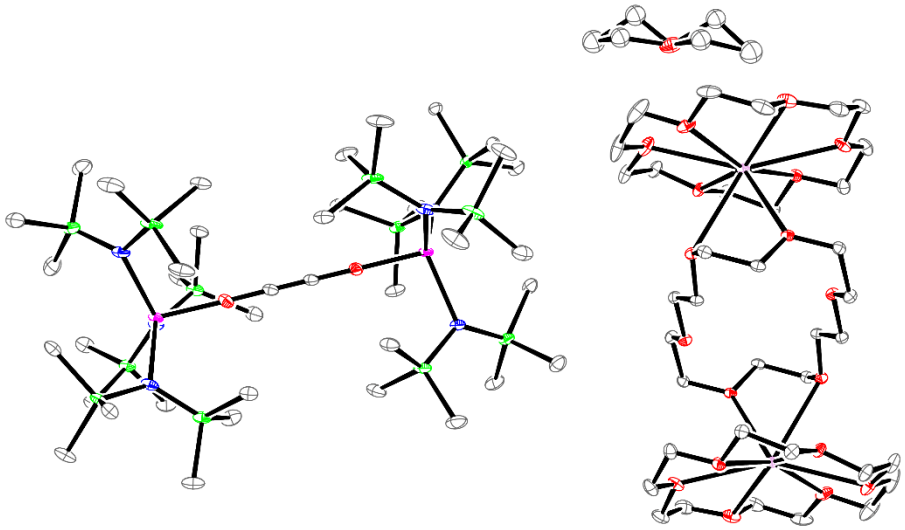

Figure 2.14. Ortep representation of **3-Tm** with thermal ellipsoids drawn at the 50% probability level. Hydrogen atoms excluded for clarity.

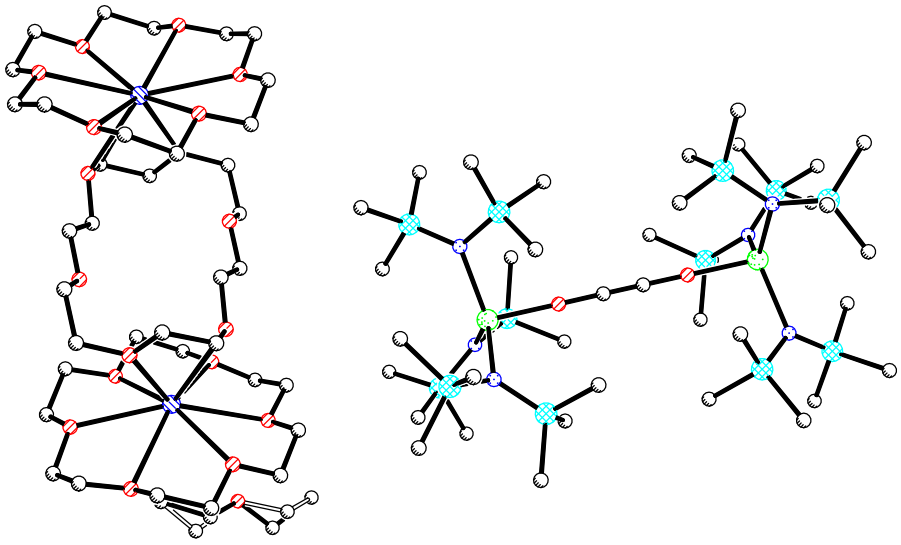

Figure 2.15. Ball and stick representation of connectivity structure of **3-Gd.** Hydrogen atoms excluded for clarity.

4- Gd. X-ray Data Collection, Structure Solution and Refinement for ajr32.

A colorless crystal of approximate dimensions 0.241 x 0.127 x 0.119 mm was mounted in a cryoloop and transferred to a Bruker SMART APEX II diffractometer. The APEX2[53] program package was used to determine the unit-cell parameters and for data collection (90 sec/frame scan time for a sphere of diffraction data). The raw frame data was processed using SAINT[54] and SADABS[55] to yield the reflection data file. Subsequent calculations were carried out using the SHELXTL[56] program. There were no systematic absences nor any diffraction symmetry other than the Friedel condition. The centrosymmetric triclinic space group $P\bar{1}$ was assigned and later determined to be correct.

The structure was solved by dual space methods and refined on F^2 by full-matrix least-squares techniques. The analytical scattering factors[57] for neutral atoms were used throughout the analysis. Hydrogen atoms were included using a riding model.

Least-squares analysis yielded wR2 = 0.0672 and Goof = 0.989 for 769 variables refined against 19003 data (0.70 Å), R1 = 0.0332 for those 14746 data with I > 2.0σ(I).

Table 2.2. Crystal data and structure refinement for ajr19 (2-Dy).

Identification code	ajr19	
Empirical formula	C42 H102 Dy K N3 O12 Si6	
Formula weight	1211.40	
Temperature	133(2) K	
Wavelength	0.71073 Å	
Crystal system	Monoclinic	
Space group	P21/n	
Unit cell dimensions	a = 11.0616(10) Å	α = 90°.
	b = 27.199(2) Å	β = 103.8855(12)°.
	c = 21.7721(19) Å	γ = 90°.

Volume	6359.0(10) Å3
Z	4
Density (calculated)	1.265 Mg/m3
Absorption coefficient	1.403 mm-1
F(000)	2560
Crystal color	blue
Crystal size	0.348 x 0.228 x 0.227 mm3
Theta range for data collection	1.781 to 29.158°
Index ranges	-14 <= h <= 15, -36 <= k <= 37, -28 <= l <= 28
Reflections collected	78631
Independent reflections	16185 [R(int) = 0.0587]
Completeness to theta = 25.500°	100.0 %
Absorption correction	Semi-empirical from equivalents
Max. and min. transmission	0.4319 and 0.3886
Refinement method	Full-matrix least-squares on F2
Data / restraints / parameters	16185 / 0 / 553
Goodness-of-fit on F2	1.023
Final R indices [I>2sigma(I) = 12098 data]	R1 = 0.0426, wR2 = 0.0928
R indices (all data, 0.73 Å)	R1 = 0.0678, wR2 = 0.1025
Extinction coefficient	n/a
Largest diff. peak and hole	1.467 and -0.704 e.Å-3

Table 2.3. Bond lengths [Å] for ajr19(2-Dy).

Dy(1)-N(3)	2.273(3)
Dy(1)-N(2)	2.278(3)
Dy(1)-N(1)	2.288(3)
Dy(2)-N(1)	2.257(5)
Dy(2)-N(3)	2.320(5)
Dy(2)-N(2)	2.337(5)

Table 2.4. Crystal data and structure refinement for ajr20 (2-Er).

Identification code	ajr20	
Empirical formula	C42 H102 Er K N3 O12 Si6	
Formula weight	1216.16	
Temperature	133(2) K	
Wavelength	0.71073 Å	
Crystal system	Monoclinic	
Space group	P21/n	
Unit cell dimensions	a = 11.064(3) Å	α = 90°.
	b = 27.080(6) Å	β = 103.991(3)°.
	c = 21.797(5) Å	γ = 90°.
Volume	6337(2) Å3	
Z	4	
Density (calculated)	1.275 Mg/m3	
Absorption coefficient	1.553 mm-1	
F(000)	2568	
Crystal color	blue	
Crystal size	0.348 x 0.228 x 0.227 mm3	
Theta range for data collection	1.222 to 28.872°	
Index ranges	-14 <= h <= 14, -34 <= k <= 34, -28 <= l <= 28	
Reflections collected	76237	
Independent reflections	15353 [R(int) = 0.0511]	
Completeness to theta = 25.500°	99.9 %	
Absorption correction	Semi-empirical from equivalents	
Max. and min. transmission	0.7458 and 0.6642	
Refinement method	Full-matrix least-squares on F2	
Data / restraints / parameters	15353 / 0 / 553	
Goodness-of-fit on F2	1.091	
Final R indices [I>2sigma(I) = 12133 data]	R1 = 0.0496, wR2 = 0.1012	
R indices (all data, 0.74 Å)	R1 = 0.0703, wR2 = 0.1081	
Extinction coefficient	n/a	
Largest diff. peak and hole	1.060 and -0.957 e.Å-3	

Table 2.5. Bond lengths [Å] for ajr20(2-Er).

Er(1)-N(3)	2.246(3)
Er(1)-N(1)	2.249(3)
Er(1)-N(2)	2.249(3)
Er(1)-Si(3)	3.3812(13)
Er(2)-N(1)	2.256(8)
Er(2)-N(2)	2.289(8)
Er(2)-N(3)	2.354(8)

Table 2.6. Crystal data and structure refinement for ajr23(2-Tb).

Identification code	ajr23	
Empirical formula	C42 H102 K N3 O12 Si6 Tb	
Formula weight	1207.82	
Temperature	133(2) K	
Wavelength	0.71073 Å	
Crystal system	Monoclinic	
Space group	P21/n	
Unit cell dimensions	a = 11.1324(18) Å	α = 90°.
	b = 27.081(4) Å	β = 103.924(2)°.
	c = 21.775(4) Å	γ = 90°.
Volume	6372.0(18) Å3	
Z	4	
Density (calculated)	1.259 Mg/m3	
Absorption coefficient	1.337 mm-1	
F(000)	2556	
Crystal color	blue	
Crystal size	0.348 x 0.228 x 0.227 mm3	
Theta range for data collection	1.786 to 29.178°	
Index ranges	-15 <= h <= 14, -36 <= k <= 35, -28 <= l <= 29	
Reflections collected	78537	
Independent reflections	16174 [R(int) = 0.0363]	

Completeness to theta = 25.500°	100.0 %
Absorption correction	Semi-empirical from equivalents
Max. and min. transmission	0.4318 and 0.3744
Refinement method	Full-matrix least-squares on F2
Data / restraints / parameters	16174 / 0 / 544
Goodness-of-fit on F2	1.024
Final R indices [I>2sigma(I) = 13695 data]	R1 = 0.0356, wR2 = 0.0804
R indices (all data, 0.73 Å)	R1 = 0.0461, wR2 = 0.0855
Extinction coefficient	n/a
Largest diff. peak and hole	1.489 and -0.680 e.Å-3

Table 2.7. Bond lengths [Å] for ajr23 (2-Tb).

Tb(1)-N(2)	2.291(2)
Tb(1)-N(3)	2.294(2)
Tb(1)-N(1)	2.295(2)

Table 2.8. Crystal data and structure refinement for ajr28 (2-Y).

Identification code	ajr28	
Empirical formula	C42 H102 K N3 O12 Si6 Y	
Formula weight	1137.81	
Temperature	133(2) K	
Wavelength	0.71073 Å	
Crystal system	Monoclinic	
Space group	$P2_1/n$	
Unit cell dimensions	a = 11.0774(7) Å	α = 90°.
	b = 27.0905(18) Å	β = 104.0003(9)°.
	c = 21.7959(14) Å	γ = 90°.
Volume	6346.5(7) $Å^3$	
Z	4	
Density (calculated)	1.191 Mg/m^3	
Absorption coefficient	1.147 mm^{-1}	
F(000)	2452	
Crystal color	violet	
Crystal size	0.348 x 0.228 x 0.227 mm^3	

Theta range for data collection	1.221 to 28.909°
Index ranges	-14 <= h <= 14, -36 <= k <= 35, -28 <= l <= 29
Reflections collected	76302
Independent reflections	15678 [R(int) = 0.0364]
Completeness to theta = 25.500°	100.0 %
Absorption correction	Semi-empirical from equivalents
Max. and min. transmission	0.7458 and 0.6480
Refinement method	Full-matrix least-squares on F^2
Data / restraints / parameters	15678 / 0 / 553
Goodness-of-fit on F^2	1.026
Final R indices [I>2sigma(I) = 12476 data]	R1 = 0.0516, wR2 = 0.1294
R indices (all data, 0.73 Å)	R1 = 0.0690, wR2 = 0.1384
Extinction coefficient	n/a
Largest diff. peak and hole	1.241 and -0.673 e.$Å^{-3}$

Table 2.9. Bond lengths [Å] for ajr28 (2-Y).

Y(1)-N(3)	2.264(2)
Y(1)-N(2)	2.2667(19)
Y(1)-N(1)	2.271(2)
Y(2)-N(1)	2.263(8)
Y(2)-N(2)	2.321(8)
Y(2)-N(3)	2.368(8)

Table 2.10. Crystal data and structure refinement for ajr29 (2-Tm).

Identification code	ajr29	
Empirical formula	C42 H102 K N3 O12 Si6 Tm	
Formula weight	1217.83	
Temperature	133(2) K	
Wavelength	0.71073 Å	
Crystal system	Orthorhombic	
Space group	P212121	
Unit cell dimensions	a = 21.956(2) Å	α = 90°.
	b = 22.554(2) Å	β = 90°.

	c = 25.737(3) Å γ = 90°.
Volume	12745(2) Å3
Z	8
Density (calculated)	1.269 Mg/m3
Absorption coefficient	1.620 mm-1
F(000)	5144
Crystal color	purple
Crystal size	0.262 x 0.217 x 0.163 mm3
Theta range for data collection	1.200 to 26.481°
Index ranges	-27 <= h <= 27, -28 <= k <= 28, -32 <= l <= 32
Reflections collected	139038
Independent reflections	26235 [R(int) = 0.1045]
Completeness to theta = 25.500°	100.0 %
Absorption correction	Semi-empirical from equivalents
Max. and min. transmission	0.4296 and 0.3637
Refinement method	Full-matrix least-squares on F2
Data / restraints / parameters	26235 / 0 / 1042
Goodness-of-fit on F2	1.009
Final R indices [I>2sigma(I) = 18684 data]	R1 = 0.0522, wR2 = 0.0910
R indices (all data, 0.73 Å)	R1 = 0.0941, wR2 = 0.1048
Absolute structure parameter	-0.006(3)
Extinction coefficient	n/a
Largest diff. peak and hole	0.981 and -1.073 e.Å-3

Table 2.11. Bond lengths [Å] for ajr29 (2-Tm).

Tm(1)-N(2)	2.335(7)
Tm(1)-N(1)	2.353(7)
Tm(1)-N(3)	2.357(6)
Tm(2)-N(5)	2.338(7)
Tm(2)-N(4)	2.346(6)
Tm(2)-N(6)	2.348(7)

Table 2.12. Crystal data and structure refinement for ajr40 (2-Gd).

Identification code	ajr40	
Empirical formula	C42 H102 Gd K N3 O12 Si6	
Formula weight	1206.15	
Temperature	133(2) K	
Wavelength	0.71073 Å	
Crystal system	Monoclinic	
Space group	P21/n	
Unit cell dimensions	a = 11.1493(11) Å	α = 90°.
	b = 27.059(3) Å	β = 104.0069(13)°.
	c = 21.755(2) Å	γ = 90°.
Volume	6368.1(11) Å3	
Z	4	
Density (calculated)	1.258 Mg/m3	
Absorption coefficient	1.269 mm-1	
F(000)	2552	
Crystal color	purple	
Crystal size	0.253 x 0.239 x 0.192 mm3	
Theta range for data collection	1.223 to 29.134°	
Index ranges	-15 <= h <= 15, -35 <= k <= 35, -28 <= l <= 28	
Reflections collected	78726	
Independent reflections	16163 [R(int) = 0.0511]	
Completeness to theta = 25.500°	100.0 %	
Absorption correction	Semi-empirical from equivalents	
Max. and min. transmission	0.4319 and 0.3744	
Refinement method	Full-matrix least-squares on F2	
Data / restraints / parameters	16163 / 0 / 544	
Goodness-of-fit on F2	1.100	
Final R indices [I>2sigma(I) = 13374 data]	R1 = 0.0466, wR2 = 0.0904	
R indices (all data, 0.73 Å)	R1 = 0.0623, wR2 = 0.0953	
Extinction coefficient	n/a	
Largest diff. peak and hole	1.009 and -1.022 e.Å-3	

Table 2.13. Bond lengths [Å] for ajr40 (2-Gd).

Gd(1)-N(2)	2.308(3)
Gd(1)-N(1)	2.310(3)
Gd(1)-N(3)	2.310(3)

Table 2.14. Crystal data and structure refinement for ajr43 (2-Ho).

Identification code	ajr43	
Empirical formula	C42 H102 Ho K N3 O12 Si6	
Formula weight	1213.83	
Temperature	133(2) K	
Wavelength	0.71073 Å	
Crystal system	Monoclinic	
Space group	P21/n	
Unit cell dimensions	a = 11.0476(11) Å	α = 90°.
	b = 27.157(3) Å	β = 103.9052(12)°.
	c = 21.797(2) Å	γ = 90°.
Volume	6347.9(11) Å3	
Z	4	
Density (calculated)	1.270 Mg/m3	
Absorption coefficient	1.475 mm-1	
F(000)	2564	
Crystal color	Blue	
Crystal size	0.378 x 0.375 x 0.367 mm3	
Theta range for data collection	1.220 to 28.873°	
Index ranges	-14 <= h <= 14, -36 <= k <= 36, -29 <= l <= 29	
Reflections collected	75935	
Independent reflections	15608 [R(int) = 0.0434]	
Completeness to theta = 25.500°	99.9 %	
Absorption correction	Semi-empirical from equivalents	
Max. and min. transmission	0.7458 and 0.6626	
Refinement method	Full-matrix least-squares on F2	
Data / restraints / parameters	15608 / 0 / 553	
Goodness-of-fit on F2	1.028	
Final R indices [I>2sigma(I) = 14019 data]	R1 = 0.0368, wR2 = 0.0883	

R indices (all data, 0.74 Å)	R1 = 0.0417, wR2 = 0.0914
Extinction coefficient	n/a
Largest diff. peak and hole	2.859 and -0.882 e.Å-3

Table 2.15. Bond lengths [Å] for ajr43 (2-Ho).

Ho(1)-N(3)	2.262(2)
Ho(1)-N(2)	2.264(2)
Ho(1)-N(1)	2.274(2)
Ho(2)-N(1)	2.258(5)
Ho(2)-N(3)	2.311(5)
Ho(2)-N(2)	2.318(4)

Table 2.16. Crystal data and structure refinement for ajr15 (3-Dy).

Identification code	ajr15	
Empirical formula	C78 H190 Dy2 K2 N6 O21 Si12	
Formula weight	2288.63	
Temperature	88(2) K	
Wavelength	0.71073 Å	
Crystal system	Monoclinic	
Space group	C2/c	
Unit cell dimensions	a = 25.4899(16) Å	$\alpha = 90°$.
	b = 18.8304(12) Å	$\beta = 103.1276(9)°$.
	c = 25.7453(16) Å	$\gamma = 90°$.
Volume	12034.4(13) $Å^3$	
Z	4	
Density (calculated)	1.263 Mg/m^3	
Absorption coefficient	1.477 mm^{-1}	
F(000)	4824	
Crystal color	colorless	
Crystal size	0.264 x 0.141 x 0.048 mm^3	
Theta range for data collection	1.357 to 29.158°	
Index ranges	-33 <= h <= 34, -25 <= k <= 25, -33 <= l <= 33	

Reflections collected	74183
Independent reflections	15305 [R(int) = 0.0735]
Completeness to theta = 25.500°	100.0 %
Absorption correction	Semi-empirical from equivalents
Max. and min. transmission	0.4319 and 0.3949
Refinement method	Full-matrix least-squares on F^2
Data / restraints / parameters	15305 / 0 / 567
Goodness-of-fit on F^2	1.114
Final R indices [I>2sigma(I) = 10683 data]	R1 = 0.0373, wR2 = 0.0667
R indices (all data, 0.73 Å)	R1 = 0.0738, wR2 = 0.0846
Extinction coefficient	n/a
Largest diff. peak and hole	0.614 and -0.651 e.$Å^{-3}$

Table 2.17. Bond lengths [Å] for ajr15 (3-Dy).

Dy(1)-O(1)	2.070(2)
Dy(1)-N(1)	2.282(3)
Dy(1)-N(2)	2.290(2)
Dy(1)-N(3)	2.296(3)
C(1)-C(1)#1	1.183(6)

Table 2.18. Crystal data and structure refinement for ajr26 (3-Ho).

Identification code	ajr26	
Empirical formula	C78 H190 Ho2 K2 N6 O21 Si12	
Formula weight	2293.49	
Temperature	133(2) K	
Wavelength	0.71073 Å	
Crystal system	Monoclinic	
Space group	C2/c	
Unit cell dimensions	a = 25.514(3) Å	α = 90°.
	b = 18.800(2) Å	β = 103.1674(15)°.
	c = 25.712(3) Å	γ = 90°.
Volume	12009(2) Å3	
Z	4	

Density (calculated)	1.269 Mg/m3
Absorption coefficient	1.553 mm-1
F(000)	4832
Crystal color	yellow
Crystal size	0.347 x 0.202 x 0.132 mm3
Theta range for data collection	1.358 to 28.864°
Index ranges	-33 <= h <= 33, -25 <= k <= 25, -34 <= l <= 32
Reflections collected	61845
Independent reflections	14710 [R(int) = 0.0318]
Completeness to theta = 25.500°	100.0 %
Absorption correction	Semi-empirical from equivalents
Max. and min. transmission	0.4316 and 0.3733
Refinement method	Full-matrix least-squares on F2
Data / restraints / parameters	14710 / 0 / 559
Goodness-of-fit on F2	1.025
Final R indices [I>2sigma(I) = 12462 data]	R1 = 0.0251, wR2 = 0.0554
R indices (all data, 0.73 Å)	R1 = 0.0345, wR2 = 0.0589
Extinction coefficient	n/a
Largest diff. peak and hole	0.631 and -0.377 e.Å-3

Table 2.19. Bond lengths [Å] for ajr26 (3-Ho).

Ho(1)-O(1)	2.0598(14)
Ho(1)-N(1)	2.2716(15)
Ho(1)-N(2)	2.2780(16)
Ho(1)-N(3)	2.2802(16)

Table 2.20. Crystal data and structure refinement for ajr41 (3-Tm).

Identification code	ajr41
Empirical formula	C78 H190 K2 N6 O21 Si12 Tm2
Formula weight	2301.49
Temperature	88(2) K

Wavelength	0.71073 Å	
Crystal system	Monoclinic	
Space group	C2/c	
Unit cell dimensions	a = 25.453(3) Å	α = 90°.
	b = 18.757(2) Å	β = 103.1418(15)°.
	c = 25.744(3) Å	γ = 90°.
Volume	11969(2) Å3	
Z	4	
Density (calculated)	1.277 Mg/m3	
Absorption coefficient	1.719 mm-1	
F(000)	4848	
Crystal color	colourless	
Crystal size	0.214 x 0.200 x 0.196 mm3	
Theta range for data collection	1.361 to 29.125°	
Index ranges	-34 <= h <= 34, -24 <= k <= 24, -33 <= l <= 34	
Reflections collected	73762	
Independent reflections	15214 [R(int) = 0.0304]	
Completeness to theta = 25.500°	100.0 %	
Absorption correction	Semi-empirical from equivalents	
Max. and min. transmission	0.7458 and 0.6513	
Refinement method	Full-matrix least-squares on F2	
Data / restraints / parameters	15214 / 0 / 559	
Goodness-of-fit on F2	1.011	
Final R indices [I>2sigma(I) = 12794 data]	R1 = 0.0244, wR2 = 0.0509	
R indices (all data, 0.73 Å)	R1 = 0.0349, wR2 = 0.0554	
Extinction coefficient	n/a	
Largest diff. peak and hole	0.652 and -1.122 e.Å-3	

Table 2.21. Bond lengths [Å] ajr41 (3-Tm).

Tm(1)-O(1)	2.0428(14)
Tm(1)-N(1)	2.2465(17)
Tm(1)-N(2)	2.2533(16)

Tm(1)-N(3)	2.2548(16)
C(1)-C(1)#1	1.184(4)

Table 2.22. Crystal data and structure refinement for ajr32 (4-Gd).

Identification code	ajr32	
Empirical formula	C52 H124 Gd2 K2 N4 O16 Si8	
Formula weight	1678.96	
Temperature	133(2) K	
Wavelength	0.71073 Å	
Crystal system	Triclinic	
Space group	P-1	
Unit cell dimensions	a = 12.6614(13) Å	α = 94.4758(13)°.
	b = 15.5498(15) Å	β = 94.0831(13)°.
	c = 21.205(2) Å	γ = 105.7458(12)°.
Volume	3987.4(7) $Å^3$	
Z	2	
Density (calculated)	1.398 Mg/m^3	
Absorption coefficient	1.929 mm^{-1}	
F(000)	1740	
Crystal color	colorless	
Crystal size	0.241 x 0.127 x 0.119 mm^3	
Theta range for data collection	0.968 to 28.896°	
Index ranges	-16 <= h <= 17, -20 <= k <= 21, -27 <= l <= 28	
Reflections collected	48467	
Independent reflections	19003 [R(int) = 0.0368]	
Completeness to theta = 25.500°	99.8 %	
Absorption correction	Semi-empirical from equivalents	
Max. and min. transmission	0.4316 and 0.3793	
Refinement method	Full-matrix least-squares on F^2	
Data / restraints / parameters	19003 / 0 / 769	
Goodness-of-fit on F^2	0.989	
Final R indices [I>2sigma(I) = 14746 data]	R1 = 0.0332, wR2 = 0.0614	
R indices (all data, 0.73 Å)	R1 = 0.0538, wR2 = 0.0672	
Extinction coefficient	n/a	

Largest diff. peak and hole 1.126 and -0.482 e.Å^{-3}

Table 2.23. Bond lengths [Å] for ajr32 (4-Gd).

Gd(1)-O(1)	2.2667(19)
Gd(1)-O(2)#1	2.2791(19)
Gd(1)-N(2)	2.322(2)
Gd(1)-N(1)	2.354(2)
Gd(1)-O(2)	2.3694(19)
Gd(1)-C(1)	2.929(3)
Gd(1)-C(2)	2.999(3)
Gd(1)-Gd(1)#1	3.8719(4)
K(1)-O(1)	2.745(2)
K(1)-O(8)	2.803(2)
K(1)-O(5)	2.865(2)
K(1)-O(11)	2.895(8)
K(1)-O(10)	2.904(3)
K(1)-O(6)	2.910(2)
K(1)-O(7)	2.957(2)
K(1)-O(9)	3.011(8)
K(1)-O(12)	3.028(4)
K(1)-C(1)	3.271(3)
K(1)-C(10)	3.467(3)
K(1)-C(34)	3.479(7)
O(2)-Gd(1)#1	2.2791(19)
C(1)-C(2)	1.334(4)
Gd(2)-O(3)	2.2598(19)
Gd(2)-O(4)#2	2.2795(19)
Gd(2)-N(4)	2.329(2)
Gd(2)-N(3)	2.356(2)
Gd(2)-O(4)	2.3738(19)
Gd(2)-C(3)	2.985(3)

Gd(2)-C(4)	3.050(3)
Gd(2)-Si(6)	3.4316(9)
Gd(2)-Gd(2)#2	3.8758(4)
K(2)-O(3)	2.778(2)
K(2)-O(18)	2.794(3)
K(2)-O(16)	2.870(2)
K(2)-O(13)	2.885(2)
K(2)-O(19)	2.888(2)
K(2)-O(14)	2.958(2)
K(2)-O(15)	2.962(2)
K(2)-O(17)	3.083(7)
K(2)-C(3)	3.282(3)
K(2)-C(61)	3.507(11)
O(4)-Gd(2)#2	2.2794(19)
C(3)-C(4)	1.331(4)

Table 2.24. Crystal data and structure refinement for ajr46 (1-Gd).

Identification code	ajr46	
Empirical formula	C36 H90 Gd K N5 O6 Si6	
Formula weight	1053.99	
Temperature	88(2) K	
Wavelength	0.71073 Å	
Crystal system	Trigonal	
Space group	R32	
Unit cell dimensions	a = 18.564(3) Å	α = 90°.
	b = 18.564(3) Å	β = 90°.
	c = 18.050(3) Å	γ = 120°.
Volume	5387(2) Å3	
Z	3	
Density (calculated)	0.975 Mg/m3	
Absorption coefficient	1.112 mm-1	
F(000)	1668	
Crystal color	Blue	

Crystal size	0.283 x 0.106 x 0.103 mm3
Theta range for data collection	1.696 to 26.389°
Index ranges	-23 <= h <= 23, -23 <= k <= 23, -22 <= l <= 22
Reflections collected	13308
Independent reflections	2478 [R(int) = 0.0525]
Completeness to theta = 25.500°	100.0 %
Absorption correction	Semi-empirical from equivalents
Max. and min. transmission	0.7454 and 0.6134
Refinement method	Full-matrix least-squares on F2
Data / restraints / parameters	2478 / 0 / 88
Goodness-of-fit on F2	1.005
Final R indices [I>2sigma(I) = 2264 data]	R1 = 0.0235, wR2 = 0.0411
R indices (all data, 0.8 Å)	R1 = 0.0304, wR2 = 0.0426
Absolute structure parameter	-0.026(6)
Extinction coefficient	n/a
Largest diff. peak and hole	0.372 and -0.271 e.Å-3

Table 2.25. Bond lengths [Å] and angles [°] for ajr46 (1-Gd).

Gd(1)-N(1)	2.315(3)
Gd(1)-N(1)#1	2.316(3)
Gd(1)-N(1)#2	2.316(3)

Symmetry transformations used to generate equivalent atoms:

#1 -x+y,-x,z #2 -y,x-y,z #3 x-y,-y,-z+1 #4 x-y+1/3,-y+2/3,-z+2/3

#5 y+1/3,x-1/3,-z+2/3 #6 -y+1,x-y,z #7 -x+4/3,-x+y+2/3,-z+2/3

#8 -x+y+1,-x+1,z

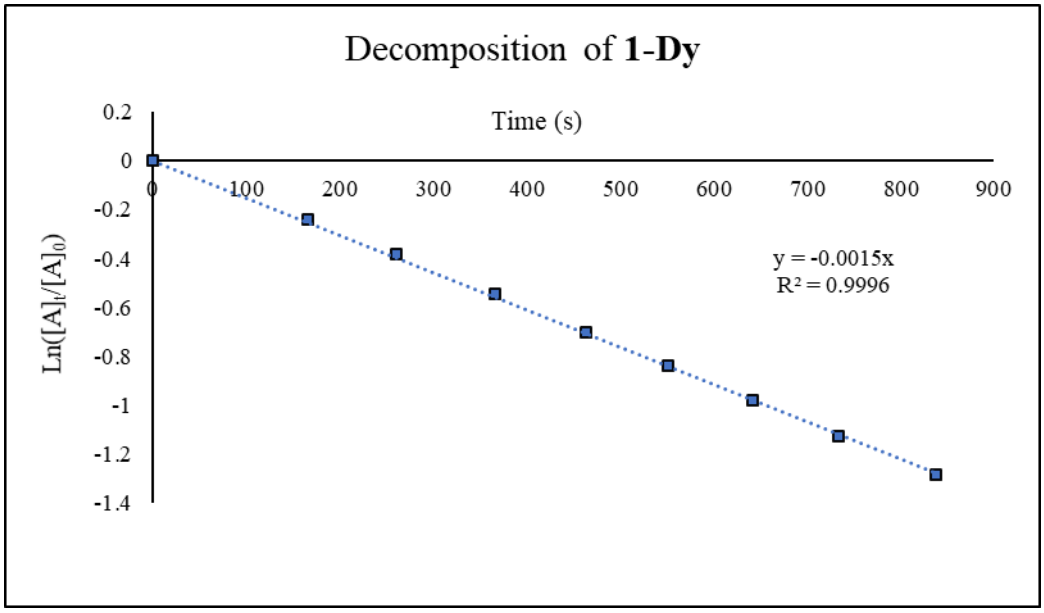

Figure 2.16. Decomposition of **1-Dy** 3mM in THF

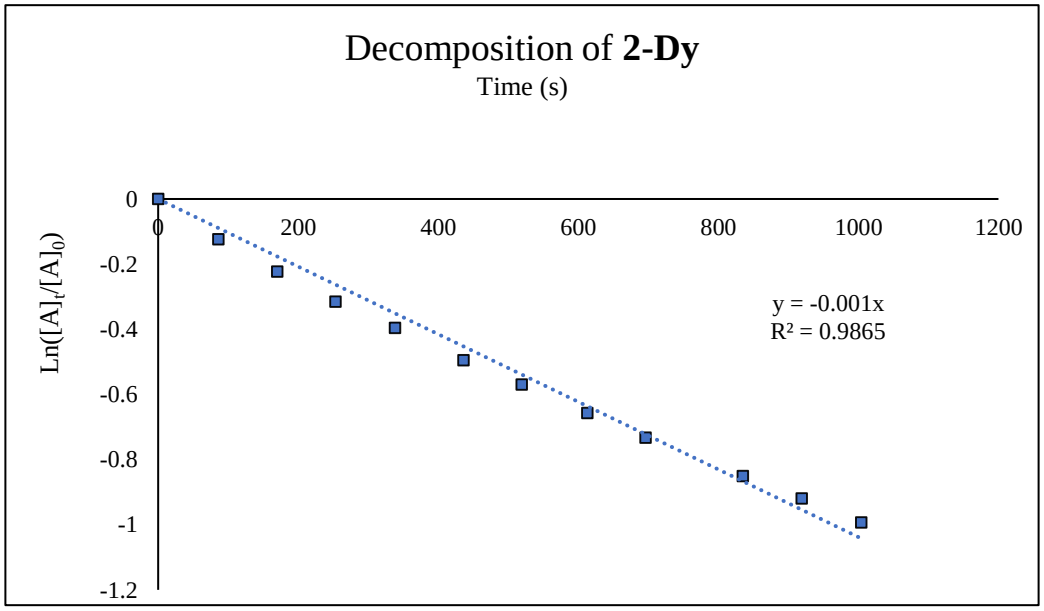

Figure 2.17. Decomposition of **2-Dy** 3mM in Et_2O

H-Tube Schematic

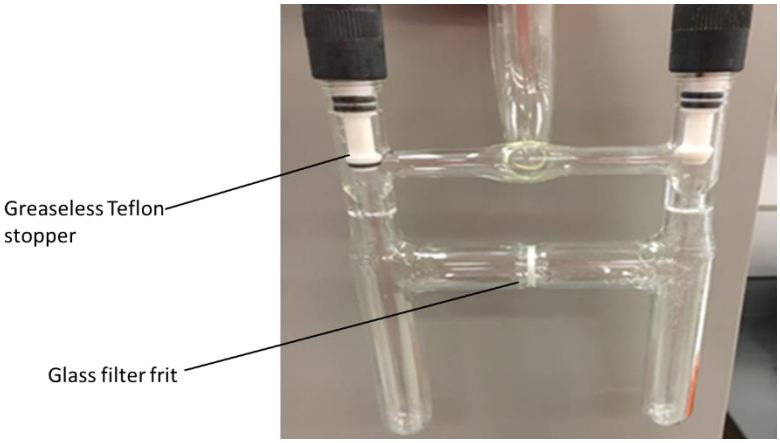

Figure 2.18. Schematic of H tube used in reactions to form **3-Ln** and **4-Ln**

References

1. M. N. Bochkarev, *Coord. Chem. Rev.*, 2004, **248**, 835-851.
2. F. Nief, in *Handbook on the Physics and Chemistry of Rare Earths*, Elsevier, 2010, vol. 40, pp. 241-300.
3. D. H. Woen and W. J. Evans, *Handbook on the Physics and Chemistry of Rare Earths*, 2016, **50**, 337-394.
4. W. J. Evans, *Organometallics*, 2016, **35**, 3088-3100.
5. P. B. Hitchcock, M. F. Lappert, L. Maron and A. V. Protchenko, *Angew. Chem. Int. Ed.*, 2008, **47**, 1488-1491.
6. M. R. MacDonald, J. W. Ziller and W. J. Evans, *J. Am. Chem. Soc.*, 2011, **133**, 15914-15917.
7. M. R. MacDonald, J. E. Bates, M. E. Fieser, J. W. Ziller, F. Furche and W. J. Evans, *J. Am. Chem. Soc.*, 2012, **134**, 8420-8423.
8. M. R. MacDonald, J. E. Bates, J. W. Ziller, F. Furche and W. J. Evans, *J. Am. Chem. Soc.*, 2013, **135**, 9857-9868.
9. W. J. Evans and D. S. Lee, *Can. J. Chem.*, 2005, **83**, 375-384.
10. W. J. Evans, D. S. Lee, C. Lie and J. W. Ziller, *Angew. Chem. Int. Ed.*, 2004, **43**, 5517-5519.
11. W. J. Evans, D. S. Lee, D. B. Rego, J. M. Perotti, S. A. Kozimor, E. K. Moore and J. W. Ziller, *J. Am. Chem. Soc.*, 2004, **126**, 14574-14582.
12. W. J. Evans, D. S. Lee, J. W. Ziller and N. Kaltsoyannis, *J. Am. Chem. Soc.*, 2006, **128**, 14176-14184.
13. J. D. Rinehart, M. Fang, W. J. Evans and J. R. Long, *Nat. Chem.*, 2011, **3**, 538-542.
14. J. D. Rinehart, M. Fang, W. J. Evans and J. R. Long, *J. Am. Chem. Soc.*, 2011, **133**, 14236-14239.
15. M. Fang, D. S. Lee, J. W. Ziller, R. J. Doedens, J. E. Bates, F. Furche and W. J. Evans, *J. Am. Chem. Soc.*, 2011, **133**, 3784-3787.
16. M. E. Fieser, M. R. MacDonald, B. T. Krull, J. E. Bates, J. W. Ziller, F. Furche and W. J. Evans, *J. Am. Chem. Soc.*, 2015, **137**, 369-382.
17. C. T. Palumbo, L. E. Darago, C. J. Windorff, J. W. Ziller and W. J. Evans, *Organometallics*, 2018, **37**, 900-905.
18. D. H. Woen, G. P. Chen, J. W. Ziller, T. J. Boyle, F. Furche and W. J. Evans, *Angew. Chem. Int. Ed.*, 2017, **56**, 2050-2053.
19. A. J. Ryan, L. E. Darago, S. G. Balasubramani, G. P. Chen, J. W. Ziller, F. Furche, J. R. Long and W. J. Evans, *Chemistry–A European Journal*, 2018, **24**, 7702-7709.
20. M. Fang, J. H. Farnaby, J. W. Ziller, J. E. Bates, F. Furche and W. J. Evans, *J. Am. Chem. Soc.*, 2012, **134**, 6064-6067.
21. R. A. Andersen, D. H. Templeton and A. Zalkin, *Inorg. Chem.*, 1978, **17**, 2317-2319.
22. J. S. Ghotra, M. B. Hursthouse and A. J. Welch, *J. Chem. Soc., Chem. Commun.*, 1973, DOI: 10.1039/C39730000669, 669-670.
23. P. B. Hitchcock, A. G. Hulkes, M. F. Lappert and Z. Li, *Dalt. Trans.*, 2004, DOI: 10.1039/B311397C, 129-136.
24. A. Herrmann Wolfgang, R. Anwander, C. Munck Florian, W. Scherer, V. Dufaud, W. Huber Norbert and R. J. Artus Georg, *Z. Naturfo. B.* 1994, **49**, 1789.
25. P. G. Eller, D. C. Bradley, M. B. Hursthouse and D. W. Meek, *Coord. Chem. Rev.*, 1977, **24**, 1-95.

26. G. Scarel, C. Wiemer, M. Fanciulli, I. L. Fedushkin, G. K. Fukin, G. A. Domrachev, Y. Lebedinskii, A. Zenkevich and G. Pavia, *Z. Anorg. Allg. Chem.*, 2007, **633**, 2097-2103.
27. P. L. Arnold, Z. R. Turner, R. M. Bellabarba and R. P. Tooze, *Chemical Science*, 2011, **2**, 77-79.
28. S. M. Mansell, N. Kaltsoyannis and P. L. Arnold, *J. Am. Chem. Soc.*, 2011, **133**, 9036-9051.
29. B. M. Gardner, J. C. Stewart, A. L. Davis, J. McMaster, W. Lewis, A. J. Blake and S. T. Liddle, *Proceedings of the National Academy of Sciences*, 2012, **109**, 9265.
30. A. S. Frey, F. G. N. Cloke, P. B. Hitchcock, I. J. Day, J. C. Green and G. Aitken, *J. Am. Chem. Soc.*, 2008, **130**, 13816-13817.
31. R. Shannon, *Acta Crystallographica Section A*, 1976, **32**, 751-767.
32. W. J. Evans, J. W. Grate and R. J. Doedens, *J. Am. Chem. Soc.*, 1985, **107**, 1671-1679.
33. E. L. Werkema, L. Maron, O. Eisenstein and R. A. Andersen, *J. Am. Chem. Soc.*, 2007, **129**, 2529-2541.
34. W. J. Evans, K. J. Forrestal and J. W. Ziller, *J. Am. Chem. Soc.*, 1995, **117**, 12635-12636.
35. W. J. Evans, S. A. Kozimor, G. W. Nyce and J. W. Ziller, *J. Am. Chem. Soc.*, 2003, **125**, 13831-13835.
36. F. H. Allen, O. Kennard, D. G. Watson, L. Brammer, A. G. Orpen and R. Taylor, *Journal of the Chemical Society, Perkin Transactions 2*, 1987, DOI: 10.1039/P298700000S1, S1-S19.
37. T. Watanabe, Y. Ishida, T. Matsuo and H. Kawaguchi, *J. Am. Chem. Soc.*, 2009, **131**, 3474-3475.
38. R. J. Schwamm, M. D. Anker, M. Lein and M. P. Coles, *Angew. Chem. Int. Ed.*, 2019, **58**, 1489-1493.
39. A. C. Fecker, A. Glöckner, C. G. Daniliuc, M. Freytag, P. G. Jones and M. D. Walter, *Organometallics*, 2013, **32**, 874-884.
40. M. C. Cassani, Y. K. Gun'ko, P. B. Hitchcock, M. F. Lappert and F. Laschi, *Organometallics*, 1999, **18**, 5539-5547.
41. T. F. Jenkins, D. H. Woen, L. N. Mohanam, J. W. Ziller, F. Furche and W. J. Evans, *Organometallics*, 2018, DOI: 10.1021/acs.organomet.8b00557.
42. J. F. Corbey, D. H. Woen, C. T. Palumbo, M. E. Fieser, J. W. Ziller, F. Furche and W. J. Evans, *Organometallics*, 2015, **34**, 3909-3921.
43. F. Jaroschik, A. Momin, F. Nief, X. F. Le Goff, G. B. Deacon and P. C. Junk, *Angew. Chem.*, 2009, **121**, 1137-1141.
44. C. T. Palumbo, D. P. Halter, V. K. Voora, G. P. Chen, A. K. Chan, M. E. Fieser, J. W. Ziller, W. Hieringer, F. Furche and K. Meyer, *Inorg. Chem.*, 2018, **57**, 2823-2833.
45. C. T. Palumbo, D. P. Halter, V. K. Voora, G. P. Chen, J. W. Ziller, M. Gembicky, A. L. Rheingold, F. Furche, K. Meyer and W. J. Evans, *Inorg. Chem.*, 2018, **57**, 12876-12884.
46. C. J. Windorff, G. P. Chen, J. N. Cross, W. J. Evans, F. Furche, A. J. Gaunt, M. T. Janicke, S. A. Kozimor and B. L. Scott, *J. Am. Chem. Soc.*, 2017, **139**, 3970-3973.
47. J. Su, C. J. Windorff, E. R. Batista, W. J. Evans, A. J. Gaunt, M. T. Janicke, S. A. Kozimor, B. L. Scott, D. H. Woen and P. Yang, *J. Am. Chem. Soc.*, 2018, **140**, 7425-7428.
48. C. Goodwin, J. Su, T. Albrecht-Schmitt, A. Blake, E. Batista, S. Daly, S. Dehnen, W. Evans, A. Gaunt, S. Kozimor, N. Lichtenberger, B. Scott and P. Yang, *Angew. Chem. Int. Ed.*, 2019, **0**.

49. S. K. Sur, *Journal of Magnetic Resonance (1969)*, 1989, **82**, 169-173.
50. M. D. Taylor, *Chem. Rev.*, 1962, **62**, 503-511.
51. D. C. Bradley, J. S. Ghotra and F. A. Hart, *J. Chem. Soc., Chem. Commun.*, 1972, DOI: 10.1039/C39720000349, 349-350.
52. D. E. Bergbreiter and J. M. Killough, *J. Am. Chem. Soc.*, 1978, **100**, 2126-2134.
53. APEX2 Version 2014.11-0, Bruker AXS, Inc., Madison, WI, 2014.
54. SAINT Version 8.34a, Bruker AXS, Inc., Madison, WI, 2013.
55. G. M. Sheldrick, SADABS, Version 2014/5, Bruker AXS, Inc., Madison, WI, 2014.
56. G. M. Sheldrick, SHELXTL, Version 2014/7, Bruker AXS, Inc., Madison, WI, 2014.
57. International Tables for Crystallography, Vol. C, Kluwer Academic Publishers, Dordrecht, 1992.
58. (a) Spek, A.L. SQUEEZE, Acta Cryst. 2015, C71, 9-19., (b) Spek, A. L. PLATON, Acta. Cryst. 2009, D65, 148-155

Chapter 3

Isolation of U(II) Compounds Using Strong Donor Ligands, C_5Me_4H and $N(SiMe_3)_2$, Including a Three-Coordinate U(II) Complex

Introduction*

The initial discoveries of crystallographically-characterizable complexes of the new +2 ions of the rare-earth metals (Introduction), and the actinides involved complexes of three silyl-substituted cyclopentadienyl ligands like $C_5H_3(SiMe_3)_2$ (Cp'')[1-5] and $C_5H_4SiMe_3$ (Cp'),[6, 7] eq 3.1.[8, 9] Complexes of +2 ions were also isolated with the tris(aryloxide) mesitylene ligand, $[(^{Ad,Me}ArO)_3mes]^{3-}$,[10-12] and with complexes containing two alkyl-substituted cyclopentadienyl ligands, $C_5H_3(CMe_3)_2$ (Cp^{tt})[13, 14] and $C_5H_2(CMe_3)_3$ (Cp^{ttt}).[15, 16]

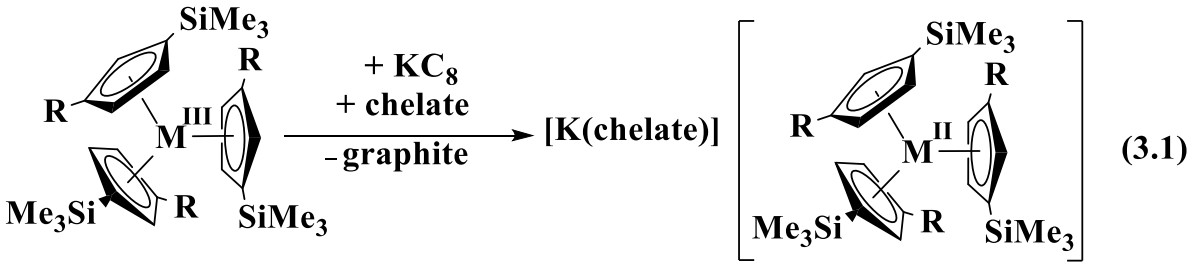

(3.1)

R = H, M = Y, La, Ce, Pr, Nd, Gd, Tb, Dy, Ho, Er, Lu, and U
R = $SiMe_3$, M = La, Ce, Pr, Th, U, Pu, and Np
chelate = 2.2.2-cryptand or 18-crown-6$(THF)_n$

A comparison of Cp'' vs Cp^{tt}, showed the more electron-donating ligand, Cp^{tt}, to be less effective in stabilizing the ions in the formal +2 oxidation state.[13, 14, 17] Consequently, it was surprising that crystallographically-characterizable rare-earth metal complexes of Ln(II) ions

* Portions of this chapter have been published: Ryan, A. J.; Angadol, M. A.; Ziller, J. W.; Evans, W. J., *Chem. Commun.* **2019,** *55* , 2325-2327.

incorporating the electron donating ligands, $N(SiMe_3)_2$[18] and C_5Me_4H,[19] were subsequently obtained. It was therefore of interest to determine if these ligands would also form isolable complexes with U(II). This would demonstrate new targets for the isolation of complexes of +2 ions of the transuranic elements, Np,[5, 20-22] Pu,[4] Am, etc. This chapter describes the synthesis and characterization of U(II) complexes utilizing Cp^{tet} ($Cp^{tet} = C_5Me_4H$) and NR_2 ($R = SiMe_3$) ligand environments.

Results and Discussion

Reaction of a green-brown solution of $Cp^{tet}{}_3U$ ($Cp^{tet} = C_5Me_4H$) in THF with a potassium smear generated a black solution from which [K(crypt)][$Cp^{tet}{}_3U$], **1**, could be isolated in 38% crystalline yield, eq 3.2. The complex was definitively identified by X-ray crystallography, Figure 3.1.

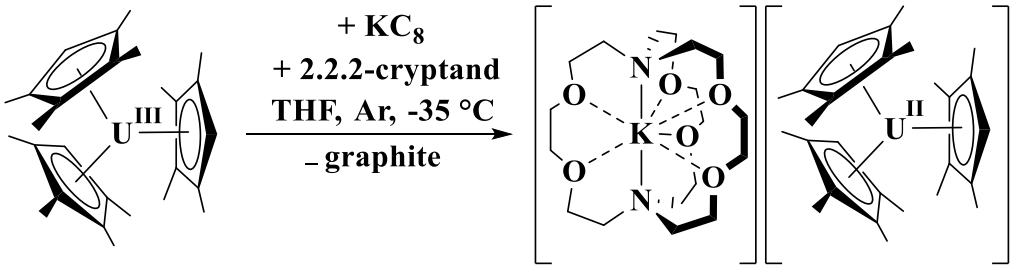

(3.2)

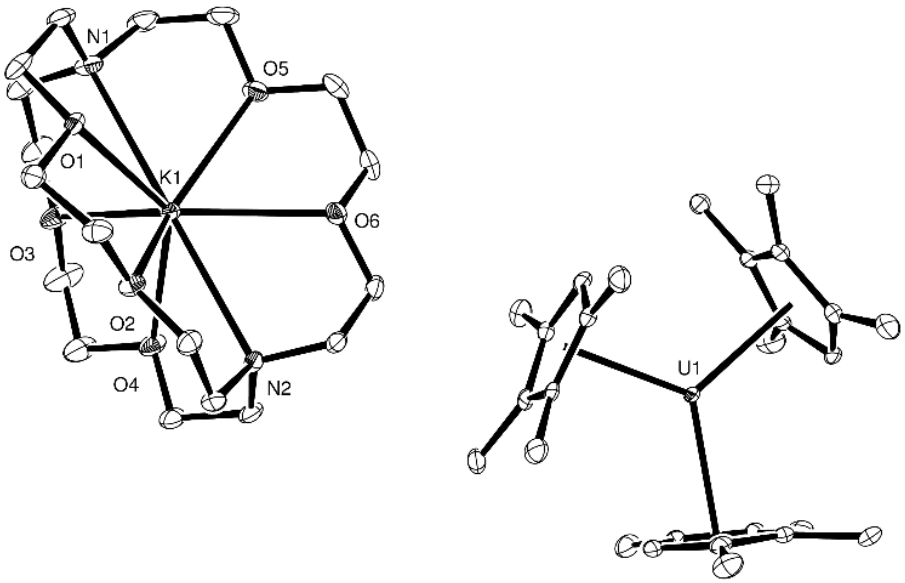

Figure 3.1. ORTEP representation of [K(crypt)][Cp^{tet}_3U], **1**, drawn at the 50% probability level. Hydrogen atoms are omitted for clarity.

Complex **1** crystallized in the *C*2/*c* space group and was isomorphous with the rare-earth complex, [K(crypt)][Cp^{tet}_3Sm].[19] The other members of the [K(crypt)][Cp^{tet}_3Ln] series crystallized in different space groups, $P2_12_12_1$ (Ln = La, Ce), $P2_1/c$ (Ln = Pr, Nd, Gd, Tb), and *R*-3*c* (Ln = Dy).[19] The 2.564 Å average U–(Cp^{tet} ring centroid) distance in **1** was closer to the 2.563 Å analog in [K(crypt)][Cp^{tet}_3Nd], than to the 2.63 Å distance in the isomorphous [K(crypt)][Cp^{tet}_3Sm]. The ionic radius of uranium is usually considered to be in between those of La and Ce based on Shannon ionic radii for +3 ions, the lowest oxidation state available in the Shannon compilation.[23] Only the six-coordinate radius is published for U(III), 1.025 Å.[23] In comparison, the six coordinate radii for La(III), Ce(III), and Nd(III) are 1.032, 1.01, and 0.983 Å, respectively.[23] The metrical data for **1** raise the possibility that the lanthanide of closest size to uranium in the +2 ion series is not the same as in other oxidation states.

The 2.564 Å average U–(Cp^{tet} ring centroid) distance in **1** is 0.041 Å larger than that of Cp^{tet}_3U.[24] This difference is similar to the 0.045–0.058 Å differences observed between the $4f^n5d^1$ [K(crypt)][Cp^{tet}_3Ln] complexes and Cp^{tet}_3Ln for Ln = La, Ce, Pr, Nd, Gd, and Tb. The 0.041 Å difference is smaller than the 0.147 and 0.099 Å differences for Ln = Sm and Dy, respectively, which have $4f^{n+1}$ configurations for the Ln(II) ions.[19] The small increase in size for **1** is consistent with a $5f^36d^1$ electron configuration[8, 9] as was found for [K(crypt)][Cp'_3U].[7]

The UV-visible spectrum of **1** was compared with those of [K(crypt)][Cp'_3U][7] [λ_{max}, nm (ε, $M^{-1}cm^{-1}$) 306(6200), 412(5000)] and [K(crypt)][Cp''_3U][25] [315(7500), 470(6000)] in Figure 2. The spectrum of **1** contained broadened absorption bands with less intensity and an absorption at lower energy, [λ_{max} = 790 nm with ε = 1800 $M^{-1}cm^{-1}$) that was not present in the spectra of the other U(II) complexes. The spectra of the [K(crypt)][Cp^{tet}_3Ln] complexes differed similarly compared to the [K(crypt)][Cp'_3Ln] complexes.[19] In contrast, the $5f^4$ complex, [K(crypt)][(($^{Ad,Me}ArO)_3mes$)U],[10] had a single absorption at λ_{max} = 400 with ε = 750 $M^{-1}cm^{-1}$. Complex **1** was stable at −35 °C for weeks, but its dark color persisted for only 4-5 h at room temperature. It therefore has intermediate stability compared to [K(crypt)][Cp'_3U][7] and [K(crypt)][Cp''_3U],[25] which had half-lives of 1.5 and 20 h, respectively, at room temperature in THF.

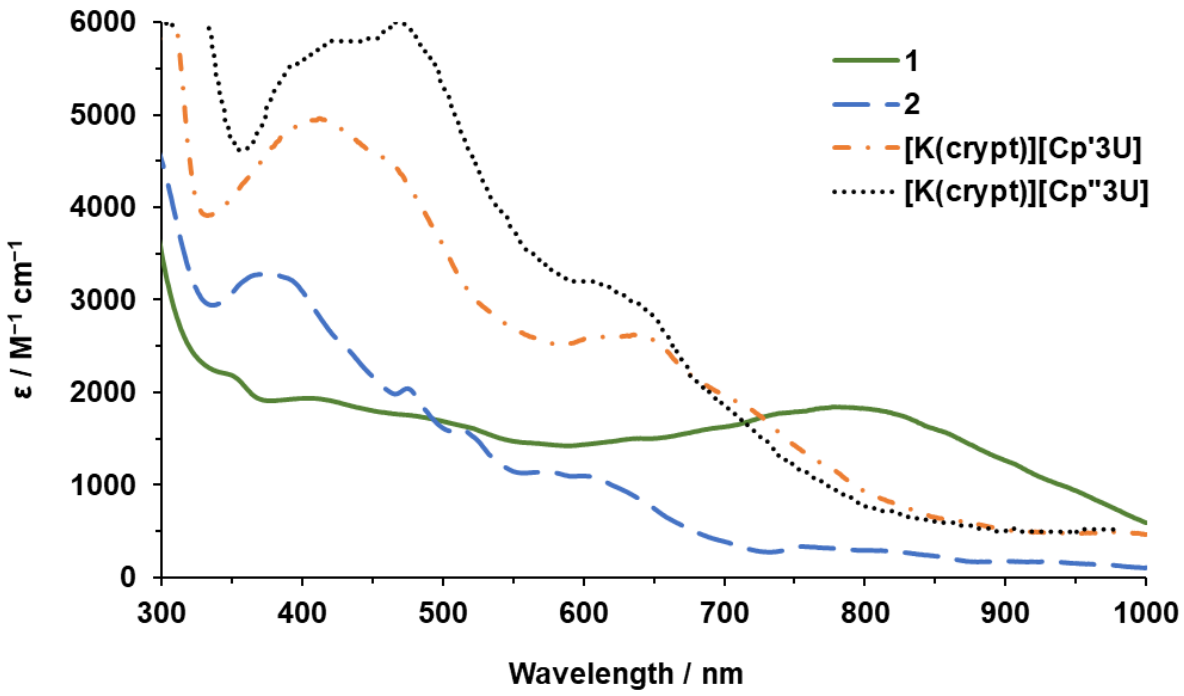

Figure 3.2. Experimental UV-Vis spectra of **1**,**2**, [K(crypt)][Cp′$_3$U],[7] and [K(crypt)][Cp″$_3$U][25] in THF at 293 K.

Reaction of a dark purple solution of U(NR$_2$)$_3$ (R = SiMe$_3$) with potassium graphite in the presence of crypt caused a color change to black. Crystals of [K(crypt)][U(NR$_2$)$_3$], **2**, were isolated in 47% yield and identified by X-ray crystallography, eq 3.3, Figure 3.3. Complex **2** crystallizes in the *R*32 space group and is not isomorphous with any [K(crypt)][Ln(NR$_2$)$_3$] complexes (Ln = Gd, Tb, Dy) or [Rb(crypt)][Ln(NR$_2$)$_3$] (Ln = Er, Ho, Tm) which crystallize in the *P*-1 space group and are all isomorphous with each other.[18] Complex **2** crystallizes with disorder in the position of the uranium atom above and below the N$_3$ plane similar to that observed in the [M(crypt)][Ln(NR$_2$)$_3$] analogs, Figure 3.4.[18]

The 2.373 Å average U–N distance in **2** is 0.052 Å longer than that in the U(III) analog, U(NR$_2$)$_3$, [26] 2.320 Å, which is consistent with a 5f^{3}6d^1 electron configuration.[8, 9] Complex **2** has a

pyramidal structure with the metal 0.411 Å above the plane of the three nitrogen donors. This is similar to the structure of $U(NR_2)_3$ in which the metal is 0.456 Å above the N_3 donor atom plane.[26] The U(II) and U(III) amides are also similar in that the closest approach of a methyl carbon of the ligands to uranium in **2** is 3.029 Å for C(2). In comparison, the smallest U…C(Me) in $U(NR_2)_3$ is 3.046 Å.[26]

The UV-visible spectrum of **2**, Figure 3.2, shows multiple features on an absorption starting in the near IR region including peaks with λ_{max}, nm (ε, $M^{-1}cm^{-1}$) of 290 (4300), 380 (3700), and 600 nm (1100). In contrast, the $[Ln(NR_2)_3]^{1-}$ (Ln = Gd, Tb, Dy) anions display a single peak at 597-607 nm with ε = 1100–3500 $M^{-1}cm^{-1}$.[18] The differences between the spectra of **1** and **2** are similar to the differences observed in the Ln(II) complexes utilizing NR_2 and Cp^{tet} ligands.[18,19] The complicated nature of the spectra apparently arises from multiple absorptions of varying intensity depending on the specific system. As a result, the data may serve more as fingerprint than an indicator of electronic structure.= . Compound **2** is stable for 2-4 hours at room temperature in THF.

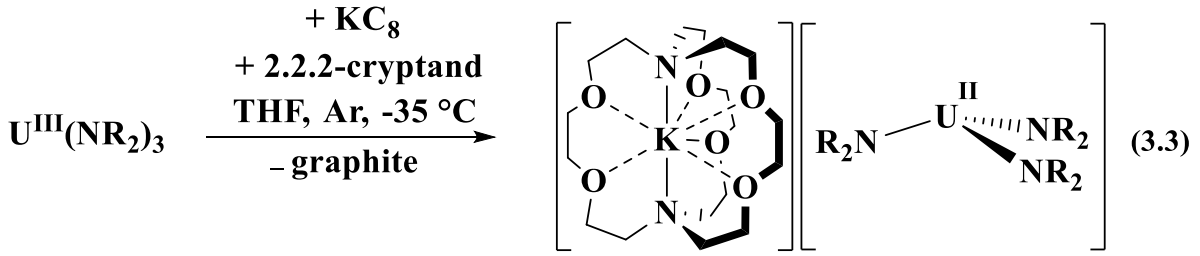

(3.3)

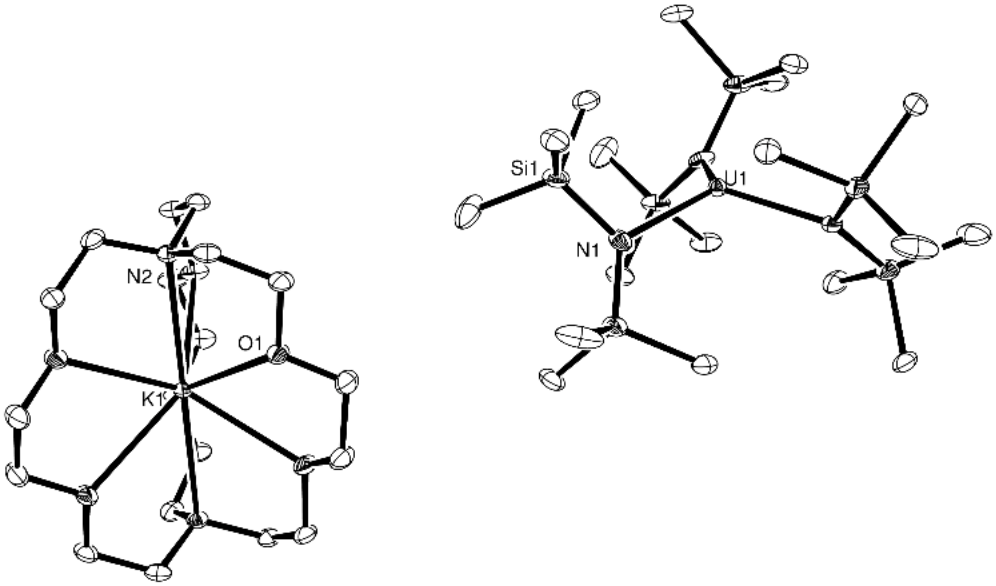

Figure 3.3. Thermal ellipsoids plot of [K(crypt)][U(NR_2)$_3$], **2**, drawn at the 50% probability level. Hydrogen atoms, disordered methyl groups, and the disorder in the uranium position are omitted for clarity.

Conclusions

In summary, crystallographically-characterizable complexes of +2 actinide ions are not limited to only $(Cp'_3)^{3-}$, $(Cp''_3)^{3-}$, and $[(^{Ad,Me}ArO)_3mes]^{3-}$ ligand sets: the electron-donating ligand sets $(Cp^{tet}_3)^{3-}$ and $[(NR_2)_3]^{3-}$ also form isolable complexes of U(II). The large size of the Cp^{tet} ligand leads to a longer U–(Cp^{tet} ring centroid) average distance, 2.564 Å, compared to the 2.521 Å U–(Cp′ ring centroid) analog in [K(crypt)][Cp'_3U].[7] This can counteract the electron donating nature of the tetramethyl-substitution pattern as discussed previously for the [K(crypt)][Cp^{tet}_3Ln] complexes.[19] However, in the three coordinate **2**, no analogous crowding is evident and it is clear that ligands with strong field donor atoms can form U(II) complexes.

Experimental Details

All manipulations and syntheses described below were conducted with the rigorous exclusion of air and water using standard Schlenk line and glovebox techniques under an argon atmosphere. Solvents were sparged with UHP argon and dried by passage through columns containing Q-5 and molecular sieves prior to use. IR samples were prepared as KBr pellets or thin films, and the spectra were obtained on a Jasco FT/IR-4700 - ATR-PRO ONE system or a Thermo Scientific Nicolet iS5 spectrophotometer with an iD5 ATR attachment. Elemental analyses were performed on a Perkin-Elmer 2400 Series II CHNS elemental analyzer. UV−vis spectra were collected in THF at 298 K using a Varian Cary 60 Scan UV−vis spectrophotometer. Potassium metal (Aldrich) was used as received. KC_8,[27] Cp^{tet}_3U[28] and $U(NR_2)_3$[29] were prepared according to literature procedures. 2.2.2-Cryptand (4,7,13,16,21,24-hexaoxa-1,10-diazabicyclo[8.8.8]hexacosane, Aldrich) was placed under vacuum (10^{-4} Torr) for 12 h before use.

[K(2.2.2-cryptand)][Cp^{tet}_3U], 1. In an argon-filled glovebox, Cp^{tet}_3U (73 mg, 0.121 mmol) and 2.2.2-cryptand (46 mg, 0.122 mmol) were dissolved in THF (2 mL) and chilled to −35 °C in the glovebox freezer. The brown solution was added to a chilled scintillation vial containing a K smear and stored at −35 °C overnight. The resultant dark black/brown solution was layered with chilled hexanes (5 mL) and stored at −35 °C for 3 days to yield **1** as black single-crystals suitable for X-ray diffraction. The mother liquor was decanted, and the crystalline solids were washed three times with 3 mL of Et_2O and dried under vacuum (3 min) to yield **1** (47 mg, 38%). IR: 2959m, 2923s, 2885s, 2853s, 1477m, 1457m, 1445m, 1354m, 1326m, 1297m, 1259m, 1238m, 1173m, 1134m, 1108s, 1080m, 951m, 933m, 833m, 822m, 753m, 741m, 709m, 697m. Anal. Calcd. for $C_{45}H_{75}N_2O_6KU$: C, 53.13; H, 7.43; N, 2.75. Found: C, 52.38; H, 7.28; N, 2.82. UV-Vis (THF) λ_{max}, nm (ε, M^{-1} cm^{-1}): 350 (2100 shoulder), 410 (1900), 790 (1800). Due to the high

reactivity and paramagnetism of **1**, it was difficult to make assignments for the resonances observed in the NMR spectra of **1** even at low temperature

[K(crypt)][U(NR$_2$)$_3$], 2. In an argon-filled glovebox, U(NR$_2$)$_3$ was combined with 2.2.2-cryptand in THF (2 mL) and cooled to −35 °C in the glovebox freezer. The cold purple solution was added to a vial containing KC_8 that had also been cooled to −35 °C and the mixture was allowed to sit for 1 min in the glovebox freezer. The solution was filtered through a pipette fitted with a glass wool filter and layered with cold hexanes before it was stored in the freezer. After 48 h, black crystals were obtained (44 mg, 47% yield). IR: 2814m, 2853w, 1477m, 1458w, 1445m, 1360m, 1354m, 1299m, 1259m, 1238m, 1234s, 1176w, 1134m, 1104s, 1079m, 1000s, 949s, 933w, 865s, 821s, 766m, 752m, 707w, 694w, 662s. Anal. Calcd. for $C_{36}H_{90}N_5O_6Si_6KU$: C, 38.10; H, 7.99; N, 6.17. Found: C, 38.45; H, 8.31; N, 6.69. UV-Vis (THF) λ_{max}, nm (ε, M^{-1} cm^{-1}): 380 (3250), 470 (2000), 515 (1580), 570 (1130), 608 (1080 shoulder), 755 (330). Due to the high reactivity and paramagnetism of **2**, it was difficult to make assignments for the resonances observed in the NMR spectra of **2** even at low temperature

X-ray Data Collection, Structure Solution and Refinement for 1.

A black crystal of approximate dimensions 0.141 x 0.195 x 0.345 mm was mounted in a cryoloop and transferred to a Bruker SMART APEX II diffractometer. The APEX2[30] program package was used to determine the unit-cell parameters and for data collection (30 sec/frame scan time for a sphere of diffraction data). The raw frame data was processed using SAINT[31] and SADABS[32] to yield the reflection data file. Subsequent calculations were carried out using the SHELXTL[33] program. The diffraction symmetry was 2/*m* and the systematic absences were

consistent with the monoclinic space groups *Cc* and *C*2/*c*. It was later determined that space group *C*2/*c* was correct.

The structure was solved by dual space methods and refined on F^2 by full-matrix least-squares techniques. The analytical scattering factors[34] for neutral atoms were used throughout the analysis. Hydrogen atoms were included using a riding model. There was one molecule of tetrahydrofuran solvent present.

Least-squares analysis yielded wR2 = 0.0864 and Goof = 1.009 for 528 variables refined against 12621 data (0.78 Å), R1 = 0.0362 for those 9615 data with $I > 2.0\sigma(I)$.

There were high residuals present in the final difference-Fourier map. It was not possible to determine the nature of the residuals although it was probable that additional tetrahydrofuran solvent was present. The SQUEEZE[35a] routine in the PLATON[35b] program package was used to account for the electrons in the solvent accessible voids.

Definitions:

$wR2 = [\Sigma[w(F_o^2-F_c^2)^2] / \Sigma[w(F_o^2)^2]]^{1/2}$

$R1 = \Sigma||F_o|-|F_c|| / \Sigma|F_o|$

$Goof = S = [\Sigma[w(F_o^2-F_c^2)^2] / (n-p)]^{1/2}$ where n is the number of reflections and p is the total number of parameters refined.

Table 3.1. Crystal data and structure refinement for **1**.

Identification code	maa7 (Mary Angadol)
Empirical formula	$C_{45}\ H_{75}\ K\ N_2\ O_6\ U \bullet C_4H_8O$
Formula weight	1089.30
Temperature	133(2) K
Wavelength	0.71073 Å

Crystal system	Monoclinic	
Space group	*C*2/*c*	
Unit cell dimensions	a = 30.199(5) Å	a= 90°.
	b = 13.568(2) Å	b= 114.7838(17)°.
	c = 30.609(7) Å	g = 90°.
Volume	11387(4) Å3	
Z	8	
Density (calculated)	1.271 Mg/m3	
Absorption coefficient	2.967 mm-1	
F(000) 4464		
Crystal color black		
Crystal size	0.345 x 0.195 x 0.141 mm3	
Theta range for data collection	1.466 to 27.174°	
Index ranges	$-38 \leq h \leq 38$, $-17 \leq k \leq 17$, $-39 \leq l \leq 39$	
Reflections collected 64077		
Independent reflections	12621 [R(int) = 0.0621]	
Completeness to theta = 25.500°	99.9 %	
Absorption correction Semi-empirical from equivalents		
Max. and min. transmission	0.7455 and 0.5981	
Refinement method Full-matrix least-squares on F2		
Data / restraints / parameters	12621 / 0 / 528	
Goodness-of-fit on F2	1.009	
Final R indices [I>2sigma(I) = 9615 data]	R1 = 0.0362, wR2 = 0.0795	

R indices (all data, 0.78 Å)	R1 = 0.0582, wR2 = 0.0864
Largest diff. peak and hole	1.941 and -0.935 e.Å^{-3}

Table 3.2. Bond lengths [Å] and angles [°] for **1**.

U(1)-Cnt1	2.566
U(1)-Cnt2	2.563
U(1)-Cnt3	2.564
Cnt1-U(1)-Cnt2	120.0
Cnt1-U(1)-Cnt3	119.8
Cnt2-U(1)-Cnt3	120.1

X-ray Data Collection, Structure Solution and Refinement for 2.

A black crystal of approximate dimensions 0.214 x 0.318 x 0.389 mm was mounted in a cryoloop and transferred to a Bruker SMART APEX II diffractometer. The APEX2[30] program package was used to determine the unit-cell parameters and for data collection (60 sec/frame scan time for a sphere of diffraction data). The raw frame data was processed using SAINT[31] and SADABS[32] to yield the reflection data file. Subsequent calculations were carried out using the SHELXTL[33] program. The systematic absences were consistent with the hexagonal space group *R*32. The trigonal space group *R*32 was assigned and later determined to be correct.

The structure was solved by dual space methods and refined on F^2 by full-matrix least-squares techniques. The analytical scattering factors[34] for neutral atoms were used throughout the

analysis. Hydrogen atoms were included using a riding model. Several atoms were disordered and included with partial site-occupancy-factors.

Least-squares analysis yielded wR2 = 0.0590 and Goof = 1.049 for 110 variables refined against 2443 data (0.80 Å), R1 = 0.0238 for those 2317 data with $I > 2.0\sigma(I)$.

There were several high residuals present in the final difference-Fourier map. It was not possible to determine the nature of the residuals although it was probable that THF solvent was present. The SQUEEZE[35a] routine in the PLATON[35b] program package was used to account for the electrons in the solvent accessible voids.

Table 3.3. Crystal data and structure refinement for **2**.

Identification code	ajr4 (Austin Ryan)	
Empirical formula	C_{36} H_{90} K N_5 O_6 Si_6 U	
Formula weight	1134.79	
Temperature	88(2) K	
Wavelength	0.71073 Å	
Crystal system	Trigonal	
Space group	*R*32	
Unit cell dimensions	a = 18.4169(17) Å	a= 90°.
	b = 18.4169(17) Å	b= 90°.
	c = 18.1996(17) Å	g = 120°.
Volume	5346.0(11) Å3	
Z	3	
Density (calculated)	1.057 Mg/m3	

Absorption coefficient	2.468 mm-1
F(000)	1752
Crystal color	Black
Crystal size	0.389 x 0.318 x 0.214 mm3
Theta range for data collection	1.698 to 26.384°
Index ranges	$-22 \leq h \leq 22$, $-22 \leq k \leq 22$, $-22 \leq l \leq 22$
Reflections collected	19702
Independent reflections	2443 [R(int) = 0.0373]
Completeness to theta = 25.500°	99.9 %
Absorption correction	Semi-empirical from equivalents
Max. and min. transmission	0.4296 and 0.3334
Refinement method	Full-matrix least-squares on F2
Data / restraints / parameters	2443 / 0 / 110
Goodness-of-fit on F2	1.049
Final R indices [I>2sigma(I) = 2317 data]	R1 = 0.0238, wR2 = 0.0583
R indices (all data, 0.80 Å)	R1 = 0.0266, wR2 = 0.0590
Absolute structure parameter	0.008(7)
Largest diff. peak and hole	1.078 and -0.449 e.Å-3

Table 3.4. Bond lengths [Å] and angles [°] for **2**.

U(1)-U(1)#1	0.8226(6)
U(1)-N(1)	2.372(4)

U(1)-N(1)#2 2.372(4)

U(1)-N(1)#3 2.372(4)

Si(1)-U(1)#1 3.3641(11)

N(1)-Si(1)#4 1.709(2)

N(1)-U(1)#1 2.372(4)

N(1)-U(1)-N(1)#2 117.060(11)

N(1)-U(1)-N(1)#3 117.060(12)

N(1)#2-U(1)-N(1)#3 117.060(11)

Symmetry transformations used to generate equivalent atoms:

#1 y,x,-z+1 #2 -y+2,x-y+1,z #3 -x+y+1,-x+2,z

#4 -x+2,-x+y+1,-z+1 #5 x-y+1,-y+2,-z+1 #6 -x+4/3,-x+y+2/3,-z+2/3

#7 -x+y+1,-x+1,z #8 y+1/3,x-1/3,-z+2/3 #9 -y+1,x-y,z

#10 x-y+1/3,-y+2/3,-z+2/3

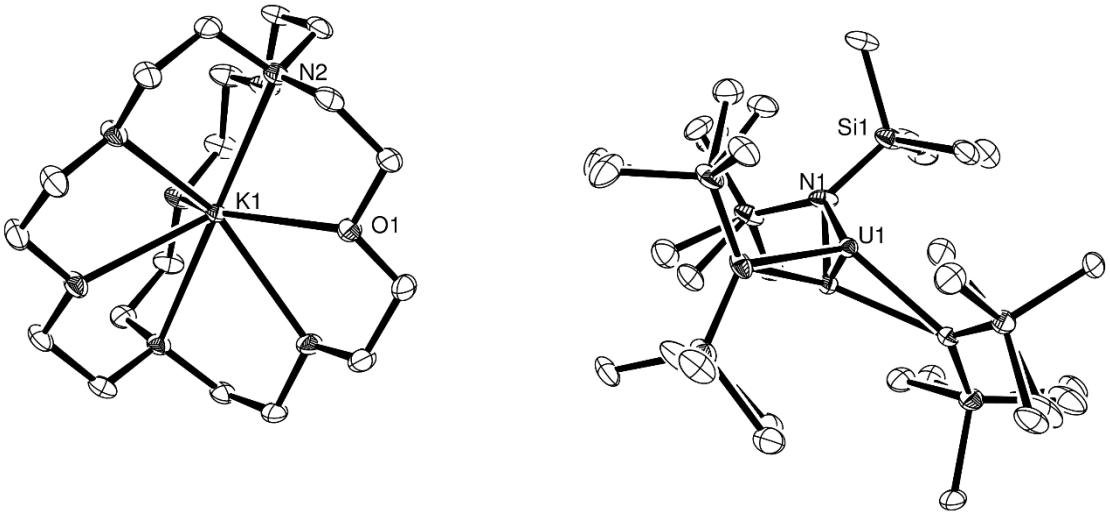

Figure 3.4. ORTEP representation of **2** with ellipsoids drawn at the 50% probability level. Hydrogen atoms omitted for clarity.

References

1. P. B. Hitchcock, M. F. Lappert, L. Maron and A. V. Protchenko, *Angew. Chem. Int. Ed.*, 2008, **47**, 1488-1491.
2. R. R. Langeslay, M. E. Fieser, J. W. Ziller, F. Furche and W. J. Evans, *Chem. Sci.*, 2015, **6**, 517-521.
3. C. J. Windorff, M. R. MacDonald, K. R. Meihaus, J. W. Ziller, J. R. Long and W. J. Evans, *Chem. Eur. J.*, 2016, **22**, 772-782.
4. C. J. Windorff, G. P. Chen, J. N. Cross, W. J. Evans, F. Furche, A. J. Gaunt, M. T. Janicke, S. A. Kozimor and B. L. Scott, *J. Am. Chem. Soc.*, 2017, **139**, 3970-3973.
5. J. Su, C. J. Windorff, E. R. Batista, W. J. Evans, A. J. Gaunt, M. T. Janicke, S. A. Kozimor, B. L. Scott, D. H. Woen and P. Yang, *J. Am. Chem. Soc.*, 2018.
6. M. R. MacDonald, J. E. Bates, J. W. Ziller, F. Furche and W. J. Evans, *J. Am. Chem. Soc.*, 2013, **135**, 9857-9868.
7. M. R. MacDonald, M. E. Fieser, J. E. Bates, J. W. Ziller, F. Furche and W. J. Evans, *J. Am. Chem. Soc.*, 2013, **135**, 13310-13313.
8. D. H. Woen and W. J. Evans, *Handbook on the Physics and Chemistry of Rare Earths*, 2016, **50**, 337-394.
9. W. J. Evans, *Organometallics*, 2016, **35**, 3088-3100.
10. H. S. La Pierre, A. Scheurer, F. W. Heinemann, W. Hieringer and K. Meyer, *Angew. Chem. Int. Ed.*, 2014, **53**, 7158-7162.
11. M. E. Fieser, C. T. Palumbo, H. S. La Pierre, D. P. Halter, V. K. Voora, J. W. Ziller, F. Furche, K. Meyer and W. J. Evans, *Chemical science*, 2017, **8**, 7424-7433.
12. C. T. Palumbo, D. P. Halter, V. K. Voora, G. P. Chen, A. K. Chan, M. E. Fieser, J. W. Ziller, W. Hieringer, F. Furche and K. Meyer, *Inorg. Chem.*, 2018, **57**, 2823-2833.
13. Y. K. Gun'ko, P. B. Hitchcock and M. F. Lappert, *J. Organomet. Chem.*, 1995, **499**, 213-219.
14. M. C. Cassani, D. J. Duncalf and M. F. Lappert, *J. Am. Chem. Soc.*, 1998, **120**, 12958-12959.
15. F. Jaroschik, F. Nief, X.-F. Le Goff and L. Ricard, *Organometallics*, 2007, **26**, 1123-1125.
16. F. Jaroschik, A. Momin, F. Nief, X.-F. Le Goff, G. B. Deacon and P. C. Junk, *Angew. Chem.*, 2009, **121**, 1137-1141.
17. C. E. Zachmanoglou, A. Docrat, B. M. Bridgewater, G. Parkin, C. G. Brandow, J. E. Bercaw, C. N. Jardine, M. Lyall, J. C. Green and J. B. Keister, *J. Am. Chem. Soc.*, 2002, **124**, 9525-9546.
18. A. J. Ryan, L. E. Darago, S. G. Balasubramani, G. P. Chen, J. W. Ziller, F. Furche, J. R. Long and W. J. Evans, *Chem. Eur. J.*, 2018, **24**, 7702-7709.
19. T. F. Jenkins, D. H. Woen, L. N. Mohanam, J. W. Ziller, F. Furche and W. J. Evans, *Organometallics*, 2018, DOI: 10.1021/acs.organomet.8b00557.
20. P. L. Arnold, M. S. Dutkiewicz and O. Walter, *Chem. Rev.*, 2017, **117**, 11460-11475.
21. M. S. Dutkiewicz, C. Apostolidis, O. Walter and P. L. Arnold, *Chem. Sci.*, 2017, **8**, 2553-2561.
22. M. S. Dutkiewicz, J. H. Farnaby, C. Apostolidis, E. Colineau, O. Walter, N. Magnani, M. G. Gardiner, J. B. Love, N. Kaltsoyannis and R. Caciuffo, *Nature chemistry*, 2016, **8**, 797-802.

23. R. Shannon, *Acta Cryst. A*, 1976, **32**, 751-767.
24. M. del Mar Conejo, J. S. Parry, E. Carmona, M. Schultz, J. G. Brennann, S. M. Beshouri, R. A. Andersen, R. D. Rogers, S. Coles and M. B. Hursthouse, *Chem. Eur. J.*, 1999, **5**, 3000-3009.
25. C. J. Windorff, M. R. MacDonald, K. R. Meihaus, J. W. Ziller, J. R. Long and W. J. Evans, *Chem. Eur. J.*, 2016, **22**, 772-782.
26. J. L. Stewart and R. A. Andersen, *Polyhedron*, 1998, **17**, 953-958.
27. D. E. Bergbreiter and J. M. Killough, J. Am. Chem. Soc., 1978, 100, 2126-2134.
28. W. J. Evans, S. A. Kozimor, J. W. Ziller, A. A. Fagin and M. N. Bochkarev, Inorg. Chem., 2005, 44, 3993-4000.
29. R. A. Andersen, Inorg. Chem., 1979, 18, 1507-1509.
30. APEX2 Version 2014.11-0, Bruker AXS, Inc.; Madison, WI 2014.
31. SAINT Version 8.34a, Bruker AXS, Inc.; Madison, WI 2013.
32. Sheldrick, G. M. SADABS, Version 2014/5, Bruker AXS, Inc.; Madison, WI 2014.
33. Sheldrick, G. M. SHELXTL, Version 2014/7, Bruker AXS, Inc.; Madison, WI 2014.
34. International Tables for Crystallography 1992, Vol. C., Dordrecht: Kluwer Academic Publishers.
35. (a) Spek, A.L. SQUEEZE, Acta Cryst. 2015, C71, 9-19., (b) Spek, A. L. PLATON, Acta. Cryst. 2009, D65, 148-155.

Chapter 4

Formation of the End-on Bound Lanthanide Dinitrogen Complexes, $[(R_2N)_3Ln{-}N{=}N{-}Ln(NR_2)_3]^{2-}$, from Divalent $[(R_2N)_3Ln]^{1-}$ Salts (R = $SiMe_3$)

Introduction*

The first reduced-dinitrogen complex containing a rare-earth metal, $[(C_5Me_5)_2Sm]_2[\mu\text{-}\eta^2{:}\eta^2\text{-}N_2]$, was reported in 1988, eq 4.1, and had a planar side-on η^2-N_2 binding mode that had

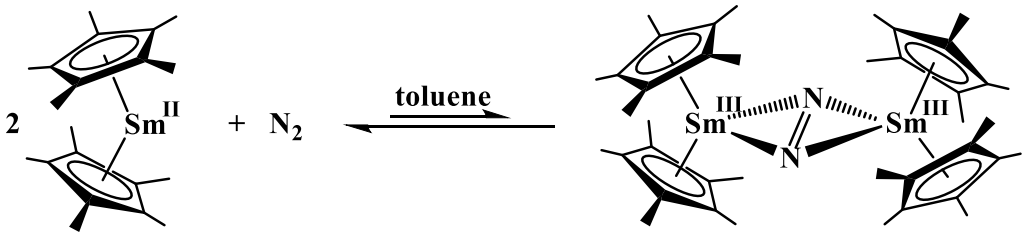

(4.1)

never been seen before in M_2N_2 dinitrogen complexes involving any metal.[1] After that initial discovery, dozens of Ln_2N_2 (Ln = rare-earth metal, i.e. Sc, Y, and lanthanides) complexes were isolated and *all of the lanthanide* compounds displayed side-on $\mu\text{-}\eta^2{:}\eta^2\text{-}N_2$ bonding, eq 4.2.[2-18]

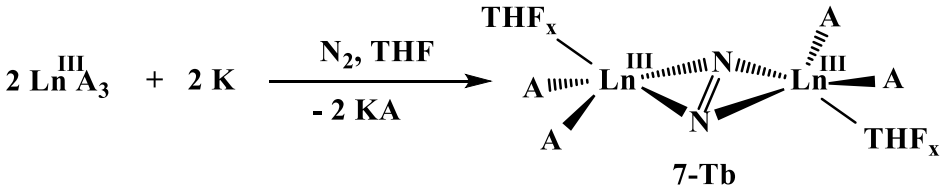

7-Tb

(4.2)

Ln = Sc, Y, La, Ce, Pr, Nd, Gd, Tb, Dy, Ho, Er, Tm, Lu
A = $N(SiMe_3)_2$, $OC_6H_3{}^tBu_2$-2,6, C_5Me_5, C_5Me_4H, $C_5H_4SiMe_3$
x = 1, 2

The general formula of these $(N{=}N)^{2-}$ complexes is $[A_2(THF)_xLn^{III}]_2[\mu\text{-}\eta^2{:}\eta^2\text{-}N_2]$ (x = 1, 2) where A is an anion, i.e. these are neutral complexes of Ln(III) ions with two anionic ligands on the metal

* Portions of this chapter were submitted for publication at the Journal of the American Chemical Sociaety

in addition to the side-on bound $(N{=}N)^{2-}$ bridge. Bimetallic lanthanide complexes of the radical trianion $(N_2)^{3-}$ [19] and the radical dianion $(NO)^{2-}$ [20] were also isolated with this planar side-on bonding mode, Figure 4.1.

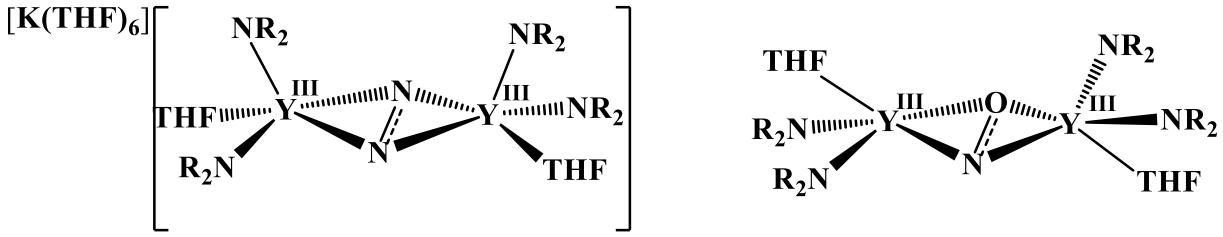

Figure 4.1. Side-on binding mode of the first $(N_2)^{3-}$ and $(NO)^{2-}$ complexes.[19 20]

Hence, it was surprising that the Sc(II) amide complex, $[Sc^{II}(NR_2)_3]^{1-}$, reacted with N_2 to make an end-on reduced dinitrogen complex, $[K(crypt)]_2\{[(R_2N)_3Sc]_2[\mu\text{-}\eta^1\text{:}\eta^1\text{-}N_2]\}$ (crypt = 2.2.2-cryptand), eq 4.3. [21] Generally, if Sc displays chemistry different from the other rare- earths, it is rationalized by the fact that scandium is much smaller. Based on the ionic radius, Sc would be 23rd in the series by size following the 0.013 Å average decrease from one lanthanide to the next. However, this scandium complex differed from the examples in eq 4.2 in that it retained all three $(NR_2)^{1-}$ ligands. If steric crowding were an issue, it might be expected that a complex with two anionic amide ligands per metal would be found as in eq 4.2.

Once $[K(crypt)]_2\{[(R_2N)_3Sc]_2[\mu\text{-}\eta^1\text{:}\eta^1\text{-}N_2]\}$ was identified, it was of interest to determine if end-on dinitrogen complexes of other rare earth metals could be made from Ln(II) precursors as shown in eq 4.3. Normally, yttrium, the congener of Sc, would be examined next since the Y(III) product would be diamagnetic. However, isolation of the Y(II) precursor, $[Y^{II}(NR_2)_3]^{1-}$, proven to be much more difficult than isolation of $[Sc^{II}(NR_2)_3]^{1-}$.[22] However, $[Ln(NR_2)_3]^{1-}$ complexes of the late lanthanides, Ln = Gd, Tb, Dy, Ho, and Er, were available (Chapters 1 and 2).[23] This was

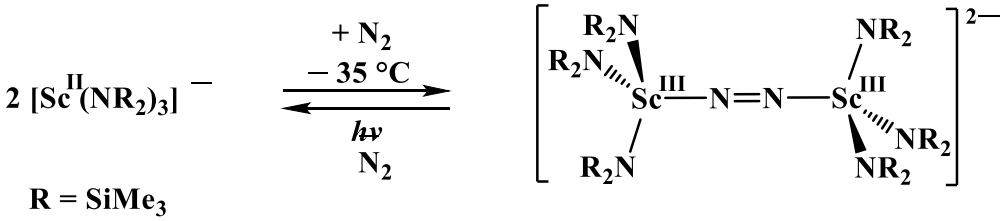

(4.3)

surprising, since traditionally, Y(III) has been a good model for trivalent lanthanides of similar size, i.e. Ho(III) and Er(III). However, the data suggested that Y(II) may not be analogous to either Sc(II) or the late lanthanide +2 ions.[23-25]

To further explore the unusual chemistry in eq 4.3, dinitrogen reduction chemistry using $[Ln(NR_2)_3]^{1-}$ complexes of the late lanthanides was examined. The two most stable members of this series, Ln = Gd and Tb,[22, 23] were chosen. Described in this chapter are the results that they also can form end-on dinitrogen complexes with three amides per metal like scandium. These are the first reduced dinitrogen complexes of lanthanides that feature end-on binding modes of the N_2 units. In addition, these reactions can also form dianionic side-on complexes with three amides per metal in single crystals containing both end-on and side-on bound dinitrogen ligands. The new $\{[(R_2N)_3Ln]_2[\mu\text{-}\eta^x\text{:}\eta^x\text{-}N_2]\}^{2-}$ dianions are potent reductants and can revert back to the highly reactive Tb(II) and Gd(II) complexes, $[Ln^{II}(NR_2)_3]^{1-}$, a reaction not observed for other $(N=N)^{2-}$ complexes of Tb and Gd.

This reaction chemistry is highly dependent on specific reaction conditions including solvent, temperature, and the specific lanthanide involved. Reactions of complexes with crypt chelated potassium counter-cations are described as well as compounds with 18-crown-6 (18-c-6) as the chelating agent.

Results

A Pure End-On Ln-N=N-Ln Complex. When crystalline samples of dark blue [K(crypt)][Tb(NR_2)$_3$], **1-Tb**, originally prepared in an argon-containing glovebox, are dissolved in Et_2O pre-chilled to −35 °C in a nitrogen-containing glovebox, the dark color disappears within five minutes as the solvent is swirled in the vial. After the resulting yellow solution is kept at −35°C overnight, single crystals of [K(crypt)]$_2${[(R_2N)$_3$Tb]$_2$[μ-η^1:η^1-N_2]}, **2-Tb**, can be isolated, eq 4.4. The reaction appears to proceed even faster at −78 °C.

X-ray crystallography revealed that the reduced dinitrogen unit in **2-Tb** is bound end-on as shown in Figure 4.2. Previously, all crystallographically-characterized Ln_2N_2 complexes of the lanthanide metals have had side-on bound structures.[2-13] Only with scandium, eq 4.3, was an end-on structure found.[21]

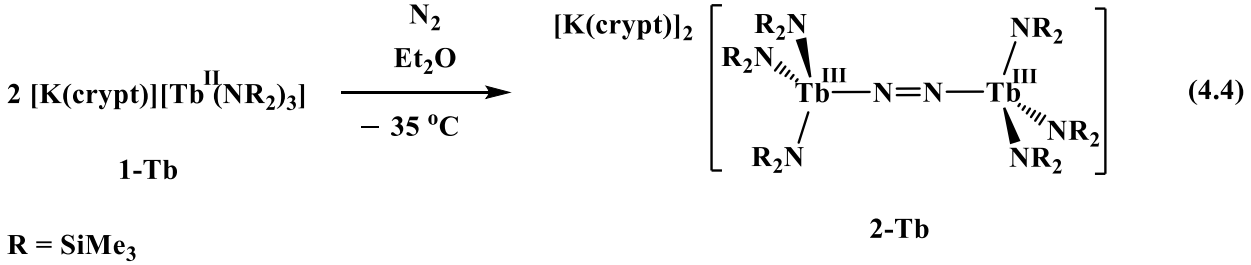

(4.4)

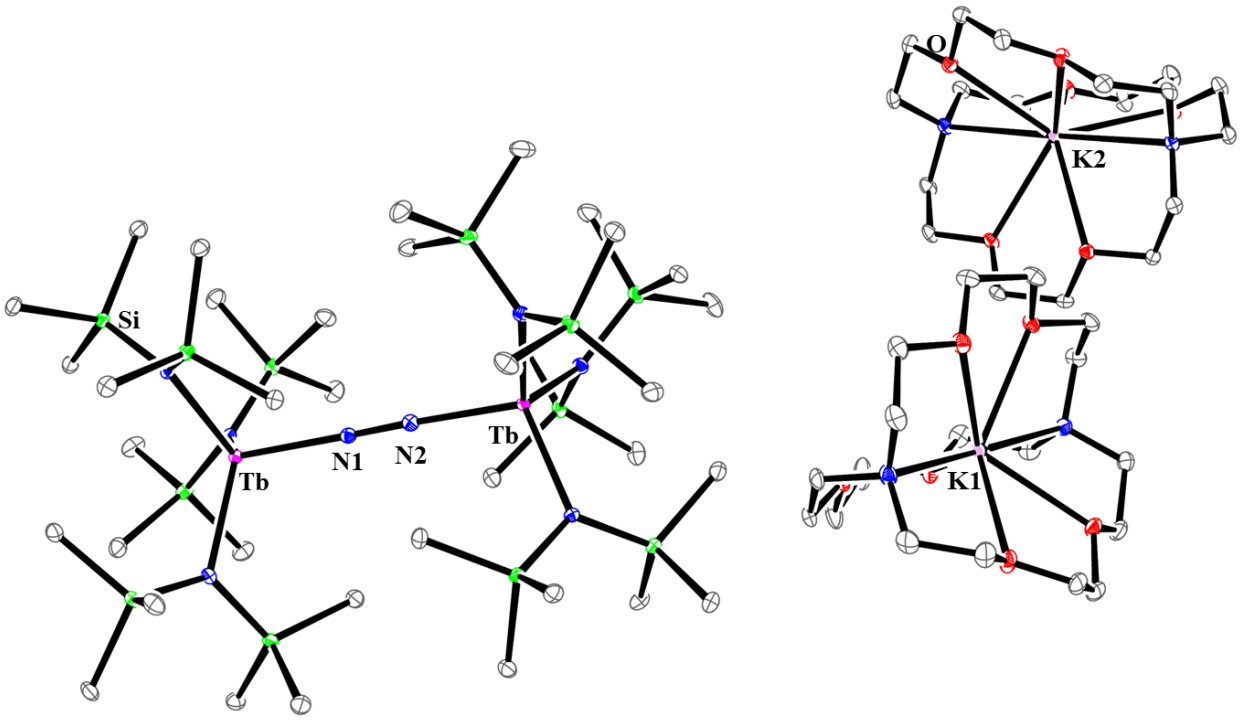

Figure 4.2. ORTEP representation of **2-Tb** drawn at the 50% probability level. Hydrogen atoms and Et_2O molecules have been excluded for clarity.

The 1.217(3) Å N−N bond length in **2-Tb** is within error of the 1.221(3) Å value in $[K(crypt)]_2\{[(R_2N)_3Sc]_2[\mu\text{-}\eta^1\text{:}\eta^1\text{-}N_2]\}$, **2-Sc**,[21] and is consistent with a double bond, i.e. $(N{=}N)^{2-}$.[26] This value is slightly smaller than the $(N{=}N)^{2-}$ distance of 1.271(4) Å measured in the side-on bound $[(R_2N)_2(THF)Tb]_2(\mu\text{-}\eta^2\text{:}\eta^2\text{-}N_2)$,[9] **7-Tb**. The Tb−N($N_2$) average distance in **2-Tb**, 2.189(2) Å, is shorter than the Tb−N(N_2) distances found in **7-Tb**, 2.301(2) and 2.328(2) Å. The Tb−N(N_2) distance in **2-Tb** is significantly shorter than the Tb−N(NR_2) distance which averages 2.326(6) Å and is similar to the Tb−N(NR_2) distances observed in **7-Tb**, 2.301(2) and 2.328(2) Å.[9] The Tb metal centers in **2-Tb** deviate from the plane of the three amide nitrogen donor atoms by 0.663 Å. In comparison, Tb is out of the plane by 0.604 Å in $Tb(NR_2)_3$,[27] 0.503 Å in $[K(crypt)][Tb(NR_2)_3]$,

1-Tb,[23] and 0.201 Å in [K(18-c-6)][Tb(NR_2)$_3$].[22] Tb is 0.629 Å out of the N(NR_2)N(NR_2)O(THF) plane in **7-Tb**.[10]

The reaction between Tb(II) and N_2 was also examined with a complex containing 18-c-6 rather than crypt as the chelate for the potassium counter-cation of the [Tb(NR_2)$_3$]$^{1-}$ anion. Differences in reactivity previously have been observed between 18-c-6 and crypt complexes of Ln(II) complexes.[22, 28, 29] When a solid sample of [K(18-c-6)$_2$][Tb(NR_2)$_3$], **3-Tb**, prepared under argon, is dissolved in a nitrogen-containing glovebox in −35 °C Et_2O saturated with dinitrogen, the color changes gradually from dark blue to pale yellow. Crystallization by filtration into a cold vial and replacement in the glovebox freezer produces the end-on complex, [K_2(18-c-6)$_3$]{[(R_2N)$_3$Tb]$_2$[μ-η^1:η^1-N_2]}, **4-Tb**. Unfortunately, crystals of this complex were not of sufficient quality for detailed metrical analysis.

The Raman spectra of **2-Tb** and **4-Tb** were nearly indistinguishable and displayed signals at 1630 and 1623 cm^{-1}, respectively, Figure 4.5. This is in the range of the Raman shift observed for the N_2 unit in **2-Sc**[21] at 1644 cm^{-1} and distinct from the more common side-on complexes, [(THF)(R_2N)$_2$Ln]$_2$[μ-η^2:η^2-N_2], **7-Ln**, known for Ln = Nd, Gd, Tb, Dy, Ho, Y, Er, and Tm, which show Raman shift values ranging from 1417 to 1447 cm^{-1}.[30] The difference in these Raman shifts is consistent with the N−N distances which are shorter in the dianionic end-on complexes, **2-Tb** and **4-Tb**, than in the neutral side-on complexes, **7-Ln**.

Mixed End-on Side-on Complexes. The gadolinium complex, [K(crypt)][Gd(NR_2)$_3$], **1-Gd**, reacted similarly but gave a different result from that obtained for **1-Tb** in eq 4.4. When **1-Gd**, prepared under Ar, is dissolved in N_2-saturated Et_2O at −35 °C, the solution turns gradually to a pale-yellow color after 5 minutes. Crystallization at −35 °C yields crystals with the same

composition as **2-Tb**, but the product contains both side-on and end-on reduced dinitrogen ligands disordered over the two binding modes: $[K(crypt)]_2\{[(R_2N)_3Gd]_2[\mu\text{-}\eta^x\text{:}\eta^x\text{-}N_2]\}$[(x = 1 and 2), **5-**

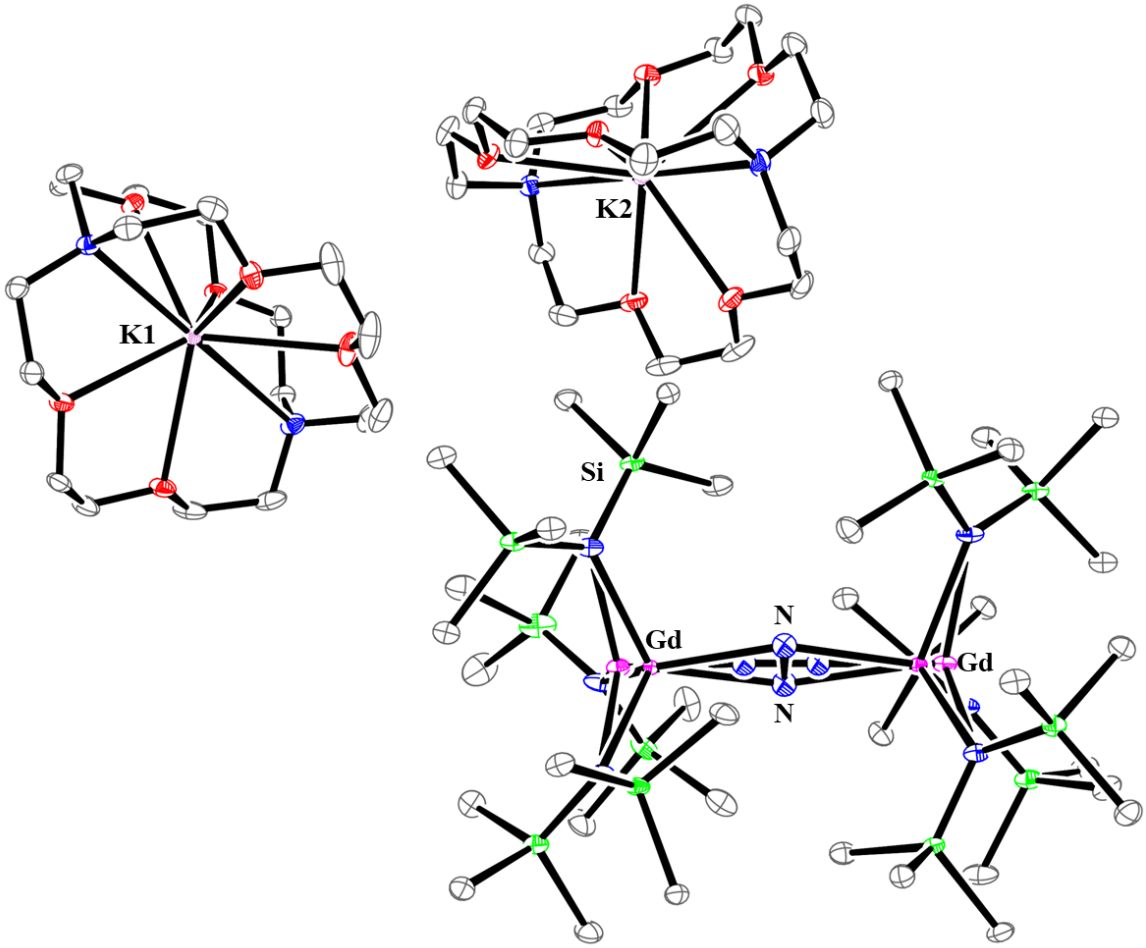

Figure 4.3. ORTEP representation of **5-Gd** drawn at the 50% probability level. Hydrogen atoms and Et_2O molecules excluded for clarity.

Gd, Figure 4.3. The crystal data were modelled best with 70% side-on and 30% end-on occupancy, respectively. This is the first example of a lanthanide complex of a side-on $(N=N)^{2-}$ ligand with three ancillary amide ligands on each lanthanide (cf. eq 4.2). The Gd center is also disordered in the structure with the same occupancies as the corresponding $(N=N)^{2-}$ binding modes.

Interestingly, the mixed binding mode complex **5-Gd** is isomorphous with the pure end-on scandium complex, $[K(crypt)]_2\{[(R_2N)_3Sc]_2[\mu\text{-}\eta^1\text{:}\eta^1\text{-}N_2]\}$, **2-Sc**. In addition, these complexes crystallize in the same space group with comparable unit cell parameters as $[K(crypt)]_2\{[(R_2N)_3Gd]_2(\mu\text{-}O)\}$, **10-Gd**, which was isolated and crystallographically-characterized as part of this study (see Supporting Information). In one instance, **5-Gd** and **10-Gd** were observed to co-crystallize with 85 % of the crystal modelled as **5-Gd(end-on)** and the other 15 % modelled as **10-Gd**. Unfortunately, neither the crystal of **10-Gd** nor the mixed crystal of **5/10-Gd** were of sufficient quality for metrical analysis.

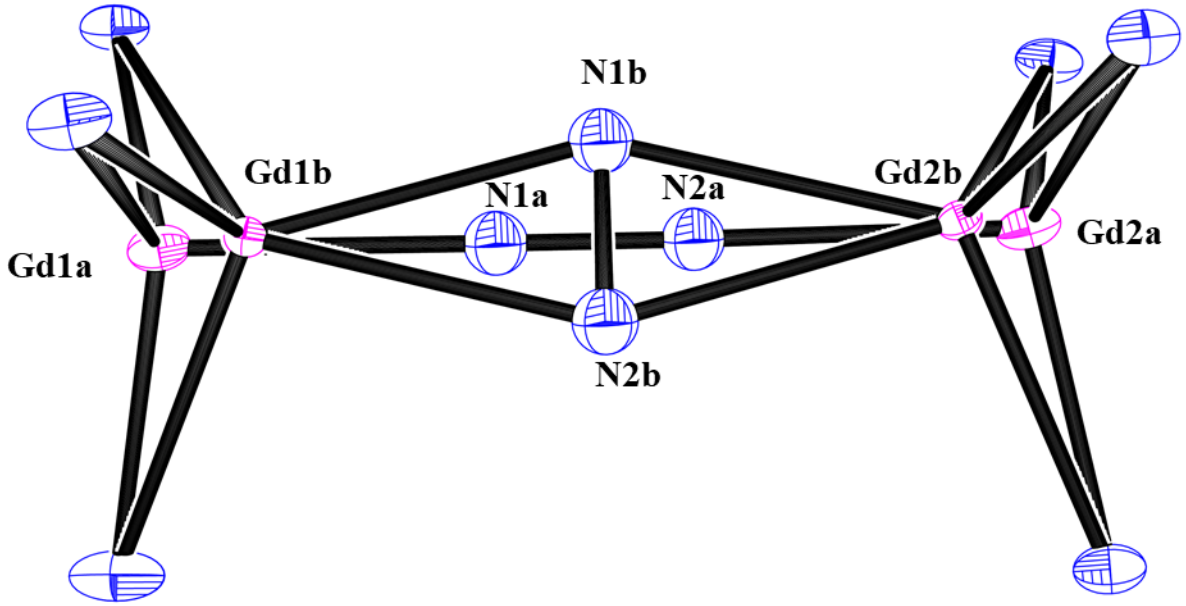

Figure 4.4. ORTEP representation of the disordered core of $[K_2(18\text{-c-}6)_3]\{[(R_2N)_3Gd]_2[\mu\text{-}\eta^x\text{:}\eta^x\text{-}N_2]\}$ (x = 1, 2), **6-Gd**, drawn at the 50% probability level. Hydrogen atoms, counter-cations, $SiMe_3$ groups and Et_2O molecules excluded for clarity.

The 18-c-6 Gd(II) complex, $[K(18\text{-c-}6)_2][Gd(NR_2)_3]$ **3-Gd**, also reacts with N_2 to form crystals containing both end-on and side-on $(N{=}N)^{2-}$: $[K_2(18\text{-c-}6)_3]\{[(R_2N)_3Gd]_2[\mu\text{-}\eta^x\text{:}\eta^x\text{-}N_2]\}$ (x

= 1, 2), **6-Gd**. The core atoms of **6-Gd** are shown in Figure 4.4. The crystal data were modelled best with 50% side-on and 50 % end-on occupancy.

The disorder in **5-Gd** and **6-Gd** limits the conclusions that can be drawn from the structural data shown in Table 4.1. The end-on components of **5-Gd** and **6-Gd** are similar and differ from the

Table 4.1. Selected bond distances (Å) of $[K(crypt)]_2\{[(R_2N)_3Sc]_2[\mu\text{-}\eta^1\text{:}\eta^1\text{-}N_2]\}$, **2-Sc**,[21] $[K(crypt)]_2\{[(R_2N)_3Tb]_2[\mu\text{-}\eta^1\text{:}\eta^1\text{-}N_2]\}$**,** **2-Tb**, $[K(crypt)]_2\{[(R_2N)_3Gd]_2[\mu\text{-}\eta^x\text{:}\eta^x\text{-}N_2]\}$[(x = 1 and 2), **5-Gd**, and $[K_2(18\text{-c-}6)_3]\{[(R_2N)_3Gd]_2[\mu\text{-}\eta^x\text{:}\eta^x\text{-}N_2]\}$ (x = 1, 2), **6-Gd**

	Ln−N$(NR_2)_{avg}$ [range]	Ln−N$(N_2)_{avg}$	Ln−$(N_3$ plane$)_{avg}$[a]	N−N(N_2)
2-Sc	2.150(6) [2.143(2) - 2.161(2)]	2.031(1)	0.678(3)	1.221(3)
2-Tb	2.326(6) [2.3126(19) - 2.3406(19)]	2.189(2)	0.663(1)	1.217(3)
5-Gd (end-on)	2.268(27) [2.216(2) - 2.295(2)]	2.155(9)	0.40(4)	1.271(12)
5-Gd (side-on)	2.408(26) [2.371(2) - 2.444(2)]	2.363(3)	0.906(12)	1.190(5)
6-Gd (end-on)	2.302(16) [2.286(3) - 2.326(3)]	2.181(2)	0.46(2)	1.234(9)
6-Gd (side-on)	2.45(3) [2.418(3) - 2.486(3)]	2.367(9)	0.97(2)	1.193(9)

[a] The distance of the Ln to the plane of the three nitrogen donor atoms of the three amide ligands.

side-on components of **5-Gd** and **6-Gd**, which are also similar. In the end-on structures, the metal is 0.40(4)-0.46(2) Å out of the plane of the three nitrogen donors of the three amide ligands. In the side-on components, the distances are 0.906(12) and 0.97(2) Å. In comparison, the pure end-on complexes, **2-Sc** and **2-Tb**, have out-of-plane distances between 0.678(3) and 0.663(1) Å, respectively.

The Ln−N(N_2) distances of the end-on components in **5-Gd** and **6-Gd** are shorter than those of the side-on components, 2.155(9) Å for **5-Gd(end-on)** vs 2.363(6) Å for **5-Gd(side-on)** and 2.181(2) Å **6-Gd(end-on)** vs 2.367(9) Å for **6-Gd(side-on)**. The Ln−N(NR_2) distances span a wide range in **5-Gd** and **6-Gd**, 2.216(2) -2.486(2) Å, but in general the end-on structures have shorter Ln−N(NR_2) distances (2.216(2) - 2.295(2) Å, **5-Gd**; 2.286(3) - 2.326(3)Å, **6-Gd**) than the side-on structures (2.371(2) - 2.444(2) Å, **5-Gd**; 2.418(3) - 2.486(3) Å, **6-Gd**). Hence, the Ln(N_3 plane), Ln−N(N_2), and Ln−N(NR_2) distances all are consistent with a more crowded coordination environment for the side-on complexes versus the end-on complexes.

It would normally be expected that the distances in **2-Tb** would be slightly shorter than those in **5-Gd** because the ionic radius of Tb is 0.013 Å smaller than that of Gd. However, the 2.189(2) Å Ln−N(N_2) distance in **2-Tb** is numerically larger and equivalent within the error limits to the 2.155(9) Å distance in **5-Gd(end-on)**. The 2.3126(19) – 2.3406(19) Å range of Ln−N(NR_2) distances in **2-Tb** is on average longer than the 2.216(2)– 2.295(2) Å Ln−N(NR_2) distance range in **5-Gd(end-on)**. The fact that the distances in **2-Tb** are not shorter as expected from the ionic radii suggests there may be more steric crowding in the Tb complex. It is also possible that the disorder in the Gd complex leads to this difference in distances.

The Raman spectra of **5-Gd** and **6-Gd** show intense signals at 1634 and 1627 cm^{-1} similar to the 1630 cm^{-1} shift of the pure end-on complexes, **2-Sc**,[21] **2-Tb**, and **4-Tb**, Figure 4.5.

This is surprising since modeling the crystallographic data shows more side-on than end-on in the solid state. However, the density functional theory (DFT) calculations (see below) show that the end-on N−N stretching vibration is approximately two orders of magnitude more intense than that of the side-on complex.

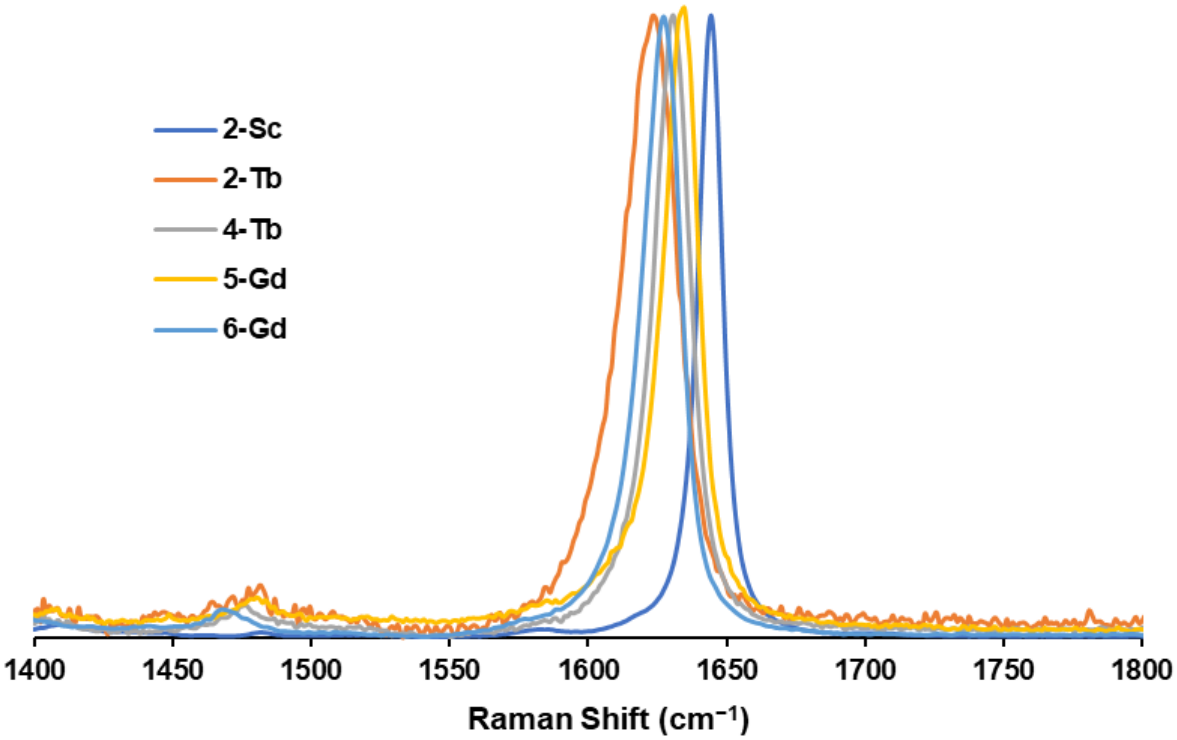

Figure 4.5. Normalized and baseline-corrected Raman spectra of **2-Sc** (1644 cm^{-1}),[21] **2-Tb** (1623 cm^{-1}), **4-Tb** (1630 cm^{-1}), **5-Gd** (1634 cm^{-1})**,** and **6-Gd** (1627 cm^{-1}). Individual spectra are shown in the Experimental Details.

Reversibility of N_2 Binding with Gd(II). If a solution of **5-Gd** or **6-Gd** at −78 °C is warmed to room temperature, a color change from pale yellow to dark blue is observed. UV-visible spectra of the dark blue color shows an broad, intense, absorbance around 600 nm consistent with

$[Gd(NR_2)_3]^{1-}$.[23] Upon cooling the solution back to −78 °C, the color reverts from deep blue back to pale yellow. The same phenomena are observed with **2-Tb** and **4-Tb**, eq 4.5.

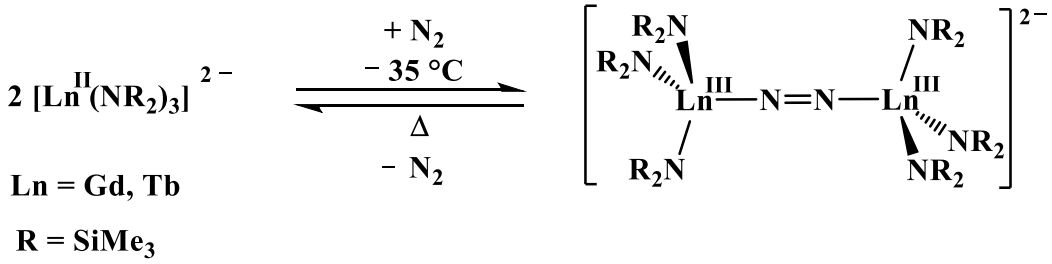

(4.5)

Isolation of a Side-On Bimetallic Complex with Five Amide Ancillary Ligands. When a solution of $Gd(NR_2)_3$ in THF cooled to −35 °C is added to a vial containing KC_8 cooled to 77 K under N_2, yet a different type of reduced dinitrogen complex is observed. At this lower temperature, a side-on $(N=N)^{2-}$ complex is isolated where one Gd center is ligated by three amides and the other is ligated by two amides and a THF, i.e. $[K(THF)_6]\{[(THF)(R_2N)_2Gd][\mu\text{-}\eta^2\text{:}\eta^2\text{-}N_2][Gd(NR_2)_3]\}$, **8-Gd**, eq 4.6 Figure 4.6. Additionally, crystals of $[K(THF)_6][Gd(NR_2)_4]$, **11-Gd**, were isolated from the same reaction mixture (Figure 4.20).

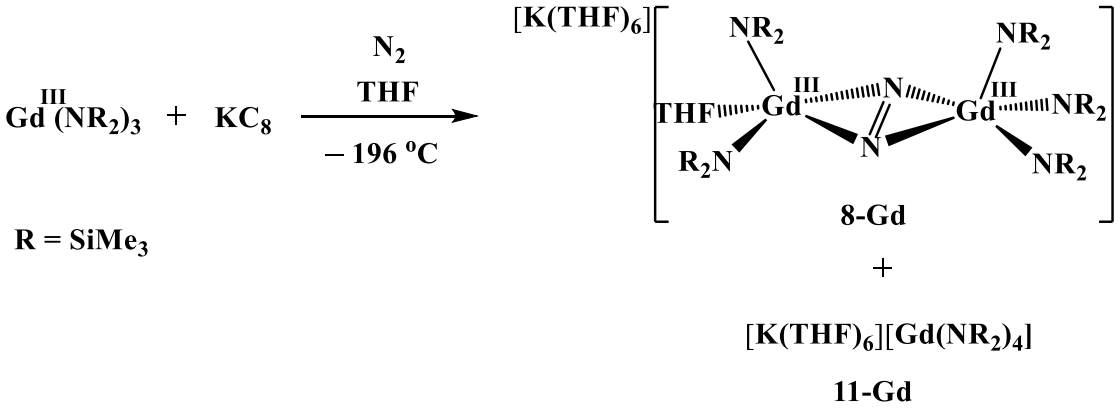

(4.6)

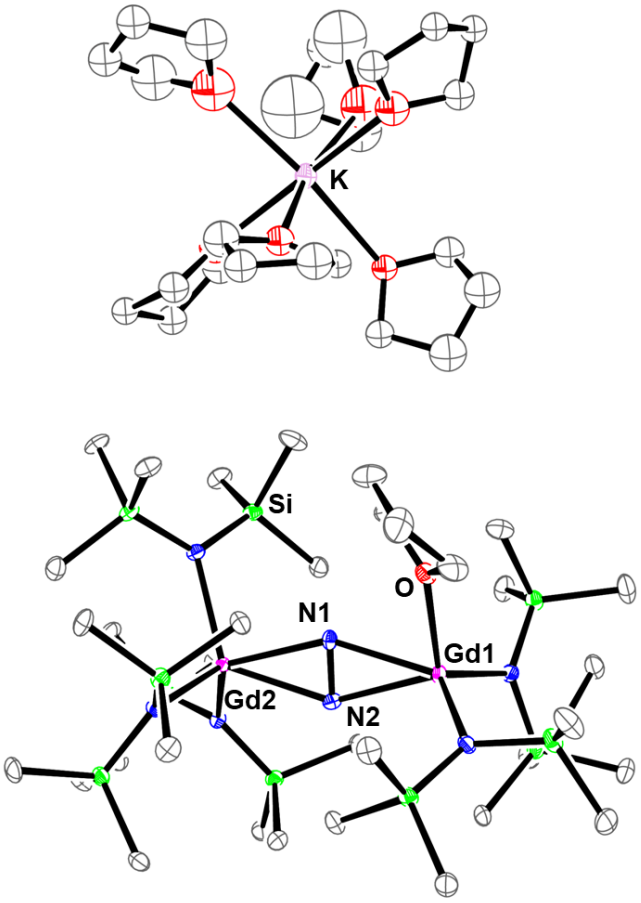

Figure 4.6. ORTEP representation of **8-Gd** drawn at the 50 % probability level. Hydrogen atoms excluded for clarity.

The structure of **8-Gd** is a monoanionic blend between the side-on neutral complex, $[(THF)(R_2N)_2Gd]_2[\mu\text{-}\eta^2\text{:}\eta^2\text{-}N_2]\}$, **7-Gd**,[9] with two amides and one THF per metal center, and the side-on components of **5-Gd** and **6-Gd**, which contain $\{[(R_2N)_3Gd]_2[\mu\text{-}\eta^x\text{:}\eta^x\text{-}N_2]\}^{2-}$ dianions and three amides per metal center. Metrical data are compared in Table 4.2. The 1.248(8) Å N−N distance in side-on **8-Gd** is numerically intermediate between the 1.278(4) Å N−N distance of side-on **7-Gd**, which has two amides per metal, and the 1.190(5) Å N−N distance in **5-Gd(side-on)**, which has three amides per metal. However, the N−N distance in **8-Gd** is equivalent within error to that in **7-Gd.** The placement of the $(N{=}N)^{2-}$ ligand between the two types of Gd ions in

Gd-8 is not symmetrical. The 2.306(7) and 2.308(6) Å Gd(1)-N(N_2) distances for the metal with two amide ligands and one THF ligand [Gd(1)] are significantly shorter than the 2.449(6) and 2.399(6) Å Gd(2)-N(N_2) distances of the metal with three amide ligands [Gd(2)]. The two 2.310(6) and 2.313(6) Å Gd(1)-N(NR_2) distances are closer to the 2.333(6), 2.357(6), and 2.362(6) Å Gd(2)-N(NR_2) lengths. In general, the Gd(1) lengths are more similar to those in **3-Gd** and the Gd(2) distances are more similar to those in **5-Gd(side-on)**, which is consistent with the coordination environments. The pyramidalization of the Gd(2) ion ligated by three amide ligands from the N_3 plane in **8-Gd**, 0.656 Å, is significantly less than that observed in **5-Gd(side-on)**, 0.902 Å. Conversely, the Gd(1) distance to the donor atom plane for the Gd ion containing two amide ligands and a THF in **8-Gd** is 0.833 Å, substantially larger than the 0.611 Å distance observed in **7-Gd**. These numbers are consistent with more steric crowding around Gd(1) which is closer to the $(N=N)^{2-}$ unit.

Table 4.2. Selected bond distances (Å) of $[K(THF)_6]\{[(THF)(R_2N)_2Gd][\mu\text{-}\eta^2\text{:}\eta^2\text{-}N_2][Gd(NR_2)_3]\}$, **8-Gd**, compared to $[(THF)(R_2N)_2Gd]_2[\mu\text{-}\eta^2\text{:}\eta^2\text{-}N_2]$, **7-Gd**,[9] and the side-on component of **5-Gd**, i.e. $[K(crypt)]_2\{[(R_2N)_3Gd]_2[\mu\text{-}\eta^2\text{:}\eta^2\text{-}N_2]\}$

	Ln(1)−N(1)(N_2)	Ln(1)−N(2)(N_2)	Ln(1)−N(1)(N_{NR_2})	Ln(1)−N(2)(N_{NR_2})	Ln(1)−O(1)(THF)/ Ln(1)−N(3)(N_{NR_2})
7-Gd	2.326(2)	2.353(2)	2.2782(19)	2.2964(19)	2.4408(17)
5-Gd (side-on)	2.361(4)	2.363(4)	2.415(2)	2.434(2)	2.381(2)
8-Gd	2.306(7)	2.308(6)	2.310(6)	2.313(6)	2.460(6)

	Ln(2)−N(1)(N_2)	Ln(2)−N(2)(N_2)	Ln(2)−N(1)(N_{NR_2})	Ln(2)−N(2)(N_{NR_2})	Ln(2)−N(3)(N_{NR_2})
7-Gd	2.326(2)	-	-	-	-
5-Gd (side-on)	2.369(4)	2.360(4)	2.371(2)	2.406(2)	2.444(2)
8-Gd	2.429(6)	2.399(6)	2.333(6)	2.357(6)	2.362(6)

	N(1)−N(2)	Ln−N_3(plane)	Ln−NNO(plane)
7-Gd	1.278(4)	-	0.611
5-Gd (side-on)	1.190(5)	0.902	-
8-Gd	1.248(8)	0.656	0.833

Formation of an $(N_2)^{3-}$ Complex from Gd(II). If a solid sample of **1-Gd** prepared under argon in −35 °C is dissolved in *THF instead of Et_2O* in a nitrogen-filled glovebox, an orange solution forms immediately. When the solution was filtered and layered with hexanes at −35 °C, crystals of the $(N_2)^{3-}$ complex [K(2.2.2-crypt)]{[(THF)$(R_2N)_2$Gd]$_2$[μ-η^2:η^2-N_2]}, **9-Gd**, were isolated, eq 4.7, Figure 4.7

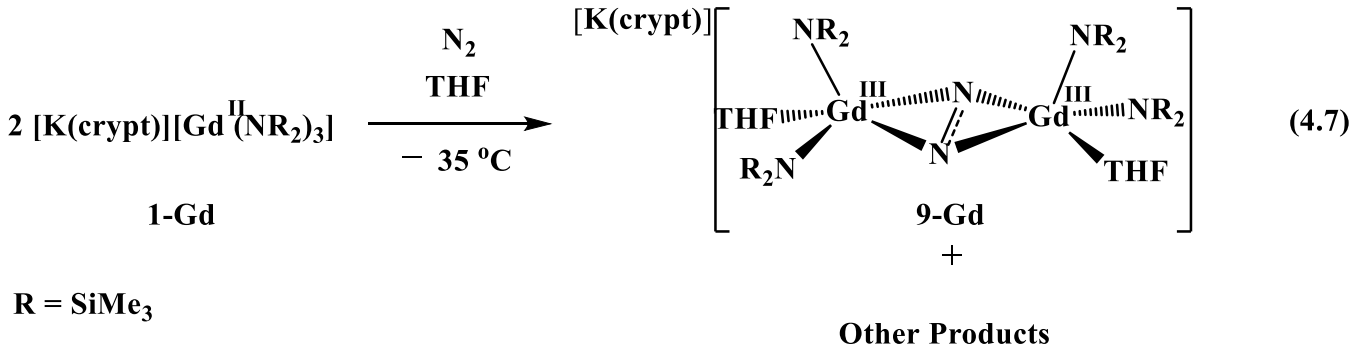

(4.7)

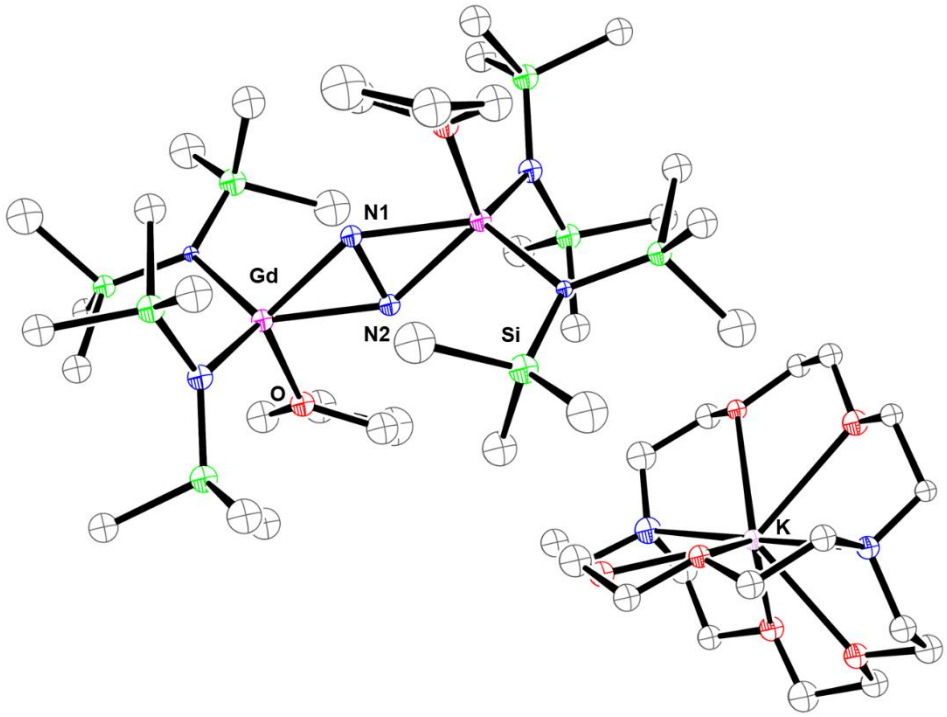

Figure 4.7. Ball and stick representation of **9-Gd**. Hydrogen atoms omitted for clarity.

The structural data on **9-Gd** were not of sufficient quality for a detailed metrical analysis and comparison with other $(N_2)^{3-}$ complexes,[19, 31-34] but this result shows that Gd(II) is sufficiently reducing to convert $(N_2)^{2-}$ to $(N_2)^{3-}$. This is consistent with earlier results that showed that $(N_2)^{3-}$ could be generated from divalent lanthanide ions, specifically with Dy(II),[19] without the use of an alkali reducing agent.

Density Functional Calculations. DFT calculations were performed by Sreeganesh Balasubramini in collaboration with the Furche group. The structures of the $\{[(NR_2)_3Gd]_2[\mu\text{-}\eta^1\text{:}\eta^1\text{-}N\}^{2-}$ (end-on) and $\{[(NR_2)_3Gd]_2[\mu\text{-}\eta^2\text{:}\eta^2\text{-}N_2]\}^{2-}$ (side-on) complexes were optimized using the TPSSh hybrid meta-generalized gradient approximation density functional and f-in-core effective

core potentials. Optimization of the end-on complex resulted in a D_3-symmetric triplet ground state, while optimization of the side-on complex resulted in a C_2-symmetric singlet ground state.

The doubly degenerate HOMOs of the end-on complex exhibit metal-to-ligand delta-bonding character due to interactions of the antibonding π* orbitals of the N_2 unit with the d_{xz} and d_{yz} orbitals of the Gd atoms, Figure 4.8. In the side-on complex, on the other hand, only one of the two N_2 π* orbitals can interfere constructively with the Gd d orbitals, producing a doubly occupied HOMO of metal-to-ligand π-bonding character, whereas the other N_2 π* orbital remains unoccupied, Figure 4.9. A qualitative MO diagram showing the electronic structure of each complex is shown in Figure 4.10.

As in the case of the Sc compound,[21] end-on orientation of the N_2 unit leads to a degenerate HOMO favoring a triplet ground state, whereas side-on orientation lifts the degeneracy of the two N_2 π* orbitals to such a degree that a singlet ground state is favorable. Based on the DFT calculations, the two structures are nearly isoenergetic, consistent with the isolation of both complexes under the same experimental conditions. The calculated geometrical details of the side-on and end-on complexes Table 4.13.

The simulated vibrational Raman spectra suggest that the experimental spectrum in the 1500-1700 cm^{-1} region is dominated by the end-on complex, whose N−N stretching vibration is approximately two orders of magnitude more intense than that of the side-on complex.

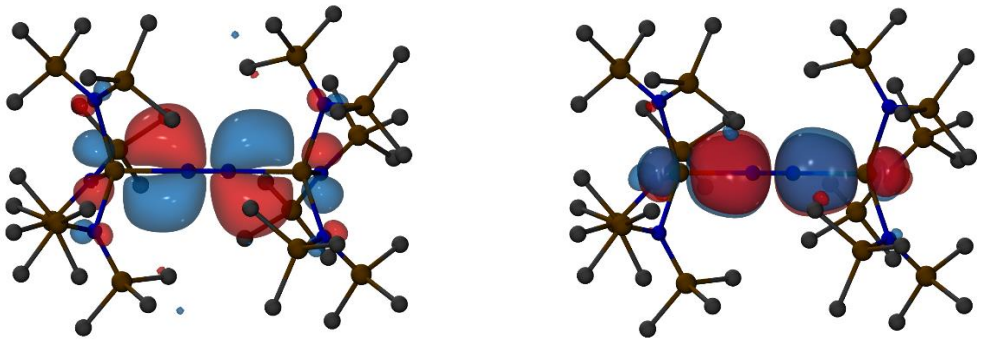

Figure 4.8. Degenerate HOMOs of $\{[(R_2N)_3Gd]_2[\mu\text{-}\eta^1\text{:}\eta^1\text{-}N_2]\}^{2-}$.

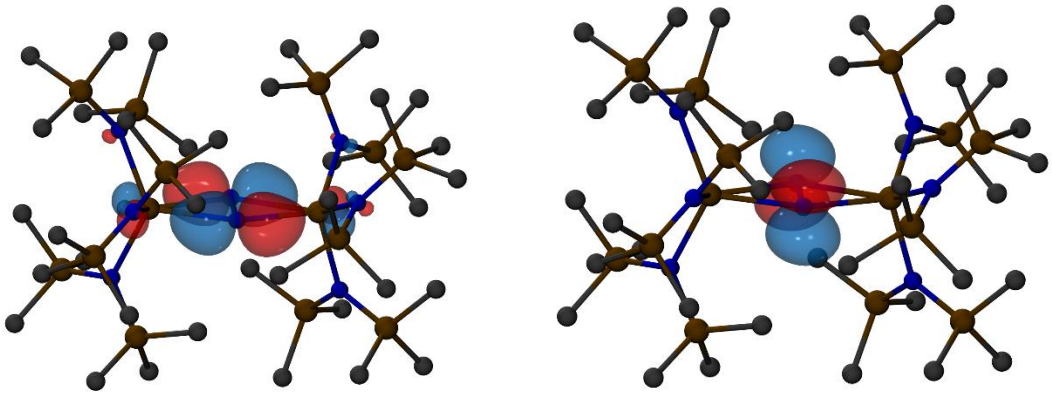

Figure 4.9. HOMO (left) and LUMO (right) of $\{[(R_2N)_3Gd]_2[\mu\text{-}\eta^2\text{:}\eta^2\text{-}N_2]\}^{2-}$.

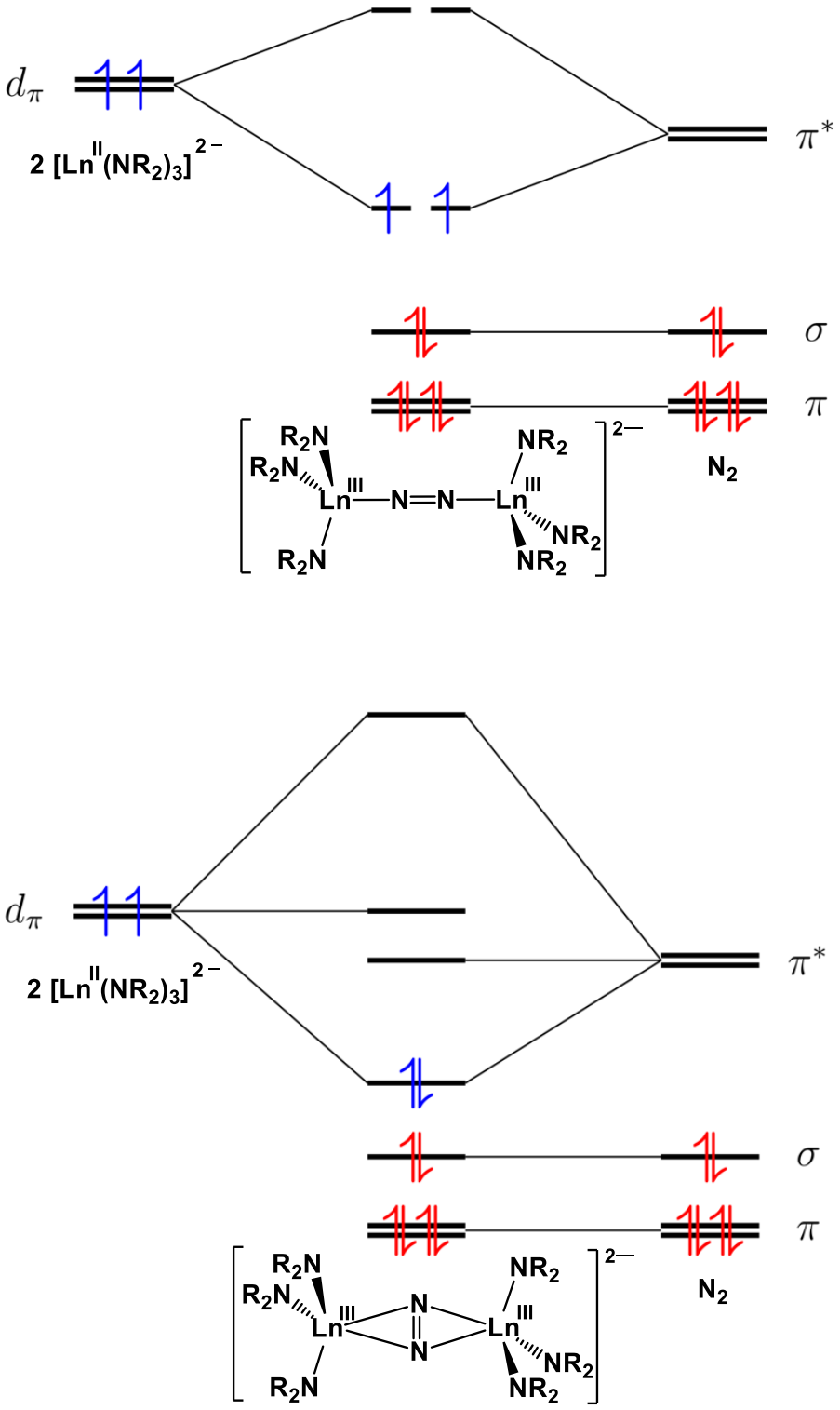

Figure 4.10. Qualitative MO representation of $\{[(R_2N)_3Gd]_2[\mu\text{-}\eta^1\text{:}\eta^1\text{-}N_2]\}^{2-}$ (top) and $\{[(R_2N)_3Gd]_2[\mu\text{-}\eta^2\text{:}\eta^2\text{-}N_2]\}^{2-}$ (bottom).

Discussion

The reactions of solid Ln(II) tris(amide) complexes, [K(crypt)][Ln(NR_2)$_3$], **1-Ln**, with N_2 to generate the reduced dinitrogen complexes, [K(crypt)]$_2${[(R_2N)$_3$Ln]$_2$[μ-η^x:η^x-N_2]}, (x = 1, **2-Tb**; x = 1, 2, **5-Gd**), constitute the first hard evidence of Ln(II) intermediates in the previously known lanthanide amide reactions, Ln(NR_2)$_3$/K/N_2, that have formed [(THF)(R_2N)$_2$Ln]$_2$[μ-η^2:η^2-N_2], **7-Ln**, complexes across the lanthanide series according to eq 4.2. Previously, it was unknown if the Ln(NR_2)$_3$/K/N_2 reactions involved Ln(II) intermediates,[9] because molecular species containing the La(II), Ce(II), Pr(II), Gd(II), Tb(II), Ho(II), Er(II), Lu(II), and Y(II) ions had not been discovered when the reduced dinitrogen complexes were isolated. Thus, the suggestion of Ln(II) intermediates in the formation of the **7-Ln** complexes was highly speculative before complexes of Ln(II) ions beyond the traditional Eu, Yb, Sm, Tm, Dy, and Nd examples were discovered.[29, 35] Interestingly, the $(N=N)^{2-}$ products isolated from the reactions of isolated Ln(II) tris(amide) precursors are not the side-on **7-Ln**, complexes with two ancillary amide ligands per metal isolated from Ln(NR_2)$_3$/K/N_2 reactions, but the end-on {[(R_2N)$_3$Ln]$_2$[μ-η^1:η^1-N_2]}$^{2-}$ dianions with three amides per lanthanide.

Since these latter dianions have the same number of amides as the [Ln(NR_2)$_3$]$^{1-}$ starting material, it is tempting to speculate that this is related to the mechanism of reduction. It is possible that the Ln(II) anion, [Ln(NR_2)$_3$]$^{1-}$, formed from Ln(NR_2)$_3$ and potassium, reduces N_2. Initial reduction could form an end-on {[(R_2N)$_3$Ln][N_2]}$^{1-}$ radical that is quickly trapped by another [Ln(NR_2)$_3$]$^{1-}$ unit to form the end-on bimetallic complex, {[(R_2N)$_3$Ln]$_2$[μ-η^1:η^1-N_2]}$^{2-}$, described for the first time in this study. These complexes could thermally decompose to reform the Ln(II) precursors, [Ln(NR_2)$_3$]$^{1-}$, as observed here, or, if an $(NR_2)^{1-}$ ligand is substituted by THF, a monoanionic complex of the type isolated in this study, {[(THF)(R_2N)$_2$Ln][μ-η^2:η^2-

$N_2][Ln(NR_2)_3]\}^{1-}$, **8-Ln**, could form. If an $(NR_2)^{1-}$ ligand in **8-Ln** is displaced by THF, the final product of the $Ln(NR_2)_3/K/N_2$ reactions results: $[(THF)(R_2N)_2Ln]_2[\mu\text{-}\eta^2\text{:}\eta^2\text{-}N_2]$, **7-Ln**. Since the earlier $Ln(NR_2)_3/K/N_2$ reactions were conducted at room temperature, the **1-Ln**, **2-Ln**, and **8-Ln** intermediates were not observed.

The fact that Gd(II) and Tb(II) complexes react with dinitrogen to form end-on bound $(N=N)^{2-}$ complexes, $\{[(R_2N)_3Ln]_2[\mu\text{-}\eta^1\text{:}\eta^1\text{-}N_2]\}^{2-}$, similar to that of Sc[21] provides another example of the similarity of late Ln(II) chemistry with Sc(II) chemistry that is not shared by Y(II). Hence, the fact that $[Y(NR_2)_3]^{1-}$ is much less stable than $[Sc(NR_2)_3]^{1-}$ as well as the $[Ln(NR_2)_3]^{1-}$ complexes of Ln = Gd, Tb, Dy, Ho, Er, is not an isolated example of non-analogous Y(II) chemistry. Hence, it seems prudent to refrain from extending the similarity of Y(III) and the late lanthanide +3 ions to the +2 oxidation state. The origin of this effect is not clear although non-periodic chemistry is sometimes observed for 4d vs 3d and 5d transition metal complexes.[36, 37]

The reversibility of eq 4.4 as the temperature is increased, i.e. eq 4.5, has parallels with the isolation of the first lanthanide dinitrogen complex, $[(C_5Me_5)_2Sm]_2[\mu\text{-}\eta^2\text{:}\eta^2\text{-}N_2]$, eq 4.1. In that case lower temperature favors the dinitrogen complex as expected based on entropy. It is clear from this study and other related studies of lanthanide amide reduction reactions,[22, 23] that the details of the specific reactions are critical to the outcome. The isolation of the gadolinium crystals with mixed end-on and side-on ligation of N_2 is consistent with the DFT calculations which show the side-on and end-on structures to be nearly isoenergetic. This is in contrast to calculations performed on the end on Sc complex which showed a hypothetical side-on bound structure to be 12 kcal/mol higher in energy than the end-on counterpart.[21] It is possible that by moving from Gd to its neighbor, Tb, which differs by being 0.013 Å smaller,[38] the balance between end-on and side-on shifts to favor the sterically less crowded end-on structure. This may be why **2-Tb** and **4-**

Tb are purely end-on. Hence, selection of one lanthanide versus its adjacent element can influence the reaction.

Subtle differences in binding modes based on metal ion size and the steric profile of the ligands have previously been observed in Ti and Zr dinitrogen chemistry. Reduction of the pentamethylcyclopentadienyl zirconium dichloride, $(C_5Me_5)_2ZrCl_2$, under a nitrogen atmosphere will reductively bind dinitrogen and form a bimetallic end-on bound N_2 complex, $[(C_5Me_5)_2(N_2)Zr]_2(\mu\text{-}\eta^1\text{:}\eta^1\text{-}N_2)$.[39, 40] In contrast, when the *tetra*methylcyclopentadienyl zirconium dichloride complex, $(C_5Me_4H)_2ZrCl_2$, is reduced under dinitrogen, the side-on bound dinitrogen complex $[(C_5Me_4H)_2Zr]_2(\mu\text{-}\eta^2\text{:}\eta^2\text{-}N_2)$, is observed.[41, 42] In the case of smaller titanium, however, both C_5Me_5 and C_5Me_4H ligands are large enough to give end-on bound dinitrogen complexes $[(C_5Me_4R)_2Ti]_2(\mu\text{-}\eta^1\text{:}\eta^1\text{-}N_2)$ (R = H, Me),[43, 44] and a trimethylcyclopentadienyl ligand is need to observe the side-on binding mode, $[(C_5Me_3H_2)_2Ti]_2(\mu\text{-}\eta^2\text{:}\eta^2\text{-}N_2)$.[45, 46].

Temperature is also crucial: under the conditions of the previously reported $Ln(NR_2)_3/K/N_2$ reactions, $[(THF)(R_2N)_2Ln]_2[\mu\text{-}\eta^2\text{:}\eta^2\text{-}N_2]$, **7-Ln**, would be the only isolated product. To observe the Ln(II) and Ln−N=N−Ln intermediates, low temperatures and fast reaction times are necessary. This study also showed that conducting these reactions in THF vs Et_2O can lead to an $(N_2)^{3-}$ product rather than $(N{=}N)^{2-}$ products. This result also shows that Gd(II) is capable of forming $(N_2)^{3-}$ since no alkali metal was present in the formation of **9-Gd**.

The structural similarity of the end-on $(N{=}N)^{2-}$, side-on $(N{=}N)^{2-}$, and O^{2-} complexes suggests that other small dianions should fit inside two $[Ln(NR_2)_3]^{1-}$ units. Long ago Lappert reported a $[(R_2N)_3Ce]_2[\mu\text{-}\eta^2\text{:}\eta^2\text{-}O_2]$ showing this structural motif with $(O_2)^{2-}$ and Ce(IV).[47] It remains to be determined if such species are best accessed through $[Ln(NR_2)_3]^{1-}$, or $\{[(R_2N)_3Ln]_2[\mu\text{-}\eta^x\text{:}\eta^x\text{-}N_2]\}^{2-}$, or some other precursor. In any case, the success of such a reaction

is likely to involve the specific counter-cation as these have been found to be crucial to isolate (and crystallize) specific samples of reduced complexes.[22, 23, 48]

Conclusion

For over 30 years, crystallographic analysis of lanthanide-based dinitrogen reduction products has provided structures of only side-on Ln_2N_2 complexes, i.e. $[(solvent)A_2Ln]_2[\mu\text{-}\eta^2\text{:}\eta^2\text{-}N_2]$ with A = anion. In this chapter, the first examples of end-on lanthanide Ln−N=N−Ln species are described, $[K(crypt)]_2\{[(R_2N)_3Ln]_2[\mu\text{-}\eta^1\text{:}\eta^1\text{-}N_2]\}$. The end-on structures were obtained by using the isolated Ln(II) complexes, $[K(chelate)][Ln(NR_2)_3]$, as the reductant instead of the in situ product generated from $Ln(NR_2)_3$ and K and by doing the reactions at low temperature. The fact that warming the Gd(III) $(N=N)^{2-}$ complex to room temperature reforms the Gd(II) precursor indicates that the Gd(III)/Gd(II) and $N_2/(N_2)^{2-}$ reduction potentials are closely matched. The isolation of the penta-amide complex, $[K(THF)_6]\{[(THF)(R_2N)_2Gd][\mu\text{-}\eta^2\text{:}\eta^2\text{-}N_2][Gd(NR_2)_3]\}$, suggests that lanthanide-based reduction of N_2 can occur by reaction of two equiv of the divalent $[Ln(NR_2)_3]^{1-}$ with N_2 to form an end-on dianion, $\{[(R_2N)_3Ln]_2[\mu\text{-}\eta^1\text{:}\eta^1\text{-}N_2]\}^{2-}$, which can lose one $(NR_2)^{1-}$ ligand per metal to form the neutral side-on $[(THF)(R_2N)_2Ln]_2[\mu\text{-}\eta^2\text{:}\eta^2\text{-}N_2]$ complex. The specific product isolated in these lanthanide-based dinitrogen reduction reactions depends critically on the details of the experimental conditions including temperature, solvent, reaction time, and the presence or absence of a chelate. This study also provided more evidence to suggest that Sc(II) and the late lanthanide Ln(II) ions are similar and differ from Y(II). Hence, Y(III) is similar to the late trivalent lanthanides and has congeneric similarities to Sc(III), yttrium in the +2 oxidation state should be considered neither a surrogate for the late lanthanides nor a congeneric analog of Sc(II).

Experimental Details

All manipulations and syntheses described below were conducted with the rigorous exclusion of air and water using standard Schlenk line and glovebox techniques under an argon or dinitrogen atmosphere. Solvents were sparged with UHP argon and dried by passage through columns containing Q-5 and molecular sieves prior to use. Elemental analyses were conducted on a Perkin-Elmer 2400 Series II CHNS elemental analyzer. Complexes of **1-Ln**[23] and **3-Ln**[22] were synthesized as previously reported. Infrared spectra were collected on an Agilent Cary 630 equipped with a diamond ATR attachment. Raman spectra were collected on solid samples in a 1mm quartz cuvette appended with a Teflon stopcock using a Renishaw inVia confocal Raman Microscope, equipped with a 122 mW laser of wavelength 785 nm (laser power 10% and a X5L objective laser). Measurements were taken on at least 3 different crystals to confirm reproducibility while one of the spectra is reported.

[K(crypt)]$_2${[(R$_2$N)$_3$Tb]$_2$[μ-η^1:η^1-N$_2$]}, **2-Tb.** In a dinitrogen filled glovebox [K(crypt)][Tb(NR$_2$)$_3$] (40 mg, 0.038 mmol), **1 Tb**, was dissolved in −35 °C, nitrogen saturated, Et$_2$O and placed in the freezer overnight. The resulting yellow solution produced crystals suitable for X-ray diffraction (9 mg, 11% yield). IR: 2942s, 2889s, 2817m, 2762w, 2730w, 2698w, 1478m, 1458m, 1446m, 1356s, 1299m, 1260s 1237s, 1135s, 1107s, 1078s, 1059s, 992s, 952s, 933m, 869s, 827s, 770m, 752m, 713m, 691m, 663s, cm^{-1}. Anal. Calcd for $C_{72}H_{180}N_{12}O_{12}Si_{12}K_2Tb_2$: C, 40.42; H, 8.48; N, 7.86. Found: C, 39.95; H, 8.04; N, 7.23.

[K$_2$(18-c-6)$_3$]{[(R$_2$N)$_3$Tb]$_2$[μ-η^1:η^1-N$_2$]}, **4-Tb.** In a dinitrogen filled glovebox [K(18c6)$_2$][Tb(NR$_2$)$_3$] (40 mg, 0.038 mmol) was dissolved in −35 °C, nitrogen saturated, Et$_2$O and placed in the freezer overnight. The resulting yellow solution produced crystals suitable for X-ray

diffraction (13 mg, 17%). IR: 2938m, 2887m, 1472w, 1453w, 1352m, 1237s, 1104s, 945s, 865m, 813s, 771m, 700m, 653s cm^{-1}.

[K(crypt)]$_2${[(R$_2$N)$_3$Gd]$_2$[μ-η^x:η^x-N$_2$]}(x = 1, 2), 5-Gd. In a nitrogen filled glovebox [K(crypt)][Gd(NR_2)$_3$] (40 mg, 0.037 mmol)was dissolved in −35 °C, nitrogen saturated, Et_2O and placed in the freezer overnight. The resulting yellow solution produced crystals suitable for X-ray diffraction (7 mg, 9%). IR: 2942s, 2890s, 2819m, 2762w, 2729w, 2697w, 1478m, 1459m, 1446m, 1356s, 1298m, 1260s 1236s, 1135s, 1107s, 1078s, 1060s, 996s, 952s, 934m, 869s, 825s, 769m, 751m, 711m, 690m, 662s, cm^{-1}. Anal. Calcd for $C_{72}H_{180}N_{12}O_{12}Si_{12}K_2Gd_2$: C, 40.49; H, 8.49; N, 7.87. Found: C, 39.35; H, 8.91; N, 7.61.

[K$_2$(18-c-6)$_3$]{[(NR$_2$)$_3$Gd]$_2$[μ-η^x:η^x-N$_2$]}(X = 1, 2), 6-Gd. In a dinitrogen filled glovebox [K(18c6)$_2$][Gd(NR_2)$_3$] (40 mg, 0.033 mmol) was dissolved in −35 °C, nitrogen saturated, Et_2O and placed in the freezer overnight. The resulting yellow solution produced crystals suitable for X-ray diffraction (15 mg, 20% yield).

[K(THF)$_6$]{[(THF)(R$_2$N)$_2$Gd][μ-η^2:η^2-N$_2$][Gd(NR$_2$)$_3$]}, 8-Gd, and [K(THF)$_6$][Gd(NR$_2$)$_4$] 11-Gd. In a dinitrogen filled glovebox Gd(NR_2)$_3$ was dissolved in −35 °C, nitrogen saturated, THF and then added to a vial containing KC_8 at 77K. The solution immediately filtered and layered with −35 °C hexanes and replaced in the glove box freezer. The resulting orange solution produced crystals of **8-Gd** and **11-Gd** suitable for X-ray diffraction after 24 hours.

[K(crypt)]{(THF)[(R$_2$N)$_2$Gd]$_2$[μ-η^2:η^2-N$_2$]}, 9-Gd. In a dinitrogen filled glovebox [K(crypt)][Gd(NR_2)$_3$] was dissolved in −35 °C, nitrogen saturated, THF and placed in the freezer overnight. The resulting orange solution produced crystals of **9-Gd** suitable for X-ray diffraction.

X-ray Data Collection, Structure, Solution, Refinement

2-Tb.

X-ray Data Collection, Structure Solution and Refinement for ajr27.

A yellow crystal of approximate dimensions 0.259 x 0.187 x 0.143 mm was mounted in a cryoloop and transferred to a Bruker SMART APEX II diffractometer. The APEX2[49] program package was used to determine the unit-cell parameters and for data collection (45 sec/frame scan time for a sphere of diffraction data). The raw frame data was processed using SAINT[50] and SADABS[51] to yield the reflection data file. Subsequent calculations were carried out using the SHELXTL[52] program. There were no systematic absences nor any diffraction symmetry other than the Friedel condition. The centrosymmetric triclinic space group $P\bar{1}$ was assigned and later determined to be correct.

The structure was solved by dual space methods and refined on F^2 by full-matrix least-squares techniques. The analytical scattering factors[53] for neutral atoms were used throughout the analysis. Hydrogen atoms were included using a riding model.

Least-squares analysis yielded wR2 = 0. 0664 and Goof = 1.012 for 1139 variables refined against 29882 data (Å), R1 = 0.0334 for those 23503 data with I > 2.0σ(I).

Table 4.3. Crystal data and structure refinement for ajr27.

Identification code	ajr27
Empirical formula	C80 H200 K2 N12 O14 Si12 Tb2
Formula weight	2287.63
Temperature	88(2) K
Wavelength	0.71073 Å
Crystal system	Triclinic
Space group	P-1

Unit cell dimensions	a = 15.437(2) Å	a= 102.9109(17)°.
	b = 16.218(2) Å	b= 96.0143(17)°.
	c = 26.133(3) Å	g = 104.6636(17)°.
Volume	6078.6(14) $Å^3$	
Z	2	
Density (calculated)	1.250 Mg/m^3	
Absorption coefficient	1.394 mm^{-1}	
F(000)	2424	
Crystal color	yellow	
Crystal size	0.259 x 0.187 x 0.143 mm^3	
Theta range for data collection	1.623 to 29.178°	
Index ranges	-21 <= h <= 21, -22 <= k <= 22, -34 <= l <= 35	
Reflections collected	75362	
Independent reflections	29882 [R(int) = 0.0401]	
Completeness to theta = 25.500°	99.8 %	
Absorption correction	Semi-empirical from equivalents	
Max. and min. transmission	0.4319 and 0.3842	
Refinement method	Full-matrix least-squares on F^2	
Data / restraints / parameters	29882 / 0 / 1139	
Goodness-of-fit on F^2	1.012	
Final R indices [I>2sigma(I) = 23503 data]	R1 = 0.0334, wR2 = 0.0608	
R indices (all data, 0.73 Å)	R1 = 0.0520, wR2 = 0.0664	
Extinction coefficient	n/a	
Largest diff. peak and hole	1.500 and -0.868 $e.Å^{-3}$	

Table 4.4. Bond lengths [Å] and angles [°] for ajr27.

Tb(1)-N(1)	2.191(2)
Tb(1)-N(3)	2.3223(19)
Tb(1)-N(5)	2.327(2)
Tb(1)-N(4)	2.3406(19)
Tb(2)-N(2)	2.187(2)
Tb(2)-N(8)	2.3126(19)
Tb(2)-N(7)	2.329(2)
Tb(2)-N(6)	2.331(2)
N(1)-N(2)	1.217(3)

N(1)-Tb(1)-N(3)	103.47(7)
N(1)-Tb(1)-N(5)	106.89(7)
N(3)-Tb(1)-N(5)	113.22(7)
N(1)-Tb(1)-N(4)	107.61(7)
N(3)-Tb(1)-N(4)	111.72(7)
N(5)-Tb(1)-N(4)	113.17(7)
N(2)-Tb(2)-N(8)	107.70(7)
N(2)-Tb(2)-N(7)	105.45(7)
N(8)-Tb(2)-N(7)	110.35(7)
N(2)-Tb(2)-N(6)	107.00(7)
N(8)-Tb(2)-N(6)	112.27(7)
N(7)-Tb(2)-N(6)	113.61(7)
N(2)-N(1)-Tb(1)	177.89(17)
N(1)-N(2)-Tb(2)	177.41(17)

4-Tb

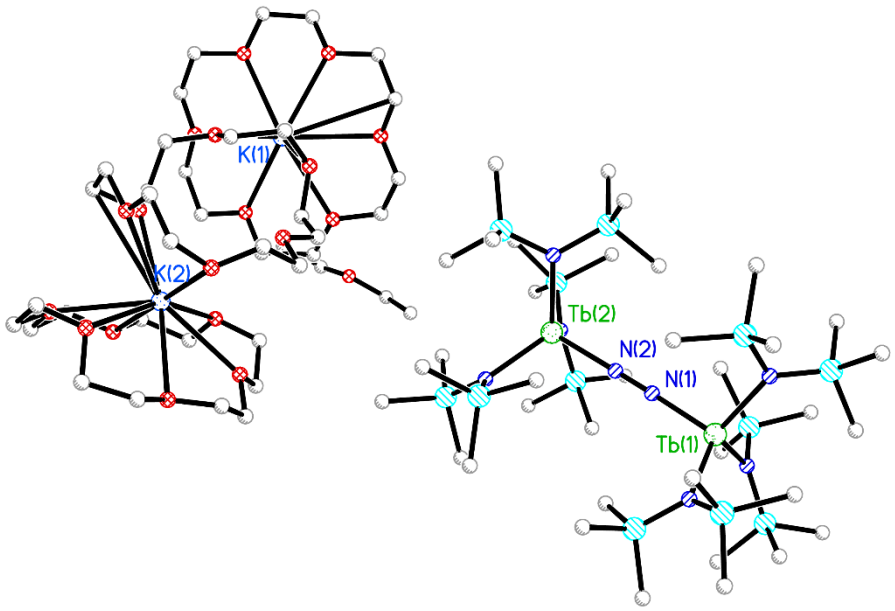

Figure 4.11. Ball and stick representation of **4-Tb**.

5-Gd.

X-ray Data Collection, Structure Solution and Refinement for ajr50.

A yellow crystal of approximate dimensions 0.388 x 0.171 x 0.145 mm was mounted in a cryoloop and transferred to a Bruker SMART APEX II diffractometer. The APEX2[49] program package was used to determine the unit-cell parameters and for data collection (90 sec/frame scan time for a sphere of diffraction data). The raw frame data was processed using SAINT[50] and SADABS[51] to yield the reflection data file. Subsequent calculations were carried out using the SHELXTL[52] program. There were no systematic absences nor any diffraction symmetry other than the Friedel condition. The centrosymmetric triclinic space group $P\bar{1}$ was assigned and later determined to be correct.

The structure was solved by dual space methods and refined on F^2 by full-matrix least-squares techniques. The analytical scattering factors[53] for neutral atoms were used throughout the analysis.

Hydrogen atoms were included using a riding model. Disordered N2 unit was modelled isotropically in parts. Disordered Gd ion was modelled anisotropically in parts of the same ration as the N2 unit

Least-squares analysis yielded wR2 = 0.0864 and Goof = 1.026 for 1202 variables refined against 29795 data (Å), R1 = 0.0362 for those 23770 data with I > 2.0σ(I).

Table 4.5. Crystal data and structure refinement for ajr50.

Identification code	ajr50
Empirical formula	C84 H210 Gd2 K2 N12 O15 Si12
Formula weight	2358.41

Temperature	133(2) K	
Wavelength	0.71073 Å	
Crystal system	Triclinic	
Space group	P-1	
Unit cell dimensions	a = 15.237(3) Å	a= 75.118(3)°.
	b = 20.708(5) Å	b= 79.221(3)°.
	c = 21.341(5) Å	g = 76.734(3)°.
Volume	6275(2) $Å^3$	
Z	2	
Density (calculated)	1.248 Mg/m^3	
Absorption coefficient	1.283 mm^{-1}	
F(000)	2504	
Crystal color	yellow	
Crystal size	0.388 x 0.171 x 0.145 mm^3	
Theta range for data collection	1.267 to 28.894°	
Index ranges	-20 <= h <= 20, -27 <= k <= 26, -27 <= l <= 27	
Reflections collected	74933	
Independent reflections	29795 [R(int) = 0.0266]	
Completeness to theta = 25.500°	99.7 %	
Absorption correction	Semi-empirical from equivalents	
Max. and min. transmission	0.7458 and 0.6575	
Refinement method	Full-matrix least-squares on F^2	
Data / restraints / parameters	29795 / 0 / 1202	
Goodness-of-fit on F^2	1.026	
Final R indices [I>2sigma(I) = 23770 data]	R1 = 0.0362, wR2 = 0.0794	
R indices (all data, 0.74 Å)	R1 = 0.0515, wR2 = 0.0864	
Extinction coefficient	n/a	
Largest diff. peak and hole	2.899 and -1.426 $e.Å^{-3}$	

Table 4.6. Bond lengths [Å] and angles [°] for ajr50.

Gd(1A)-N(1A)	2.154(9)
Gd(1A)-N(4)	2.216(2)
Gd(1A)-N(3)	2.264(2)
Gd(1A)-N(5)	2.293(2)
Gd(1A)-Si(4)	3.3146(12)

Gd(1A)-Si(2)	3.3983(12)
Gd(1A)-Si(5)	3.4008(12)
Gd(1B)-N(1B)	2.361(4)
Gd(1B)-N(2B)	2.363(4)
Gd(1B)-N(5)	2.381(2)
Gd(1B)-N(3)	2.415(2)
Gd(1B)-N(4)	2.434(2)
Gd(2A)-N(2A)	2.155(9)
Gd(2A)-N(6)	2.257(3)
Gd(2A)-N(7)	2.285(2)
Gd(2A)-N(8)	2.295(2)
Gd(2A)-Si(9)	3.4212(16)
Gd(2A)-Si(11)	3.4277(16)
Gd(2A)-Si(7)	3.4428(16)
Gd(2A)-Si(8)	3.4452(17)
Gd(2B)-N(2B)	2.360(4)
Gd(2B)-N(1B)	2.369(4)
Gd(2B)-N(8)	2.371(2)
Gd(2B)-N(7)	2.406(2)
Gd(2B)-N(6)	2.444(2)
N(1A)-N(2A)	1.271(12)
N(1B)-N(2B)	1.190(5)
N(1A)-Gd(1A)-N(4)	98.9(2)
N(1A)-Gd(1A)-N(3)	100.2(2)
N(4)-Gd(1A)-N(3)	117.36(9)
N(1A)-Gd(1A)-N(5)	98.6(2)
N(4)-Gd(1A)-N(5)	119.64(9)
N(3)-Gd(1A)-N(5)	115.40(8)
N(1B)-Gd(1B)-N(2B)	29.19(13)
N(1B)-Gd(1B)-N(5)	111.60(10)
N(2B)-Gd(1B)-N(5)	109.43(10)
N(1B)-Gd(1B)-N(3)	125.60(11)
N(2B)-Gd(1B)-N(3)	101.90(10)
N(5)-Gd(1B)-N(3)	106.82(7)
N(1B)-Gd(1B)-N(4)	98.86(11)
N(2B)-Gd(1B)-N(4)	124.84(11)

N(5)-Gd(1B)-N(4)	108.06(8)
N(3)-Gd(1B)-N(4)	104.22(8)
N(2A)-Gd(2A)-N(6)	101.4(2)
N(2A)-Gd(2A)-N(7)	100.6(2)
N(6)-Gd(2A)-N(7)	117.33(9)
N(2A)-Gd(2A)-N(8)	102.0(2)
N(6)-Gd(2A)-N(8)	115.18(9)
N(7)-Gd(2A)-N(8)	116.22(9)
N(2B)-Gd(2B)-N(1B)	29.16(13)
N(2B)-Gd(2B)-N(8)	107.91(10)
N(1B)-Gd(2B)-N(8)	115.16(10)
N(2B)-Gd(2B)-N(7)	101.24(10)
N(1B)-Gd(2B)-N(7)	120.89(11)
N(8)-Gd(2B)-N(7)	108.97(7)
N(2B)-Gd(2B)-N(6)	125.81(11)
N(1B)-Gd(2B)-N(6)	97.57(11)
N(8)-Gd(2B)-N(6)	105.88(7)
N(7)-Gd(2B)-N(6)	106.21(7)
N(2A)-N(1A)-Gd(1A)	177.7(7)
N(2B)-N(1B)-Gd(1B)	75.5(3)
N(2B)-N(1B)-Gd(2B)	75.0(3)
Gd(1B)-N(1B)-Gd(2B)	150.43(18)
N(1A)-N(2A)-Gd(2A)	179.0(8)
N(1B)-N(2B)-Gd(2B)	75.9(3)
N(1B)-N(2B)-Gd(1B)	75.3(3)
Gd(2B)-N(2B)-Gd(1B)	151.18(17)

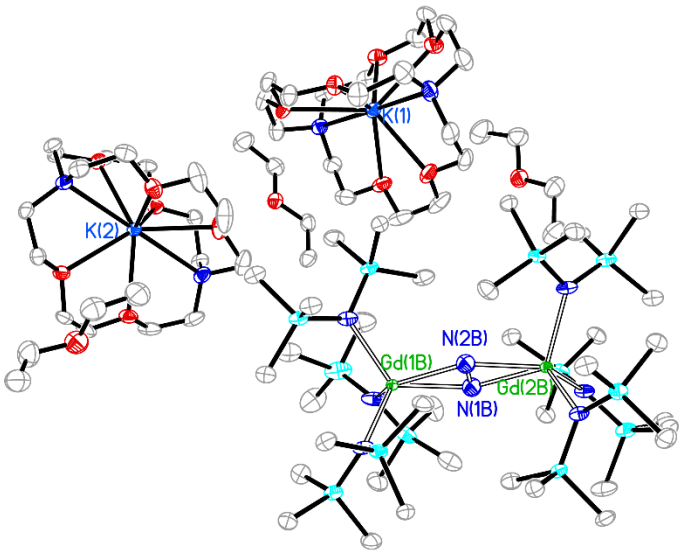

Figure 4.12. Thermal ellipsoid plot of **5-Gd(side-on)** drawn at the 50% probability level

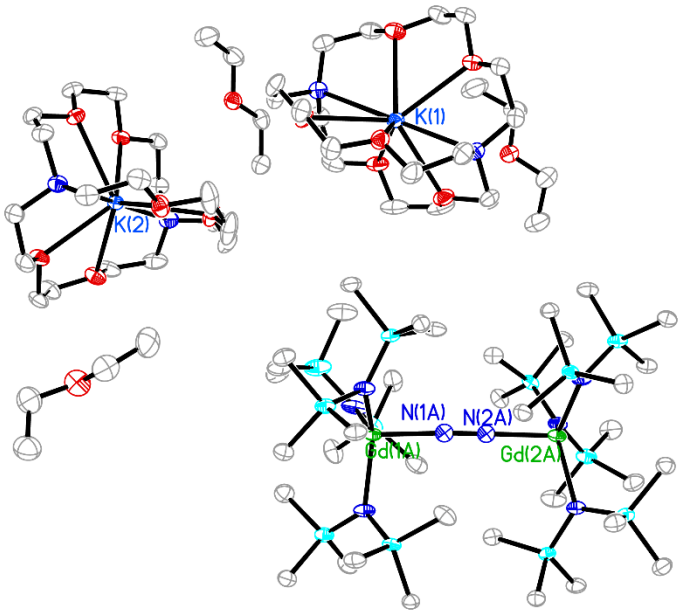

Figure 4.13. Thermal ellipsoid plot of **5-Gd(end-on)** drawn at the 50% probability level

6-Gd.

X-ray Data Collection, Structure Solution and Refinement for ajr33.

A yellow crystal of approximate dimensions 0.374 x 0.259 x 0.200 mm was mounted in a cryoloop and transferred to a Bruker SMART APEX II diffractometer. The APEX2[49] program package was used to determine the unit-cell parameters and for data collection (90 sec/frame scan time for a sphere of diffraction data). The raw frame data was processed using SAINT[50] and SADABS[51] to yield the reflection data file. Subsequent calculations were carried out using the SHELXTL[52] program. There were no systematic absences nor any diffraction symmetry other than the Friedel condition. The centrosymmetric triclinic space group $P\bar{1}$ was assigned and later determined to be correct.

The structure was solved by dual space methods and refined on F^2 by full-matrix least-squares techniques. The analytical scattering factors[53] for neutral atoms were used throughout the analysis. Hydrogen atoms were included using a riding model.

Least-squares analysis yielded wR2 = 0.1129 and Goof = 1.041 for 1123 variables refined against 28562 data (Å), R1 = 0.0465 for those 20565 data with I > 2.0σ(I).

Table 4.7. Crystal data and structure refinement for ajr33.

Identification code	ajr33	
Empirical formula	C76 H190 Gd2 K2 N8 O19 Si12	
Formula weight	2250.13	
Temperature	88(2) K	
Wavelength	0.71073 Å	
Crystal system	Triclinic	
Space group	P-1	
Unit cell dimensions	a = 15.658(3) Å	a= 78.975(2)°.
	b = 16.014(3) Å	b= 77.363(2)°.
	c = 24.347(4) Å	g = 82.456(3)°.
Volume	5821.7(18) $Å^3$	
Z	2	

Density (calculated)	1.284 Mg/m^3
Absorption coefficient	1.381 mm^{-1}
F(000)	2376
Crystal color	yellow
Crystal size	0.374 x 0.259 x 0.200 mm^3
Theta range for data collection	1.438 to 29.096°
Index ranges	-21 <= h <= 21, -21 <= k <= 21, -33 <= l <= 33
Reflections collected	72119
Independent reflections	28562 [R(int) = 0.0435]
Completeness to theta = 25.500°	99.8 %
Absorption correction	Semi-empirical from equivalents
Max. and min. transmission	0.4318 and 0.3904
Refinement method	Full-matrix least-squares on F^2
Data / restraints / parameters	28562 / 0 / 1123
Goodness-of-fit on F^2	1.041
Final R indices [I>2sigma(I) = 20565 data]	R1 = 0.0465, wR2 = 0.1014
R indices (all data, 0.73 Å)	R1 = 0.0739, wR2 = 0.1129
Extinction coefficient	n/a
Largest diff. peak and hole	1.588 and -0.789 $e.Å^{-3}$

Table 4.8. Bond lengths [Å] and angles [°] for ajr33.

Gd(1A)-N(1A)	2.179(6)
Gd(1A)-N(7)	2.286(3)
Gd(1A)-N(8)	2.295(3)
Gd(1A)-N(6)	2.295(3)
Gd(1A)-Si(7)	3.3991(14)
Gd(1A)-Si(12)	3.4406(13)
Gd(2A)-N(2A)	2.184(7)
Gd(2A)-N(5)	2.287(3)
Gd(2A)-N(4)	2.325(3)
Gd(2A)-N(3)	2.326(3)
Gd(2A)-Si(4)	3.4344(15)
Gd(1B)-N(2B)	2.370(7)
Gd(1B)-N(1B)	2.370(7)
Gd(1B)-N(6)	2.424(3)

Gd(1B)-N(7)	2.469(3)
Gd(1B)-N(8)	2.486(3)
Gd(2B)-N(2B)	2.351(7)
Gd(2B)-N(1B)	2.377(7)
Gd(2B)-N(4)	2.419(3)
Gd(2B)-N(3)	2.448(3)
Gd(2B)-N(5)	2.486(3)
N(1A)-N(2A)	1.234(9)
N(1B)-N(2B)	1.193(9)
N(1A)-Gd(1A)-N(7)	102.90(18)
N(1A)-Gd(1A)-N(8)	100.65(17)
N(7)-Gd(1A)-N(8)	116.71(11)
N(1A)-Gd(1A)-N(6)	99.50(17)
N(7)-Gd(1A)-N(6)	115.85(11)
N(8)-Gd(1A)-N(6)	116.74(11)
N(2A)-Gd(2A)-N(5)	103.23(18)
N(2A)-Gd(2A)-N(4)	100.88(17)
N(5)-Gd(2A)-N(4)	116.96(11)
N(2A)-Gd(2A)-N(3)	102.77(18)
N(5)-Gd(2A)-N(3)	116.96(11)
N(4)-Gd(2A)-N(3)	112.82(10)
N(2B)-Gd(1B)-N(1B)	29.2(2)
N(2B)-Gd(1B)-N(6)	113.43(17)
N(1B)-Gd(1B)-N(6)	113.84(18)
N(2B)-Gd(1B)-N(7)	102.37(17)
N(1B)-Gd(1B)-N(7)	126.86(18)
N(6)-Gd(1B)-N(7)	104.99(11)
N(2B)-Gd(1B)-N(8)	124.66(17)
N(1B)-Gd(1B)-N(8)	99.33(18)
N(6)-Gd(1B)-N(8)	105.48(11)
N(7)-Gd(1B)-N(8)	103.81(10)
N(2B)-Gd(2B)-N(1B)	29.2(2)
N(2B)-Gd(2B)-N(4)	109.33(17)
N(1B)-Gd(2B)-N(4)	115.31(17)
N(2B)-Gd(2B)-N(3)	127.79(17)
N(1B)-Gd(2B)-N(3)	100.13(18)

N(4)-Gd(2B)-N(3)	105.49(10)
N(2B)-Gd(2B)-N(5)	100.28(17)
N(1B)-Gd(2B)-N(5)	121.87(18)
N(4)-Gd(2B)-N(5)	106.52(10)
N(3)-Gd(2B)-N(5)	105.67(10)
N(2A)-N(1A)-Gd(1A)	176.7(5)
N(1A)-N(2A)-Gd(2A)	178.7(6)
N(2B)-N(1B)-Gd(1B)	75.4(5)
N(2B)-N(1B)-Gd(2B)	74.2(5)
Gd(1B)-N(1B)-Gd(2B)	149.6(3)
N(1B)-N(2B)-Gd(2B)	76.6(5)
N(1B)-N(2B)-Gd(1B)	75.4(5)

Gd(2B)-N(2B)-Gd(1B)	152.0(3)

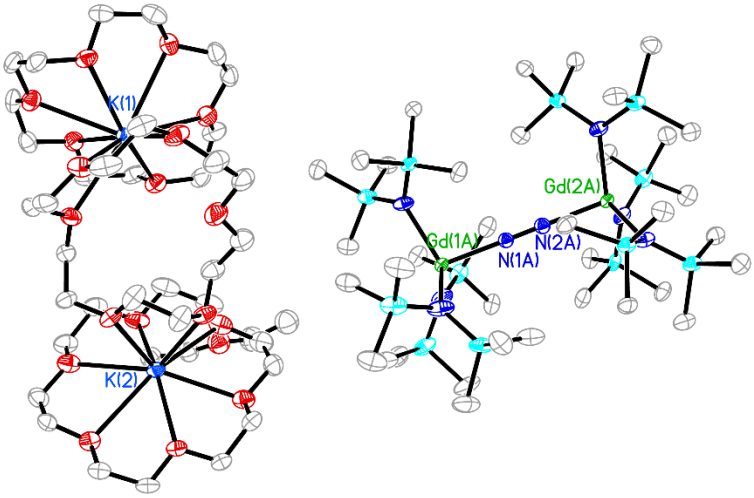

Figures 4.14. Thermal ellipsoid plot of **6-Gd (end-on)** drawn at the 50% probability level with hydrogen atoms excluded for clarity.

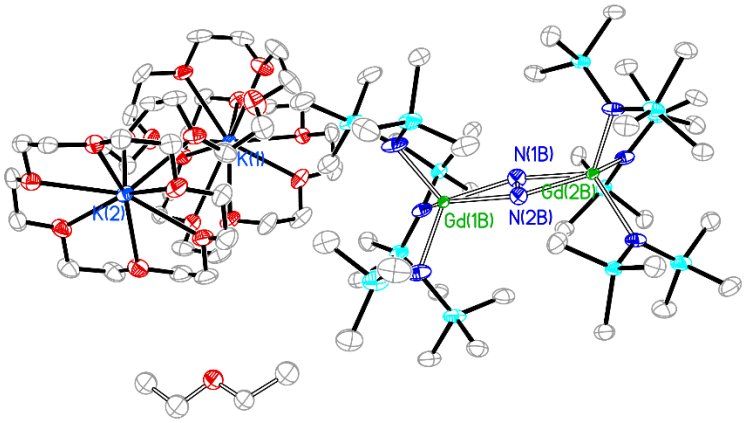

Figure 4.15. Thermal ellipsoid plot of **6-Gd(side-on)** draw at the 50% probability level. Hydrogen atoms excluded for clarity

8-Gd.

X-ray Data Collection, Structure Solution and Refinement for ajr56.

A yellow crystal of approximate dimensions 0.465 x 0.460 x 0.440 mm was mounted in a cryoloop and transferred to a Bruker SMART APEX II diffractometer. The APEX2[49] program package and the CELL_NOW[54] were used to determine the unit-cell parameters. Data was collected using a 15 sec/frame scan time for a sphere of diffraction data. The raw frame data was processed using SAINT[50] and TWINABS[55] to yield the reflection data file (HKLF 5 format)[55]. Subsequent calculations were carried out using the SHELXTL[52] program. The diffraction symmetry was 2/*m* and the systematic absences were consistent with the monoclinic space group $P2_1$ that was later determined to be correct.

The structure was solved by dual space methods and refined on F^2 by full-matrix least-squares techniques. The analytical scattering factors[53] for neutral atoms were used throughout the analysis. Hydrogen atoms were included using a riding model.

Least-squares analysis yielded wR2 = 0.0862 and Goof = 1.068 for 647 variables refined against 10403 data (0.77 Å), R1 = 0.0333 for those 10154 data with I > 2.0σ(I). The structure was refined as a two-component twin, BASF[55] = 0.30365. Flack paramater[56] was not relevant due to twinned structure.

Table 4.9. Crystal data and structure refinement for ajr56.

Identification code	ajr56	
Empirical formula	C58 H146 Gd2 K N7 O7 Si10	
Formula weight	1688.31	
Temperature	88(2) K	
Wavelength	0.71073 Å	
Crystal system	Monoclinic	
Space group	$P2_1$	
Unit cell dimensions	a = 12.6104(11) Å	a= 90°.
	b = 20.7558(17) Å	b= 93.7131(11)°.
	c = 16.9683(14) Å	g = 90°.
Volume	4431.9(6) $Å^3$	
Z	2	
Density (calculated)	1.265 Mg/m^3	
Absorption coefficient	1.709 mm^{-1}	
F(000)	1772	
Crystal color	yellow	
Crystal size	0.465 x 0.460 x 0.440 mm^3	
Theta range for data collection	1.552 to 27.485°	
Index ranges	-16 <= h <= 16, 0 <= k <= 26, 0 <= l <= 22	
Reflections collected	10403	
Independent reflections	10403 [R(int) = merged]	
Completeness to theta = 25.500°	100.0 %	
Absorption correction	Semi-empirical from equivalents	
Max. and min. transmission	0.745829 and 0.745829	
Refinement method	Full-matrix least-squares on F^2	
Data / restraints / parameters	10403 / 12 / 647	
Goodness-of-fit on F^2	1.068	
Final R indices [I>2sigma(I) = 10154 data]	R1 = 0.0333, wR2 = 0.0846	

R indices (all data, 0.77 Å)	R1 = 0.0352, wR2 = 0.0862
Absolute structure parameter	0.115(8)
Extinction coefficient	n/a
Largest diff. peak and hole	1.032 and -0.811 e.Å^{-3}

Table 4.10. Bond lengths [Å] and angles [°] for ajr56.

Gd(1)-N(4)	2.333(6)
Gd(1)-N(3)	2.357(6)
Gd(1)-N(5)	2.362(6)
Gd(1)-N(2)	2.399(6)
Gd(1)-N(1)	2.429(6)
Gd(1)-Si(6)	3.455(2)
Gd(2)-N(1)	2.306(7)
Gd(2)-N(2)	2.308(6)
Gd(2)-N(6)	2.310(6)
Gd(2)-N(7)	2.313(6)
Gd(2)-O(1)	2.460(6)
N(1)-N(2)	1.248(8)
N(4)-Gd(1)-N(3)	118.4(2)
N(4)-Gd(1)-N(5)	111.3(2)
N(3)-Gd(1)-N(5)	107.63(19)
N(4)-Gd(1)-N(2)	107.5(2)
N(3)-Gd(1)-N(2)	116.2(2)
N(5)-Gd(1)-N(2)	92.8(2)
N(4)-Gd(1)-N(1)	102.1(2)
N(3)-Gd(1)-N(1)	95.9(2)
N(5)-Gd(1)-N(1)	121.2(2)
N(2)-Gd(1)-N(1)	30.0(2)
N(1)-Gd(2)-N(2)	31.4(2)
N(1)-Gd(2)-N(6)	112.3(2)
N(2)-Gd(2)-N(6)	126.8(2)
N(1)-Gd(2)-N(7)	107.7(2)
N(2)-Gd(2)-N(7)	113.8(2)
N(6)-Gd(2)-N(7)	115.6(2)
N(1)-Gd(2)-O(1)	109.4(2)

N(2)-Gd(2)-O(1)	80.9(2)
N(6)-Gd(2)-O(1)	90.7(2)
N(7)-Gd(2)-O(1)	120.3(2)

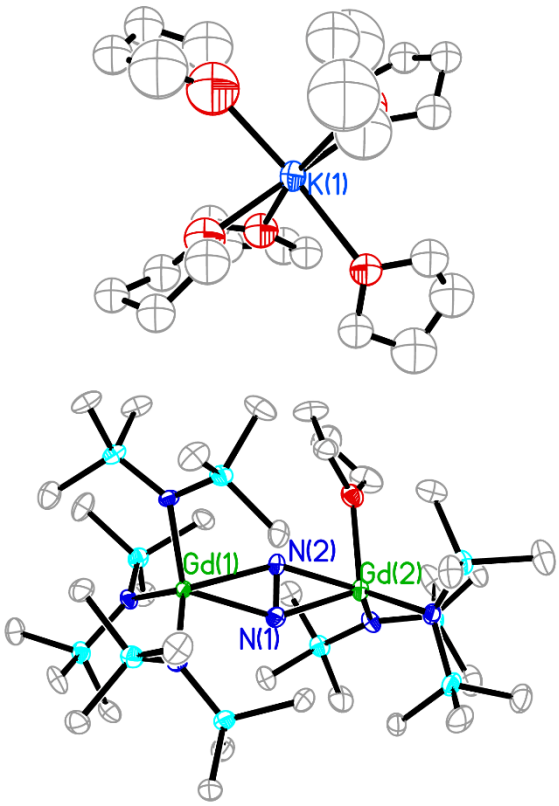

Figure 4.16 Thermal ellipsoid plot of **8-Gd** drawn at the 50 % probability level. Hydrogen atoms excluded for clarity.

9-Gd.

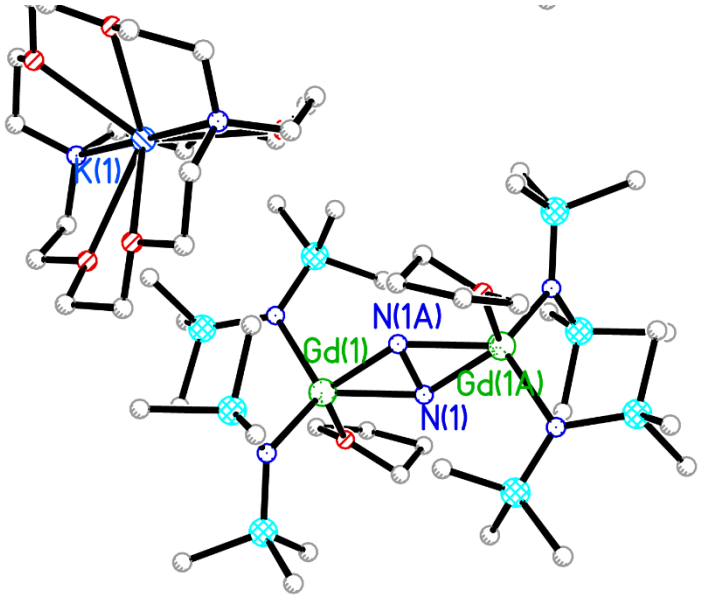

Figure 4.17. Ball and stick model of **9-Gd.**

10-Gd.

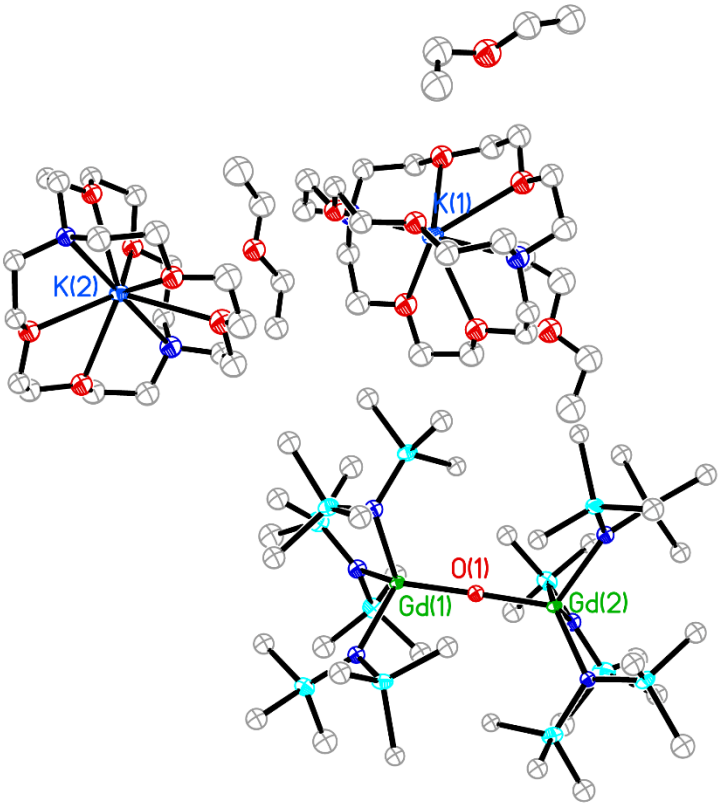

Figure 4.18. Ball and stick model of **10-Gd**

5/10-Gd.

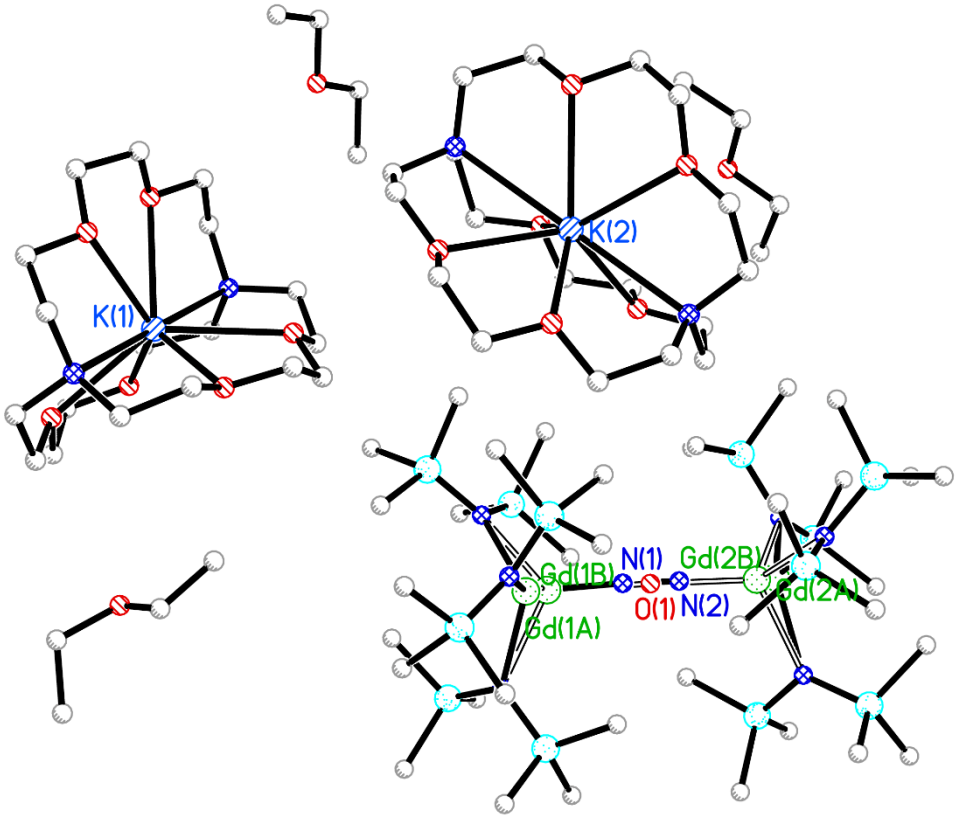

Figure 4.19. Ball and stick model of **5/10-Gd**

11-Gd.

X-ray Data Collection, Structure Solution and Refinement for ajr57.

A colorless crystal of approximate dimensions 0.471 x 0.362 x 0.317 mm was mounted in a cryoloop and transferred to a Bruker SMART APEX II diffractometer. The APEX2[49] program package was used to determine the unit-cell parameters and for data collection (30 sec/frame scan time for a sphere of diffraction data). The raw frame data was processed using SAINT[50] and SADABS[51] to yield the reflection data file. Subsequent calculations were carried out using the SHELXTL[52] program. The diffraction symmetry was 2/*m* and the systematic absences were consistent with the monoclinic space groups *Cc* and *C*2/*c*. It was later determined that space group *C*2/*c* was correct.

The structure was solved by dual space methods and refined on F^2 by full-matrix least-squares techniques. The analytical scattering factors[53] for neutral atoms were used throughout the analysis. Hydrogen atoms were included using a riding model. Disordered $SiMe_3$ groups were modelled isotropically in parts.

Least-squares analysis yielded wR2 = 0.1760 and Goof = 1.037 for 502 variables refined against 17021 data (0.74Å), R1 = 0.0638 for those 14459 data with $I > 2.0\sigma(I)$.

Table 4.11. Crystal data and structure refinement for ajr57.

Identification code	ajr57	
Empirical formula	C48 H120 Gd K N4 O6 Si8	
Formula weight	1270.54	
Temperature	133(2) K	
Wavelength	0.71073 Å	
Crystal system	Monoclinic	
Space group	C2/c	
Unit cell dimensions	a = 26.421(3) Å	a= 90°.
	b = 30.378(4) Å	b= 90.8796(17)°.
	c = 17.244(2) Å	g = 90°.
Volume	13839(3) $Å^3$	
Z	8	
Density (calculated)	1.220 Mg/m^3	
Absorption coefficient	1.198 mm^{-1}	
F(000)	5432	
Crystal color	colourless	
Crystal size	0.471 x 0.362 x 0.317 mm^3	
Theta range for data collection	1.341 to 28.868°	
Index ranges	-34 <= h <= 35, -39 <= k <= 40, -23 <= l <= 23	
Reflections collected	82756	
Independent reflections	17021 [R(int) = 0.0282]	
Completeness to theta = 25.500°	100.0 %	
Absorption correction	Semi-empirical from equivalents	
Max. and min. transmission	0.7458 and 0.6444	

Refinement method	Full-matrix least-squares on F^2
Data / restraints / parameters	17021 / 0 / 502
Goodness-of-fit on F^2	1.037
Final R indices [I>2sigma(I) = 14459 data]	R1 = 0.0638, wR2 = 0.1665
R indices (all data, 0.74 Å)	R1 = 0.0743, wR2 = 0.1760
Extinction coefficient	n/a
Largest diff. peak and hole	1.872 and -1.299 e.$Å^{-3}$

Table 4.12. Bond lengths [Å] and angles [°] for ajr57.

Gd(1)-N(3)	2.349(4)
Gd(1)-N(4)	2.351(4)
Gd(1)-N(1)	2.360(4)
Gd(1)-N(2)	2.362(4)
N(3)-Gd(1)-N(4)	102.76(16)
N(3)-Gd(1)-N(1)	110.35(14)
N(4)-Gd(1)-N(1)	115.70(15)
N(3)-Gd(1)-N(2)	113.89(14)
N(4)-Gd(1)-N(2)	110.30(17)
N(1)-Gd(1)-N(2)	104.21(13)

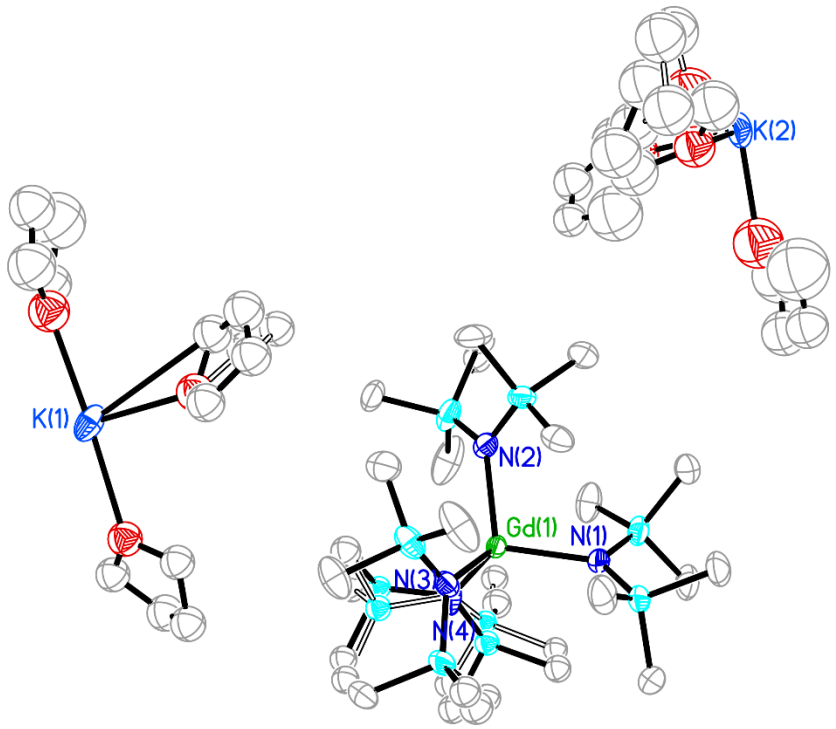

Figure 4.20. Thermal ellipsoid plot of **11-Gd** drawn at the 50% probability level.

Theoretical Details

Ground state density functional theory (DFT) calculations were carried out using the TPSSh[57] hybrid meta-generalized-gradient-approximation functional with Grimme's D3 dispersion[58,59] correction. The structures of the complexes $\{[(NR_2)_3Gd]_2[\mu\text{-}\eta^1\text{:}\eta^1\text{-}N_2]\}^{2-}$ (**5-Gd** end-on) and $\{[(NR_2)_3Gd]_2[\mu\text{-}\eta^2\text{:}\eta^2\text{-}N_2]\}^{2-}$ (**5-Gd** side-on) were optimized starting from the experimental X-ray structures. Karlsruhe polarized split valence (def2-SVP[60]) basis sets were used for the amide ligands and the Gd atoms, whereas larger polarized triple-ζ valence (def2-TZVPP[61]) basis sets were used for the bridging N atoms. Large core relativistic effective core potentials (ECPs) optimized by the Stuttgart-Dresden group[62] were used for the Gd atoms. Resolution of identity approximation was used for calculating the Coulomb integrals (RIJ)[63] in

the DFT calculations, quadrature grids of size m4 or larger[64] were employed along with a self-consistent field (SCF) convergence thresholds of 10-7H. Structures were converged to a gradient norm of 10-4a.u.. To account for solvation effects of THF, the COSMO continuum solvation model[65] was utilized with a dielectric constant of 7.52[66]. Optimization of **5-Gd** (end-on) resulted in a D_3-symmetric a triplet ground state, whereas optimization of **5-Gd** (side-on) resulted in a C_2-symmetric singlet ground state. The optimized ground states were confirmed to be minima by performing normal mode analysis[67]. The harmonic vibrational frequencies thus computed need to be scaled by a factor of 0.96[68] to account for anharmonicity in order to compare with experimental spectra. Calculated structural parameters as well as the harmonic vibrational frequency corresponding to the N-N stretching mode are reported in Table 4.13.

Table 4.13. Experimental values from **5-Gd** and calculated values from optimized DFT structures for select metrical parameters of $\{[(R_2N)_3Gd]_2[\mu\text{-}\eta^x\text{:}\eta^x\text{-}N_2]\}^{2-}$ (x = 1,2) and Raman stretching frequencies.

	Method	N−N(Å)	Gd−N(N_2)$_{avg}$(Å)	Gd−N(NR_2)$_{range}$(Å)	N=N $\nu(cm^{-1})$
$\{[(R_2N)_3Gd]_2[\mu\text{-}\eta^1\text{:}\eta^1\text{-}N_2]\}^{2-}$	TPSSh	1.206	2.213	2.379	1663
	Exp	1.271(12)	2.155(9)	2.216(2) - 2.295(2)	1630(3)
$\{[(R_2N)_3Gd]_2[\mu\text{-}\eta^2\text{:}\eta^2\text{-}N_2]\}^{2-}$	TPSSh	1.246	2.373	2.407	1468
	Exp	1.190(5)	2.363(3)	2.371(2) - 2.444(2)	—

To analyze the experimental Raman spectra of **5-Gd,** Raman scattering cross-sections were computed using the *egrad* module of TURBOMOLE[69,70]. For calculating the polarizability derivatives along the normal modes, the PBE0[71] hybrid GGA functional was used. The m4 DFT

integration grid used along with a SCF convergence threshold of 10^{-7} for these calculations. Solvation effects were taken into account at the level of the unperturbed Kohn-Sham (KS) orbitals. The Raman scattering cross sections for **5-Gd** (end-on) and **5-Gd** (side-on) were calculated as 0.25×10^{-12} and 0.23×10^{-14} $Bohr^2/sr$, respectively.

Table 4.14. Calculated values of the electronic energy at 0 K, enthalpy and entropy at 298.15 K using the TPSSh density functional for the optimized structures of **5-Gd (end-on)** and **5-Gd (side-on)** complexes.

	End-on	Side-on
Electronic Energy (E)	−5419.835815 H	−5419.838522 H
Enthalpy (H)	3895.88 kJ/mol	3905.64 kJ/mol
Entropy (S)	1974.52 J/(mol K)	1901.42 J/(mol K)

In Table 4.14 we report the ground state electronic energy (E) at 0 K as well as the enthalpy and entropy calculated at 298.15 K calculated using the quasi rigid-rotor harmonic oscillator approximation (quasi-RRHO) approach where the free-rotor entropy was used instead of vibrational entropy for all modes less than 100 cm^{-1}.[72] The Gibbs free energy change corresponding to the equilibrium between the **5-Gd (end-on)** and **5-Gd (side-on)** complexes can be calculated at 298.15 K as G = −24.39 kJ/mol, where $G = G_{end\text{-}on} - G_{side\text{-}on}$ and G = E + H − TS. This corresponds to an equilibrium constant of $K_{eq}=1.87 \times 10^4$ in favor of the **5-Gd (end-on)** structure and equilibrium mole fractions of 0.999946 and 5.33×10^{-5} for the **5-Gd (end-on)** and **5-Gd (side-on)** complexes, respectively in solution phase. Scaling the Raman scattering cross sections with these equilibrium mole fractions is required to compare the calculations with the experiments. The resulting scaled Raman intensities for the **5-Gd (end-on)** and **5-Gd (side-on)**

complexes are $2.5x10^{-13}$ and $1.2x10^{-19}$ $Bohr^2/sr$, respectively. This explains the intense peak in the experimental Raman spectra at 1630 cm^{-1} corresponding to the pure end-on complex.

Raman Spectra.

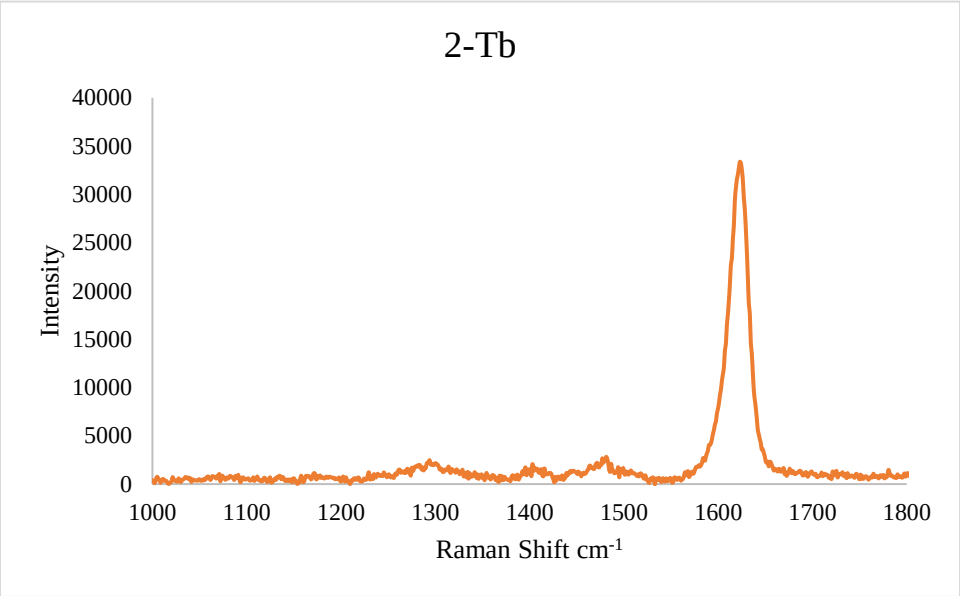

Figure 4.21. Raman spectrum of **2-Tb**

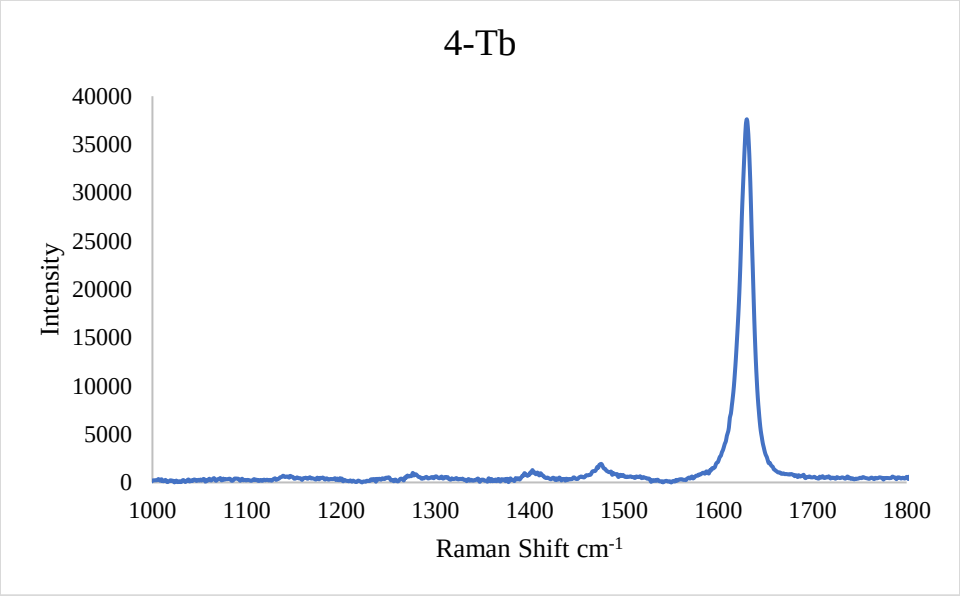

Figure 4.22. Raman spectrum of **4-Tb**

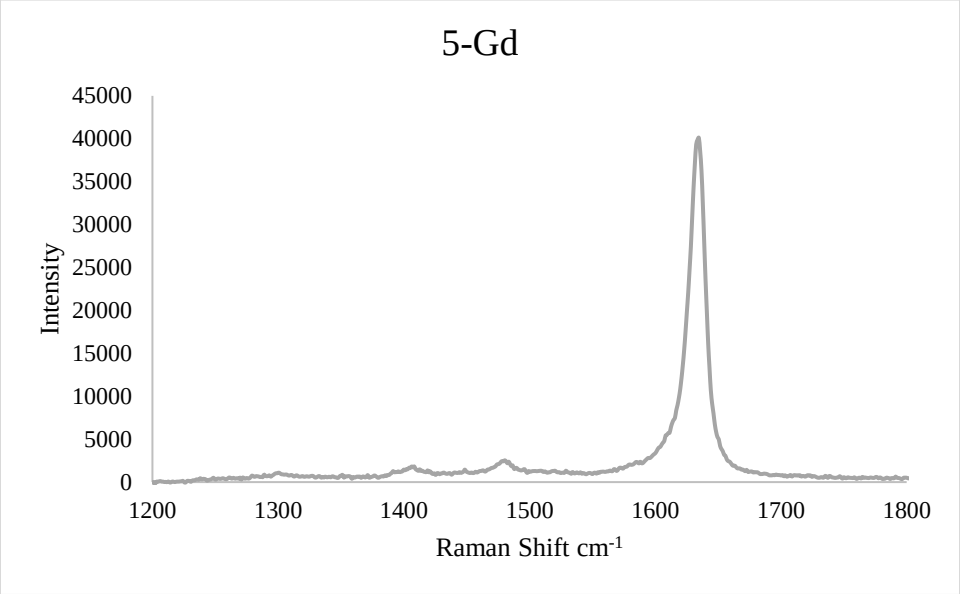

Figure 4.23. Raman spectrum of **5-Gd**

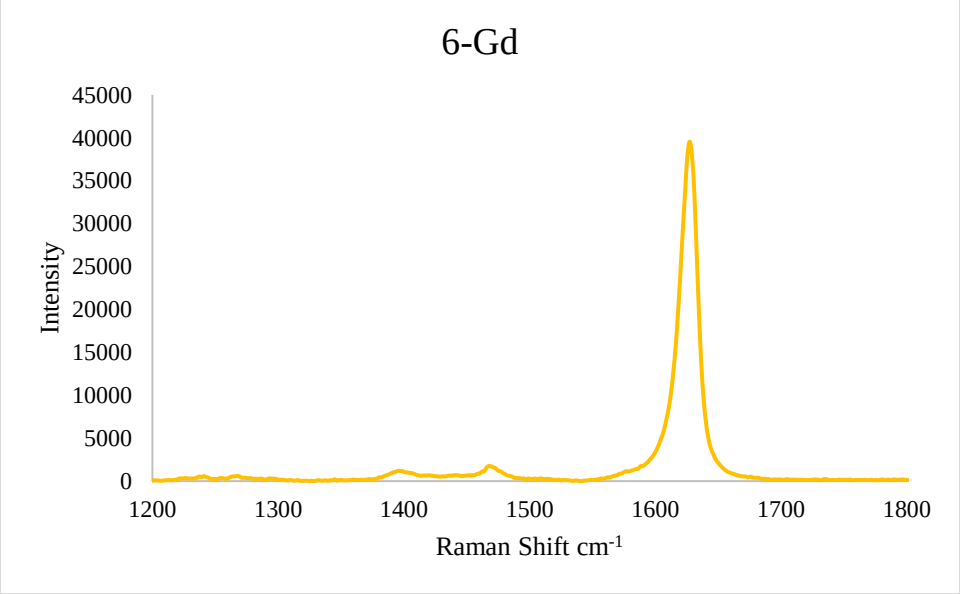

Figure 4.24. Raman spectrum of **6-Gd**

References.

1. W. J. Evans, T. A. Ulibarri and J. W. Ziller, *Journal of the American Chemical Society*, 1988, **110**, 6877-6879.
2. Y. Tanabe, in *Transition Metal-Dinitrogen Complexes*, 2019, DOI: 10.1002/9783527344260.ch9, pp. 441-474.
3. W. J. Evans, N. T. Allen and J. W. Ziller, *Journal of the American Chemical Society*, 2001, **123**, 7927-7928.
4. W. J. Evans, N. T. Allen and J. W. Ziller, *Angew. Chem. Int. Ed.*, 2002, **41**, 359-361.
5. W. J. Evans, S. A. Kozimor and J. W. Ziller, *Journal of the American Chemical Society*, 2003, **125**, 14264-14265.
6. W. J. Evans and D. S. Lee, *Can. J. Chem.*, 2005, **83**, 375-384.
7. W. J. Evans, D. S. Lee, M. A. Johnston and J. W. Ziller, *Organometallics*, 2005, **24**, 6393-6397.
8. W. J. Evans, D. S. Lee, C. Lie and J. W. Ziller, *Angew. Chem. Int. Ed.*, 2004, **43**, 5517-5519.
9. W. J. Evans, D. S. Lee, D. B. Rego, J. M. Perotti, S. A. Kozimor, E. K. Moore and J. W. Ziller, *Journal of the American Chemical Society*, 2004, **126**, 14574-14582.
10. W. J. Evans, D. S. Lee and J. W. Ziller, *Journal of the American Chemical Society*, 2004, **126**, 454-455.
11. W. J. Evans, D. S. Lee, J. W. Ziller and N. Kaltsoyannis, *Journal of the American Chemical Society*, 2006, **128**, 14176-14184.
12. W. J. Evans, G. Zucchi and J. W. Ziller, *Journal of the American Chemical Society*, 2003, **125**, 10-11.
13. S. M. Mansell, N. Kaltsoyannis and P. L. Arnold, *Journal of the American Chemical Society*, 2011, **133**, 9036-9051.
14. E. Campazzi, E. Solari, C. Floriani and R. Scopelliti, *Chem. Commun.*, 1998, DOI: 10.1039/A807405D, 2603-2604.
15. J. Cheng, J. Takats, M. J. Ferguson and R. McDonald, *Journal of the American Chemical Society*, 2008, **130**, 1544-1545.
16. F. G. N. Cloke and P. B. Hitchcock, *Journal of the American Chemical Society*, 2002, **124**, 9352-9353.
17. P. Roussel and P. Scott, *Journal of the American Chemical Society*, 1998, **120**, 1070-1071.
18. F. Jaroschik, A. Momin, F. Nief, X. F. Le Goff, G. B. Deacon and P. C. Junk, *Angew. Chem.*, 2009, **121**, 1137-1141.
19. W. J. Evans, M. Fang, G. Zucchi, F. Furche, J. W. Ziller, R. M. Hoekstra and J. I. Zink, *Journal of the American Chemical Society*, 2009, **131**, 11195-11202.
20. W. J. Evans, M. Fang, J. E. Bates, F. Furche, J. W. Ziller, M. D. Kiesz and J. I. Zink, *Nat. Chem.*, 2010, **2**, 644.
21. D. H. Woen, G. P. Chen, J. W. Ziller, T. J. Boyle, F. Furche and W. J. Evans, *Journal of the American Chemical Society*, 2017, **139**, 14861-14864.
22. A. J. Ryan, J. W. Ziller and W. Evans, *Chemical Science*, 2020, **7**, 2006-2014.
23. A. J. Ryan, L. E. Darago, S. G. Balasubramani, G. P. Chen, J. W. Ziller, F. Furche, J. R. Long and W. J. Evans, *Chemistry–A European Journal*, 2018, **24**, 7702-7709.

24. J. F. Corbey, D. H. Woen, C. T. Palumbo, M. E. Fieser, J. W. Ziller, F. Furche and W. J. Evans, *Organometallics*, 2015, **34**, 3909-3921.
25. S. A. Moehring, M. J. Beltrán-Leiva, D. Páez-Hernández, R. Arratia-Pérez, J. W. Ziller and W. J. Evans, *Chemistry – A European Journal*, 2018, **24**, 18059-18067.
26. P. L. Holland, *Dalt. Trans.*, 2010, **39**, 5415-5425.
27. P. B. Hitchcock, A. G. Hulkes, M. F. Lappert and Z. Li, *Dalt. Trans.*, 2004, DOI: 10.1039/B311397C, 129-136.
28. M. R. MacDonald, J. W. Ziller and W. J. Evans, *Journal of the American Chemical Society*, 2011, **133**, 15914-15917.
29. M. R. MacDonald, J. E. Bates, J. W. Ziller, F. Furche and W. J. Evans, *Journal of the American Chemical Society*, 2013, **135**, 9857-9868.
30. M. E. Fieser, D. H. Woen, J. F. Corbey, T. J. Mueller, J. W. Ziller and W. J. Evans, *Dalt. Trans.*, 2016, **45**, 14634-14644.
31. K. R. Meihaus, J. F. Corbey, M. Fang, J. W. Ziller, J. R. Long and W. J. Evans, *Inorg. Chem.*, 2014, **53**, 3099-3107.
32. M. Fang, J. E. Bates, S. E. Lorenz, D. S. Lee, D. B. Rego, J. W. Ziller, F. Furche and W. J. Evans, *Inorg. Chem.*, 2011, **50**, 1459-1469.
33. J. D. Rinehart, M. Fang, W. J. Evans and J. R. Long, *Nat. Chem.*, 2011, **3**, 538-542.
34. J. D. Rinehart, M. Fang, W. J. Evans and J. R. Long, *Journal of the American Chemical Society*, 2011, **133**, 14236-14239.
35. M. R. MacDonald, J. E. Bates, M. E. Fieser, J. W. Ziller, F. Furche and W. J. Evans, *Journal of the American Chemical Society*, 2012, **134**, 8420-8423.
36. N. Leconte, J. Moutet, T. Constantin, F. Molton, C. Philouze and F. Thomas, *Eur. J. Inorg. Chem.*, 2018, **2018**, 1752-1761.
37. Y. Shimazaki, T. D. P. Stack and T. Storr, *Inorg. Chem.*, 2009, **48**, 8383-8392.
38. R. Shannon, *Acta Crystallographica Section A*, 1976, **32**, 751-767.
39. J. M. Manriquez and J. E. Bercaw, *Journal of the American Chemical Society*, 1974, **96**, 6229-6230.
40. R. D. Sanner, J. M. Manriquez, R. E. Marsh and J. E. Bercaw, *Journal of the American Chemical Society*, 1976, **98**, 8351-8357.
41. J. A. Pool, E. Lobkovsky and P. J. Chirik, *Nature*, 2004, **427**, 527-530.
42. W. H. Bernskoetter, E. Lobkovsky and P. J. Chirik, *Journal of the American Chemical Society*, 2005, **127**, 14051-14061.
43. H. Brintzinger and J. E. Bercaw, *Journal of the American Chemical Society*, 1971, **93**, 2045-2046.
44. J. M. de Wolf, R. Blaauw, A. Meetsma, J. H. Teuben, R. Gyepes, V. Varga, K. Mach, N. Veldman and A. L. Spek, *Organometallics*, 1996, **15**, 4977-4983.
45. T. E. Hanna, W. H. Bernskoetter, M. W. Bouwkamp, E. Lobkovsky and P. J. Chirik, *Organometallics*, 2007, **26**, 2431-2438.
46. S. P. Semproni, C. Milsmann and P. J. Chirik, *Organometallics*, 2012, **31**, 3672-3682.
47. M. P. Coles, P. B. Hitchcock, A. V. Khvostov, M. F. Lappert, Z. Li and A. V. Protchenko, *Dalt. Trans.*, 2010, **39**, 6780-6788.
48. D. N. Huh, J. W. Ziller and W. J. Evans, *Dalt. Trans.*, 2018, **47**, 17285-17290.
49. APEX2 Version 2014.11-0, Bruker AXS, Inc.; Madison, WI 2014.
50. SAINT Version 8.34a, Bruker AXS, Inc.; Madison, WI 2013.
51. Sheldrick, G. M. SADABS, Version 2014/5, Bruker AXS, Inc.; Madison, WI 2014.

52. Sheldrick, G. M. SHELXTL, Version 2014/7, Bruker AXS, Inc.; Madison, WI 2014.
53. International Tables for Crystallography 1992, Vol. C., Dordrecht: Kluwer Academic Publishers.
54. Sheldrick, G. M. CELL_NOW, Version 2008/4, Bruker AXS, Inc.; Madison, WI 2008.
55. Sheldrick, G. M. TWINABS, Version 2012/1, Bruker AXS, Inc.; Madison, WI 2012.
56. Parsons, S., Flack, H. D., Wagner, T. Acta Cryst. B69, 249-259, 2013.
57. Staroverov, V.; Scuseria, G. E.; Tao, J.; Perdew, J. P. *J. Chem. Phys.* **2003**, 119 (23), 12129-12137.
58. Grimme, S., Semiempirical GGA-type density functional constructed with a long-range dispersion correction. *J. Comput. Chem.* **2006**, 27, 1787-1799.
59. Grimme, S.; Antony, J.; Ehrlich, S.; Krieg, H. *J. Chem. Phys.* **2010**, 132, 154104-154123.
60. Eichkorn, K.; Weigend, F.; Treutler, O.; Ahlrichs, R. *Theor. Chem. Acc.* **1997**, *97, 119-124.*
61. Werigend, F.; Haeser, M.; Patzelt, H.; Ahlrichs, R. *Chem. Phys. Lett.* **1998**, *294 (1), 143-152.*
62. Dolg, M.; Stoll, H.; Preuss, H. *Theor. Chim. Acta* **1993**, *85, 441.*
63. Eichkorn, K.; Weigend, F.; Treutler, O.; Ahlrichs, R. *Theor. Chem. Acc.* **1997**, 97, 119-124.
64. Treutler, O.; Ahlrichs, R., Efficient molecular numerical integration schemes. *J. Chem. Phys.* **1995**, *102, 346.*
65. Klamt, A.; Schüürmann, G. *J. Chem. Soc., Perkin Trans.* **1993**, *2, 799-805.*
66. In CRC Handbook of Chemistry and Physics; Lide, D. R., Ed.; CRC Press: Boca Raton, FL, **2008**; Vol. 88, p 136-136.
67. Deglmann, P.; Furche, F.; Ahlrichs, R. *Chem. Phys. Lett.* **2002**, 362(5), 511-518.
68. D. O. Kashinski, D. O.; Chase, G. M.; Nelson, R. G.; Di Nallo, O. E.; Scales, A. N.; VanderLey, D. L.; Byrd, E. F. C. *J. Phys. Chem. A*, **2017**, 121, 11, 2265-2273.
69. Furche, F.; Ahlrichs, R.; Haettig, C.; Klopper, W.; Sierka, M.; Weigend, F., TURBOMOLE. *WIREs Comput. Mol. Sci.*, **2013**, 4, 91-100.
70. Rappoport, D.; Furche, F. *J. Chem. Phys.* **2007**, 126, 201104.
71. Adamo, C.; Barone, V. *J. Chem. Phys.* **1998**, 110, 6158.
72. Grimme, S. *Chem. Eur. J.* **2012**, 18, 9955–9964.

Chapter 5

Reactivity of Gd(II) with Toluene and the Formation of Trivalent and Divalent Gd Coordination Polymers

Introduction

Reductive chemistry of the Ln(III) ions in the presence of arenes has resulted in an array of interesting reduced arene lanthanide complexes.[1-9] Early work by Lappert, et al. showed that reduction of tris(silylcyclopentantadienyl) lanthanide complexes of the type $LnCp''_3$ or $[LnCp''_2(\mu\text{-}Cl)]_2$ ($Cp'' = C_5H_3(SiMe_3)_2$ Ln = La, Ce, Nd) with K in the presence of 18-crown-6 (18-c-6) in benzene allowed the isolation of the cyclohexadienyl complex $[K(18\text{-}c\text{-}6)][(C_6H_6)LnCp''_2]$, eq 5.1.[1, 3]

If, however, 1.5 equivalents of potassium are used instead of an excess then a compound postulated to contain a bridging benzene monoanion, $[K(18\text{-crown-}6)(THF)_2][(Cp''_2La)_2(\mu\text{-}\eta^6\text{:}\eta^6\text{-}C_6H_6)]$, is produced.[2] This hypothesis was confirmed to be correct when Palumbo, et. al synthesized the complex in question in 2018, eq 5.2.[9] When the all carbon analog of Cp″, namely $C_5H_3(CMe_3)_2$ (Cp^{tt}), is used under similar conditions analogous products are isolated.[10] The less sterically demanding $C_5H_4SiMe_3$ ligand, Cp′, was also used to explore reductive arene chemistry. Reduction of Cp'_3Ln with 4 equivalents of KC_8 in the presence of 4 equivalents of 2.2.2-cryptand (crypt) in benzene resulted in the isolation of a benzene dianion bridging two divalent lanthanide centers, eq 5.3. This dependency of the reaction products on chelating agent and steric considerations of the ligand is consistent with observations in the reductive chemistry described for the Ln(II) tris(amide) systems in Chapters 1, 2 and 4. To date there have been no reported examples of reduced toluene or benzene systems of lanthanides supported by amide ligands. Described in this chapter is the reactivity of toluene with $Gd(NR_2)_3$ under reducing conditions.

Reaction of the isolated Gd(II) tris(amide) complex, [K(crypt)][Gd(NR_2)$_3$], with toluene is detailed in addition to LnA_3/M/chelate reactivity where LnA_3 = Gd(NR_2)$_3$, M = K and chelate = crypt or 18-c-6.

Results and Discussion

Toluene with Gd(II) Generated In Situ. Addition of a pre-chilled solution of Gd(NR_2)$_3$ (R = $SiMe_3$) and 18-crown-6 (18-c-6) in Et_2O (−35 °C) containing 5 drops of toluene to a prechilled vial containing 4 equivalents of KC_8 results in a color change from colorless to deep blue. Initially, the reaction was allowed to proceed for approximately 5 minutes before being layered into hexanes and replaced in the glovebox freezer at −35 °C. Two types of crystals grew overnight both suitable for X-ray diffraction. One set were deep blue crystals which exhibited a polymeric structure containing Gd(II) ions, {[K(18-c-6)][Gd(NR_2)$_3$]}$_x$, **1-Gd**, Figure 5.1.

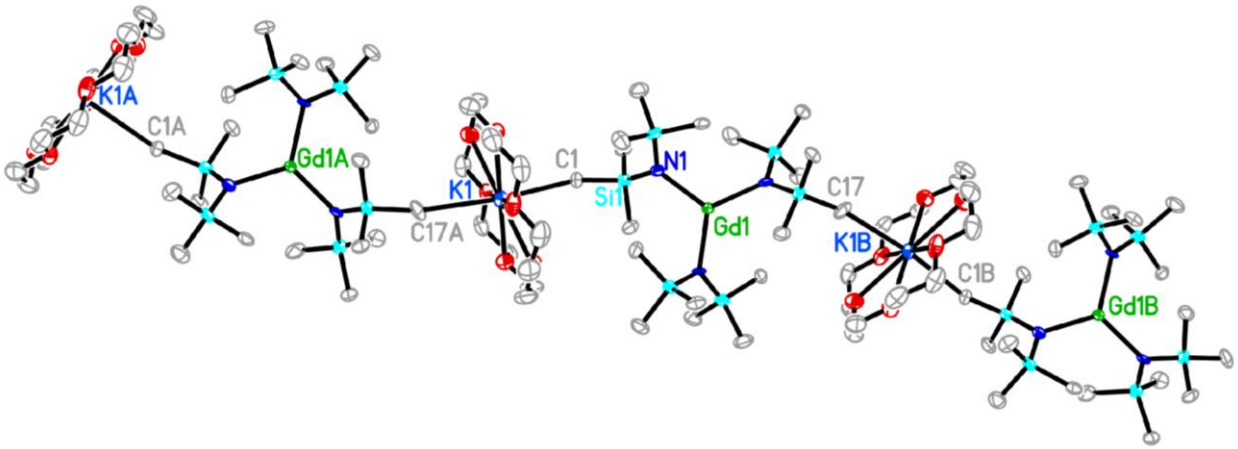

Figure 5.1. Thermal ellipsoid plot of **1-Gd** drawn at the 50% probability level. Hydrogen atoms have been excluded for clarity.

The second set were dichroic and looked either purple or green depending on the orientation of the crystal under the microscope. Diffraction of these crystals revealed the

structure of a Gd(III) reduced toluene complex, $\{[K(18\text{-}c\text{-}6)][(C_6H_5Me)Gd(NR_2)_2]\}_x$, **2-Gd**, which also was polymeric, Figure 5.2.

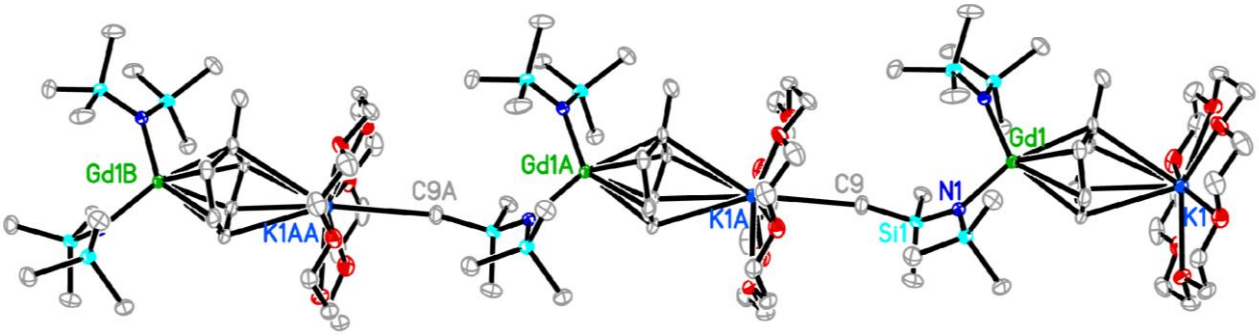

Figure 5.2. Thermal ellipsoid plot of **2a-Gd** drawn at the 50% probability level. Hydrogen atoms were excluded for clarity.

If the reaction is allowed to proceed overnight over KC_8 in the glove box freezer at −35 °C then **2-Gd** is isolated exclusively after filtration and layering into hexanes, eq 5.4. These results suggest that reduction from Gd(III) to Gd(II) may first be required to facilitate the toluene reduction.. If the solution is allowed to warm to room temperature the color changes deep purple/green to orange over the course of 24 hours.

In contrast, if a solution of $Gd(NR_2)_3$ and 2.2.2-cryptand (crypt) in THF (THF is used in place of ether due to the limited solubility of crypt in Et_2O) with 5 drops of toluene are added to a vial containing KC_8 at −35 °C, a dark color results. However, upon layering with hexanes and placement in the glovebox freezer, the ring-opened THF product $[K(crypt)][C_4H_9OGd(NR_2)_3]$, **3-Gd,** is isolated, eq 5.4 Figure 5.3. Ring-opened THF complexes of Sm, $(C_5Me_5)_2Sm[O(CH_2)_4C_5Me_5](THF)$ and $(C_5Me_5)_2Sm[O(CH_2)_4AsPh_2](THF)$, have previously been reported and are proposed to arise from nucleophilic attack of a $(\eta^1\text{-}C_5Me_5)^{1-}$ or $(AsPh_2)^{1-}$ anion on a THF activated by coordination to the Sm ion.[11, 12] In the case of **3-Gd**, the formula

would be consistent with nucleophilic attack by a hydride generated over the course of the reaction.

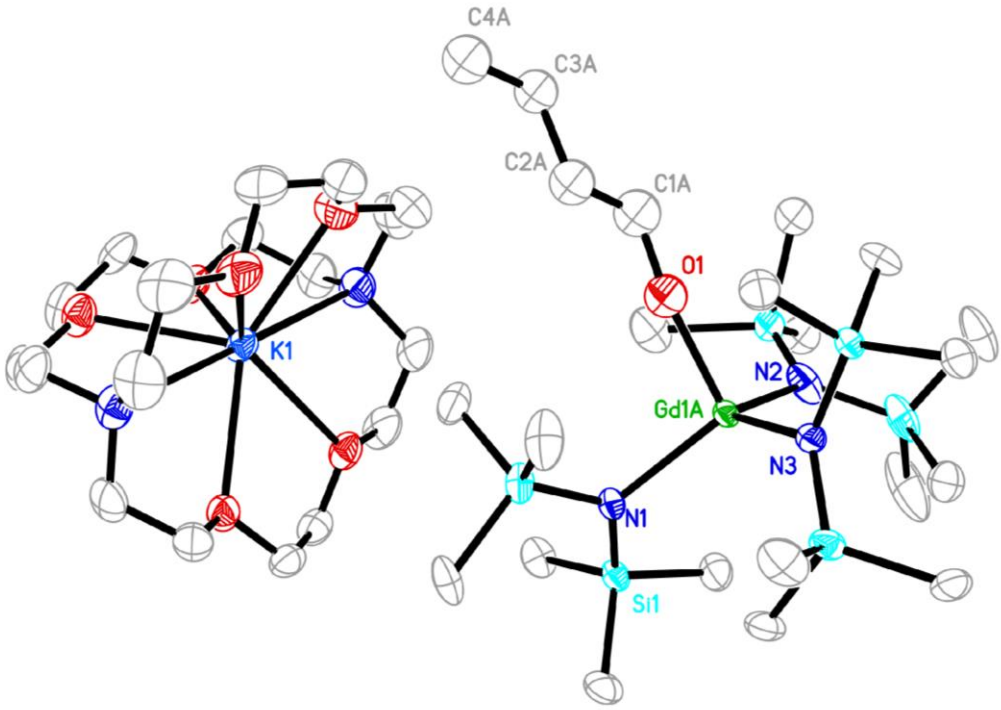

Figure 5.3. Thermal ellipsoid plot of **3-Gd** drawn at the 50% probability level. Hydrogen atoms and disordered ^{n}butoxide, TMS group, and Gd excluded for clarity.

Toluene with Isolated Gd(II) Complexes. Reactions of the isolated divalent gadolinium complex, [K(crypt)][Gd(NR$_2$)$_3$] (crypt = 2.2.2-cryptand), with toluene were also attempted. Dissolving [K(crypt)][Gd(NR$_2$)$_3$] in toluene and layering with hexanes results in recovery of the Gd(II) starting material [K(crypt)][Gd(NR$_2$)$_3$], **4-Gd**. Interestingly, the complex is isolated in a different unit cell than the previously isolated version of the complex described in Chapter 1. **4-Gd** crystallized in the R*32* space group showing only one sixth of the anion and one sixth of the cation respectively.

Structure of {[K(18-c-6)][Gd(NR$_2$)$_3$]}$_x$, 1-Gd. Complex **1-Gd** crystallizes in the P2$_1$/c space group with one [K(18-c-6)]$^{1+}$ unit per [Gd(NR$_2$)$_3$]$^{1-}$ anion in a polymeric structure where methyl groups from the NR$_2$ ligands have close contacts to the axial positions of the [K(18-c-6)]$^{1+}$ cation, Figure 5.1. The K…C(methyl) distances for the methyl contacts are 3.139(9) and 3.140(9) Å. These distances are similar to previously recorded agostic interactions of methyl groups with potassium cations in complexes of [K(arene)$_2$][Mg(NR$_2$)$_3$]$_x$ (arene = benzene, toluene, p-xylene) 3.177(2) - 3.228(3) Å.[13] These methyl K contacts are also seen in [K(18-c-6)$_2$][Tm(NR$_2$)$_3$] which crystallizes in the P2$_1$2$_1$2$_1$ space group and displays a K…C(methyl) contact distance of 3.322(9) Å, Figure 2.10. The structure of **1-Gd** contrasts with all of the other [K(18-c-6)$_2$][Ln(NR$_2$)$_3$] complexes, described in Chapter 2, which all crystallize in the P2$_1$/n space group (except for Ln = Tm) and contain two 18-c-6 chelates per K$^+$ ion and monomeric structures, Figure 2.1. The Gd–N distances in **1-Gd** range from 2.289(6) - 2.318(6) Å and are similar to the 2.301(3) - 2.308(3) Å range observed for the [K(18-c-6)$_2$]$^{1+}$ analog. The pyramidalization of the Gd ion from the N$_3$ donor plane in **1-Gd** is 0.029 Å which is significantly less than the 0.129 and 0.523 Å pyramidalizations observed in [K(18-c-6)$_2$][Ln(NR$_2$)$_3$] (Table 2.1) and [K(crypt)][Ln(NR$_2$)$_3$] (Table 2.1) respectively. Bond metrics are summarized in Table 5.1.

Table 5.1. Comparison of metal ligand distances (Å) of {[K(18-c-6)][Gd(NR$_2$)$_3$]}$_x$ **(1-Gd)**, [K(18-c-6)$_2$][GdNR$_2$)$_3$], [K(crypt)][Gd(NR$_2$)$_3$] (R32), and [K(crypt)][Gd(NR$_2$)$_3$] (P-1).

	{[K(18-c-6)][Gd(NR$_2$)$_3$]}$_x$	[K(18-c-6)$_2$]-[GdNR$_2$)$_3$]	[K(crypt)][Gd(NR$_2$)$_3$] (R32)	[K(crypt)][Gd(NR$_2$)$_3$] (P-1)
Ln–N (range)	2.289(6) - 2.318(6)	2.301(3) - 2.308(3)	2.315(3)- 2.316(3)	2.289(2) - 2.342(18)
Ln–N$_{plane}$ (avg)	0.029	0.158	0	0.523

Structure of {[K(18-c-6)][(C_6H_5Me)Gd(NR_2)$_2$]}$_x$, 2-Gd. Complex **2-Gd** was found to crystallize in both the P-1 (**2a-Gd**) and the C2/c (**2b-Gd**) space groups. Both structures contain polymeric structures where the $[K(18\text{-c-}6)]^{1+}$ cation is coordinated by four carbon atoms of the toluene dianion and a methyl group of an NR_2 ligand, Figure 5.2. The orientation of the reduced toluene species is slightly different from **2a-Gd** to **2b-Gd** in that the close contacts to the K^{1+} ion contain the methyl-substituted carbon in **2a-Gd**, but not in **2b-Gd**. The bond metrics of **2a-Gd** and **2b-Gd** are within error of each other except for the closest carbon contacts to the K^{1+} cation which are slightly shorter in **2b-Gd** than in **2a-Gd** potentially due to a more tightly packed cell in the monoclinic vs triclinic space group, respectively. For clarity the details of **2a-Gd** will be discussed here with metrics for both **2a-Gd** and **2b-Gd** summarized in Table 5.2

The reduced toluene ligand has metrical parameters consistent with a cyclohexadienyl dianion.[3, 10] In **2a-Gd** the reduced toluene shows bond lengths consistent with C−C double bonds for the C1−C2 and C4−C5 bonds, 1.364(2) and 1.360(2) Å, respectively, Figure 5.4. The other four C−C bonds in the ring have distances ranging from 1.470(3) - 1.483(2) Å. These distances are in line with those reported for [K(18-c-6)][(C_6H_6)LnCp″$_2$] which show 4 longer bond lengths 1.445(7) - 1.480(9) and 2 shorter bonds 1.337(11) - 1.363(7) Å.[1, 3] The reduced toluene has a boat configuration with a dihedral angle of 29.7° between the C6 C1 C2 C3 and C6 C5 C4 C3 planes similar to, but slightly larger than, the dihedral angles observed in the [K(18-c-6)][(C_6H_6)LnCp″$_2$] analogs, 23.5 - 24.7°. The C6 and C3 carbons have the shortest distances to the Gd ion of the six ring carbons, 2.4570(17) and 2.4808(16) Å respectively, vs a range of 2.6979(15) - 2.7264(16) Å for the four other carbons. Carbons C6 and C3 also have the longest C−C_{ring} distances, 1.470(3) - 1.483(2).

The Gd−N distances are 2.3238(12) and 2.3408(12) Å where the longer distance belongs to the NR_2 ligand whose methyl group coordinates the K ion. In **2a-Gd** the K…C interaction from the methyl group of the NR_2 ligand is 3.4337(18) Å, which is longer than those observed in **1-Gd** or $[K(arene)_2][Mg(NR_2)_3]$, 3.177(2) - 3.228(3). If the C_6 ring coordinated is taken to occupy three coordination sites with two anionic donors then an appropriate comparison can be made with the bis(amide) bridging chloride complex $\{Gd[N(SiMe_3)_2]_2(\mu\text{-}Cl)(THF)\}_2$ which contains a five coordinate Gd ion supported by two NR_2 ligands and two bridging chloride ligands in addition to a THF.[14] The Gd−N distances in this compound are 2.239(5) and 2.264(5) Å, shorter than those observed in **2a-Gd**. It should be taken into account however that the two chlorides coordinated in $\{Gd[N(SiMe_3)_2]_2(\mu\text{-}Cl)(THF)\}_2$ are 2.740(4) and 2.765(4) Å from the Gd ion while the all six of the carbons on the methylcyclohexadienyl dianion are within 2.726(16) Å of the Gd ion in **2a-Gd**.

There are four carbon atoms on the ring with close contacts to the K ion ranging from 3.0949(16) - 3.4245(16) Å. The range of the ring carbon contacts is similar to those observed in $[K(18\text{-}c\text{-}6)][(C_6H_6)LnCp''_2]$ (Ln = La, Ce, Nd; Cp″ = $C_5H_3(SiMe_3)_2$), 3.046(5) – 3.395(5) Å, however, they occur at different carbon positions. For $[K(18\text{-}c\text{-}6)][(C_6H_6)LnCp''_2]$ the close C…K contacts occur with the pairs of carbon atoms involved in double bonds in a cyclohexadienyl structure, positions 1, 2, 4, and 5, while the close contacts in **2a-Gd** occur at the C1, C2, C3 and C4 where C1 and C2 correspond to a double bond while C3 is an anionic carbon singly bound to C2 and C4 which is subsequently doubly bound to C5, Figure 5.4.

Table 5.2. Comparison of metal ligands distances (Å) and ring dihedral angles (°) of **2a-Gd**, **2b-Gd**, and [K(18-c-6)][(C_6H_6)NdCp″$_2$].

Bond/angle	**2a-Gd**	**2b-Gd**	[K(18-c-6)][(C_6H_6)NdCp″$_2$]
Ln−C(anionic)	2.457(2), 2.480(2)	2.465(3), 2.483(3)	2.555(5) – 2.572(5)
Ln−N	2.323(1), 2.340(1)	2.324(2), 2.348(2)	-
C=C(ring)	1.360(3), 1.364(2)	1.357(4), 1.374(4)	1.363(7), 1.344(7)
C−C(ring)$_{range}$	1.470(2) - 1.483(2)	1.462(4) - 1.481(4)	1.439(7) - 1.452(7)
Dihedral angle(ring)	29.7	29.5	24.7
K−C(ring)$_{range}$	3.095(1) – 3.424(1)	3.063(3) - 3.391(3)	3.046(5) - 3.395(5)
K−C(methyl)	3.433(1)	3.331(3)	-

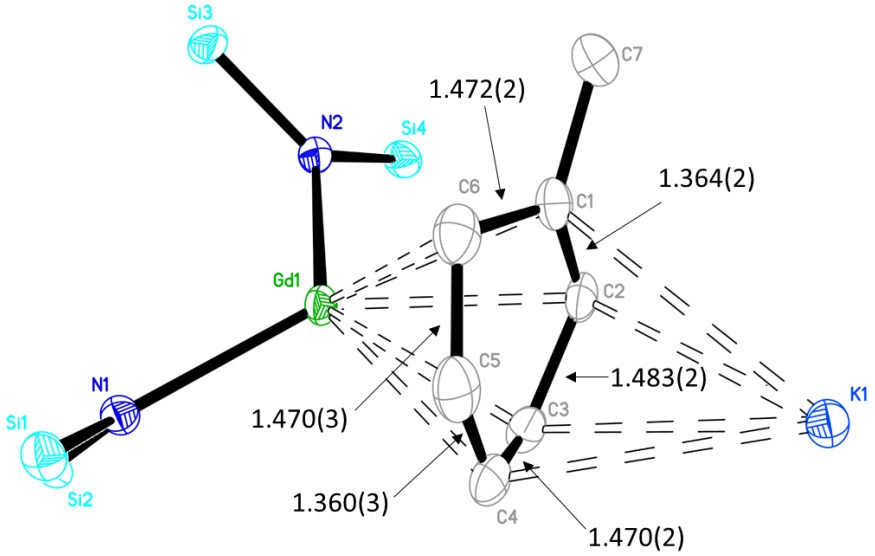

Figure 5.4. Close up thermal ellipsoid plot of **2a-Gd** drawn at the 50% probability level. 18-c-6, methyl groups and hydrogen atoms have been excluded for clarity. Ring bond distances are shown in Å.

Structure of [K(crypt)][$C_4H_9OGd(NR_2)_3$], 3-Gd. Complex **3-Gd** crystallized in the $P2_1/c$ space group as a two-component twin. The Gd ion has a small disorder of 3% similar to that seen in [K(18-c-6)$_2$][Ln(NR_2)$_3$] described in Chapter 2. The major Gd component (97%) shows a pseudo tetrahedral coordination environment with three amide ligands and the n-butoxide ligand. This is the first example of a ring-opened THF complex with a Gd ion. The

Gd−N distances range from 2.338(4) - 2.340(4) Å, while the Gd−O distance is significantly shorter 2.090(4) Å. Comparing **3-Gd** to $LGd(NR_2)_2$ (L = $CH_3C(O)=CHC(CH_3)=NCH_2CH_2(2\text{-}C_5H_4N)$, R = $SiMe_3$)[15] which contains a five coordinate Gd(III) ion ligated by two NR_2 ligands as well as two neutral nitrogen donors and an anionic oxygen atom, the Gd−NR_2 distances are slightly longer, 2.338(4) - 2.340(4) vs 2.289(2) - 2.311(2), respectively. The Gd−O distance on the other hand is longer in $LGd(NR_2)_2$, 2.189(2) Å, than in **3-Gd**, 2.090(4) Å . The significantly longer Gd−O distance in $LGd(NR_2)_2$ can be accounted for by the delocalization of the ligand L which is conjugated between the oxygen donor and one of the N donors. There are two ring-opened THF Sm complexes, $((C_5Me_5)_2Sm[O(CH_2)_4C_5Me_5](THF)$ and $(C_5Me_5)_2Sm[O(CH_2)_4AsPh_2](THF)$, which show Ln−O distances of 2.08(1) and 2.085(5) Å respectively, similar to that of **3-Gd**.

Table 5.3 Selected bond distances (Å) of $[K(crypt)][C_4H_9OGd(NR_2)_3]$ (**3-Gd**), $LGd(NR_2)_2$ (L = $CH_3C(O)=CHC(CH_3)=NCH_2CH_2(2\text{-}C_5H_4N)$),[15] $(C_5Me_5)_2Sm[O(CH_2)_4C_5Me_5](THF)$[11] and $(C_5Me_5)_2Sm[O(CH_2)_4AsPh_2](THF)$[12].

	[K(crypt)] $[C_4H_9OGd(NR_2)_3]$	$LGd(NR_2)_2$	$(C_5Me_5)_2Sm$ $[O(CH_2)_4C_5Me_5](THF)$	$(C_5Me_5)_2Sm$ $[O(CH_2)_4AsPh_2](THF)$
Ln− O	2.090(4)	2.189(2)	2.08(1)	2.085(5)
Ln−NR_2	2.289(2) - 2.311(2)	,2.338(4) - 2.340(4)	-	-

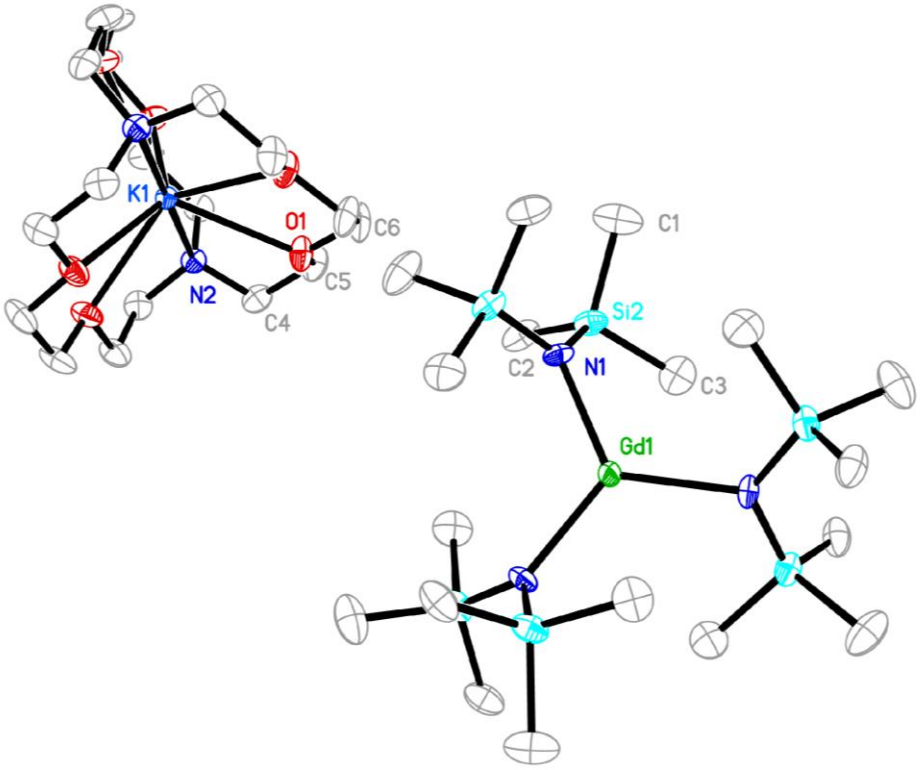

Figure 5.5. Thermal ellipsoid plot of **4-Gd** drawn at the 50% probability level. Hydrogen atoms were omitted for clarity.

Structure of [K(crypt)][Gd(NR$_2$)$_3$], 4-Gd. Complex **4-Gd** crystallizes in the R*32* space group showing one sixth of the structure where the rest is generated by symmetry, Figure 5.4. Unlike the previously reported example of [K(crypt)][GdNR$_2$)$_3$] which crystallized in the P-1 space group, there is no pyramidalization of the Gd ion from the N$_3$ donor plane. The Gd−N distance is 2.315(3) Å, within error of the previously reported [Gd(NR$_2$)$_3$]$^{1-}$ complexes[16, 17] (Chapters 1 and 2) Table 5.1.

Spectroscopy. A UV-visible spectrum was acquired for **2-Gd** for comparison to the [K(18-c-6)][(C$_6$H$_6$)LnCp″$_2$] complex of Lappert.[2, 3] The spectrum shows a broad absorbance around 410 nm (ε = 600 cm^{-1}mol^{-1}) in addition to a stronger absorbance at 275 nm (ε = 4000 cm^{-1}mol^{-1}), Figure 5.6, similar to those of [K(18-c-6)][(C$_6$H$_6$)LnCp″$_2$] which showed

absorbances at 463, 348 and 280 nm.[3] Notably, the shoulder at 348 nm was not observed for **2-Gd**. This shoulder could arise from the Cp″ ligands which are not present in **2-Gd**. Solutions of dicyclohexyl-18-crown-6 in benzene or toluene will dissolve potassium metal and show absorbances at 300 and 435 nm[18, 19] attributed to the respective arene anion at −80 °C, similar to those observed in **2-Gd**. Decomposition of **2-Gd** leads to a light orange solution whose spectrum shows the disappearance of the band at 410 nm and reduction of peak at 275 nm to a shoulder.

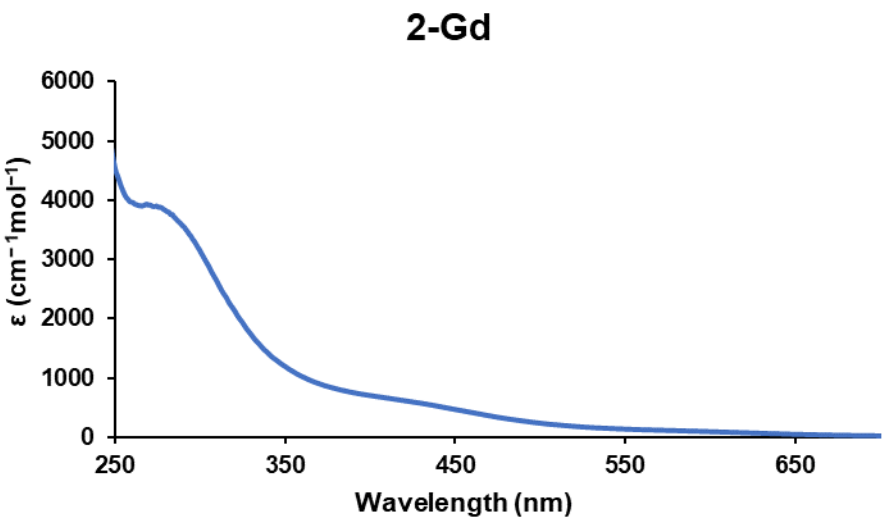

Figure 5.6. UV-visible spectrum of **2-Gd** in Et_2O (6mM) at 293K.

Conclusion

Reductive chemistry of $Gd(NR_2)_3$ in Et_2O allowed for isolation of a reduced arene complex having a polymeric solid state structure, $\{[K(18\text{-c-}6)][(C_6H_5Me)Gd(NR_2)_2]\}_x$, **1-Gd**. This marks the first example of a lanthanide reduced arene complex supported by amide ligands. Additionally the polymeric Gd(II) complex $\{[K(18\text{-c-}6)][(C_6H_5Me)Gd(NR_2)_2]\}_x$, **2-Gd**, was isolated which contrasts with the previously isolated monomeric $[K(18\text{-c-}6)_2][Ln(NR_2)_3]$ complexes (Ln = Gd, Tb, Dy, Ho, Er, and Tm) which were isolated with two 18-c-6 units per K^+ ion even in cases when only one equivalent of 18-c-6 was added.[17] This result highlights the

sensitivity of the reductive chemistry to solvent since the only noticeable difference in the reaction pathway leading to **1-Gd** is the presence of toluene in the Et_2O.

Isolation of [K(crypt)][$Gd(NR_2)_3$] from toluene in a new unit cell showing a perfectly planar coordination of amide ligands around the Gd(II) ion shows some consistency with previous reports of in situ IR studies outlining a lack of in situ pyramidalization of the trivalent $Ln(NR_2)_3$ complexes when measured in arene solvents vs a significant pyramidalization when measured in ethereal solvents.[20] Further, when the reduction of $Gd(NR_2)_3$ is performed in a THF/toluene mix in the presence of crypt no reduced arene or Gd(II) complexes are recovered, rather, a ring opened THF product, [K(crypt)][$C_4H_9OGd(NR_2)_3$], **3-Gd**, is observed. The origin of the hydrogen atom that has added to C_4H_8O is unknown, but there is precedent for forming rare earth hydrides in Ln(II) reactions.[21-24]

The broad range of isolable compounds isolated from similar reactions with minor alterations to conditions such as reaction time, chelating agent, and solvent emphasizes the importance of minor details in tuning the reductive reactivity of these Ln(II) amide complexes.

Experimental Details

All manipulations and syntheses described below were conducted with the rigorous exclusion of air and water using standard Schlenk line and glovebox techniques under an argon atmosphere. Solvents were sparged with UHP argon and dried by passage through columns containing Q-5 and molecular sieves prior to use. Infrared spectra were collected as thin films on an Agilent Cary 630 equipped with a diamond ATR attachment. UV-visible spectra were collected on an Agilent Cary 60 UV-visible spectrometer. Anhydrous $GdCl_3$,[25] $Gd(NR_2)_3$ ($R=SiMe_3$),[26] and KC_8[27] were prepared according to literature procedures. 18-Crown-6 (Alfa

Aesar) was sublimed before use. 2.2.2-cryptand (Alfa Aesar) was dried under vacuum overnight before use.

[K(18-c-6)][Gd(NR$_2$)$_3$]$_x$ 1-Gd and [K(18-c-6)][(C$_6$H$_5$Me)Gd(NR$_2$)$_2$]}$_x$, 2-Gd. Gd(NR$_2$)$_3$ and 18-c-6 were dissolved in about 2 ml of Et$_2$O with 5 drops of toluene and chilled to −35 °C before being added to a pre-chilled vial of KC$_8$. The solution was allowed to react for about 1 min before being filtered, layered with hexanes and replaced in the freezer. X-ray quality crystals of both [K(18-c-6)][(C$_6$H$_5$Me)Gd(NR$_2$)$_2$]}$_x$ and [K(18-c-6)][Gd(NR$_2$)$_3$]$_x$ were recovered from the reaction mixture. When the same reaction is performed but allowed to react with KC$_8$ for 8h **2-Gd** is recovered exclusively.

[K(18-c-6)][(C$_6$H$_5$Me)Gd(NR$_2$)$_2$]}$_x$, 2-Gd (only). Gd(NR$_2$)$_3$ (60 mg, 0.094 mmol) and 18-c-6 (25 mg, 0.094 mmol) were dissolved in about 2 ml of Et$_2$O with 5 drops of toluene and chilled to −35 °C before being added to a pre-chilled vial of KC$_8$ (50 mg. The solution was allowed to react overnight before being filtered, layered with hexanes and replaced in the freezer. After 10 hours X-ray quality crystals of **2-Gd** (62 mg 75%) were recovered exclusively. UV−vis (Et$_2$O) λ_{max}, nm (ε, M^{-1} cm^{-1}): 275 (4000), 410 (600). IR: 2937m 2885m, 1475w, 1452w, 1351m, 1284w, 1233s, 1104s, 990m, 959m, 866m, 816s, 748m, 660m, cm^{-1}.

[K(crypt)][Gd(NR$_2$)$_3$], 4-Gd. [K(crypt)][Gd(NR$_2$)$_3$] was dissolved in about 3 mL of room temp toluene before being layered into cold hexanes (−35 °C) and replaced in the glovebox freezer. Dark purple crystals of **4-Gd** grew overnight.

[K(crypt)][C$_4$H$_9$OGd(NR$_2$)$_3$], 3-Gd. Gd(NR$_2$)$_3$ and crypt were dissolved in about 2 ml of THF with 5 drops of toluene and chilled to −35 °C before being added to a pre-chilled vial of KC$_8$. The solution was allowed to react for about 1 min before being filtered and layered with

hexanes followed by placement in the freezer. X-ray quality crystals of [K(crypt)][$C_4H_9OGd(NR_2)_3$] were recovered from the reaction mixture after 5 days.

X-ray Data Collection, Structure Solution and Refinement for ajr49 **(1-Gd)**. A dark blue crystal of approximate dimensions 0.273 x 0.215 x 0.189 mm was mounted on a glass fiber and transferred to a Bruker SMART APEX II diffractometer. The APEX2[27] program package was used to determine the unit-cell parameters and for data collection (120 sec/frame scan time for a sphere of diffraction data). The raw frame data was processed using SAINT[28] and SADABS[29] to yield the reflection data file. Subsequent calculations were carried out using the SHELXTL[30] program. The diffraction symmetry was 2/*m* and the systematic absences were consistent with the monoclinic space group $P2_1/c$ that was later determined to be correct.

The structure was solved by dual space methods and refined on F^2 by full-matrix least-squares techniques. The analytical scattering factors[31] for neutral atoms were used throughout the analysis. Hydrogen atoms were calculated using a riding model.

At convergence, wR2 = 0.1979 and Goof = 1.031 for 442 variables refined against 9366 data (0.83Å), R1 = 0.072 for those 5929 with $I > 2.0\sigma(I)$.

Table 5.4. Bond lengths [Å] and angles [°] for ajr49.

Gd(1)-N(1)	2.289(6)
Gd(1)-N(3)	2.307(6)
Gd(1)-N(2)	2.318(6)
Gd(1)-Si(2)	3.444(2)
Gd(1)-Si(1)	3.453(2)
Gd(1)-Si(4)	3.458(2)
K(1)-O(3)	2.755(7)
K(1)-O(6)	2.755(7)
K(1)-O(2)	2.761(6)
K(1)-O(5)	2.785(6)

K(1)-O(4)	2.804(7)
K(1)-O(1)	2.815(7)
K(1)-C(17)#1	3.139(9)
K(1)-C(1)	3.140(9)
C(17)-K(1)#2	3.139(9)

N(1)-Gd(1)-N(3)	118.8(2)
N(1)-Gd(1)-N(2)	119.0(2)
N(3)-Gd(1)-N(2)	122.2(2)
C(17)#1-K(1)-C(1)	173.4(2)

X-ray Data Collection, Structure Solution and Refinement for ajr45 (**2a-Gd)**. A purple/green crystal of approximate dimensions 0.361 x 0.271 x 0.257 mm was mounted in a cryoloop and transferred to a Bruker SMART APEX II diffractometer. The APEX2[27] program package was used to determine the unit-cell parameters and for data collection (20 sec/frame scan time for a sphere of diffraction data). The raw frame data was processed using SAINT[28] and SADABS[29] to yield the reflection data file. Subsequent calculations were carried out using the SHELXTL[30] program. There were no systematic absences nor any diffraction symmetry other than the Friedel condition. The centrosymmetric triclinic space group $P\bar{1}$ was assigned and later determined to be correct.

The structure was solved by direct methods and refined on F^2 by full-matrix least-squares techniques. The analytical scattering factors[31] for neutral atoms were used throughout the analysis. Hydrogen atoms were located from a difference-Fourier map and refined (x,y,z and U_{iso}).

Least-squares analysis yielded wR2 = 0.0476 and Goof = 1.040 for 678 variables refined against 10265 data (0.74 Å), R1 = 0.0188 for those 9886 data with $I > 2.0\sigma(I)$.

Table 5.5. Bond lengths [Å] and angles [°] for ajr45.

Gd(1)-N(2)	2.3238(12)
Gd(1)-N(1)	2.3408(12)
Gd(1)-C(6)	2.4570(17)
Gd(1)-C(3)	2.4808(16)
Gd(1)-C(2)	2.6979(15)
Gd(1)-C(1)	2.7058(15)
Gd(1)-C(5)	2.7176(16)
Gd(1)-C(4)	2.7264(16)
K(1)-O(2)	2.7979(12)
K(1)-O(3)	2.8346(13)
K(1)-O(6)	2.8497(13)
K(1)-O(5)	2.8541(12)
K(1)-O(4)	2.8667(12)
K(1)-O(1)	2.8773(13)
K(1)-C(2)	3.0949(16)
K(1)-C(4)	3.2733(17)
K(1)-C(3)	3.3252(17)
K(1)-C(1)	3.4245(16)
K(1)-C(9)#1	3.4337(18)
C(1)-C(2)	1.364(2)
C(1)-C(6)	1.472(2)
C(1)-C(7)	1.505(2)
C(2)-C(3)	1.483(2)
C(3)-C(4)	1.470(2)
C(4)-C(5)	1.360(3)
C(5)-C(6)	1.470(3)
C(9)-K(1)#2	3.4338(18)

N(2)-Gd(1)-N(1)	113.95(4)
C(2)-K(1)-C(9)#1	150.87(5)
C(4)-K(1)-C(9)#1	158.68(5)
C(3)-K(1)-C(9)#1	154.44(5)
C(1)-K(1)-C(9)#1	151.84(4)
C(2)-C(1)-C(6)	120.16(15)

C(2)-C(1)-C(7)	122.62(17)
C(6)-C(1)-C(7)	116.55(16)
C(1)-C(2)-C(3)	121.99(15)

X-ray Data Collection, Structure Solution and Refinement for ajr53 **(2b-Gd)**. An orange crystal of approximate dimensions 0.655 x 0.326 x 0.215 mm was mounted on a cryoloop and transferred to a Bruker SMART APEX II diffractometer. The APEX2[27] program package was used to determine the unit-cell parameters and for data collection (60 sec/frame scan time for a sphere of diffraction data). The raw frame data was processed using SAINT[28] and SADABS[29] to yield the reflection data file. Subsequent calculations were carried out using the SHELXTL[30] program. The diffraction symmetry was 2/*m* and the systematic absences were consistent with the monoclinic space groups *Cc* and *C*2/*c*. It was later determined that space group *C*2/*c* was correct.

The structure was solved by dual space methods and refined on F^2 by full-matrix least-squares techniques. The analytical scattering factors[31] for neutral atoms were used throughout the analysis. Hydrogen atoms were located from a difference-Fourier map and refined (x,y,z and U_{iso}) and using a riding model. Disordered methyl groups were modelled isotropically in parts and disordered silicon atoms were modelled anisotropically in parts.

At convergence, wR2 = 0.0754 and Goof = 1.053 for 588 variables refined against 11545 data (0.74 Å), R1 = 0.0339 for those 9843 data with $I > 2.0\sigma(I)$.

Table 5.6. Bond lengths [Å] and angles [°] for ajr53.

Gd(1)-N(2)	2.324(2)
Gd(1)-N(1)	2.348(2)
Gd(1)-C(2)	2.465(3)
Gd(1)-C(5)	2.483(3)
Gd(1)-C(4)	2.706(3)

Gd(1)-C(3)	2.714(3)
Gd(1)-C(6)	2.723(3)
Gd(1)-C(1)	2.728(3)
K(1)-C(4)	3.063(3)
K(1)-C(3)	3.283(3)
K(1)-C(11)#1	3.331(3)
K(1)-C(6)	3.334(3)
K(1)-C(5)	3.391(3)
C(1)-C(6)	1.374(4)
C(1)-C(2)	1.476(4)
C(1)-C(7)	1.492(4)
C(2)-C(3)	1.471(4)
C(3)-C(4)	1.357(4)
C(4)-C(5)	1.462(4)
C(5)-C(6)	1.481(4)
C(20)-C(21)	1.500(5)

N(2)-Gd(1)-N(1)	109.25(9)

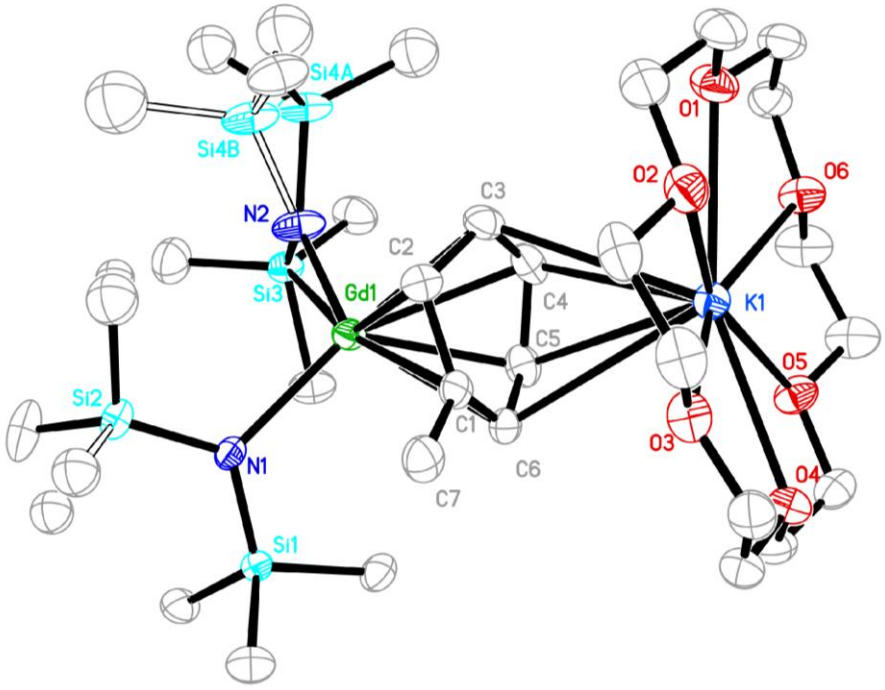

Figure 5.7. Thermal ellipsoid plot of **2b-Gd** drawn at the 50% probability level. Hydrogen atoms excluded for clarity.

X-ray Data Collection, Structure Solution and Refinement for ajr46 **(4-Gd)**. A blue crystal of approximate dimensions 0.283 x 0.106 x 0.103 mm was mounted in a cryoloop and transferred to a Bruker SMART APEX II diffractometer. The APEX2[27] program package was used to determine the unit-cell parameters and for data collection (240 sec/frame scan time for a sphere of diffraction data). The raw frame data was processed using SAINT[28] and SADABS[29] to yield the reflection data file. Subsequent calculations were carried out using the SHELXTL[30] program. The systematic absences were consistent with the trigonal space group *R32*. The non-centrosymmetric space group *R*32 was assigned and later determined to be correct.

The structure was solved by direct methods and refined on F^2 by full-matrix least-squares techniques. The analytical scattering factors[31] for neutral atoms were used throughout the analysis. Hydrogen atoms were included using a riding model.

Least-squares analysis yielded wR2 = 0.0426 and Goof = 1.005 for 88 variables refined against 2478 data (0.80 Å), R1 = 0.0235 for those 2264 data with $I > 2.0\sigma(I)$.

There were several high residuals present in the final difference-Fourier map. It was not possible to determine the nature of the residuals although it was probable that toluene solvent was present. The SQUEEZE[32a] routine in the PLATON[32b] program package was used to account for the electrons in the solvent accessible voids.

Table 5.7. Bond lengths [Å] and angles [°] for ajr46.

Gd(1)-N(1)	2.315(3)
Gd(1)-N(1)#1	2.316(3)
Gd(1)-N(1)#2	2.316(3)
N(1)-Gd(1)-N(1)#1	120.0
N(1)-Gd(1)-N(1)#2	120.000(1)
N(1)#1-Gd(1)-N(1)#2	120.0

X-ray Data Collection, Structure Solution and Refinement for ajr51 **(3-Gd)**.

A blue crystal of approximate dimensions 0.504 x 0.368 x 0.234 mm was mounted in a cryoloop and transferred to a Bruker SMART APEX II diffractometer. The APEX2[27] program package and the CELL_NOW[33] were used to determine the unit-cell parameters. Data was collected using a 15 sec/frame scan time for a sphere of diffraction data. The raw frame data was processed using SAINT[28] and TWINABS[34] to yield the reflection data file (HKLF 4/5 format)[34]. Subsequent calculations were carried out using the SHELXTL[30] program. The diffraction

symmetry was 2/*m* and the systematic absences were consistent with the monoclinic space group $P2_1/c$ that was later determined to be correct.

The structure was solved by dual space methods and refined on F^2 by full-matrix least-squares techniques. The analytical scattering factors[31] for neutral atoms were used throughout the analysis. Hydrogen atoms were located from a difference-Fourier map and refined (x,y,z and U_{iso}). Disordered carbon atoms on ^{n}butoxide ligand were modelled isotropically in parts. Minor disorder of Gd ion was modelled anisotropically in parts.

Least-squares analysis yielded wR2 = 0.1148 and Goof = 1.070 for 559 variables refined against 17663 data (0.75 Å), R1 = 0.0469 for those 15419 with $I > 2.0\sigma(I)$. The structure was refined as a non-merohedral twin, BASF[34] = 0.24361.

Table 5.8. Bond lengths [Å] and angles [°] for ajr51 (**3-Gd**).

Gd(1A)-O(1)	2.090(4)
Gd(1A)-N(2)	2.338(4)
Gd(1A)-N(3)	2.340(3)
Gd(1A)-N(1)	2.340(3)
Gd(1B)-N(2)	2.107(8)
Gd(1B)-N(1)	2.427(7)
Gd(1B)-N(3)	2.447(7)
O(1)-Gd(1A)-N(2)	100.60(16)
O(1)-Gd(1A)-N(3)	104.73(13)
N(2)-Gd(1A)-N(3)	113.98(13)
O(1)-Gd(1A)-N(1)	102.21(13)
N(2)-Gd(1A)-N(1)	115.79(12)
N(3)-Gd(1A)-N(1)	116.53(11)

References

1. M. C. Cassani, Y. K. Gun'ko, P. B. Hitchcock and M. F. Lappert, *Chem. Commun.*, 1996, DOI: 10.1039/CC9960001987, 1987-1988.
2. M. C. Cassani, D. J. Duncalf and M. F. Lappert, *Journal of the American Chemical Society*, 1998, **120**, 12958-12959.
3. M. C. Cassani, Y. K. Gun'ko, P. B. Hitchcock, M. F. Lappert and F. Laschi, *Organometallics*, 1999, **18**, 5539-5547.
4. Y. K. Gun'ko, P. B. Hitchcock and M. F. Lappert, *Organometallics*, 2000, **19**, 2832-2834.
5. C. M. Kotyk, M. E. Fieser, C. T. Palumbo, J. W. Ziller, L. E. Darago, J. R. Long, F. Furche and W. J. Evans, *Chemical Science*, 2015, **6**, 7267-7273.
6. C. M. Kotyk, M. R. MacDonald, J. W. Ziller and W. J. Evans, *Organometallics*, 2015, **34**, 2287-2295.
7. R. P. Kelly, L. Maron, R. Scopelliti and M. Mazzanti, *Angew. Chem. Int. Ed.*, 2017, **56**, 15663-15666.
8. R. P. Kelly, D. Toniolo, F. F. Tirani, L. Maron and M. Mazzanti, *Chem. Commun.*, 2018, **54**, 10268-10271.
9. C. T. Palumbo, L. E. Darago, M. T. Dumas, J. W. Ziller, J. R. Long and W. J. Evans, *Organometallics*, 2018, **37**, 3322-3331.
10. M. C. Cassani, D. J. Duncalf and M. F. Lappert, *Journal of the American Chemical Society*, 1998, **120**, 12958-12959.
11. W. J. Evans, T. A. Ulibarri, L. R. Chamberlain, J. W. Ziller and D. Alvarez, *Organometallics*, 1990, **9**, 2124-2130.
12. W. J. Evans, J. T. Leman, J. W. Ziller and S. I. Khan, *Inorg. Chem.*, 1996, **35**, 4283-4291.
13. G. C. Forbes, A. R. Kennedy, R. E. Mulvey, B. A. Roberts and R. B. Rowlings, *Organometallics*, 2002, **21**, 5115-5121.
14. H. C. Aspinall, D. C. Bradley, M. B. Hursthouse, K. D. Sales, N. P. C. Walker and B. Hussain, *J. Chem. Soc., Dalton Trans.*, 1989, DOI: 10.1039/DT9890000623, 623-626.
15. X. Gu, S. Wang, Y. Wei, X. Zhu, S. Zhou, Z. Huang and X. Mu, *New J. Chem.*, 2017, **41**, 7723-7728.
16. A. J. Ryan, L. E. Darago, S. G. Balasubramani, G. P. Chen, J. W. Ziller, F. Furche, J. R. Long and W. J. Evans, *Chemistry–A European Journal*, 2018, **24**, 7702-7709.
17. A. J. Ryan, J. W. Ziller and W. J. Evans, *Chemical Science*, 2020, DOI: 10.1039/C9SC05794C.
18. C. L. Gardner, *The Journal of Chemical Physics*, 1966, **45**, 572-575.
19. B. Kaempf, S. Raynal, A. Collet, F. Schué, S. Boileau and J. M. Lehn, *Angewandte Chemie International Edition in English*, 1974, **13**, 611-612.
20. P. G. Eller, D. C. Bradley, M. B. Hursthouse and D. W. Meek, *Coord. Chem. Rev.*, 1977, **24**, 1-95.
21. F. Jaroschik, A. Momin, F. Nief, X. F. Le Goff, G. B. Deacon and P. C. Junk, *Angew. Chem.*, 2009, **121**, 1137-1141.
22. J. F. Corbey, D. H. Woen, C. T. Palumbo, M. E. Fieser, J. W. Ziller, F. Furche and W. J. Evans, *Organometallics*, 2015, **34**, 3909-3921.
23. M. E. Fieser, C. T. Palumbo, H. S. La Pierre, D. P. Halter, V. K. Voora, J. W. Ziller, F. Furche, K. Meyer and W. J. Evans, *Chemical science*, 2017, **8**, 7424-7433.

24. C. T. Palumbo, D. P. Halter, V. K. Voora, G. P. Chen, A. K. Chan, M. E. Fieser, J. W. Ziller, W. Hieringer, F. Furche and K. Meyer, *Inorg. Chem.*, 2018, **57**, 2823-2833.
25. M. D. Taylor, *Chem. Rev.*, 1962, **62**, 503-511.
26. D. C. Bradley, J. S. Ghotra and F. A. Hart, *J. Chem. Soc., Chem. Commun.*, 1972, DOI: 10.1039/C39720000349, 349-350.
27. D. E. Bergbreiter and J. M. Killough, *Journal of the American Chemical Society*, 1978, **100**, 2126-2134.
27. APEX2 Version 2014.11-0, Bruker AXS, Inc.; Madison, WI 2014.
28. SAINT Version 8.34a, Bruker AXS, Inc.; Madison, WI 2013.
29. Sheldrick, G. M. SADABS, Version 2014/5, Bruker AXS, Inc.; Madison, WI 2014.
30. Sheldrick, G. M. SHELXTL, Version 2014/7, Bruker AXS, Inc.; Madison, WI 2014.
31. International Tables for Crystallography 1992, Vol. C., Dordrecht: Kluwer Academic Publishers.
32. (a) Spek, A.L. SQUEEZE, Acta Cryst. 2015, C71, 9-19., (b) Spek, A. L. PLATON, Acta. Cryst. 2009, D65, 148-155.
33. Sheldrick, G. M. CELL_NOW, Version 2008/4, Bruker AXS, Inc.; Madison, WI 2008.
34. Sheldrick, G. M. TWINABS, Version 2012/1, Bruker AXS, Inc.; Madison, WI 2012.

Chapter 6

Reductive Reactivity of $[Gd(NR_2)_3]^{1-}$ with $PnPh_3$ (Pn = P, Bi)

Introduction

The study of element−element bonds is a fundamental part of chemistry allowing us to define and study the chemical properties and reactivity of the elements involved. Much of the periodic table has been explored in this area though one area that remains limited is heavy main group element bonding to f elements, specifically group 15 metals such as Sb and Bi. The first example of an f element Bi bond was reported in 1991 by Evans and coworkers through a reductive reaction of Cp^*_2Sm ($Cp^* = C_5Me_5$) with $BiPh_3$ which produced the dibismuth bridged complex $(Cp^*_2Sm)_2(\mu\text{-}\eta^2\text{:}\eta^2\text{-}Bi_2)$, in addition to Sm phenyl complex Cp^*_2SmPh eq 6.1.[1]

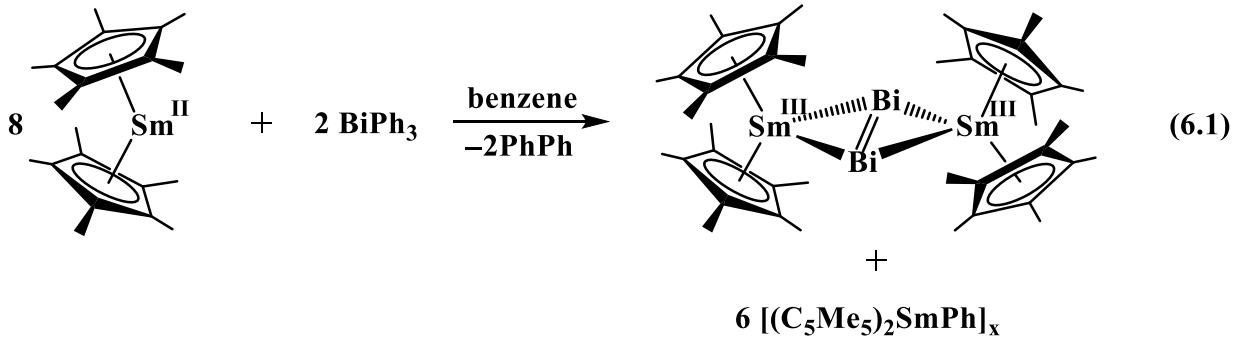

(6.1)

This chemistry was further investigated with the pnictiogens of group 15 using $PnPh_3$ (Pn = P, As, Sb).[2] Interestingly, no other Sm−Pn bond formation was observed, and only with $SbPh_3$ was a reductive reaction observed through formation of $Cp^*_2SmPh(THF)$ by NMR. Upon moving to $Ph_2PnPnPh_2$ reagents, reactions were observed with the smaller Pn elements (Pn = P, As).[2] This Cp^*_2Sm chemistry contrasted the reductive chemistry of the alkali metals and $PnPh_3$ complexes studied by Gilman et al. which showed a reaction to form MPh and $MPnPh_2$ (M = Li, Na, K; Pn = P, As, Sb) products for all Pn except Pn = Bi in which case only benzene was observed, eq 6.2.[3]

$$2\,M + PnPh_3 \xrightarrow{NH_3\ (liquid)} MPh + MPnPh_2 \qquad (6.2)$$

M = Li, Na, K; Pn = P, As, Sb

No other Ln−Bi bonds have been reported beyond eq 6.1 despite growing interest in heavy main group element effects for investigations of single molecule magnets (SMMs).[4-6] Recent work by Liddle et al. has unearthed the first example of a U−Bi bond utilizing KBi(SiMe$_3$), eq 6.3. [7] The following chapter describes the reactivity of the isolated divalent Gd complex [K(chelate)$_x$][Gd(NR$_2$)$_3$] (chelate = crypt, x = 1; chelate = 18-c-6, x = 2) with both the heaviest and lightest non-nitrogen PnPh$_3$ complexes (Pn = P, Bi).

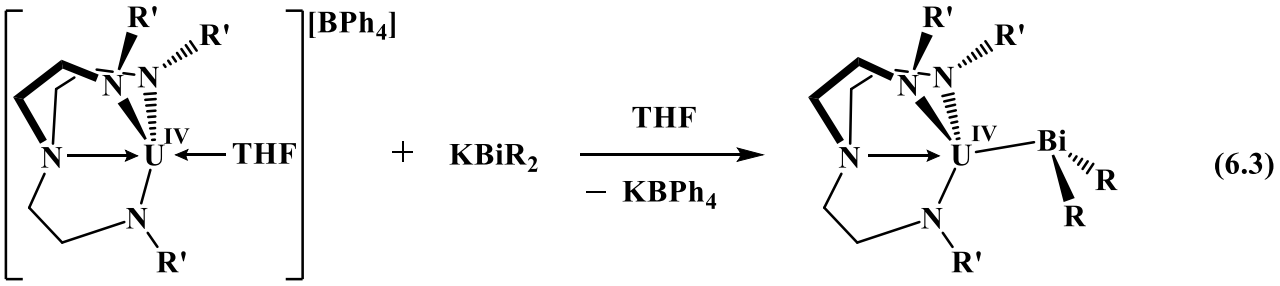

(6.3)

R' = SiMe$_3$Bu^t

R = SiMe$_3$

Results and Discussion

Synthesis of [K(crypt)][Ph$_2$BiGd(NR$_2$)$_3$], 1-Gd. Adding solid [K(crypt)][Gd(NR$_2$)$_3$] (crypt = 2.2.2-cryptand; R = SiMe$_3$) to a solution of BiPh$_3$ in Et$_2$O at room temperature results in an immediate color change from colorless to orange. Upon layering in hexanes and placement in the glovebox freezer at −35 °C, an orange/brown oil collected in the bottom of the vial overnight. After another 24 hours in the freezer bright green crystals were produced from the oil. X-ray diffraction of the green crystals showed them to be of composition [K(crypt)][Ph$_2$BiGd(NR$_2$)$_3$],

1-Gd. This complex is the first example of a Gd−Bi bond, only the second example of a Ln−Bi bond, and the third example of an f element Bi bond, eq 6.4.

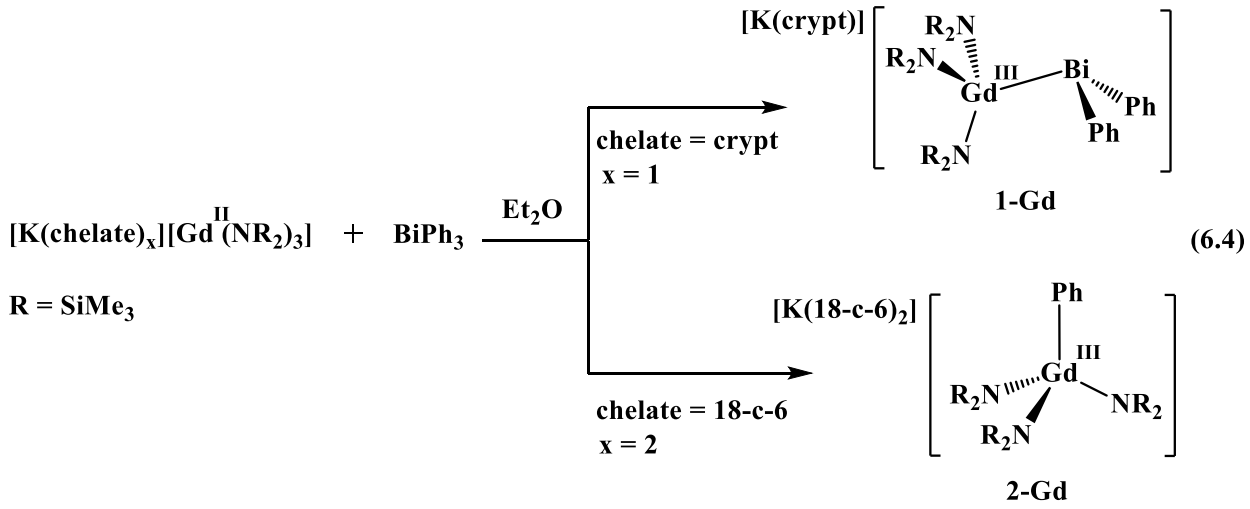

Synthesis of [K(18-c-6)][PhGd(NR$_2$)$_3$], 2-Gd. If the same reaction protocol described for **1-Gd** is applied using the 18-crown-6 Gd(II) starting material, [K(18-c-6)$_2$][Gd(NR$_2$)$_3$], blue crystals identified as the phenyl complex [K(18-c-6)$_2$][PhGd(NR$_2$)$_3$], **2-Gd**, are isolated rather than a Gd−Bi containing product, eq 6.4. Deep red crystals were observed in the product mixture, but they were too small for X-ray diffraction studies.

The mechanism of formation of **1-Gd** and **2-Gd** is unknown. However, reductive cleavage of a Ph$_2$Bi−Ph bond to make the (Ph$_2$Bi)$^{1-}$ and Ph^{1-} ligands found in **1-Gd** and **2-Gd** respectively, is reasonable. This is also along the lines of the reductive chemistry in eq 6.1 and 6.2.

Reactions of [Gd(NR$_2$)$_3$]$^{1-}$ with PPh$_3$. Reactions of PPh$_3$ with both [K(crypt)][Gd(NR$_2$)$_3$] and [K(18-c-6)][Gd(NR$_2$)$_3$] were also performed to examine the chemistry throughout the pnictoctogens. While a similar color change from colorless to orange was observed upon addition of Gd(II) species to PPh$_3$ in Et$_2$O only the cyclometallated product

[(RNSiMe$_2$CH$_2$-κ*C*,*N*)Gd(NR$_2$)$_2$]$^{1-}$ was recovered The fact that a reaction is observed indicates a deviation from Cp*$_2$Sm chemistry in which no reductive chemistry is observed with PPh$_3$.[2]

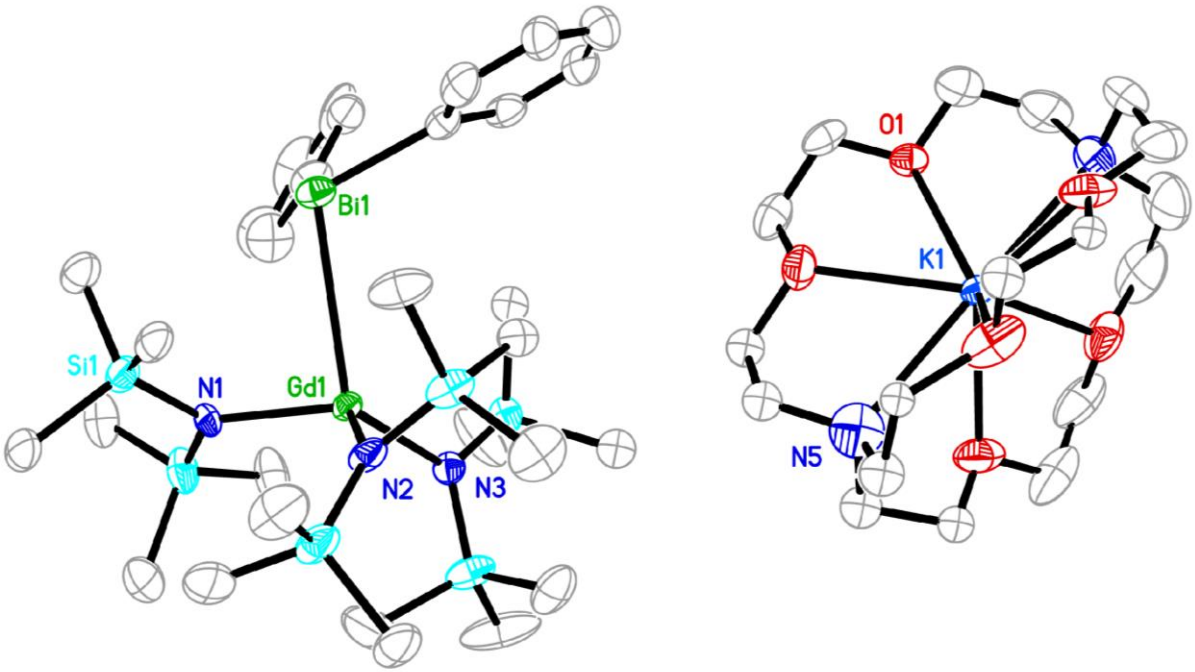

Figure 6.1. Thermal ellipsoid plot of **1-Gd** drawn at the 50% probability level. Hydrogen atoms and disordered SiMe$_3$ group omitted for clarity.

Structure of [K(crypt)][Ph$_2$BiGd(NR$_2$)$_3$], 1-Gd. 1-Gd crystallizes in the P-1 space group with a pseudo-tetrahedral coordination environment around the Gd ion containing three NR$_2$ (R = SiMe$_3$) ligands and one BiPh$_2$ ligand, Figure 6.1. The Bi−Gd−N bond angles range from 88 - 120° where the largest angle is formed with the NR$_2$ ligand (N2 in Figure 6.1) that is oriented toward the two phenyl groups of the BiPh$_2$ unit. The N−Gd−N angles range from 106 - 117°, similar to those seen in [K(crypt)][C$_4$H$_9$OGd(NR$_2$)$_3$] which range from 114 - 117° (Chapter 5). The coordination environment around the Bi atom is trigonal pyramidal with Gd−Bi−C and C−Bi−C angles ranging from 97 - 110°. Similarities in the bond metrics of **1-Gd** can be seen when compared to [U(TrenDMBS){Bi(SiMe$_3$)$_2$}] (TrenDMBS = N(CH$_2$CH$_2$NSiMe$_2$But)$_3$), **UBi**,

a U(IV) complex coordinated by three anionic amide donor ligands and an anionic $Bi(SiMe_3)_2$. The bond angles are similar for **1-Gd** and **UBi** with Bi−U−N_{amide} angles ranging from 91 - 136° and angles from 94 - 120° around the Bi atom, Table 6.1. The Gd−Bi bond in **1-Gd** is similar to the U−Bi in **UBi**, 3.3516(5) Å vs 3.3208(4) Å, respectively.

The similarities in metrical parameters extend to the M−N_{amide} bonds with distances ranging from, 2.286(6) Å - 2.296(6) Å for **1-Gd** vs 2.232(6) - 2.247(6) Å in **UBi**, again differing by about 0.04 Å. The Gd−N bond distances in **1-Gd** are also similar to the range observed for Gd−N_{amide} bonds in the four coordinate Gd(III) complex $[K(crypt)][C_4H_9OGd(NR_2)_3]$, 2.338(4) - 2.340(4) Å (Chapter 5). In this case, the shorter distances in **1-Gd** can be accounted for by the reduced steric strain coming from difference in bond length of the non NR_2 ligand ($BiPh_2$ vs OC_4H_9). The Gd−Bi bond distance, 3.3516(5) Å, is more than an Angstrom longer than the Gd−O bond of the OC_4H_9 ligand in $[K(crypt)][C_4H_9OGd(NR_2)_3]$, 2.090(4) Å. Bond metrics are summarized in Table 6.1.

Table 6.1. Bond distances (Å) and angles (°) of $[K(crypt)][Ph_2BiGd(NR_2)_3]$ **(1-Gd),** [U(TrenDMBS){Bi(SiMe3)2}] (TrenDMBS = $N(CH_2CH_2NSiMe_2But)_3$) (**UBi)**, $[K(crypt)][C_4H_9OGd(NR_2)_3]$, and $[K(18\text{-}c\text{-}6)_2][PhGd(NR_2)_3]$ (**2-Gd)**. Where NR_2 is the $N(SiMe_3)_2$ ligand for **1-Gd**, **2-Gd**, and $[K(crypt)][C_4H_9OGd(NR_2)_3]$, or the anionic N donors in the TrenDMBS ligand for **UBi**. L are the ligands coordinated to the Bi atom in the respective compounds.

	[K(crypt)] $[Ph_2BiGd(NR_2)_3]$	[U(TrenDMBS) $\{Bi(SiMe_3)_2\}$]	[K(crypt)] $[C_4H_9OGd(NR_2)_3]$	[K(18-c-6)] $[PhGd(NR_2)_3]$
M−Bi/O/C	3.3516(5)	3.3208(4)	2.090(4)	2.525(5)
M−NR_2	2.286(6) - 2.296(6)	2.232(6) - 2.247(6)	2.338(4) - 2.340(4)	2.301(4) - 2.326(4)
Bi/O/C−M−N	88 - 124	91 - 136	100 - 104	98- 113
N_{amide}−M−N_{amide}	106 - 117	100 - 124	114 - 117	103 - 120
L−Bi−L	94 - 120	96 - 110	-	-

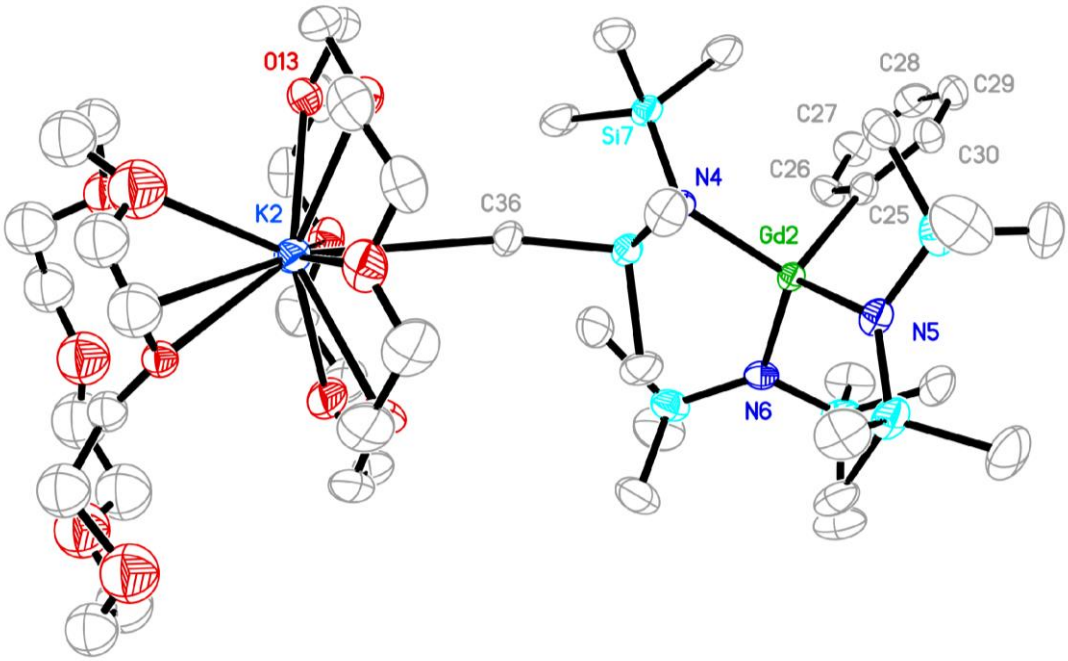

Figure 6.2. Thermal ellipsoid plot of **2-Gd** drawn at the 50% probability level. Hydrogen atoms, disordered TMS group and one ion pair of the unit cell are excluded for clarity.

Structure of [K(18-c-6)$_2$][PhGd(NR$_2$)$_3$], 2-Gd. 2-Gd crystallizes in the P-1 space group with 2 molecules of [K(18-c-6)$_2$][PhGd(NR$_2$)$_3$] per unit cell. In one ion pair the anionic [PhGd(NR$_2$)$_3$]$^{1-}$ unit is well separated from the [K(18-c-6)$_2$]$^+$ cation. The other shows a close K…C(methyl) contact between an NR$_2$ ligand and [K(18-c-6)$_2$]$^+$ cation, 3.391(5) Å, Figure 6.2. This K…C(methyl) contact is comparable to that observed in the structure and [K(18-c-6)$_2$][Tm(NR$_2$)$_3$], 3.322(9) Å[8] (Chapter 2). The metrical parameters around the two Gd ions are the same within error. Therefore, only one will be discussed in this section with selected distances included in Table 6.1. The Gd−N distances range from 2.301(4) - 2.326(4) Å and are consistent with those observed in [K(crypt)][C$_4$H$_9$OGd(NR$_2$)$_3$], 2.338(4) - 2.340(4) Å (Chapter 5). The Gd−C distance is longer at 2.525(5) Å than the Gd-N distances as well as the 2.41(2) Å Gd-C(Ph) bond in seven coordinate C$_6$H$_5$GdCl$_2$(4THF)[9], the only other structurally-characterized

example of a complex containing a Gd−Ph bond. The known eight-coordinate $Cp^*_2SmPh(THF)$ complex, produced by a similar reaction protocol with $BiPh_3$, displays a Sm−Ph bond length of 2.511(8) Å similar to that observed in **1-Gd**.[1, 10]

Conclusion

Reactions of the isolated Gd(II) complexes, $[K(chelate)_x][Gd(NR_2)_3]$, with $BiPh_3$ results in bond cleavage and isolation of either $[K(crypt)][Ph_2BiGd(NR_2)_3]$, if the chelate is crypt and x = 1, or $[K(18\text{-c-}6)_2][PhGd(NR_2)_3]$ if the chelate is 18-c-6 and x = 2. This reaction shares similarities with those observed by both Cp^*_2Sm and $BiPh_3$,[1] eq 6.1, as well as reactions of alkali metals with the smaller triphenylpnictides,[3] P, As, Sb, eq 6.2 (but not BiPh3). The Cp^*_2Sm reactions with $BiPh_3$ however produces a $Cp^*_2SmPh(THF)$ similar to that observed with in this study. However no product containing bismuth-bismuth bonds was observed in the $[Gd(NR_2)_3]^{1-}$ reactions described here.

Reactions of $[Gd(NR_2)_3]^{1-}$ with PPh3 failed to produce phosphorus- or phenyl-containing products regardless of chelating agent used: only cyclometallated products were recovered. This contrasts both the reactions of alkali metals and Cp^*_2Sm with PPh_3 which display PPh_3 bond cleavage and Sm−PPh_3 adduct formation respectively.[2, 3]

The results presented here offer insights into the unique chemistry of these non-traditional Ln(II) ions and present routes to synthesizing new types of compounds not seen before with physical properties of potential interest in the field of single molecule magnetism. Differences in isolated products here highlight the variability in crystallization of products with choice of chelating agent in compliment to that seen and discussed in Chapters 2, 4 and 5.

Experimental Details

All manipulations and syntheses described below were conducted with the rigorous exclusion of air and water using standard Schlenk line and glovebox techniques under an argon or dinitrogen atmosphere. Solvents were sparged with UHP argon and dried by passage through columns containing Q-5 and molecular sieves prior to use. [K(crypt)]Gd(NR_2)$_3$][11] and [K(18-c-6)]Gd(NR_2)$_3$][12] were synthesized as previously reported. $BiPh_3$ (Alfa Aesar) was used as received and PPh_3 (sigma) was sublimed under high vacuum before use.

[K(crypt)][Ph_2BiGd(NR_2)$_3$], 1-Gd. Solid [K(crypt)][Gd(NR_2)$_3$] (crypt = 2.2.2-cryptand; R = $SiMe_3$) (60 mg) was added to a solution of $BiPh_3$ in Et_2O (9 mg) at room temperature resulting in an immediate color change from colorless to orange. The solution was allowed to react for about 1 minute before being filtered and layered into hexanes. Placement into the glovebox freezer at −35 °C overnight resulted in an orange/brown oil collected in the bottom of the vial. After another 24 hours in the freezer small bright green crystals of **1-Gd** were grew from the oil.

[K(18-c-6)][PhGd(NR_2)$_3$], 2-Gd. Following the same reaction protocol described for **1-Gd**, [K(18-c-6)$_2$][Gd(NR_2)$_3$] (60 mg) reacted with $BiPh_3$ to produce blue crystals identified as **2-Gd**, in addition to red crystals which were too small for x-ray diffraction studies.

X-ray Data Collection, Structure Solution and Refinement for ajr59 (**1-Gd**).

A green crystal of approximate dimensions 0.145 x 0.143 x 0.086 mm was mounted in a cryoloop and transferred to a Bruker SMART APEX II diffractometer. The APEX2[12] program package was used to determine the unit-cell parameters and for data collection (240 sec/frame scan time for a sphere of diffraction data). The raw frame data was processed using SAINT[13] and SADABS[14] to yield the reflection data file. Subsequent calculations were carried out using the

SHELXTL[15] program. There were no systematic absences nor any diffraction symmetry other than the Friedel condition. The centrosymmetric triclinic space group $P\bar{1}$ was assigned and later determined to be correct.

The structure was solved by dual space methods and refined on F^2 by full-matrix least-squares techniques. The analytical scattering factors[16] for neutral atoms were used throughout the analysis. Hydrogen atoms were included using a riding model. Disordered $SiMe_3$ groups were modelled isotropically in parts.

Least-squares analysis yielded wR2 = 0.1259 and Goof = 0.952 for variables refined against 13613 data (0.83 Å), R1 = 0.0555 for those 8442 data with $I > 2.0\sigma(I)$.

There were several high residuals present in the final difference-Fourier map. It was not possible to determine the nature of the residuals although it was probable that two ether solvent molecules were present. The SQUEEZE[17a] routine in the PLATON[17b] program package was used to account for the electrons in the solvent accessible voids.

Table 6.2. Crystal data and structure refinement for ajr59.

Identification code	ajr59	
Empirical formula	C48 H100 Bi Gd K N5 O6 Si6	
Formula weight	1417.19	
Temperature	88(2) K	
Wavelength	0.71073 Å	
Crystal system	Triclinic	
Space group	P-1	
Unit cell dimensions	a = 14.5635(10) Å	a= 105.9130(10)°.
	b = 16.5028(12) Å	b= 102.5720(10)°.
	c = 16.6146(12) Å	g = 92.6360(10)°.
Volume	3724.2(5) $Å^3$	
Z	2	
Density (calculated)	1.264 Mg/m^3	
Absorption coefficient	3.433 mm^{-1}	

F(000)	1442
Crystal color	green
Crystal size	0.145 x 0.143 x 0.086 mm^3
Theta range for data collection	1.291 to 25.350°
Index ranges	-17 <= h <= 17, -19 <= k <= 19, -20 <= l <= 20
Reflections collected	40179
Independent reflections	13613 [R(int) = 0.1051]
Completeness to theta = 25.350°	99.9 %
Absorption correction	Semi-empirical from equivalents
Max. and min. transmission	0.4296 and 0.3587
Refinement method	Full-matrix least-squares on F^2
Data / restraints / parameters	13613 / 0 / 618
Goodness-of-fit on F^2	0.952
Final R indices [I>2sigma(I) = 8442 data]	R1 = 0.0555, wR2 = 0.1113
R indices (all data, 0.83 Å)	R1 = 0.1104, wR2 = 0.1259
Extinction coefficient	n/a
Largest diff. peak and hole	1.689 and -1.024 e.$Å^{-3}$

Table 6.3. Bond lengths [Å] and angles [°] for ajr59.

Bi(1)-C(1)	2.268(9)
Bi(1)-C(7)	2.270(9)
Bi(1)-Gd(1)	3.3516(5)
Gd(1)-N(2)	2.286(6)
Gd(1)-N(1)	2.296(6)
Gd(1)-N(3)	2.296(6)
C(1)-Bi(1)-C(7)	98.0(3)
C(1)-Bi(1)-Gd(1)	96.9(2)
C(7)-Bi(1)-Gd(1)	110.4(2)
N(2)-Gd(1)-N(1)	112.1(2)
N(2)-Gd(1)-N(3)	106.9(2)
N(1)-Gd(1)-N(3)	117.9(2)
N(2)-Gd(1)-Bi(1)	106.45(17)
N(1)-Gd(1)-Bi(1)	88.33(16)
N(3)-Gd(1)-Bi(1)	124.00(16)

X-ray Data Collection, Structure Solution and Refinement for ajr64 (**2-Gd)**.

A yellow crystal of approximate dimensions 0.347 x 0.253 x 0.161 mm was mounted in a cryoloop and transferred to a Bruker SMART APEX II diffractometer. The APEX2[12] program package was used to determine the unit-cell parameters and for data collection (90 sec/frame scan time for a sphere of diffraction data). The raw frame data was processed using SAINT[13] and SADABS[14] to yield the reflection data file. Subsequent calculations were carried out using the SHELXTL[15] program. There were no systematic absences nor any diffraction symmetry other than the Friedel condition. The centrosymmetric triclinic space group $P\bar{1}$ was assigned and later determined to be correct.

The structure was solved by dual space methods and refined on F^2 by full-matrix least-squares techniques. The analytical scattering factors[16] for neutral atoms were used throughout the analysis. Hydrogen atoms were included using a riding model. Disordered $SiMe_3$ group and carbon atoms on 18-c-6 chelates were modelled isotropically in parts

Least-squares analysis yielded wR2 = 0.1503 and Goof = 1.037 for 1241 variables refined against 27315 data (0.76 Å), R1 = 0.0564 for those 20840 data with I > 2.0σ(I).

Table 6.4. Crystal data and structure refinement for ajr64.

Identification code	ajr64	
Empirical formula	C48 H107 Gd K N3 O12 Si6	
Formula weight	1283.25	
Temperature	133(2) K	
Wavelength	0.71073 Å	
Crystal system	Triclinic	
Space group	P-1	
Unit cell dimensions	a = 18.077(3) Å	a= 88.109(2)°.
	b = 18.516(3) Å	b= 68.771(2)°.
	c = 22.029(4) Å	g = 77.424(2)°.
Volume	6700(2) $Å^3$	

Z	4
Density (calculated)	1.272 Mg/m^3
Absorption coefficient	1.211 mm^{-1}
F(000)	2716
Crystal color	blue
Crystal size	0.347 x 0.253 x 0.161 mm^3
Theta range for data collection	1.239 to 26.372°
Index ranges	-22 <= h <= 22, -23 <= k <= 23, -27 <= l <= 27
Reflections collected	73238
Independent reflections	27315 [R(int) = 0.0384]
Completeness to theta = 25.500°	99.8 %
Absorption correction	Semi-empirical from equivalents
Max. and min. transmission	0.7456 and 0.5802
Refinement method	Full-matrix least-squares on F^2
Data / restraints / parameters	27315 / 0 / 1241
Goodness-of-fit on F^2	1.037
Final R indices [I>2sigma(I) = 20840 data]	R1 = 0.0564, wR2 = 0.1384
R indices (all data, ? Å)	R1 = 0.0790, wR2 = 0.1503
Extinction coefficient	n/a
Largest diff. peak and hole	3.200 and -0.794 $e.Å^{-3}$

Table 6.5. Bond lengths [Å] and angles [°] for ajr64.

Gd(1)-N(1)	2.301(4)
Gd(1)-N(2)	2.314(4)
Gd(1)-N(3)	2.326(4)
Gd(1)-C(1)	2.525(5)
Gd(2)-N(5)	2.313(4)
Gd(2)-N(4)	2.323(4)
Gd(2)-N(6)	2.326(4)
Gd(2)-C(25)	2.494(5)
K(2)-C(36)	3.391(5)
N(1)-Gd(1)-N(2)	103.92(15)
N(1)-Gd(1)-N(3)	110.86(15)
N(2)-Gd(1)-N(3)	120.09(14)
N(1)-Gd(1)-C(1)	113.04(16)
N(2)-Gd(1)-C(1)	111.44(16)

N(3)-Gd(1)-C(1)	97.84(16)
N(5)-Gd(2)-N(4)	106.42(14)
N(5)-Gd(2)-N(6)	115.64(15)
N(4)-Gd(2)-N(6)	116.66(15)
N(5)-Gd(2)-C(25)	111.84(15)
N(4)-Gd(2)-C(25)	108.82(15)
N(6)-Gd(2)-C(25)	97.17(15)

References

1. W. J. Evans, S. L. Gonzales and J. W. Ziller, *Journal of the American Chemical Society*, 1991, **113**, 9880-9882.
2. W. J. Evans, J. T. Leman, J. W. Ziller and S. I. Khan, *Inorg. Chem.*, 1996, **35**, 4283-4291.
3. D. Wittenberg and H. Gilman, *The Journal of Organic Chemistry*, 1958, **23**, 1063-1065.
4. S. C. Coste, B. Vlaisavljevich and D. E. Freedman, *Inorg. Chem.*, 2017, **56**, 8195-8202.
5. T. Pugh, V. Vieru, L. F. Chibotaru and R. A. Layfield, *Chemical Science*, 2016, **7**, 2128-2137.
6. T. Pugh, N. F. Chilton and R. A. Layfield, *Chemical Science*, 2017, **8**, 2073-2080.
7. T. M. Rookes, E. P. Wildman, G. Balázs, B. M. Gardner, A. J. Wooles, M. Gregson, F. Tuna, M. Scheer and S. T. Liddle, *Angew. Chem. Int. Ed.*, 2018, **57**, 1332-1336.
8. A. J. Ryan, J. W. Ziller and W. J. Evans, *Chemical Science*, 2020, DOI: 10.1039/C9SC05794C.
9. G. Lin, Z. Jin, Y. Zhang and W. Chen, *J. Organomet. Chem.*, 1990, **396**, 307-313.
10. W. J. Evans, I. Bloom, W. E. Hunter and J. L. Atwood, *Organometallics*, 1985, **4**, 112-119.
11. A. J. Ryan, L. E. Darago, S. G. Balasubramani, G. P. Chen, J. W. Ziller, F. Furche, J. R. Long and W. J. Evans, *Chemistry–A European Journal*, 2018, **24**, 7702-7709.
12. A. J. Ryan, J. W. Ziller and W. J. Evans, *Chemical Science*, 2020, **11**, 2006-2014.
12. APEX2 Version 2014.11-0, Bruker AXS, Inc.; Madison, WI 2014.
13. SAINT Version 8.34a, Bruker AXS, Inc.; Madison, WI 2013.
14. Sheldrick, G. M. SADABS, Version 2014/5, Bruker AXS, Inc.; Madison, WI 2014.
15. Sheldrick, G. M. SHELXTL, Version 2014/7, Bruker AXS, Inc.; Madison, WI 2014.
16. International Tables for Crystallography 1992, Vol. C., Dordrecht: Kluwer Academic Publishers.
17. (a) Spek, A.L. SQUEEZE, Acta Cryst. 2015, C71, 9-19., (b) Spek, A. L. PLATON, Acta. Cryst. 2009, D65, 148-155.

Epilogue

The intent of this study was to expand the understanding of $4f^n5d^1$ Ln(II) ions of the non-traditional ions Ln = La, Ce, Pr, Nd, Gd, Tb, Dy, Er, Ho and Lu by investigating a non-cyclopentadienyl ligand set, specifically the bis(trimethylsilylamide) NR_2 (R = $SiMe_3$). Over the course of this dissertation it was revealed that complexes of the type $[Ln(NR_2)_3]^{1-}$ for the smaller lanthanide ions Ln = Nd, Gd, Tb, Dy, Er, and Ho could be isolated from potassium reductions of their trivalent precursors $Ln(NR_2)_3$ (Chapter 1). An example of $[Y(NR_2)_3]^{1-}$ was finally isolated in a crystalline by switching to two equivalents of 18-crown-6 (18-c-6) to chelate the K^{1+} cation (Chapter 2). This Y(II) complex exhibited significantly less stability than its size congeners Ho and Er. While Y was long used as a convenient diamagnetic analog to assess the trivalent chemistry of the late lanthanides, it would appear that upon reduction this analogy should not be taken as true. Given that Y(II) involves a 4d electron as opposed to a 5d electron in the non-traditional Ln(II) ions, it is possible that there are parallels to the transition metals, where the 2nd row transition metals are known to be more reactive than their 3rd row congeners.

Reduction reactions were observed to occur with $Pr(NR_2)_3$ and $Ce(NR_2)_3$ through color changes to deep blue upon treatment with potassium even after filtration away from the reducing agent. The fact that these complexes were never isolated may be due to the fact that the size of the metal ion is simply too large to be sufficiently sterically saturated by the NR_2 ligand to allow isolation. Since the reduction is observed, it is possible that reduction in the presence of substrates could still take advantage of the reductive chemistry of these putative Ln(II) ions. In the case of La however, no color change to deep blue was ever observed. Reduction reactions

simply resulted in orangish brown solutions even when performed at low temperature indicating there could be other factors at play.

In the case of the smallest lanthanide Lu, reduction reactions were observed and darkly colored crystalline material was even recovered. Unfortunately, the crystals never survived long enough to make it onto a diffractometer. While $[Sc(NR_2)_3]^{1-}$ was observed to be stable at room temperature,[1] this was not the case for any of the analogous lanthanide complexes in this study. The most stable ion from throughout this work was found to be $[Gd(NR_2)_3]^{1-}$, neither the largest nor smallest ion and therefore neither the least nor most sterically saturated Ln(II) ion. It could be that there are electronic factors at play here that are worth investigating.

Reactivity studies of $[Ln(NR_2)_3]^{1-}$ complexes showed a range of reduction products (Chapters 3, 4, 5, and 6) many of which were never observed when looking at $[Cp'_3Ln]^{1-}$ reductive chemistry ($Cp' = C_5H_4SiMe_3$). One reason for this could be the ability of the $[Ln(NR_2)_3]^{1-}$ to maintain all three amide ligands upon reduction of a substrate. This could lead to cleaner reaction mixtures allowing for more facile crystal formation, a key technique in identification of these paramagnetic ions. Evident in the isolation of the reduced N_2 complexes of Chapter 4, $\{[(R_2N)_3Ln]_2[\mu\text{-}\eta^x\text{:}\eta^x\text{-}N_2]\}$, is the ability of the NR_2 ligands to splay back to accommodate steric strain. Solvent is a critical factor as well. The $[Ln(NR_2)_3]^{1-}$ complexes are all ether soluble allowing reaction chemistry to be carried out in a solvent less coordinating than THF. This was not the case for $[LnCp'_3]^{1-}$ complexes which were only soluble in THF.[2] In the case of the dinitrogen chemistry, where the strain on the NR_2 ligands is quite pronounced, use of Et_2O was essential to isolation of the complexes. The more strongly coordinating THF was able to displace an NR_2 ligand in this case. Displacement of an NR_2 ligand is not necessarily a bad

thing with the potential to lead new and interesting reaction products and it should be encouraged that any future work with these complexes be attempted in a variety of solvents.

The ability to isolate the end-on bound dinitrogen complexes with the lanthanide metals was unprecedented and unexpected. This result bridged a gap between the previously observed LnA_3/M chemistry that yielded the neutral Ln_2N_2 complexes $[(R_2N)_2(THF)Ln]_2(\mu\text{-}\eta^2\text{:}\eta^2\text{-}N_2)^3$ and the isolated Ln(II) ions. The isolation of the $[K(2.2.2\text{-crypt})]\{[(THF)(R_2N)_2Gd]_2[\mu\text{-}\eta^2\text{:}\eta^2\text{-}N_2]\}$ with only Gd(II) present as a possible reducing agent indicated that these Ln(II) ions are reducing enough to take $(N_2)^{2-}$ to $(N_2)^{3-}$. Examples of $(N_2)^{3-}$ ions with K coordinated showed that there was room for further coordination on the dinitrogen unit. With this result in mind it may worth investigating if LnI_2 reductants such as DyI_2 or NdI_2 could serve a similar function resulting in magnetically interesting trimetallic species. Additionally, the ability to isolate the end-on complexes could be expanded to other somewhat bulky donor scaffolds, namely, OAr′ (OAr′ = $OC_6H_2tBu_2$-2,6-Me-4) which was used in isolation of the first Nd, and Dy dinitrogen complexes[4] or CHR_2 (R = $SiMe_3$) a ligand known to make three coordinate lanthanide species in a manner similar to NR_2 .

The results from Chapters 5 and 6 lend themselves to similarities of the non-traditional ions to alkali metal reduction chemistry. This may be an area of the periodic table to look to when searching for new substrates and bond cleavage products to isolate.

Overall the sensitivity of these systems to reaction conditions such as solvent, chelating agent, and even choice of reductant leaves questions as to what can be discovered when the right combination is found. One thing that is certain is none of this chemistry would have come about if reactions that were thought to be impossible were not simply carried out.

References

1. D. H. Woen, G. P. Chen, J. W. Ziller, T. J. Boyle, F. Furche and W. J. Evans, *Angew. Chem. Int. Ed.*, 2017, **56**, 2050-2053.
2. M. R. MacDonald, J. E. Bates, J. W. Ziller, F. Furche and W. J. Evans, *Journal of the American Chemical Society*, 2013, **135**, 9857-9868.
3. W. J. Evans, D. S. Lee, D. B. Rego, J. M. Perotti, S. A. Kozimor, E. K. Moore and J. W. Ziller, *Journal of the American Chemical Society*, 2004, **126**, 14574-14582.
4. W. J. Evans, G. Zucchi and J. W. Ziller, *Journal of the American Chemical Society*, 2003, **125**, 10-11.

Appendix A

Structures and Spectroscopic Data of $\{[(R_2N)_3Ln]_2[\mu\text{-}\eta^x\text{:}\eta^x\text{-}N_2]\}^{2-}$ Complexes

(R = $SiMe_3$; Ln = Dy, x = 1, 2; Ln = Tb, Y, x = 1)

Introduction

The isolation of the $\{[(R_2N)_3Ln]_2[\mu\text{-}\eta^x\text{:}\eta^x\text{-}N_2]\}^{2-}$ (R = $SiMe_3$) complexes described in Chapter 4 suggested a trend that based on Ln ion size the coordination mode of the N_2 unit could be influenced, i.e. a smaller metal ion would result in more steric strain and a purely end on binding mode of the N_2 unit. Reactions to form Dy and Y analogs of $\{[(R_2N)_3Ln]_2[\mu\text{-}\eta^x\text{:}\eta^x\text{-}N_2]\}^{2-}$ were performed to test this theory. The synthesis of Y had the dual utility to allow spectroscopic probing into the DFT proposed triplet state of the N_2 unit by EPR spectroscopy.

Additionally, UV-visible spectroscopy of the N_2 complex $[K(crypt)]\{[(R_2N)_3Ln]_2[\mu\text{-}\eta^1\text{:}\eta^1\text{-}N_2]\}$ (crypt = 2.2.2-cryptand) was carried out at low temperatures in attempts to observe the reversible nature of the N_2 binding.

Results and Discussion

$[K_2(18\text{-c-}6)_3]\{[(R_2N)_3Dy]_2[\mu\text{-}\eta^x\text{:}\eta^x\text{-}N_2]\}$, 1-Dy. Dissolving solid $[K(18\text{-c-}6)_2][Dy(NR_2)_3]$ (R = $SiMe_3$; 18-c-6 = 18-crown-6) in dinitrogen saturated Et_2O at −78 °C produced an immediate color change to yellow. Placement in the glovebox freezer at −35 °C resulted in small yellow crystals of $[K(18\text{-c-}6)_2]\{[(R_2N)_3Dy]_2[\mu\text{-}\eta^x\text{:}\eta^x\text{-}N_2]\}$ (x = 1, 2), **1-Dy.** This complex was found to be isomorphous to $[K(18\text{-c-}6)_2]\{[(R_2N)_3Gd]_2[\mu\text{-}\eta^x\text{:}\eta^x\text{-}N_2]\}$ of Chapter 4. **2-Dy** showed a 50:50 disordering of end on and side on coordination of the dinitrogen unit, Figure A.1. This was unexpected given that the Tb analog showed a purely end on coordination mode. The structure was of low quality and allowed for observation of connectivity only.

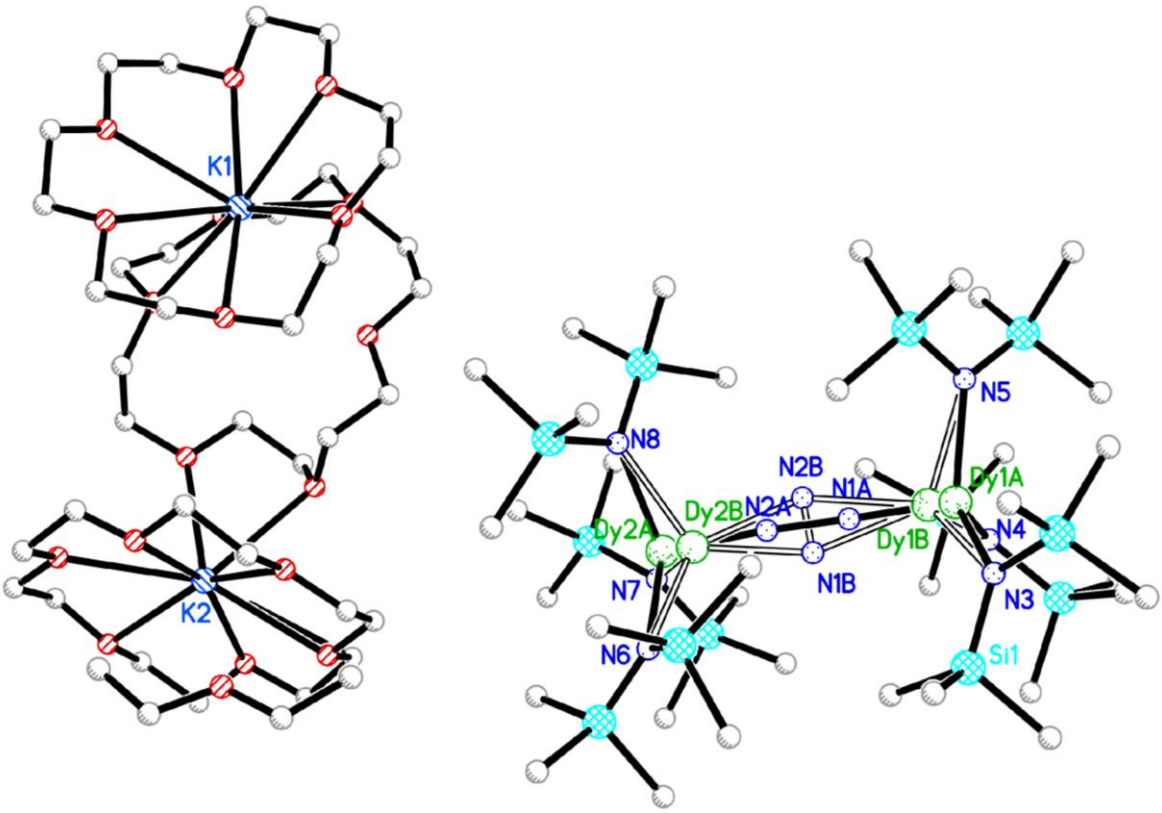

Figure A.1. Ball and stick representation of **1-Dy.**

[K(crypt)]$_2${[(R$_2$N)$_3$Y]$_2$[μ-η^1:η^1-N$_2$]}, 2-Y. Addition of a solution containing Y(NR$_2$)$_3$ and 2.2.2-cryptand in dinitrogen saturated Et$_2$O to a pre chilled vial (− 78 °C) of KC$_8$ in a dinitrogen filled glove box resulted in an immediate color change from colorless to yellow. Filtration followed by placement in the glovebox freezer at −35 °C resulted in small yellow crystals of [K(crypt)]$_2${[(R$_2$N)$_3$Y]$_2$[μ-η^1:η^1-N$_2$]}, **2-Y**. The crystals were suitable for X-ray diffraction but were only of quality to support a connectivity structure. **2-Y** was not isomorphous with any of the other [K(crypt)]$_2${[(R$_2$N)$_3$Ln]$_2$[μ-η^x:η^x-N$_2$]} complexes from Chapter 4. **2-Y**

crystallized in the $P2_1/n$ space group and displayed a purely end-on coordination of the bridging N_2 unit to the two Y centers with two outer sphere $[K(crypt)]^{1+}$ cations, Figure A.2.

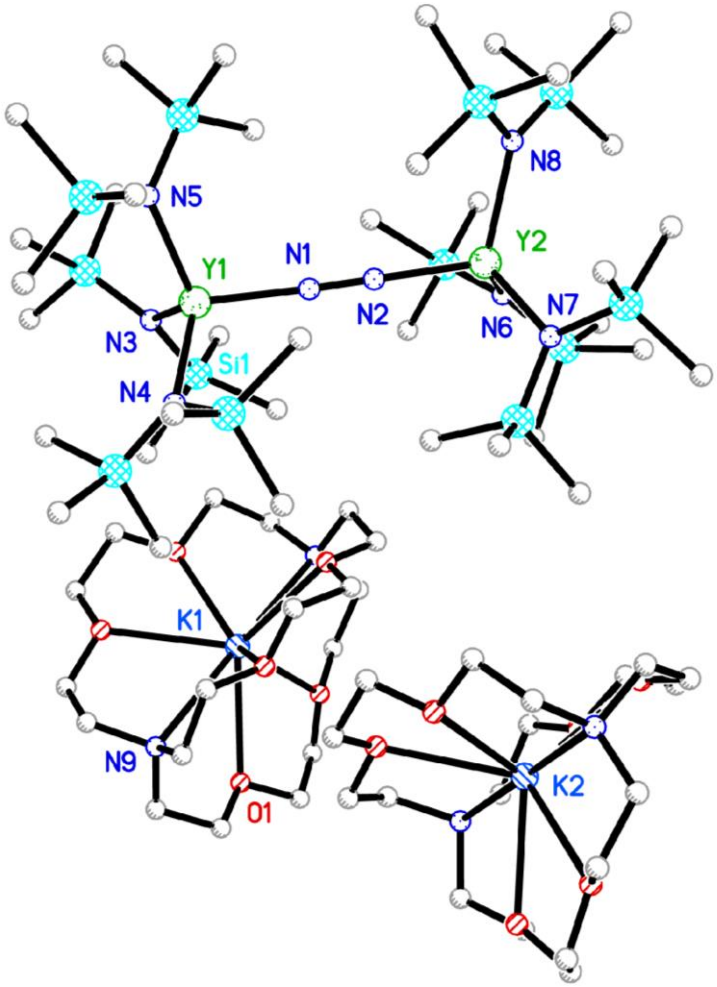

Figure A.2. Ball and stick representation of **2-Y**.

EPR Spectroscopy of 2-Y. 2-Y was generated in situ as stated above before being filtered into an EPR tube which was immediately frozen and transported to the EPR spectrometer where 8 K spectra in both parallel and perpendicular mode were collected on the yellow solution.

The spectra were not so straightforward but are displayed below. The parallel mode spectrum shows features at g values of 22, 11.7, 7.1, 4.9, 3.7 and 2.5. The perpendicular mode spectrum shows two signals somewhat resembling the two-line pattern commonly observed in Y(II) complexes. If taken as a doublet, however, the signal is centered at g = 2.82 with an A value of 2090 G, these values are not consistent with any Y(II) species observed to date. There also appears to be fine structure on the two lines of the perpendicular mode spectrum potentially originating from the nitrogen donor atoms. Clearly further investigation is required.

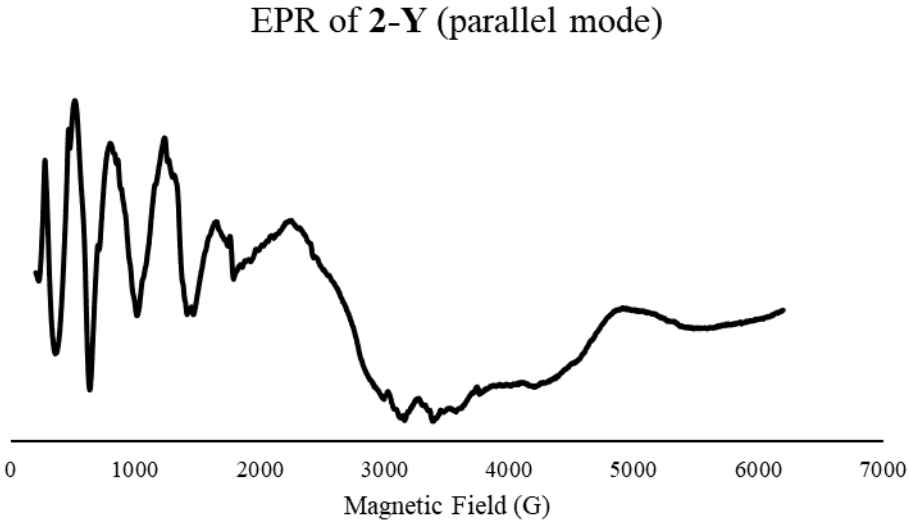

Figure A.3. Parallel mode EPR spectrum of **2-Y** taken on a X-band EPR spectrometer collected at 8K.

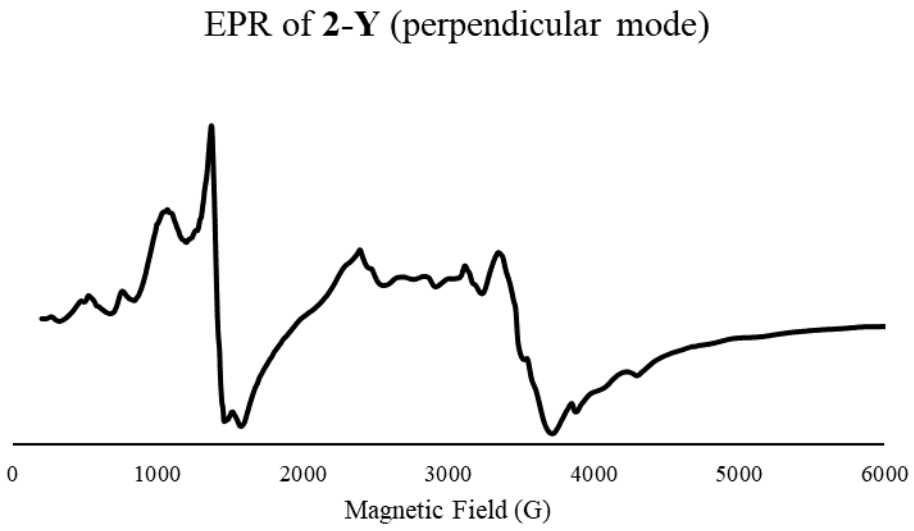

Figure A.4. Perpendicular mode EPR spectrum of **2-Y** collected on a X-band EPR spectrometer collected at 8K.

Optical Spectra of [K(crypt)]{[(R$_2$N)$_3$Tb]$_2$[μ-η^1:η^1-N$_2$]}, 2-Tb. Low temperature UV-visible experiments were performed on the [K(crypt)]{[(R$_2$N)$_3$Tb]$_2$[μ-η^x:η^x-N$_2$]} complex described in Chapter 4 in an attempt to investigate the reversible binding nature of the dinitrogen unit. To perform the experiment solid [K(crypt)][Tb(NR$_2$)$_3$] was dissolved in Et$_2$O at −78 °C in a 1 cm UV-vis cell fitted with a septum. The spectrum collected at −78 °C showed a two signals, Figure A.5, one at 600 nm which is consistent with divalent ion in solution and one at 400 nm which is consistent with a reduced N$_2$ species like that observed for [K(crypt)]{[(R$_2$N)$_3$Sc]$_2$[μ-η^x:η^x-N$_2$]}[1]. There did not appear to be any growing of the 400 nm peak as the temperature was held steady but a reduction of the peak at 600 nm was observed over time.

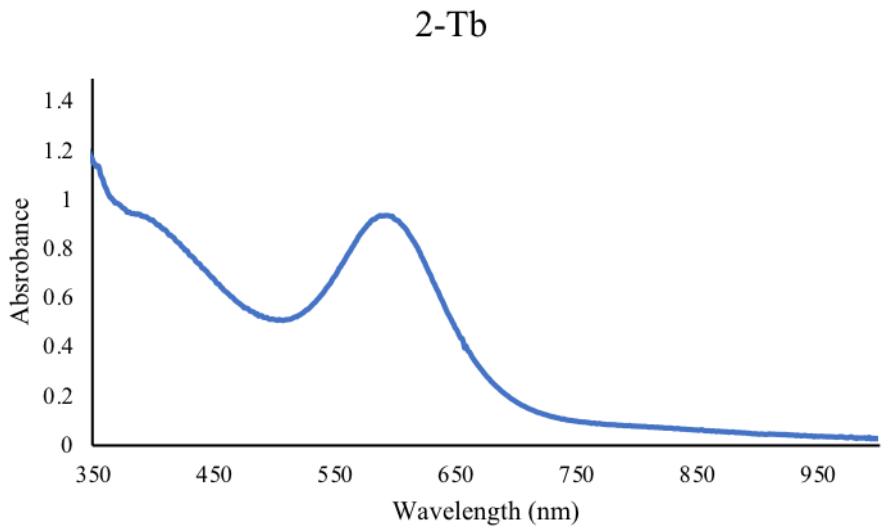

Figure A.5. UV-Visible spectrum of **2-Tb** collected in Et_2O at −78 °C

Experimental Details

All manipulations and syntheses described below were conducted with the rigorous exclusion of air and water using standard Schlenk line and glovebox techniques under an argon or dinitrogen atmosphere. Solvents were sparged with UHP argon and dried by passage through columns containing Q-5 and molecular sieves prior to use. $[K(crypt)]Tb(NR_2)_3]$[2] and $[K(18\text{-}c\text{-}6)]Dy(NR_2)_3]$[3] were synthesized as previously reported. Electronic absorption spectra were recorded in a 1 cm cuvette on an 8453 Agilent UV-Vis spectrometer equipped with an Unisoku Unispeks cryostat. X-band (9.28 GHz) EPR spectra were collected as frozen solutions using a Bruker EMX spectrometer equipped with an ER041XG microwave bridge.

$[K_2(18\text{-}c\text{-}6)_3]\{[(R_2N)_3Dy]_2[\mu\text{-}\eta^x\text{:}\eta^x\text{-}N_2]\}$, 1-Dy. Solid $[K(18\text{-}c\text{-}6)_2][Dy(NR_2)_3]$ was dissolved in dinitrogen saturated Et_2O at −78 °C. The solution immediately turned yellow and was replaced in the glovebox freezer at −35 °C. Small yellow crystals of **1-Dy** formed overnight.

[K(crypt)]$_2${[(R$_2$N)$_3$Y]$_2$[μ-η^x:η^x-N$_2$]}, 2-Y. Y(NR$_2$)$_3$ and 2.2.2-cryptand were added as a solution in dinitrogen saturated Et$_2$O to a pre chilled vial (− 78 °C) of resulting in an immediate color change from colorless to yellow. The solution was filtered cold and placed in the glovebox freezer at −35 °C. Small yellow crystals of **2-Y were** formed overnight.

References

1. D. H. Woen, G. P. Chen, J. W. Ziller, T. J. Boyle, F. Furche and W. J. Evans, *Journal of the American Chemical Society*, 2017, **139**, 14861-14864.
2. A. J. Ryan, L. E. Darago, S. G. Balasubramani, G. P. Chen, J. W. Ziller, F. Furche, J. R. Long and W. J. Evans, *Chemistry–A European Journal*, 2018, **24**, 7702-7709.
3. A. J. Ryan, J. W. Ziller and W. Evans, *Chemical Science*, 2019, **Under Review**.

Appendix B

Attempts to synthesize $U(hfac)_3(solvent)_x$

Introduction

There is interest in generating volatile uranium complexes for applications in isotope enrichment for the nuclear fuel process. The hexafluoracetylacetonate (hfac) ligand was found to coordinate to the lanthanide metals and create volatile monomeric complexes capable at being sublimed under vacuum at 80 °C.[1] An example of a $U(hfac)_3$(diglyme) complex was synthesized once by former Evans group member Dimitri Giarikos from reactions $(UO_2)^{2+}$ with the protonated ligand Hhfac, but this was not ever reproduced.[2]

Results and Discussion

Initial investigations were carried out through reaction of UI_3 and Na(hfac) in an effort to produce the $U(hfac)_3$ complex described above. Addition of solid UI_3 to a solution of Na(hfac) in THF led to a color change to brown. Upon filtration and layering into hexanes crystals of an octa(uranium) cluster were isolated reproducibly from the reaction mixture. The structure features eight uranium centers and eight Na ions twelve fully intact $(hfac)^{1-}$ ligands in addition to six interstitial O^{2-} donors two fused ligands of the type $(C_{10}H_6F_{12}O_4)^{2-}$ two fused ligands of the type $[(O_5C_6H_2(CF_3)_2]^{5-}$ and four fragmented hfac ligands of the type $O_2C(CF_3)^{1-}$, **$[U_8Na_8]$**. The total anionic charge arising from the complex was counted at −42. Taking into consideration the eight Na^{1+} ions that leaves a charge of −36 to be accounted for by the eight U centers. Considering the two most stable oxidation states of uranium, U(IV) and U(VI), the charge can be balanced considering the eight U ions in the cluster to be composed of two U(VI) centers and six U(IV) ions. Later crystallizations were performed in the presence of a magnet and crystal

formation was greatest in the area covered by the magnet. This would be consistent with the suggestion of a high number of U(IV) ions in the complex giving the cluster a high moment.

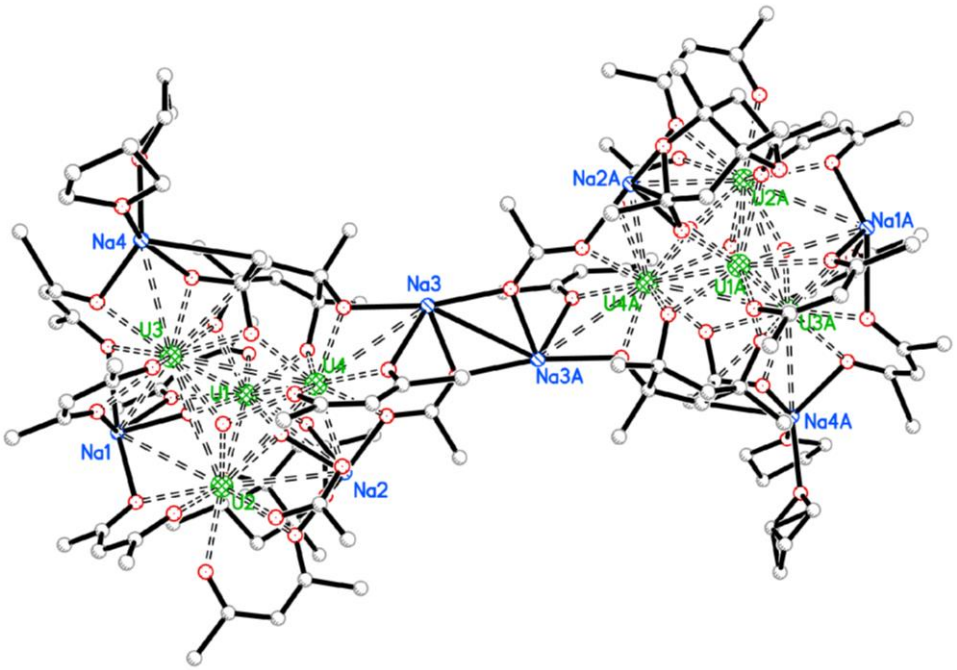

Figure B.1. Ball and stick representation of the octa(uranium) cluster octa(sodium) cluster, **[U_8Na_8]**. Fluorine and hydrogen atoms excluded for clarity.

If the same reaction was performed at low temperature (−78 °C), a different product was isolated, Figure B.2. The structure from the low temperature reaction showed a dimeric species of two U(IV) centers bridged by a fused hfac ligand, $[(hfac)_2U(THF)_2]_2(O_4C_{10}F_{12})$. The structure shows a reductive coupling of two hfac ligands to form the tetra-anionic $(O_4C_{10}F_{12})^{4-}$ unit. This result sheds light on the difficulties in isolating $U(hfac)_3$(solvent) given that the U(III) ion is obviously reducing enough to react with the hfac ligand.

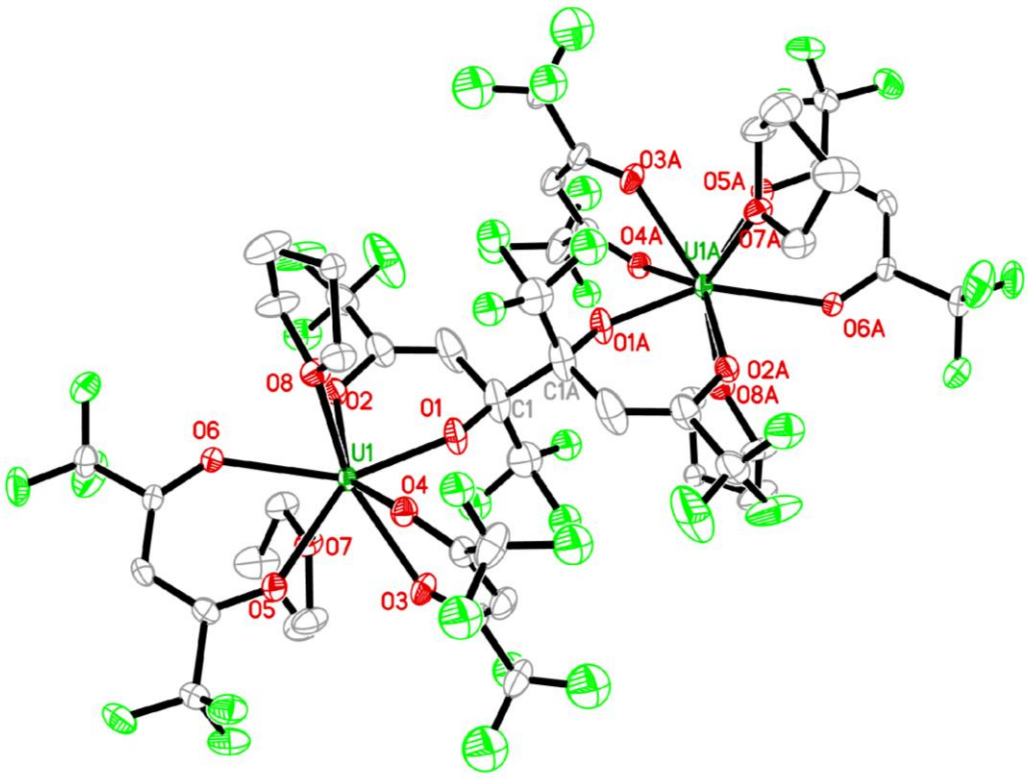

Figure B.2. Thermal ellipsoid plot of $[(hfac)_2U(THF)_2]_2(O_4C_{10}F_{12})$ drawn at the 50% probability level. Hydrogen atoms excluded for clarity.

Experimental Details

All manipulations and syntheses described below were conducted with the rigorous exclusion of air and water using standard Schlenk line and glovebox techniques under an argon or dinitrogen atmosphere. Solvents were sparged with UHP argon and dried by passage through columns containing Q-5 and molecular sieves prior to use. Na(hfac) was dissolved in THF and stored over 3Å molecular sieves for a week before use. UI_3 was synthesized according to literature precedent.[3]

[U_8Na_8]. Addition of UI_3 to a stirring solution of Na(hfac) at room temperature results in the formation a color change to brown. Upon filtration and layering into hexanes, crystals of **[U_8Na_8]** formed overnight.

[$(hfac)_2U(THF)_2]_2(O_4C_{10}F_{12}$). Following the same procedure described for the formation of **[U_8Na_8]** but at −78 °C, crystals of $[(hfac)_2U(THF)_2]_2(O_4C_{10}F_{12})$ were isolated overnight when the layered solution was placed in the glovebox freezer at −35 °C.

References

1. W. J. Evans, D. G. Giarikos, M. A. Johnston, M. A. Greci and J. W. Ziller, *J. Chem. Soc., Dalton Trans.*, 2002, DOI: 10.1039/B104095M, 520-526.
2. D. G. Giarikos, PhD, University of California - Irvine, 2003.
3. W. J. Evans, S. A. Kozimor, J. W. Ziller, A. A. Fagin and M. N. Bochkarev, *Inorg. Chem.*, 2005, **44**, 3993-4000.

Appendix C

Investigation of $C_5Me_4(SiMe_2{}^tBu)$ as a Ligand for Rare Earth and Uranium Complexes

Introduction

Recent work by Mills and coworkers has resulted in a near linear dysprosocenium complex displaying magnetic hysteresis up to 60 K, $[DyCp^{ttt}_2]^{1+}$ ($Cp^{ttt} = C_5H_2(CMe_3)_3$).[1] The near linearity was achieved by utilizing the sterically demanding tri(tert-butyl)-substituted cyclopentadienyl ligand Cp^{ttt}. Long and Harvey expanded upon this work by generating a series of near-linear dysprococenium complexes $[Dy(C_5{}^iPr_4X)]^{1+}$ using ligands $C_5{}^iPr_4X$ where X was varied between H Me, Et and ^{i}Pr and measuring their subsequent magnetic properties.[2] The largest Cp(cnt)–Dy–Cp(cnt) angle was achieved with $C_5{}^iPr_5$. Surprisingly, this complex did not show the highest blocking temperature. Rather, the $C_5{}^iPr_4Me$ ligand showed a blocking temperature 6 K higher.[2] The result was rationalized by the increase in bond distances found in $[(C_5{}^iPr_5)_2Dy]^{1+}$ vs $[(C_5{}^iPrMe)_2Dy]^{1+}$ ligand which led to a decreased reinforcement the magnetic anisotropy. The $C_5{}^iPr_5$ ligand was however found to be useful in the stabilization of Ln(II) ions for Dy and Tb in the form of $(C_5{}^iPr_5)_2Ln$.[3]

To this end, the $C_5Me_4(SiMe_2{}^tBu)$ (Cp^S) ligand was investigated due to its ability to facilitate linear bis(cyclopentadienyl) complexes of both Pb[4] and Sn[5], which, even with the relatively bulky $C_5H_3(SiMe_3)_2$ ligand, form bent metallocene complexes[6-8] similar to those seen in the lanthanides.

Results and Discussion

Initial reactions were carried out with two equivalents of $LiCp^S$ ($Cp^S = C_5Me_4(SiMe_2{}^tBu)$) and $Y(OTf)_3$ as the rare earth precursor in THF. While NMR evidence suggested formation of the a yttrium Cp^S product, no crystalline material was isolated.

The most success with this ligand was observed with UI_3 as the starting material. Reaction of UI_3 with two equivalents of $LiCp^S$ in THF resulted in a gradual color change from purple to green. Removal of THF and extraction into toluene followed by cooling in the glovebox freezer resulted in crystals of $Cp^S{}_2U(\mu\text{-}I_2)Li(THF)_2$ as determined by X-ray diffraction, Figure C.1.

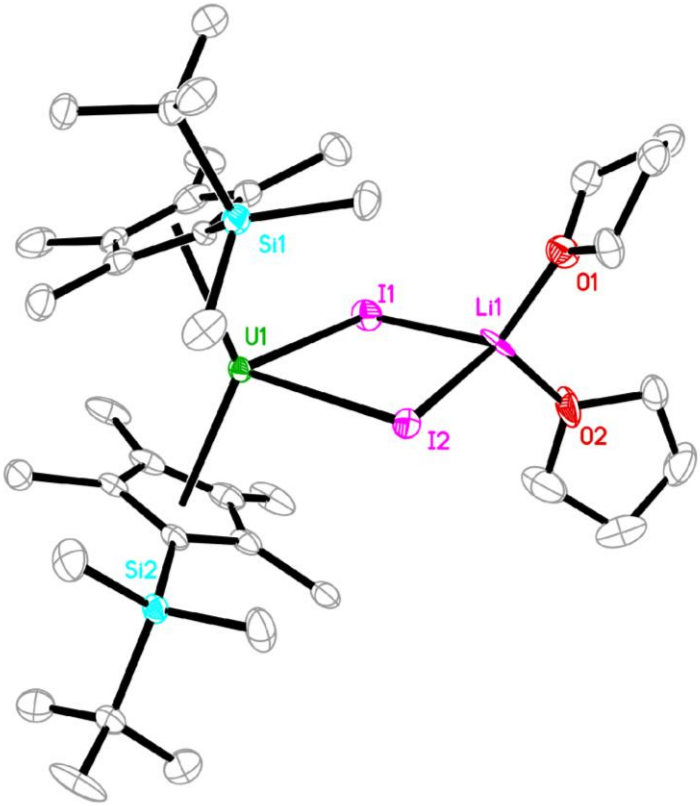

Figure C.1. Thermal ellipsoid plot of $Cp^S{}_2U(\mu\text{-}I_2)Li(THF)_2$ drawn at the 50% probability level. Hydrogen atoms excluded for clarity.

Reactions of $Cp^{S}_{2}U(\mu\text{-}I_2)Li(THF)_2$ in toluene over KC_8 were carried out in order to evaluate the reductive chemistry. Upon filtration the KC_8 appeared to be used up and the toluene solution was layered into hexanes and placed in the glovebox freezer at −35 °C. Bright green crystals formed overnight. X-ray diffraction showed the structure to be the monoiodide complex $Cp^{S}_{2}UI(THF)$, Figure C.2.

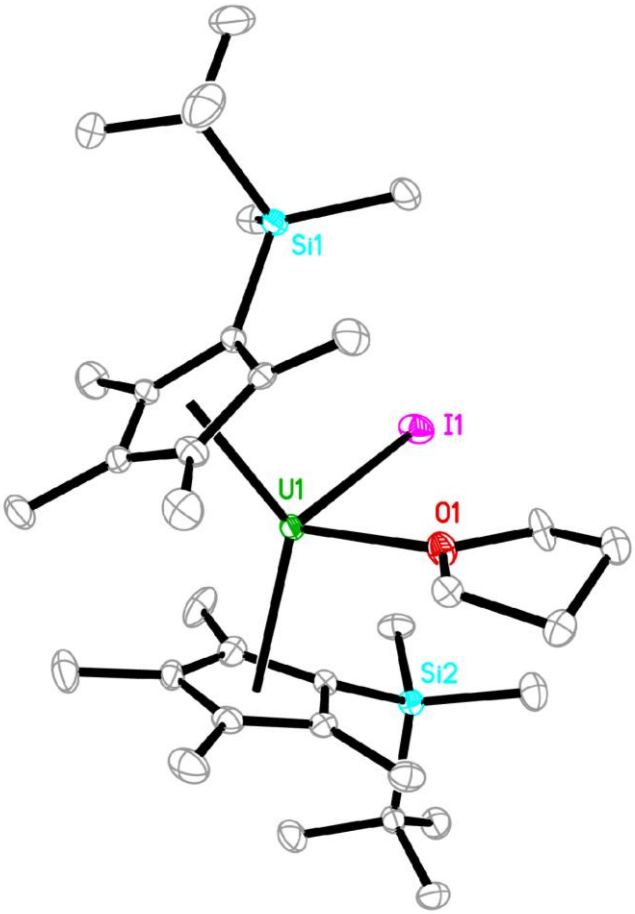

Figure C.2. Thermal ellipsoid plot of $Cp^{S}_{2}UI(THF)$ drawn at the 50% probability level. Hydrogen atoms excluded for clarity.

Experimental Details

All manipulations and syntheses described below were conducted with the rigorous exclusion of air and water using standard Schlenk line and glovebox techniques under an argon or dinitrogen atmosphere. Solvents were sparged with UHP argon and dried by passage through columns containing Q-5 and molecular sieves prior to use. $Y(OTf)_3$ was dried on high vacuum before use. UI_3[9] and $LiC_5Me_4(SiMe_2{}^tBu)$ [4] were synthesized as previously reported.

Reaction of $Y(OTf)_3$ with $LiCp^S$. $LiCp^S$ was added as a solution in THF to a stirring solution of $Y(OTf)_3$ in THF. The solution was allowed to stir overnight and a white precipitate gradually formed. The solvent was removed and solids were extracted into toluene. No crystals were formed upon placement in the glovebox freezer at −35 °C.

$Cp^S{}_2U(\mu\text{-}I_2)Li(THF)_2$. $LiCp^S$ was added as a solution in THF to a stirring suspension of UI_3 in THF. The solution was allowed to stir overnight, and a white precipitate gradually formed. The solvent was removed, and solids were extracted into toluene. Crystals of $Cp^S{}_2U(\mu\text{-}I_2)Li(THF)_2$ grew from toluene overnight.

$Cp^S{}_2UI(THF)$. $Cp^S{}_2U(\mu\text{-}I_2)Li(THF)_2$ was dissolved in toluene and added to a vial containing KC_8. The reaction was allowed to proceed over 3 days before being filtered and layered into hexanes. Crystals of $Cp^S{}_2UI(THF)$ formed overnight.

References

1. C. A. P. Goodwin, F. Ortu, D. Reta, N. F. Chilton and D. P. Mills, *Nature*, 2017, **548**, 439-442.
2. K. Randall McClain, C. A. Gould, K. Chakarawet, S. J. Teat, T. J. Groshens, J. R. Long and B. G. Harvey, *Chemical Science*, 2018, **9**, 8492-8503.
3. C. A. Gould, K. R. McClain, J. M. Yu, T. J. Groshens, F. Furche, B. G. Harvey and J. R. Long, *Journal of the American Chemical Society*, 2019, **141**, 12967-12973.
4. S. P. Constantine, P. B. Hitchcock and G. A. Lawless, *Organometallics*, 1996, **15**, 3905-3906.
5. S. P. Constantine, P. B. Hitchcock, G. A. Lawless and G. M. De Lima, *Chem. Commun.*, 1996, DOI: 10.1039/CC9960001101, 1101-1102.
6. M. P. Coles, P. B. Hitchcock, M. F. Lappert and A. V. Protchenko, *Organometallics*, 2012, **31**, 2682-2690.
7. J. L. Atwood, W. E. Hunter, A. H. Cowley, R. A. Jones and C. A. Stewart, *J. Chem. Soc., Chem. Commun.*, 1981, DOI: 10.1039/C39810000925, 925-927.
8. A. H. Cowley, P. Jutzi, F. X. Kohl, J. G. Lasch, N. C. Norman and E. Schlüter, *Angewandte Chemie International Edition in English*, 1984, **23**, 616-617.
9. W. J. Evans, S. A. Kozimor, J. W. Ziller, A. A. Fagin and M. N. Bochkarev, *Inorg. Chem.*, 2005, **44**, 3993-4000.